Long-term variability of ocean chemistry: Implications for deep-time palaeothermometry and the carbon cycle

Dissertation
zur Erlangung des Doktorgrades der Naturwissenschaften

vorgelegt beim Fachbereich Geowissenschaften/Geographie (FB 11)
der Johann Wolfgang Goethe-Universität

in Frankfurt am Main

von
Romi Nambiar
aus Ahmedabad, India

Frankfurt 2024

(D 30)

vom Fachbereich Geowissenschaften/ Geographie (FB 11) der
Johann Wolfgang Goethe-Universität als Dissertation angenommen.

Dekan:
Prof. Dr. Joachim Curtius

Gutachter:
Prof. Dr. Wolfgang Müller
Dr. David Evans

Datum der Disputation: 18th April 2024

Abstract

While high-quality climate reconstructions of some past warm periods in the Cenozoic era now exist, the geological processes responsible for driving the observed long-term changes in atmospheric CO_2 are not sufficiently well understood. The long-term change in atmospheric CO_2 across the Cenozoic has been proposed to be driven by processes such as terrestrial weathering, organic carbon production and burial, reverse weathering, and volcanic degassing. One way of constraining the relative importance of the various driving forces proposed so far is to better understand the degree to which ocean chemistry has changed because the chemistry of seawater responds to geologic processes that drive atmospheric CO_2. In addition, knowledge of the concentration of the major elements in seawater is crucial for accurately applying proxies such as those based on the boron isotopic composition and Mg/Ca of marine carbonates (a proxy for palaeo pH/CO_2 and palaeotemperature, respectively). Previously reported records of seawater composition are primarily derived from fluid inclusions in marine evaporites; however, the results are sparse due to the limited availability of such deposits. In this thesis, changes in the Eocene seawater chemistry were reconstructed using trace element (elements/Ca) and isotopic ($\delta^{26}Mg$) proxies in a Larger Benthic Foraminifera (LBFs), i.e., *Nummulites* sp., to constrain the driving processes of long-term changes in seawater chemistry.

To achieve the objective of this thesis, first, a measurement protocol was established using LA-ICPMS to measure the K/Ca ratio simultaneously with other element/calcium ratios, which is challenging due to the interference of ArH^+ on K^+. Utilising this newly established measurement protocol, laboratory-cultured *Operculina ammonoides* grown at different seawater calcium concentrations ($[Ca^{2+}]$), repeated at different temperatures, as well as modern *O. ammonoides* collected from different regions exhibiting a range of seawater parameters, were investigated. A significant correlation was observed between K/Ca_{sw} and

K/Ca_{LBF}, allowing K/Ca_{LBF} to potentially be used as a proxy for seawater major ion reconstructions. In addition, modern *O. ammonoides* demonstrated no significant influence of most seawater parameters (temperature, salinity, pH, or $[CO_3^{2-}]$) on K/Ca_{LBF}. Modern *O. ammonoides* were also assessed for their Mg isotopic composition ($\delta^{26}Mg$), revealing no significant effect of temperature or salinity on $\delta^{26}Mg_{LBF}$. Furthermore, the Mg isotopic fractionation in *O. ammonoides* was found to be close to that of inorganic calcite, indicating minimal vital effects in these large benthic foraminifera.

Operculina ammonoides is the nearest living relative of the abundant Eocene genus *Nummulites*, enabling the reconstruction of seawater chemistry using the calibration based on *O. ammonoides*. The trace elemental/calcium proxies, including Na/Ca, K/Ca, and Mg/Ca, as well as the $\delta^{26}Mg$ proxy, were investigated in Eocene *Nummulites*. The result showed that during the Eocene, $[Ca^{2+}]_{sw}$ was 1.6-2 times higher, while $[K^+]_{sw}$ was ~2 times lower than the modern seawater composition. Furthermore, $[Mg^{2+}]_{sw}$ decreased from the early Eocene ($54.3^{+7.9}_{-9.6}$ mmol kg^{-1} at ~55 Ma) to Late Eocene ($37.8^{+4.4}_{-4.3}$ mmol kg^{-1} at ~31 Ma), followed by an increase toward modern seawater [Mg]. In contrast, the variability in $\delta^{26}Mg_{sw}$ values remained within a narrow range of ~0.3 ‰ throughout the Cenozoic. The reconstructed $[Ca^{2+}]_{sw}$ agrees with the suggestion that Cenozoic seawater chemistry changes can be explained via a change in the seafloor spreading rate. When combined with existing records, the observed minimal change in $\delta^{26}Mg_{sw}$ with an increase in $[Mg^{2+}]_{sw}$ suggests an additional possible role of a decrease in the formation of authigenic clay minerals coincident with the Cenozoic decline in deep ocean temperature, which is also supported by the increase in the $[K^+]_{sw}$ reconstructed here for the first time. This finding highlights that the reduction in seafloor-spreading rate and decline in reverse weathering during the Cenozoic era has played a significant role in the evolution of seawater chemistry, emphasizing the importance of these processes in driving long-term changes in the carbon cycle.

Kurzzusammenfassung

Zwar gibt es inzwischen qualitativ hochwertige Klimarekonstruktionen für einige vergangene Warmzeiten im Känozoikum, doch sind die geologischen Prozesse, die für die beobachteten langfristigen Veränderungen des atmosphärischen CO_2 verantwortlich sind, nicht hinreichend gut bekannt. Es wird angenommen, dass die langfristigen Veränderungen des atmosphärischen CO_2 im Känozoikum durch Prozesse wie terrestrische Verwitterung, Produktion und Ablagerung von organischem Kohlenstoff, umgekehrte Verwitterung und vulkanische Entgasung verursacht werden. Eine Möglichkeit, die relative Bedeutung der verschiedenen bisher vorgeschlagenen Antriebskräfte einzugrenzen, besteht darin, besser zu verstehen, inwieweit sich die Ozeanchemie verändert hat, weil die Chemie des Meerwassers auf geologische Prozesse, die den CO_2 Gehalt der Atmosphäre beeinflussen, reagiert. Für die präzise Anwendung von geochemischen Proxys ist darüber hinaus das Wissen über die Konzentration der wichtigsten Elemente im Meerwasser, wie z. B. der Bor-Isotopenzusammensetzung und des Mg/Ca-Gehalts von Meereskarbonaten (ein Näherungswert für pH/CO_2 bzw. die Paläotemperatur), von entscheidender Bedeutung. Bisherige Aufzeichnungen über die Zusammensetzung des Meerwassers stammen in erster Linie von Flüssigkeitseinschlüssen in marinen Evaporiten; die Ergebnisse sind jedoch aufgrund der begrenzten Verfügbarkeit dieser Ablagerungen spärlich. In dieser Arbeit wurden Veränderungen in der Meerwasserchemie des Eozäns anhand von Spurenelementen (Elemente/Ca) und Isotopen ($\delta^{26}Mg$) in benthischen Großforaminiferen (*Nummulites* sp.) rekonstruiert, um die treibenden Prozesse langfristiger Veränderungen der Meerwasserchemie einzugrenzen.

Um das Ziel dieser Arbeit zu erreichen, wurde zunächst ein Messprotokoll unter Verwendung von LA-ICPMS erstellt, um das K/Ca-Verhältnis gleichzeitig mit anderen Element/Calcium-Verhältnissen zu messen, was aufgrund der Interferenz von ArH^+ auf K^+

eine Herausforderung darstellt. Unter Verwendung dieses neu eingeführten Messprotokolls wurden *Operculina ammonoides* untersucht, die in unterschiedlichen Meerwasser-Kalziumkonzentrationen ($[Ca^{2+}]$) und bei verschiedenen Temperaturen im Labor kultiviert wurden. Zusätzlich wurden moderne, im Gelände gesammelte *O. ammonoides* aus verschiedenen Regionen, die in eine Reihe von verschiedenen Meerwasserparametern gewachsen sind, untersucht. Es wurde eine signifikante Korrelation zwischen K/Ca_{sw} und K/Ca_{LBF} festgestellt, so dass K/Ca_{LBF} möglicherweise als Proxy für die Rekonstruktion der häufigsten Ionen im Meerwasser verwendet werden kann. Darüber hinaus war in den modernen *O. ammonoides* kein signifikanter Einfluss der meisten Meerwasserparameter (Temperatur, Salzgehalt, pH-Wert oder $[CO_3^{2-}]$) auf K/Ca_{LBF} zu erkennen. Bei modernen *O. ammonoides* wurde zudem die Mg-Isotopenzusammensetzung untersucht, wobei sich kein signifikanter Einfluss von Temperatur und Salzgehalt auf $\delta^{26}Mg_{LBF}$ ergab. Darüber hinaus wurde festgestellt, dass die Mg-Isotopenfraktionierung in *O. ammonoides* nahe an der von anorganischem Kalzit liegt, was auf minimale Vitaleffekte hinweist.

Operculina ammonoides ist die nächste lebende Verwandte der im Eozän weit verbreiteten Gattung *Nummulites*, was die Rekonstruktion vergangener Meerwasserchemie anhand von Nummuliten durch eine Kalibrierung an *O. ammonoides* ermöglicht. An den eozänen Nummuliten wurden Spurenelement-/Kalzium-Proxys einschließlich Na/Ca, K/Ca und Mg/Ca sowie $\delta^{26}Mg$-Proxys untersucht. Das Ergebnis zeigte, dass $[Ca^{2+}]_{sw}$ im Eozän 1,6-2 mal höher war, während $[K^+]_{sw}$ ~2 mal niedriger war verglichen mit der modernen Meerwasserzusammensetzung. Außerdem nahm $[Mg^{2+}]_{sw}$ vom frühen Eozän ($54.3^{+7.9}_{-9.6}$ mmol kg^{-1} bei ~55 Ma) bis zum späten Eozän ($37.8^{+4.4}_{-4.3}$ mmol kg^{-1} bei ~31 Ma) ab, gefolgt von einem Anstieg in Richtung der modernen $[Mg^{2+}]_{sw}$-Werte. Im Gegensatz dazu blieb die Variabilität der $\delta^{26}Mg_{sw}$-Werte während des gesamten Känozoikums innerhalb eines engen Bereichs von ~0,3 ‰. Die rekonstruierten $[Ca^{2+}]_{sw}$-Werte passen zu dem Vorschlag, dass die Veränderungen in der Meerwasserchemie im Känozoikum durch eine Veränderung der

Ozeanbodenspreizungsrate erklärt werden können. In Verbindung mit den vorhandenen Aufzeichnungen deutet die beobachtete minimale Änderung von $\delta^{26}Mg_{sw}$ bei einem Anstieg von $[Mg^{2+}]_{sw}$ darauf hin, dass der Rückgang der Bildung authigener Tonminerale zusammen mit dem känozoischen Rückgang der Tiefseetemperatur eine mögliche Rolle spielt, was auch durch den hier erstmals rekonstruierten Anstieg von $[K^{+}]_{sw}$ bekräftigt wird. Dieses Ergebnis hebt hervor, dass die Verringerung der Ozeanbodenspreizungsrate und der Rückgang der umgekehrten Verwitterung während des Känozoikums eine bedeutende Rolle bei der Entwicklung der Meerwasserchemie gespielt hat, was die Wichtigkeit dieser Prozesse für langfristige Veränderungen im Kohlenstoffkreislauf betont.

Zusammenfassung

Die Bestimmung vergangener Veränderungen in der Meerwasserchemie ist ein wichtiger Anknüpfungspunkt um großräumige geologische Prozesse, die langfristige Veränderungen im Kohlenstoffkreislauf bewirken, besser verstehen zu können. In dieser Arbeit wurden Veränderungen von $[Ca^{2+}]_{sw}$, $[Mg^{2+}]_{sw}$, $[K^{+}]_{sw}$ und $\delta^{26}Mg_{sw}$ im Eozän anhand von Spurenelement-/Calcium-Proxies (K/Ca, Na/Ca, Mg/Ca) in Kombination mit zuvor berichteten Mg/Ca_{sw}-Werten (Evans et al., 2018) sowie Messungen der Magnesium-Isotopenzusammensetzung ($\delta^{26}Mg$) in benthischen Großforaminiferen (*Nummulites* sp.) rekonstruiert.

In Kapitel 2 wurde das Messprotokoll für die Messung von K/Ca in schwach K-haltigen Karbonatproben mittels LA-ICPMS entwickelt (Nambiar et al., 2024). Es wurde eine Reihe von Referenzmaterialien untersucht, darunter verschiedene MPI-DING-Gläser (GOR 128-G, GOR 132-G, ATHO-G, KL2-G und StHs 6/80-G) sowie Karbonat-Referenzstandards (JCp-1NP, JCt-1NP und MACS-3NP) unter Verwendung von LA-ICPMS im Modus mittlerer und hoher Massenauflösung. Die Ergebnisse zeigen, dass die mittlere Massenauflösung (MR) ausreicht, um die Auswirkungen der ArH^{+}-Interferenz auf den K^{+}-Peak zu minimieren und genaue Ergebnisse (<1 %) mit einer langfristigen Präzision (mittlere Reproduzierbarkeit) von <6 % (RSD) für den Karbonat-Referenzstandard JCp-1NP zu erzielen. Darüber hinaus zeigte sich, dass Kalium anfällig für Oberflächenkontaminationen ist und eine sorgfältige Oberflächenreinigung, Vorabtragung oder Datenvorverarbeitung durch Eliminierung der ursprünglichen (oberflächenbeeinflussten) Daten empfohlen wird. Die Analyse der ursprünglichen Pulverversion des Karbonat-Referenzmaterials JCp-1 ergab unterschiedliche K/Ca-Werte in Abhängigkeit von der Analysetechnik und/oder der Wahl der Auflösungsmethode vor der Messung. Diese Beobachtung zeigt, dass das ursprüngliche JCp-1-Referenzmaterial zwar homogenisiert, aber möglicherweise mit Al und K verunreinigt ist.

Es wurden unterschiedliche Fraktionierung von K/Ca und Na/Ca im Bohrloch bei einer Reihe von Referenzstandards in Bezug auf den Kalibrierungsstandard (NIST SRM 610) beobachtet. Die Auswirkung dieser Bohrlochfraktionierung konnte mit Hilfe eines elementspezifischen Fraktionierungsfaktors korrigiert werden, was zu einer höheren Genauigkeit führte.

Nach den Erkenntnissen über die unterschiedliche Bohrlochfraktionierung für Alkalielemente (Kapitel 2) wurden in Kapitel 3 für eine Reihe von Elementen in verschiedenen geologischen Referenzmaterialien weitere Untersuchungen zur Bohrlochfraktionierung und deren Korrektur durchgeführt. In dieser Studie ging es darum, 1) die Bohrlochfraktionierung für Elemente wie Li, B, Na, K, Mg, Fe, Zn, Sr und Ba in verschiedenen geologischen Referenzmaterialien (RM) im Vergleich zu den Kalibrierstandards NIST SRM 610/612 zu bewerten und 2) die Auswirkungen der Korrektur mit Hilfe der elementspezifischen Bohrlochfraktionierung auf die Datenqualität zu beurteilen (Nambiar et al., eingereicht). Die Ergebnisse zeigten, dass die Mittelwerte vor und nach der vorgeschlagenen element-spezifischen Bohrlochfraktionierungskorrektur signifikant voneinander abweichen, insbesondere bei Alkalielementen und flüchtigen Elementen aller untersuchten Standards sowie bei Bor im Falle der Karbonatstandards. Im Gegensatz dazu wiesen die Erdalkalimetalle die geringste Fraktionierung auf, wobei die El/Ca-Werte vor und nach Anwendung der Bohrlochfraktionierungskorrektur statistisch nicht voneinander zu unterscheiden waren. Die vorgeschlagene Korrektur der Bohrlochfraktionierung verbesserte die Genauigkeit für Elemente wie Alkalielemente erheblich, während sich in einigen wenigen Fällen (z. B. B in JCp-1NP) die Genauigkeit verschlechterte, was potenzielle Probleme bei den bekannten Werten für das Referenzmaterial unterstreicht. Ungeachtet dessen kann die routinemäßige Anwendung der Korrektur für die Bohrlochfraktionierung die Datenqualität verbessern.

Die oben beschriebenen methodischen Entwicklungen wurden genutzt, um K/Ca zusammen mit anderen El/Ca-Werten in modernen im Gelände gesammelten und im Labor

gezüchteten Exemplaren der benthischen Großforaminiferen (LBF) *Operculina ammonoides* zu untersuchen (Kapitel 4). Die im Labor kultivierten *Operculina ammonoides* sind unter drei verschiedenen Temperaturen und dort jeweils in vier verschiedenen $[Ca^{2+}]_{sw}$ gewachsen. Es wurde ein signifikanter Zusammenhang zwischen K/Ca_{sw} und K/Ca_{LBF} beobachtet, der jedoch im Vergleich zu den meisten anderen Spurenelementen, über die früher berichtet wurde (z. B. Mg/Ca und Na/Ca; Evans et al., 2015; Hauzer et al., 2021), weniger stark ausgeprägt ist. Dieser leichte Zusammenhang zwischen Meerwasser und K/Ca in der Schale könnte durch einen Effekt der Kristallwachstumsrate auf den K-Einbau bedingt sein, der durch Anwendung einer Wachstumsratenkorrektur unter Verwendung der Beziehung zwischen K/Ca und dem Sättigungszustand (Ω_C) korrigiert wurde, wozu eine weitere Reihe von Kulturexperimenten mit *O. ammonoides* bei unterschiedlichen pH-Werten verwendet wurde. Um die Auswirkungen von Meerwasserparametern auf den K/Ca-Proxy weiter zu testen, wurden moderne *O. ammonoides* aus verschiedenen Regionen untersucht. Es wurde kein eindeutiger Einfluss von Temperatur, Salzgehalt, pH-Wert oder $[CO_3]^{2-}$ auf die K-Inkorporation in *O. ammonoides* festgestellt, so dass K/Ca_{LBF} als potenzieller Proxy zur Rekonstruktion der Meerwasserchemie der Vergangenheit dienen kann. Wenn das Konzept eines konstanten Meerwasser-$[K^+]$-Wertes während des gesamten Phanerozoikums zutrifft (Horita et al., 2002), könnte der K/Ca-Proxy als direktes Instrument zur Untersuchung vergangener Veränderungen des Meerwasser-$[Ca^{2+}]$-Wertes genutzt werden, und zwar nach einem ähnlichen Konzept wie der Na/Ca-Proxy (Hauzer et al., 2018). Alternativ könnte ein Multi-Proxy-Ansatz verwendet werden, bei dem sowohl Na/Ca als auch K/Ca kombiniert werden, um zu überprüfen, ob das $[K^+]$ im Meerwasser konstant war. Dies ist das erste Mal, dass ein K/Ca-Proxy in Foraminiferen entwickelt wurde. Da *O. ammonoides* eine nahe lebende Verwandte der Nummuliten ist, die während des Paläogens reichlich vorhanden waren, könnte diese Gruppe zusammen mit der in dieser Arbeit vorgestellten Kalibrierung eine wertvolle Quelle für die Rekonstruktion der känozoischen Meerwasserchemie darstellen.

Unter Verwendung des in Kapitel 4 etablierten K/Ca-Proxys und anderer Proxys, einschließlich Na/Ca, Mg/Ca und Mg-Isotopenzusammensetzung der Schale, wurden eozäne Nummulitenfossilien aus dem Pariser Becken, dem Hampshire-Becken und tropischen Regionen (Tansania, Indonesien und Indien) untersucht (Kapitel 5). Mithilfe des Na/Ca-Proxys wurde $[Ca^{2+}]_{sw}$ aus dem Eozän rekonstruiert. In Kombination dieser rekonstruierten Werte mit zuvor veröffentlichten Mg/Ca_{sw}-Werten (Evans et al., 2018) wurde $[Mg^{2+}]_{sw}$ bestimmt. Dies ist das erste Mal, dass die Konzentrationen von Ca und Mg im Meerwasser während des Eozäns anhand von Foraminiferen rekonstruiert wurden. Die rekonstruierten eozänen $[Ca^{2+}]_{sw}$-Werte waren 1,6-2 mal höher als die heutigen, während $[Mg^{2+}]_{sw}$ vom frühen Eozän ($54.3^{+7.9}_{-9.6}$ mmol kg-1 bei ~55 Ma) bis zum späten Eozän ($37.8^{+4.4}_{-4.3}$ mmol kg-1 bei ~31 Ma) abnahm, gefolgt von einem Anstieg in Richtung der modernen Meerwasserzusammensetzung. In dieser Studie wird zum ersten Mal nachgewiesen, dass der $[K^+]$-Wert des Meerwassers in der Vergangenheit schwankte und im Eozän ~2 mal niedriger war als der heutige Wert des Meerwassers. Darüber hinaus deuten die mit Hilfe von LBF (*Nummulites* sp.) rekonstruierten $\delta^{26}Mg_{sw}$-Werte aus dem Eozän darauf hin, dass $\delta^{26}Mg_{sw}$ während des Känozoikums relativ konstant blieb (innerhalb von ~0,3 ‰ der heutigen Meerwassersignatur). Die $\delta^{26}Mg_{sw}$-Ergebnisse stimmen gut mit anderen bekannten Werten von verschiedenen marinen Archiven (pelagische Massenkarbonate: Higgins und Schrag, 2015; aragonitische Korallen: Gothmann et al., 2017) überein. Ein Vergleich der Ergebnisse dieser Arbeit mit bestehenden Datensätzen legt alternativ nahe, dass alle hier betrachteten Element- und Isotopendaten durch einen Rückgang Ozeanbodenspreizungsrate und eine Verringerung der authigenen Tonbildung erklärt werden kann, was die Bedeutung dieser Prozesse für langfristige Veränderungen im Kohlenstoffkreislauf betont.

Dedicated to

my loving parents,

Mrs. Nalini Nambiar and Mr. Rajagopalan Nambiar

&

my nephew,

Aayansh

Acknowledgements

I am greatly indebted to my supervisors, Wolfgang Müller and David Evans, for their expert guidance, kindness, and insightful feedback throughout my PhD journey. Their constant motivation and encouragement have been fundamental to the success of this project. I am thankful to Wolfgang for all his support and constructive outlook throughout my PhD journey. I am extremely grateful to David for introducing me to the research field of seawater chemistry reconstructions and generously sharing his expertise and knowledge, which have significantly contributed to my academic and professional growth. I am also thankful for his consistently prompt responses and support whenever I needed his help or guidance. His dedication and enthusiasm towards research have always inspired me greatly. I could not have wished for better supervisors.

My PhD project is part of the VeWA consortium, which was funded by the Hessen State Ministry for Higher Education, Research, and the Arts through the LOEWE program, which is gratefully acknowledged. I also want to extend my sincere thanks to the entire VeWA member for all the constructive meetings, discussions, collaborative spirit, and productive exchanges.

Being a proud member of the FIERCE lab, I express my deepest gratitude to all the amazing members of this lab. Working alongside such a dedicated and talented group has been an enriching experience for me. The commitment towards maintaining a well-organized lab with high standards has undoubtedly contributed to the positive outcomes of this research. I am grateful for the support and learning opportunities that this lab has provided.

My time at Goethe University has been special, especially because of my friends. I am thankful to Douglas Coenen, Laura Fink, Vanessa Schlidt, Max Fursman, Iris Arndt,

Jie Xu, Catharina Heckel, Julian Fuchs, and Anthea Arns for the joyful times at the university. A special shout-out to Douglas Coenen, with whom I have closely collaborated; working and conversing with him, has been a constant joy and a huge support during my PhD journey. I am also grateful to Iris Arndt for her help with German translations and administration process. I appreciate the wonderful times spent with Anshu, Mahil, Veera, Srilakshmi, Jyoti, Jo, Lei, Ashwin, and Elena; thank you for the memorable moments! I also want to thank Lohitesh, for his kind help and support during my stay in Germany.

Field trips and collaborative work were essential parts of this project, and many have helped me in effectively completing these tasks. Huge thanks to David Evans, Wolfgang Müller, Silke Voigt, Laura Cotton, Douglas Coenen, Vanessa Schlidt, Sandra Huber, and Jorit Kniest for making our research field trip successful and creating lasting memories. The field trip was undeniably one of the best experiences I have had in my PhD journey. I am also grateful to Michael Henehan, Jutta Schlegel, and Josefine Holtz for their support during the Mg isotope measurements at GFZ, Potsdam.

I acknowledge my family's generous support and love throughout my academic and personal journey. My parents have always inspired me to overcome challenges, and their boundless belief in my potential has fuelled my aspirations. I want to thank my brothers, Rineesh and Roshan, for their support and encouraging cheers. I extend my deepest gratitude to Harsh for his constant support, love, encouragement, and always believing in me.

Table of Contents

Chapter 1: Introduction

1.1. Cenozoic climate change

Atmospheric CO_2 has varied significantly throughout the Earth's history (Royer, 2014; Anagnostou et al., 2016; O'Brien et al., 2017; Rae et al., 2021). Reconstructing past climatic responses to atmospheric CO_2 changes helps understand the relationship between CO_2 and climate, allowing more accurate predictions of future climate. While the available instrumental data based on direct measurement represents only the past ~200 years (Jones and Bradley, 1992), palaeoclimatic records from older periods (on million-year timescale) play an essential role in achieving a deeper understanding of global carbon cycle mechanisms and improving future predictions (Lunt et al., 2012).

The Cenozoic represents the last 65 million years of the Earth's history, during which climate transitioned from a greenhouse to an icehouse state (Westerhold et al., 2020). These shifts were accompanied by significant variations in both short-term and long-term greenhouse gas concentrations (Zachos et al., 2001, 2008; Hyland et al., 2017). The paleoclimate reconstruction for the Cenozoic era is widely based on the $\delta^{18}O$ proxy in foraminifera, which reflects changes in deep-sea temperature as well as ice volume (Zachos et al., 2001; Cramer et al., 2009). Long-term Cenozoic $\delta^{18}O$ reconstructions using foraminifera began in the mid-1950s (Urey et al., 1951; Emiliani, 1955), following which several other studies revised the records (Savin et al., 1975; Shackleton, 1975; Miller et al., 1987; Zachos et al., 2001, 2008; Cramer et al., 2009; Westerhold et al., 2011, 2018, 2020). Zachos et al. (2001) reported an overall Cenozoic benthic $\delta^{18}O$ variability of 5.4 ‰, with ~3.1 ‰ reflecting deep-sea cooling and remaining ~2.3 ‰ resulting from the growth of ice sheets in Antarctica and the Northern Hemisphere. Westerhold et al., (2011, 2018) presented a high-resolution (~5 kyr) benthic foraminifera record spanning from

the Paleocene to early Eocene that helped define the onset, duration, and demise of hyperthermals events (rapid extreme warming events). These studies were extended by further investigations of benthic foraminifera records spanning the late Miocene and middle to late Eocene, which aided in defining distinct climatic states of the Cenozoic era based on its response to astronomical forcing and polar ice volume (Westerhold et al., 2020). The reconstruction based on benthic $\delta^{18}O$ has estimated that global temperatures were ~12 °C higher than today during the warmest period (early Eocene) of the Cenozoic (Zachos et al., 2001; Westerhold et al., 2020). The development of new temperature proxies, such as clumped isotopes, has been recognized as a potent tool for enhancing the accuracy of palaeotemperature estimations. Clumped isotopes offer a distinct advantage as they are independent of seawater composition, pH and physiological factors during formation of marine carbonates shell (Ghosh et al., 2006; Hill et al., 2014; Peral et al., 2018), leading to their growing application for palaeotemperature reconstructions (Evans et al., 2018; Modestou et al., 2020; Agterhuis et al., 2022; Meckler et al., 2022). The overall Cenozoic deep-ocean temperature reconstructed based on clumped isotope measurement in foraminifera showed much warmer results than $\delta^{18}O$-based reconstructions, highlighting the possible influence of changes in deep ocean pH and/or seawater $\delta^{18}O$ composition (Meckler et al., 2022), suggesting further investigation to achieve a more accurate Cenozoic temperature reconstruction.

Changes in atmospheric CO_2 played a significant role in shaping the Cenozoic climate (Anagnostou et al., 2016). Several studies have been carried out to reconstruct Cenozoic atmospheric CO_2 using different marine archives, including foraminifera (Pearson and Palmer, 1999; Anagnostou et al., 2016), fossil leaf stomata (Rundgren and Björck, 2003) and alkenone (Pagani et al., 1999). Following the pioneer studies of atmospheric CO_2 reconstructions of the Cenozoic era (Pagani et al., 1999; Pearson and

Palmer, 1999), several further investigations were carried out that refined and improved the Cenozoic records (Pearson and Palmer, 2000; Beerling and Royer, 2011; Anagnostou et al., 2016; Rae et al., 2021). The atmospheric CO_2 levels were ~1500 ppm during the early Eocene, which decreased to ~600 ppm in the early Neogene, with a peak during the mid-Miocene Climate Optimum. Following this, atmospheric CO_2 levels dropped to around ~400 ppm during the Pliocene and further to 300-180 ppm in the late Pleistocene ice ages (Rae et al., 2021).

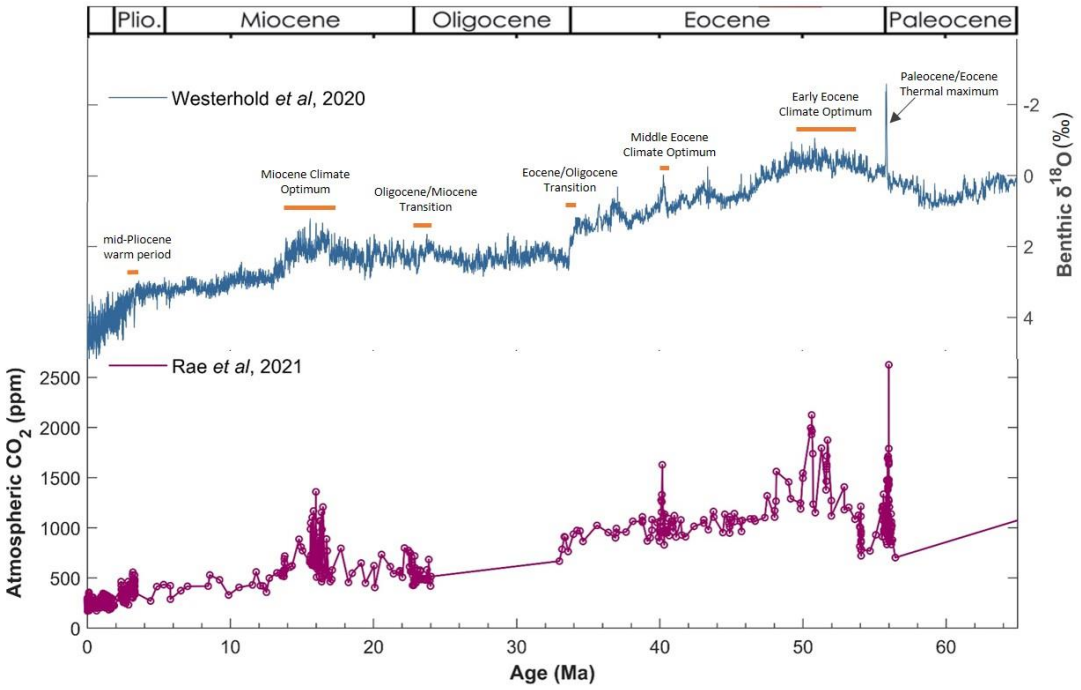

Figure 1. Compilation of existing records of Cenozoic benthic $\delta^{18}O$ and atmospheric CO_2 (Westerhold et al., 2020; Rae et al., 2021 and references therein).

Different studies propose varying explanations for the decline in atmospheric CO_2 levels during the Cenozoic era. Earlier studies suggested the dominant role of negative feedback from temperature-controlled silicate weathering for the drawdown of atmospheric CO_2 during the Cenozoic (Walker et al., 1981; Caldeira and Berner, 1998); however, the increase in the silicate weathering has also been attributed to tectonic activity (Raymo and Ruddiman, 1992; Misra and Froelich, 2012) or increased land surface

reactivity (Caves Rugenstein et al., 2019; Deng et al., 2022). Additionally, some studies suggest that a decrease in reverse weathering led to a reduction in authigenic clay formation, contributing to the decline in atmospheric CO_2 over the Cenozoic (Higgins and Schrag, 2015; Dunlea et al., 2017; Isson and Planavsky, 2018). Furthermore, alterations in seafloor spreading rates and associated hydrothermal processes have been proposed as significant drivers of Cenozoic carbon cycling (Coggon et al., 2010; Coogan and Dosso, 2015).

While high-quality climate reconstructions of some past warm periods in the Cenozoic era now exist (Figure 1), the geological processes responsible for driving the long-term changes in atmospheric CO_2 are still under debate. One way of constraining the relative importance of the various driving forces proposed so far is to better understand the degree to which seawater chemistry has varied in response to geological processes. Since the long-term geological processes influencing atmospheric CO_2 also influence the cycling of elements in seawater, reconstruction of long-term seawater chemistry can help unravel the interactions between geological processes and carbon cycling. Moreover, understanding seawater chemistry is essential to apply trace elements-based proxies accurately beyond the residence time of elements. For example, the residence time of Mg and Ca in seawater is ~10 and ~1 million years, respectively (Broecker and Peng, 1982); therefore, to utilise Mg/Ca proxy as palaeothermometry beyond ~1 million years, it is important to have the accurate reconstructions of seawater Mg/Ca values (Evans et al., 2015, 2016). In addition, since $[Ca^{2+}]$ and $[Mg^{2+}]$ play a crucial role in influencing the equilibrium constants of the carbonate system, reconstructions of seawater $[Ca^{2+}]$ and $[Mg^{2+}]$ are essential for accurate reconstruction of long-term atmospheric CO_2 using the $\delta^{11}B$ proxy (Zeebe and Wolf-Gladrow, 2001; Rae et al., 2021).

1.2. Drivers of the long-term changes in seawater chemistry

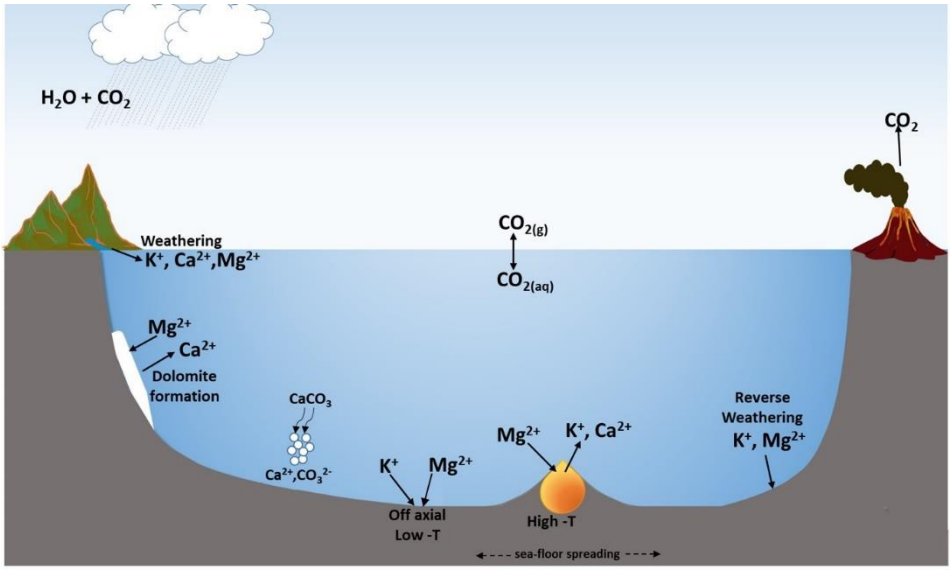

Figure 2. Long-term cycling of major cations in seawater, with arrows indicating whether each process serves as a source or sink for the elements.

The chemistry of seawater, in terms of major ion compositions, has varied throughout the Phanerozoic eon (Turchyn and DePaolo, 2019). Processes such as continental weathering, hydrothermal processes, reverse weathering (formation of authigenic clay), and marine carbon burial that drives atmospheric CO_2 also influence the major-ion composition of seawater (Berner et al., 1983; Hardie, 1996; Li et al., 2009; Lowenstein et al., 2013; Hain et al., 2015) (Figure 2). Several modelling studies have attempted to explain the drivers of the long-term changes in seawater chemistry (Hardie, 1996; Stanley and Hardie, 1998; Demicco et al., 2005; Holland, 2005; Coogan and Dosso, 2022). However, the conclusions of these modelling studies are not in agreement. For instance, a change in the seafloor spreading rate and associated low and high-temperature hydrothermal processes as a significant driver of seawater chemistry has been proposed (Hardie, 1996; Stanley and Hardie, 1998; Holland and Zimmermann, 2000; Demicco et al., 2005; Coogan and Dosso, 2022). However, an alternative explanation has also been suggested, i.e., the variation in the ratio of dolomite to limestone deposition

and the rate of gypsum vs. anhydrite deposition were considered more important processes (Wilkinson and Algeo, 1989; Holland and Zimmermann, 2000; Holland, 2005). Given the differences in the proposed explanation, palaeoreconstructions using marine archives may serve as crucial information to understand the factors driving seawater chemistry. Reconstructions of long-term changes in Cenozoic seawater Mg/Ca using marine archives are in reasonable agreement, which suggested that seawater Mg/Ca has experienced a 2-3 fold increase from the Eocene to the present-day (Horita et al., 2002; Coggon et al., 2010; Gothmann et al., 2015; Evans et al., 2016, 2018). In contrast, Cenozoic Sr/Ca_{sw} values remained relatively constant near the present-day value of 8.4 mmol/mol (Gothmann et al., 2015; Turchyn and DePaolo, 2019).

While the Mg/Ca and Sr/Ca ratios in seawater during the Cenozoic have been widely investigated, information on the individual concentrations of major ions in the seawater is limited (Horita et al., 2002; Brennan et al., 2013; Zhou et al., 2021). Much of the available data are derived from fluid inclusions in marine halite. However, due to their high solubility, they are poorly preserved in the geological records, resulting in their limited availability and scarce data records. Recently, given the long residence time of Na in seawater (~100 Myr; Broecker and Peng, 1982), the Na/Ca proxy as a direct tool for reconstructing $[Ca^{2+}]_{sw}$ was developed for large benthic foraminifera (Hauzer et al., 2018) and planktonic foraminifera (Zhou et al., 2021). Using the Na/Ca proxy in fossil planktonic foraminifera, a high temporal reconstruction of $[Ca^{2+}]_{sw}$ was achieved for the last ~16 million years (Zhou et al., 2021). The existing Cenozoic records of seawater $[Ca^{2+}]$ and $[Mg^{2+}]$ (Horita et al., 2002; Brennan et al., 2013; Zhou et al., 2021) are close to the modeled data by Stanley and Hardie, (1998). However, given the sparsity of data, further investigation of proxy records is essential to identify the drivers of seawater chemistry changes (Figure 3).

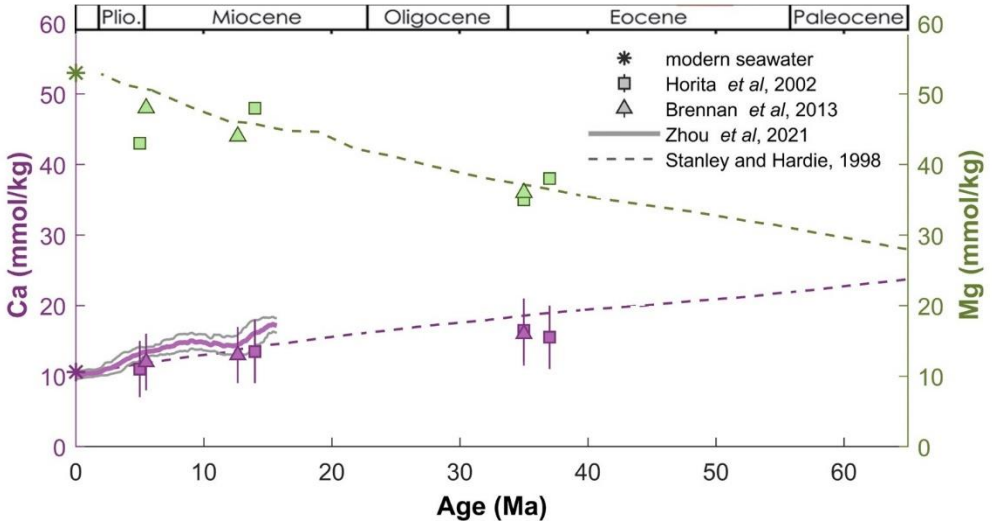

Figure 3. Cenozoic record of seawater [Ca^{2+}] and [Mg^{2+}]. The square and triangle symbols represent the record derived from fluid inclusion in marine halite (Horita et al., 2002; Brennan et al., 2013). The solid purple line represents data derived from planktonic foraminifera (Zhou et al., 2021). The dashed line represents modelled data (Stanley and Hardie, 1998).

Potassium is a major element of seawater, with a residence time of ~12 million years and a present-day concentration of 10.2 mmol kg^{-1} (Broecker and Peng, 1982). Riverine input and high-temperature hydrothermal processes are primary sources of potassium in seawater (Kronberg, 1985). Spencer and Hardie, (1990) demonstrated that the major ion composition of modern seawater, such as Ca^{2+}, Mg^{2+}, Na^{+}, and SO_4^{2-}, can be fairly explained by the balance between riverine input and hydrothermal processes; however, seawater [K^{+}] requires an additional major sink to achieve a steady state, as both riverine and high-temperature hydrothermal processes are sources of potassium. Several studies have suggested that authigenic clay formation during reverse weathering and low-temperature hydrothermal processes are major processes for removing K^{+} from seawater (Bloch and Bischoff, 1979; Michalopoulos and Aller, 1995). Despite being a major seawater cation, to our knowledge, only one study investigated the secular variation of Cenozoic $[K^{+}]_{SW}$. Horita et al., (2002) examined fluid inclusions in marine halite to reconstruct past changes in seawater elemental composition. Unlike estimates of

seawater [Mg^{2+}], [Ca^{2+}] or [SO_4^{2-}], the seawater [K^+] reconstruction using fluid inclusions in marine halite is based on several assumptions, i.e., the K/Br ratio in fluid inclusions has not changed over time, and [Br^-] has remained invariant due to its long residence time (Horita et al., 2002; Lowenstein et al., 2013). Building upon this assumption, Horita et al. (2002) reported that seawater [K^+] has remained relatively constant, close to the present-day value of ~11 mmol/kg throughout the Phanerozoic eon (last ~600 Ma). In order to maintain constant seawater [K^+] throughout Phanerozoic, there has to be a strong balance between the input and removal of K^+ from seawater. The sink of seawater [K^+] at the off-axis hydrothermal process (at ridge flanks) has been considered an important sink (Demicco et al., 2005) and is hypothesized to play a major role in balancing the enhanced K flux from continental weathering into the ocean during the Late Mesozoic (Coogan and Gillis, 2013). Nevertheless, further investigation is essential to better understand the seawater K cycle and its driving process.

1.2.1 Cenozoic record of seawater $\delta^{26}Mg$

Magnesium (Mg) is an element closely linked to long-term carbon cycling, and the distinct isotopic signature in both sources and sinks of Mg in the ocean makes it a potential indicator of processes influencing seawater chemistry and the global carbon cycle (Pogge Von Strandmann et al., 2014; Higgins and Schrag, 2015; Gothmann et al., 2017). Magnesium has three stable isotopes: ^{24}Mg (78.99%), ^{25}Mg (10.00%), and ^{26}Mg (11.01%), and its isotopic composition is reported relative to the standard solution, DSM-3 (provided by Dead Sea Magnesium Ltd., Israel) in delta notation as $\delta^x Mg = [(({}^xMg/{}^{24}Mg)_{sample}/ ({}^xMg/{}^{24}Mg_{DSM\text{-}3})) - 1] \times 1000$, where x = 25 or 26 (Galy et al., 2003). The present-day seawater $\delta^{26}Mg$ composition is -0.82 ± 0.01 ‰ (Foster et al., 2010). The primary source of Mg into the ocean is from riverine input, predominantly consisting of products from silicate and carbonate-weathering reactions with a mean global $\delta^{26}Mg$

composition of -1.09 ± 0.05 ‰ (Tipper et al., 2006). Groundwater discharge contributes a relatively minor portion, constituting ~10 % of the total Mg riverine input (Mayfield et al., 2021). Mg is predominantly removed from seawater through high-temperature hydrothermal systems, involving the quantitative uptake of Mg at high temperatures (i.e., no isotopic fractionation) (Elderfield et al., 1996). Additionally, the formation of dolomite acts as a sink of Mg, leading to an isotope fractionation of $\varepsilon_{dol\text{-}sw} \approx$ -2‰ (Higgins and Schrag, 2015). Recently, Shalev et al. (2019) indicated a temperature-dependent preferential removal of heavier isotopes by a low-temperature hydrothermal (LTH) process occurring at ridge flanks, leaving the ocean enriched with isotopically lighter Mg isotope. They estimated the global Mg isotope fractionation associated with the LTH sink is ~1.6‰.

Few studies have attempted to reconstruct the secular variation of the seawater magnesium isotope composition ($\delta^{26}Mg_{sw}$) during the Cenozoic using different marine archives, including planktic foraminifera (Pogge Von Strandmann et al., 2014), pelagic carbonates (Higgins and Schrag, 2015), and corals (Gothmann et al., 2017). However, the reconstructed $\delta^{26}Mg_{sw}$ values do not agree (Figure 4), leading to different conclusions regarding the mechanisms driving the Cenozoic seawater magnesium cycle (Pogge Von Strandmann et al., 2014; Higgins and Schrag, 2015; Gothmann et al., 2017). Studies by Higgins and Schrag (2015) and Gothmann et al. (2017) suggested that the reduction of Mg uptake in low-temperature authigenic clay formation or increase in Mg silicate weathering are responsible for Cenozoic Mg cycling; however, Pogge Von Strandmann et al. (2014) argued dolomite formation and riverine flux are the primary controlling factors for seawater Mg cycling. Thus, further investigations into seawater $\delta^{26}Mg$ reconstructions can contribute to a better understanding of the Cenozoic Mg cycle.

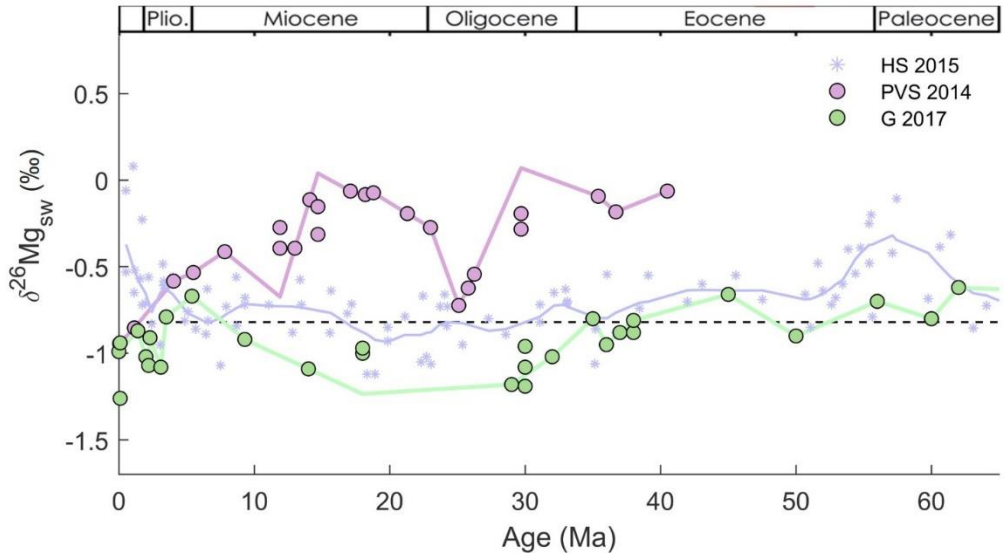

Figure 4. Existing Cenozoic record of seawater $\delta^{26}Mg$ composition reconstructed using different marine carbonates, including planktic foraminifera (Pogge Von Strandmann et al., 2014), pelagic carbonates (Higgins and Schrag, 2015), and corals (Gothmann et al., 2017). The solid line is the Lowess fit line. The dashed line represents present-day $\delta^{26}Mg_{sw}$ composition.

1.3. Foraminifera: Marine archives for palaeoclimatic reconstruction

Researchers have been using a range of marine and terrestrial proxy methods to study palaeoclimate. Within marine archives, foraminifera, which inhabited the ocean for more than 500 million years (BouDagher-Fadel, 2008), have gained considerable attention and have been widely assessed for palaeoclimatic reconstruction. Foraminifer is a cell organism encased by a shell (test) that can be classified as either calcareous (composed of $CaCO_3$), arenaceous (built of sediment particles), or organic (made of tectin), with calcareous foraminifera being the most abundant due to its good preservation potential and greater diversity (Binczewskaa et al., 2015). Foraminifera are primarily categorised into three groups: i) planktonic, ii) smaller benthic, and iii) the larger benthic (distinguished as a different group due to their larger size and complex interior) (Boersma, 1998). Foraminifera are sensitive to environmental changes. This sensitivity of foraminifera allows scientists to use foraminifera as an indicator of past

environmental and climatic conditions. However, the process of foraminifer's shell precipitation from surrounding seawater is complex and biologically controlled (Erez, 2003b; Bentov et al., 2009; De Nooijer et al., 2009). These biological imprints, termed as vital effects, cannot be easily predicted through a simple chemical thermodynamic perspective (Erez, 2003a). Consequently, the relationship between shell chemistry and ambient physical or chemical conditions must be empirically calibrated (Lea et al., 1999; Keul et al., 2013; Evans et al., 2015; Hauzer et al., 2018; Nambiar et al., 2023).

The measurement of $\delta^{18}O$ in foraminifera is one of the earliest, and widely investigated proxies utilised for palaeoclimatic studies (Urey et al., 1951; Emiliani, 1955; Savin et al., 1975; Shackleton, 1975; Miller et al., 1987; Zachos et al., 2008, 2001; Cramer et al., 2009; Westerhold et al., 2011, 2018, 2020). This development in proxies significantly expanded the scope of palaeoclimatic research and led to the exploration of a wide range of chemical signatures in foraminifera, which have been established as palaeo-proxies. For instance, elemental ratios such as Mg/Ca and Li/Ca have been shown to reconstruct ocean temperature (Rosenthal et al., 1997; Lea et al., 1999; Marchitto et al., 2018; Gray and Evans, 2019). Additionally, elemental ratios like B/Ca and Zn/Ca have been employed to study the carbonate system (Marchitto Jr et al., 2000; Brown et al., 2011; Allen and Hönisch, 2012; van Dijk et al., 2017), while Ba/Ca ratios have been used to infer salinity (Weldeab et al., 2007). Furthermore, Cd/Ca has been proposed as a potential proxy for the reconstruction of nutrient concentration (Boyle, 1981; Rickaby and Elderfield, 1999). Although species-specific proxy relations have basic similarities, they can produce different estimates when applied to different species. While existing proxies have significantly contributed to palaeoclimatic reconstruction, continued exploration of species-specific proxy and understanding the fundamental basis of these techniques are critical for more precise and reliable palaeoclimatic reconstructions.

1.3.1. Larger benthic foraminifera (LBFs)

The larger benthic foraminifera are a group of foraminifera with complex internal morphologies and normally exceed 3 mm^3 in volume (Ross, 1974). Their size ranges from as small as 0.02 mm in diameter to 110 mm or more, with most species within 0.1 - 1.0 mm range (Hallock, 1985). Larger foraminifera are commonly found in shallow tropical regions, with many species hosting symbiotic algae within their shell (Cowen, 1983; Hallock, 1985; Beavington-Penney and Racey, 2004). In a nutrient-deficient environment, a symbiotic relationship with algae offers an advantage to the foraminifera, enabling them to thrive despite limited nutrient availability (Hallock, 1985). However, the success of hosting symbiotic algae depends on the presence of sufficient organic particles as the host collects and digests particulate organic matter, and the symbiont feeds on the waste product, and in turn, the host uses the energy produced by the symbiont (Hallock, 1981; Renema, 2002). The metabolic rate of LBFs is higher in warm water than in cold water, making them more likely to live in sufficiently oligotrophic conditions in tropical than in temperate seas (Renema, 2002). The highest diversity of LBFs is observed in the Indo-Pacific region, with the Nummulitidae being one of the most long-ranging and abundant LBFs of the Cenozoic era (Hohenegger et al., 2000; Renema et al., 2008; Cotton et al., 2020). *Operculina ammonoides* is the closest living relative of the nummulitid foraminifera, which were abundant during the Paleogene (Hallock, 1985; Holzmann et al., 2003).

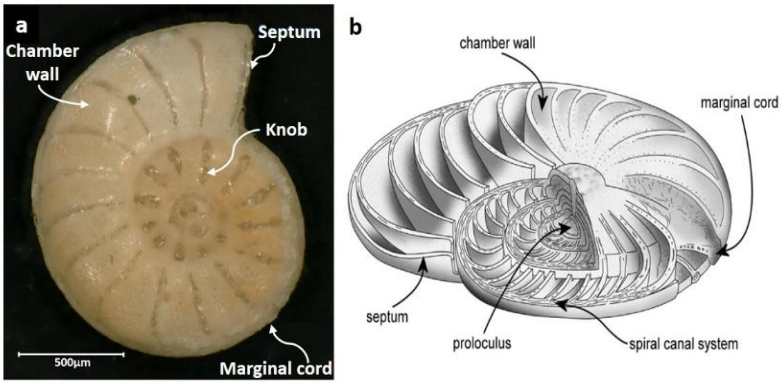

Figure 5 Representative specimen highlighting the major morphological features of *Operculina ammonoides*. Modified after Evans et al. (2013)

Although the morphology of LBF may vary between genera, Figure 5 illustrates the common primary morphological features in nummulitid foraminifera. The initial chamber consists of a spherical proloculus located at the center of the test, from where the growth of the spiral chamber begins. A curved plate, called a septum, separates each chamber, and the imperforate equatorial rim perpendicular to the septum is known as the marginal cord (Renema, 2002; Beavington-Penney and Racey, 2004). Larger benthic foraminifera have the ability to reproduce both asexually through binary fission and sexually giving rise to numerous offspring during the latter process (BouDagher-Fadel, 2008). The asexual reproductive process produces LBF with a large proloculus and a smaller test size with fewer number of chambers (also referred to as megalospheric generation or A forms), whereas a microspheric generation (B-form) reproduces sexually, which consists of a small proloculus and is larger, with numerous chambers (Dettmering et al., 1998; BouDagher-Fadel, 2008). Due to such a reproductive process, the same species can produce at least two distinct morphological generations.

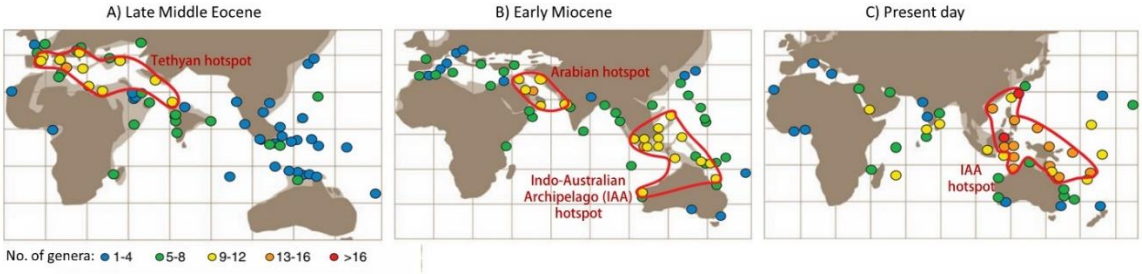

Figure 6. Global diversity of larger benthic foraminifera (LBFs) during A) late Middle Eocene, B) Early Miocene, and C) present-day seawater. The solid red line represents hotspot regions (modified after Renema et al., 2008).

Fossils of larger benthic foraminifera are widely used for biostratigraphy due to their rapid diversification and abrupt extinctions. They are commonly found in shallow-water limestone, especially in geological periods such as Permian-Pennsylvanian, Cretaceous, Eocene, and Late Oligocene to Early Miocene (Hallock, 1985). Following the Cretaceous–Paleogene (K–P) event, during which 80% of LBFs were lost, LBFs began to recover in the Early Paleocene (BouDagher-Fadel, 2008; Prazeres and Renema, 2019). Over the past 50 million years, at least three marine biodiversity hotspots have been identified, shifting across the globe with major tectonic events (Renema et al., 2008) (Figure 6). During the Eocene epoch, the highest diversity of LBFs (number of genera at a single location) was observed in southwest Europe, northwest Africa, and the eastern coast of the Arabian Peninsula, Pakistan, and West India (Renema, 2007). The disappearance of the Arabian hotspot during the Middle to Late Miocene was caused by the loss of habitat due to regional uplift during the Arabia-Eurasia collision. The fossil record of LBFs from the last 20 million years shows that the Indo-Australian Archipelago has remained the hotspot of larger benthic foraminifera (Renema et al., 2008). Studies have reported the influence of warming on the rapid expansion of the geographic range of LBF fossil records. For instance, *Nummulites* species have been recorded to occur as far north as 57°N during Paleocene–Eocene thermal maximum (PETM), whereas during Middle Eocene Climatic Optimum (MECO), *Nummulites* fossils are found in Alaska (55°N)

and the southern region of Belgium (51°N) (Adams et al., 1990; King, 2016; Prazeres and Renema, 2019). In contrast, the geographic range extended in the southern hemisphere as far as southern Australia during MMCO (Prazeres and Renema, 2019). The *Nummulites sp.* and *Operculina sp.* collected from the same Eocene bed have shown considerable similarity in their elemental composition (Evans et al., 2013), opening up opportunities for paleo-reconstruction using proxies established in modern *Operculina ammonoides*, which belongs to the same Nummulitidae family. Moreover, previous studies have demonstrated the effective utilisation of Eocene *Nummulites* for both seasonality reconstruction and long-term paleo-reconstructions using proxies based on modern *O. ammonoides* (Evans et al., 2013, 2018).

1.4. Laser ablation-ICP-MS for El/Ca ratio measurement in marine carbonates

Spot or spatially-resolved measurement, also known as solid sample analysis, is a widely utilised technique in Earth Sciences (Bellotto and Miekeley, 2000; Jochum et al., 2012; Evans and Müller, 2013; Müller and Fietzke, 2016). In-situ solid analysis, the techniques commonly used include electron microprobe, secondary ion mass spectrometry (SIMS), and laser ablation. In the electron microprobe technique, a high-energy electron beam is directed onto the solid sample, with the capability to precisely focus a small spot of 1-2 microns and analyse elemental concentration down to 100's ppm level; however, isotope measurements are unattainable (Fernández-Suárez et al., 2021). An ion microprobe, i.e., secondary ion mass spectrometry (SIMS), involves the generation of secondary ions by directing a beam of primary ions onto the sample, forming a sputter pit of 10-30 µm diameter, allowing high spatial resolution with a limit of detection near parts per billion (ng/g) (Fitzsimons et al., 2000). Laser ablation coupled to ICP-MS (Inductively coupled plasma mass spectrometry), first implemented in the 1980s to analyse granite's elemental and Pb-isotope composition (Gray, 1985), marked

the beginning of this measurement technique. This development resulted in a rapid increase in the advancement and application of LA-ICP-MS in the field of Earth Science and Environmental Science. The application of spatially resolved laser ablation analysis, offering a means for sample introduction into ICP-MS, is experiencing rapid growth due to its capability to measure sub-ng/g elemental concentration as well as isotopic ratios at high spatial resolution with high precision (Russo et al., 2000; Müller and Fietzke, 2016; Evans and Müller, 2018). The laser ablation (LA) coupled to magnetic sector field inductively coupled plasma mass spectrometry (SF-ICP-MS) has the capability to measure in three different mass resolution modes, providing higher resolved spectra, reduced interferences, and enhanced sensitivity. While conventionally used quadrupole (Q) mass analyser offer a mass resolution (R) of ~300, SF-ICP-MS (utilized in this study) offer distinct mass resolution modes: low (R ≈ 300), medium (R ≈ 4000), and high (R ≈ 10,000).

Briefly, laser ablation systems consist of a laser source, beam delivery optics, and an ablation cell. The LA technique involves focusing a high energy-density pulsed laser beam onto a sample surface, usually placed within an air-tight ablation chamber in He atmosphere, liberating sample aerosols. The laser wavelength is a critical parameter influencing the sample aerosol, with common choices for applications in Earth Sciences being 193 nm (ArF excimer) and 213 nm (Nd-YAG) (Jeffries et al., 1998; Günther and Heinrich, 1999; Wang et al., 2006; Hathorne et al., 2008; Müller and Fietzke, 2016; Evans and Müller, 2018). A set of mirrors and lenses are used to deliver the laser beam onto the sample. The energy of photons from the laser source incident on the sample is converted into thermal energy, which ejects particles from the sample surface and generates aerosols. The sample is placed in an air-tight ablation cell consisting of a window made up of material that is transparent at the laser's wavelength, through which the laser enters the ablation cell. The design of the laser ablation cell is crucial. To accommodate a larger

number of solid samples while ensuring rapid washout time, a two-volume laser ablation cell was designed (Müller et al., 2009). The two-volume cell consists of a funnel-shaped hollow cone located within the closed ablation cell, positioned above the sample holder surrounding the ablation site, which remains stationary, and the sample holder beneath is moved to access the sampling site. The two-volume cell system demonstrated faster washout, reducing dispersion of the ablation signal and higher signal-to-noise ratios (Müller et al., 2009; Wang et al., 2013; Douglas et al., 2015; Müller and Fietzke, 2016; Evans and Müller, 2018). The ablation is typically conducted in a helium atmosphere, with the optional use of additional gas added downstream of the ablation cell, e.g., the addition of N_2 gas that improves sensitivity (Durrant, 1994). The aerosol generated is transferred to the ICP-MS via a carrier gas, usually He or Ar. The amount and size of sample particles removed per laser pulse depend on laser parameters, including laser wavelength, laser energy, laser power, pulse duration, pulse repetition rate, irradiation time, spot size, and laser beam profile (Guillong and Günther, 2002; Guillong et al., 2003; Diwakar et al., 2013).

LA-ICP-MS is increasingly utilised for the analysis of marine carbonates. Müller and Fietzke (2016) conducted a comparative analysis of laser ablation tracks on calcite at 213 nm and 193 nm wavelengths, recommending the utilisation of 193 nm for controlled ablation. One of the challenges for LA-ICP-MS measurements of marine carbonate is the non-availability of a homogeneous matrix-matched reference material. Due to the lack of a matrix-matched standard for $CaCO_3$, elemental/calcium ratios in carbonates are frequently measured using soda-lime glass standards (NIST SRM 61x) as an external standard and Ca as an internal standard (Jochum et al., 2012; Müller and Fietzke, 2016; Evans and Müller, 2018). Presently, the best available reference values for the NIST SRM61x glass standards were revised and derived following the ISO guidelines protocol and the IAG protocol for certified reference materials by Jochum et al. (2011).

Nevertheless, re-evaluating values for some elements, such as the Mg/Ca values, within these glass standards may be warranted, as suggested by Evans and Müller (2018). While a well characterised homogenous carbonate reference material would be the ideal calibration standard for marine carbonate analysis, studies have demonstrated that calibrating with NIST 610 yields satisfactory results when using a 193 nm laser (Jochum et al., 2012; Evans and Müller, 2018). Application of LA-ICPMS has been notably successful in the investigation of a range of marine carbonates, including speleothem (Jochum et al., 2012), ostracod shell (Jochum et al., 2012), and foraminifera shell (Eggins et al., 2003). Besides this, the high spatial resolution capability of LA-ICP-MS enabled the investigation of inter and intra-chamber variability of marine calcite shells, providing insights into biomineralisation processed.

Chapter 2: Accurate measurement of K/Ca in low [K] carbonate samples using laser ablation ICPMS

Citation:
Nambiar R., Kniest J. F., Schmidt A., Raddatz J., Müller W. and Evans D. (2024) Accurate measurement of K/Ca in low [K] carbonate samples using laser-ablation sector-field inductively coupled plasma mass spectrometry. *Rapid Communications in Mass Spectrometry* 38. doi: 10.1002/rcm.9692.

Accurate measurement of K/Ca in low [K] carbonate samples using laser-ablation sector-field inductively coupled plasma mass spectrometry

Romi Nambiar[1,2,*], Jorit F Kniest[1,2], Alexander Schmidt[1,2], Jacek Raddatz[1,2], Wolfgang Müller[1,2], David Evans[1,2,a]

[1]Institute of Geosciences, Goethe University Frankfurt, Altenhöferallee 1, 60438 Frankfurt am Main, Germany

[2]Frankfurt Isotope and Element Research Center (FIERCE), Goethe University Frankfurt, 60438 Frankfurt am Main, Germany

[a]Now at: School of Ocean and Earth Science, University of Southampton, Southampton, SO14 3ZH, UK

*Corresponding author: Email address: Nambiar@geo.uni-frankfurt.de (R. Nambiar)

Abstract

Potassium (K) is a major component of several silicate minerals and seawater, and therefore constraining past changes in the potassium cycle is a promising way of tracing large-scale geologic processes on Earth. However, [K] measurement using ICP-MS is challenging due to an ArH^+ interference, which may be of a similar magnitude to the K^+ ion beam in samples with <0.1 % m/m [K]. In this work, we investigated the effect of the ArH^+ interference on K/Ca data quality by comparing results from LA-ICP-MS measured in medium and high mass resolution modes, as well as validating our LA results via solution ICP-OES and solution ICP-MS measurements. To do so, we used a wide range of geological

reference materials, with a particular focus on marine carbonates, which are potential archives of past changes in the K cycle but are typically characterized by [K] <200 µg/g. In addition, we examine the degree to which trace element data quality is driven by down-hole fractionation during LA-ICP-MS measurements. Our results show that medium mass resolution mode (MR) is sufficiently capable of minimising the effect of the ArH^+ interference on K^+. However, the rate of down-hole fractionation for Na and K varies between different samples as a result of their differing bulk composition, resulting in matrix-specific inaccuracy. We show how this can be accounted for via down-hole fractionation corrections, resulting in an accuracy of better than 1 % and a long-term reproducibility (intermediate precision) of <6 % (RSD) in JCp-1NP using LA-ICP-MS in MR. Our [K] measurement protocol is demonstrably precise and accurate, and applicable to a wide range of materials. The measurement of K/Ca in relatively low-[K] marine carbonates is presented here as a key example of a new application opened up by these advances.

1. Introduction

Since the first trace element measurements using laser ablation (LA) as a sample introduction technique for inductively coupled plasma (ICP)-based analytical approaches in the mid-late 1980s (Gray, 1985), there has been both a steady and rapid advance in both LA and ICP-MS instrumentation and methodologies. For example, LA-ICP-MS has been widely used to investigate the elemental and isotopic composition of various geological samples at high spatial resolution, including fluid inclusions in minerals (Audetat et al., 1998; Günther and Heinrich, 1999; Günther et al., 2001), speleothems (Treble et al., 2005; Stoll et al., 2012), ostracod shells (Jochum et al., 2012), and foraminifera (Eggins et al., 2003; Evans and Müller, 2013). In addition, the high spatial resolution capability of LA-ICP-MS, especially in the vertical direction when conducting spot analysis via depth profiling, has facilitated the investigation of compositional heterogeneity at sub-μm resolution (Eggins et al., 2003; Hathorne et al., 2003; Evans et al., 2015), providing insights into (e.g.) biomineralisation processes.

While LA-ICP-MS has become increasingly common, interferences by atomic or molecular (polyatomic) ions with the same mass-to-charge ratio (m/z) as the analyte of interest remain a source of inaccuracy and/or imprecision. The molecular/polyatomic ion interferences are produced from the interaction of ions with Ar or other common ions present in the sample matrix or carrier gases, such as H, N, O, and Cl. For instance, interferences such as $^{40}Ar^{1}H^{+}$ on $^{41}K^{+}$, $^{38}Ar^{1}H^{+}$ on $^{39}K^{+}$, $^{40}Ar^{16}O^{+}$ on $^{56}Fe^{+}$, $^{40}Ar^{16}O^{1}H^{+}$ on $^{57}Fe^{+}$, $^{40}Ar^{14}N^{+}$ on $^{54}Fe^{+}$, and $^{40}Ar^{35}Cl^{+}$ on $^{75}As^{+}$ are an issue (O'Brien et al., 2003; Schönbächler, 2016;

Sader and Ryan, 2020; Lomax-Vogt et al., 2021). In addition, interferences can also be caused by spectral overlapping that often results when the abundance of an interference is significantly larger than the peak of adjacent mass, with the magnitude of the issue dependent on the mass-resolving power of the instrument. Conventional quadrupole (Q) mass analysers are capable of a mass resolution (R) of ~300 (Schönbächler, 2016), whereas magnetic sector field ICP-MS instruments ((SF)-ICP-MS), such as the ThermoFisher Scientific Element XR (utilized here) offers different mass resolution modes, i.e., low (R= ~300), medium (R= ~4000) and high (R= ~10,000), with the separation of polyatomic interferences from analytes of interest requiring medium or high resolution. The issue of both polyatomic interference and abundance sensitivity is important for the measurement of K/Ca, the principal focus of this contribution.

Potassium is a major component of the solid Earth, with an average mass fraction of 260 µg/g in the Earth's mantle, 2.8% m/m in the upper continental crust, and ~1350 µg/g in mid-ocean ridge basalt (Taylor and McLennan, 1995; Gale et al., 2013; Palme et al., 2014). Potassium is also a major ion in seawater (~10.2 mmol/kg; ~380 µg/g), and is incorporated to a substantial degree in authigenic clay minerals and marine $CaCO_3$ (Martin and Whitfield, 1983). Since it is present at a relatively high concentration in a wide range of materials, potassium has been identified as a potential indicator for global-scale geochemical processes (Parendo et al., 2017; Santiago Ramos et al., 2018; S. Li et al., 2019; W. Li et al., 2019).

Trace element incorporation into marine carbonates is an important tool for palaeoclimate and palaeoenvironmental reconstruction (Delaney et al., 1989; Rosenthal et al., 1997; Rickaby and Elderfield, 1999; Weldeab et al., 2007; Allen and Hönisch, 2012; Evans et al., 2018; Hauzer et al., 2018; Gray and Evans, 2019). However, despite the potential for reconstructions of the K cycle for determining past changes in (e.g.) Earth surface processes, only a few studies have measured K/Ca in marine carbonates, which are typically characterized by K/Ca of 0.17-0.23 mmol/mol, equivalent to 63-85 µg/g of [K] (measured by AAF-AAS: air-acetylene flame atomic absorption spectrophotometry (Mitsuguchi and Kawakami, 2012), and ICP-OES: inductively coupled plasma optical emission spectroscopy (Bell et al., 2018; Ram and Erez, 2021). However, to our knowledge, even fewer studies have determined [K] using in situ microanalysis at low (<1000 µg/g) concentrations (Geerken et al., 2019; Levi et al., 2019), presumably because of the analytical difficulties associated with this measurement described above. In addition to these, the lack of well-characterized carbonate reference materials has meant that determining the accuracy of LA-ICP-MS measurements is not currently straightforward (to our knowledge, only one previous study has reported the K mass fraction of a commonly used carbonate reference material (JCp-1 using atomic absorption spectrometry; Okai et al., 2002). Likewise, most previous K measurements in marine samples reported earlier were determined using techniques other than ICP-MS, such as AAS (Rosenthal and Katz, 1989; Mitsuguchi and Kawakami, 2012), ICP-OES (Ram and Erez, 2021), or nanoSIMS (Geerken et al., 2019).

While there are only limited studies of potassium in marine carbonates, materials with higher [K] have been widely investigated using both solution-based techniques and in

situ microanalysis (Cooper, 1963; Rice, 1976; Halter et al., 2002; Heinrich et al., 2003; Jochum et al., 2006). Various approaches have been proposed to reduce the magnitude of the ArH^+ interference on ICP-MS measurements: 1) Measurement in medium or high mass resolution mode is capable of resolving polyatomic molecular interferences (e.g., $^{23}Na^{16}O$ and $^{38}Ar^{1}H^+$ on ^{39}K) (Lomax-Vogt et al., 2021). The required mass resolution (R) to separate $^{39}K^+$ and $^{38}Ar^{1}H^+$ is ~5600, and high mass resolution measurements on sector-field instruments are thus capable of separating the interference, with an associated reduction in sensitivity. 2) The use of reaction cell instruments, if available, with H_2 as the cell gas decreases the ArH^+ interference by forming Ar plus H_2 or H_3^+(Eiden et al., 1996; Russell et al., 2021). 3) Working in 'cool plasma' conditions, achieved by reducing the plasma RF power, resulted in a substantial reduction of most severe polyatomic interferences derived from Ar complexes (Tanner, 1995; Murphy et al., 2002). However, cold plasma conditions increase the risk of matrix-dependent fractionations occurring in the plasma (Tanner, 1995).

Here, we evaluate the quality of K/Ca measurements by LA-SF-ICP-MS and establish a methodology for K/Ca measurement for low K marine carbonate samples, including a comparison of LA-ICPMS measurements made in MR (partially resolving the ArH interference) to solution ICP-MS measurements in HR (full resolving the interference). Given the lack of carbonate reference materials with well-characterised [K], we also report the long-term data quality of K/Ca in several carbonate reference materials (JCp-1NP, JCt-1NP, and MACS-3NP) determined by laser ablation and compare the results to new solution-SF-ICP-MS (HR) and ICP-OES measurements.

2. Materials and Methods

To establish a methodology suitable for the determination of K/Ca in relatively low [K] carbonate samples (<200 µg/g), we performed experiments using LA-SF-ICP-MS in both medium and high mass resolution modes. The principal aim of doing so was to investigate the extent of the ArH^+ interference on K/Ca measured in geological reference materials with a wide range of K mass fractions. Given that the measurement of alkali elements are of widespread interest in the Earth sciences but are known to be potentially characterized by strong methodologically-induced fractionations during laser ablation measurement (Míková et al., 2009; Evans and Müller, 2018), we extend this analysis to include other (alkali) elements, including sodium. In addition, we report solution-based ICP-OES measurements of carbonate reference materials to determine the accuracy of our laser ablation K/Ca results. We also investigated a range of low [K] marine carbonate samples using LA-ICP-MS (MR and HR) as well as solution-based ICP-MS (HR) to demonstrate that our LA methodology produces accurate results.

2.1. LA-SF-ICP-MS

A RESOlution M-50 193 nm ArF laser ablation system, equipped with a Laurin Technic S-155 two-volume laser-ablation cell (Müller et al., 2009), connected to a magnetic sector-field ICP-MS (ThermoFisher Scientific Element XR) at the Frankfurt Isotope and Element Research Center (FIERCE), Goethe University Frankfurt was used for all LA-ICP-MS measurements. Ablation was carried out in a helium atmosphere with argon added into the top of the smaller-volume inner cell and an additional diatomic gas, N_2, added downstream

of the ablation cell. The LA-ICP-MS operating parameters used in this study are described in Table 1. The instrument was tuned daily by measuring NIST SRM612 (60 µm; 6 Hz) to maximise sensitivity i.e., >4.5 million cps on ^{238}U while maintaining the oxide production rate <1% (ThO/Th; m/z 248/232) and the doubly charged production rate <2% (m/z 22/44) in low mass resolution mode (LR), achieved using the laser and ICPMS parameters given in Table 1. A range of reference materials were analysed, including the NIST glasses (NIST SRM610, NIST SRM612, NIST SRM614, and NIST SRM616), which were used for primary standardisation, the MPI-DING glasses (GOR 128-G, GOR 132-G, ATHO-G, KL2-G, and StHs 6/80-G) as well as the carbonate reference materials (JCp-1, JCt-1, and MACS-3). Monitored masses (m/z) were ^{11}B, ^{23}Na, ^{24}Mg, ^{25}Mg, ^{27}Al, ^{39}K, and ^{43}Ca and ^{88}Sr. In the case of our laser ablation measurements, we used the nano-pellet versions of the original carbonate reference materials (JCp-1NP, JCt-1NP, and MACS-3NP) (Garbe-Schönberg and Müller, 2014), which are more homogeneous than the original carbonate reference materials (Jochum et al., 2019). The nano-pellets of the carbonate reference materials used in this study were provided to WM/DE by Dr Dieter Garbe-Schönberg in 2014-2015 and have been stored in the presence of moisture-absorbing granules and later in a designated low-humidity chamber.

In addition, we investigated a range of marine $CaCO_3$ samples including corals, foraminifera, and molluscs using LA-ICP-MS in both high and medium mass resolution modes (see the supplementary materials for a sample list). All the marine carbonates were treated with 1% NaOCl in an ultrasonic bath for 5 min to oxidise any organic material.

Samples were then rinsed 2-3 times with 18.2 MΩ cm deionized water (milli-Q), followed by a final cleaning step with methanol in an ultra-sonication bath.

Data reduction followed established protocols (e.g., Heinrich et al., 2003) and was performed using an in-house Matlab script (Evans and Müller, 2018), which subtracts blank values from sample data and calibrates trace element ratios using a depth-dependent measured/reported element/^{43}Ca ratio derived from repeat analysis of the NIST SRM61X glasses (^{43}Ca was used as the internal standard in all cases). The elemental mass fractions of the NIST glasses were taken from Jochum et al., (2011) with the exception of Mg in NIST SRM610, for which we use that of Pearce et al., (1997) following the recommendation of Evans and Müller, (2018). For the purposes of determining the accuracy of the measurements when treating the secondary reference materials as unknowns, the elemental values of the MPI-DING glasses were taken from Jochum et al., (2006) and we initially used the JCp-1 values of Okai et al., (2002) but revisit these in light of our own data in the discussion section.

Table 1. Summary of the laser ablation system and ICP-MS operating parameters.

Laser Ablation (RESOlution M-50)		
Sampling mode	Spot; line	
Wavelength	193 nm	
Fluence	~6.3 J cm^{-2}	
Repetition rate	3 Hz	
Spot size	50 µm	
He	300 - 400 mL min^{-1}	
N_2	3.5 - 4.0 mL min^{-1}	
SF-ICP-MS (ThermoFisher Scientific Element XR)		
	Laser Ablation	**Solution**
Resolution mode	medium (R= ~4000) and high mass (R= ~8000) resolution	high mass resolution (R= ~8000)
Torch RF power (W)	1330 - 1380 W	1350-1400 W
Sample cone	Ni Jet cone	Ni Jet cone
Skimmer cone	Ni H cone	Ni H cone
Sample gas flow (l min^{-1})	0.80 - 1.00 l min^{-1}	1.10 - 1.15 l min^{-1}
Auxiliary gas flow (l min^{-1})	0.60 - 0.90 l min^{-1}	0.70 l min^{-1}
Sensitivity	4-7 million cps of ^{238}U (NIST SRM612, 60 µm, 6 Hz) in LR mode	6-8 million cps of ^{238}U at ~1 ppb in LR mode

2.2. Solution-based measurement of carbonate reference materials and a suite of marine carbonates samples

Measurements of carbonate reference materials were performed with solution-based analysis with both SF-ICP-MS in HR and ICP-OES to compare bulk values determined with the LA-ICP-MS method described in Sec. 2.1. A range of marine carbonates samples including corals, foraminifera, and molluscs were also investigated with solution-based analysis by ICP-MS in HR. While the nano-pellets of carbonate reference materials (JCp-1NP,

JCt-1NP, and MACS-3NP) were measured using LA-ICP-MS, the solution measurements were performed on original carbonate powder reference materials (referred to here as JCp-1, JCt-1, MACS-3). In the case of MACS-3, we used fragments of the USGS pressed powder pellets as, to our knowledge, a MACS-3 powder reference material is unavailable.

For solution ICP-MS analysis, ~0.8 mg of JCp-1 and a range of marine carbonate samples were treated with different cleaning methods (Table 2) and finally dissolved in 2 mL 0.5 N HNO_3 (resulting in a [Ca] of ~160 µg/g) for analysis. Three aliquots of ~0.8 mg of each sample were divided into three groups. The first group was not subjected to any pre-treatment. The second group was treated with 500 µL 1% alkali buffered H_2O_2 (freshly prepared solution of 100 µL H_2O_2 in 10 mL 0.1 N NH_4OH). The third group was treated with 500 µL 1% alkali buffered H_2O_2, followed by 300 µL 0.0005 N HNO_3. The treatments with 1% alkali buffered H_2O_2 and 0.0005 N HNO_3 were carried out for 8 min and 2 min, respectively, in an ultrasonic bath. Both treatments were followed by rinsing with 18.2 MΩ cm deionized water (milli-Q). After each step, samples were centrifuged for 10 min at 5000 rpm, after which the supernatant was carefully removed. Finally, samples were dissolved in 0.5 N HNO_3. The K/Ca of the carbonate reference material JCp-1 and the marine carbonate samples were determined using a ThermoFisher Scientific Element XR in high mass resolution mode. ICP-MS operating conditions are given in Table 1. Standardisation was performed using a set of standards with K concentrations of 2.5, 5, 10, 20, 35, 50, 75, and 100 µg/g and a constant Ca concentration of 160 µg/g (the Ca concentration was set to be identical to all unknowns). This ratio calibration approach has been shown to improve the precision of carbonate samples during ICP-OES measurements (de Villiers et al., 2002). All calibration standards

were prepared with double distilled 0.5 M HNO_3. Sample K/Ca was determined by normalising ^{39}K count rates to the internal standard ^{43}Ca.

For ICP-OES analysis, powder of the reference materials JCp-1, JCt-1, and fragments of a MACS-3 pellet were directly dissolved in ~0.5 N HNO_3 (Table 2). These solutions were then used to prepare five aliquots of each reference material by mixing with a Yttrium solution and adjusting the Ca concentration to 100 mg/L (JCp-1, JCt-1) or 300 mg/L (MACS-3). The Y concentration was set to 1 mg/L for each aliquot, which was used for internal standardisation. In this approach, yttrium is utilized as an internal standard, in order to correct for potential non-spectral interference introduced by e.g., carbon or the acids used, as well as, the difference in view mode (axial or radial) (Vogiatzis and Zachariadis, 2011; Scheffler and Pozebon, 2013; Drava and Minganti, 2020). For external calibration, four multi-element solutions were prepared by mixing single-element ICP standard solutions. The concentrations of Mg, Na, Sr, and K in these calibration standards were adjusted to cover the typical range of element/Ca ratios of the reference materials (Okai et al., 2002; Jochum et al., 2019). ICP-OES measurements were performed with a ThermoFisher Scientific iCap 6300 (dual viewing) at Goethe University Frankfurt. Intensities for K, Mg, and Sr were measured in axial mode using lines 766.4 nm, 279.5 nm, and 421.5 nm, while Na and Ca were measured radially at 589.5 nm and 315.8 nm, respectively. The background-subtracted intensities of all elements of interest were normalised internally using the Y values obtained from the nearest spectral line out of the three selected for Y measurements. Following the Y normalisation, elements are ratioed to calcium, and the calibration is performed using intensity ratio method as suggested by de Villiers et al., (2002).

Table 2. Sample treatment procedures for solution ICP-MS/ICP-OES.

Analytical method	Treatment No.	Treatment	Dissolution
Solution-ICP-MS	1	untreated	Dissolution in 0.5 M HNO_3
	2	1% H_2O_2 (in 0.1 N NH_4OH)	
	3	1% H_2O_2 (in 0.1 N NH_4OH)+ 0.0005 N HNO_3	
Solution-ICP-OES	-	untreated	Dissolution in 0.5 M HNO_3

3. Results and discussion

3.1. The influence of surface contamination on LA-ICP-MS K/Ca measurements

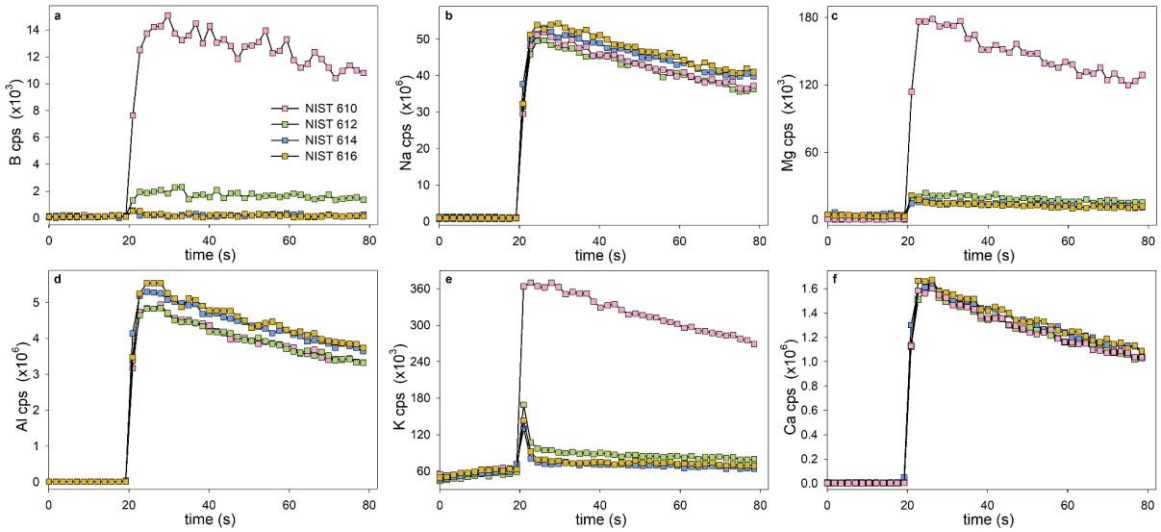

Figure 1. Representative element count rate responses during ablation of the NIST SRM61x glasses: a) boron, b) sodium, c) magnesium, d) aluminium, e) potassium, and f) calcium. For an equivalent plot displayed as El/Ca ratios see Figure S1.

In our laboratory, the NIST glass reference materials are routinely cleaned with ethanol prior to analysis in order to remove the bulk of any previous ablation blanket and

other possible surface contamination. To test whether this is an effective procedure for minimizing surface K contamination, we compare ^{39}K LA depth profiles through four NIST glasses to other common analytes. No initial spike in count rates indicative of surface contamination was observed for any major element, including Ca, Na, or Al (Figure 1), and although boron is well known for being contamination-prone (Marschall and Ludwig, 2004; Tiepolo et al., 2005; Kent and Ungerer, 2006), no initial B spike was observed (Figure 1a). Similarly, no initial spike was observed for Mg. However, an initial K spike was regularly observed in NIST SRM612/4/6, having K mass fraction of ~62, 30, and 29 µg/g, respectively (Figure. 1e). A similar phenomenon has been reported for other low-mass fraction contamination-prone analytes. For example, Russo et al., (2000) reported high initial peaks for Pb/Ca in the NIST SRM61x glass reference materials using a 266 nm laser, while Evans and Müller, (2013) demonstrated substantial degrees of Zn contamination in the absence of pre-ablation cleaning. This is the case whether or not the data are ratioed to Ca (Figure S1). Given that we only observe surface K spikes for the NIST glasses with lower K mass fractions, which implies that the observation is unlikely to be driven by laser-sample surface coupling effects (Diwakar et al., 2013), we identify remnant surface contamination as a likely cause for the initial K spikes. Modifying our cleaning procedure for the NIST glasses to involve a step with a few drops of 0.01 M HNO_3, followed by sonication in ultra-pure ethanol and Milli-Q rinsing, removed the initial peaks for K, confirming this hypothesis. Hence, in order to measure K/Ca in low [K] samples, it is necessary to follow an effective cleaning procedure with either chemical cleaning, pre-ablation, or at the very least, to ensure that these portions of the dataset are not considered when processing the data.

3.2. K/Ca measurements by LA-SF-ICP-MS in medium and high mass resolution mode

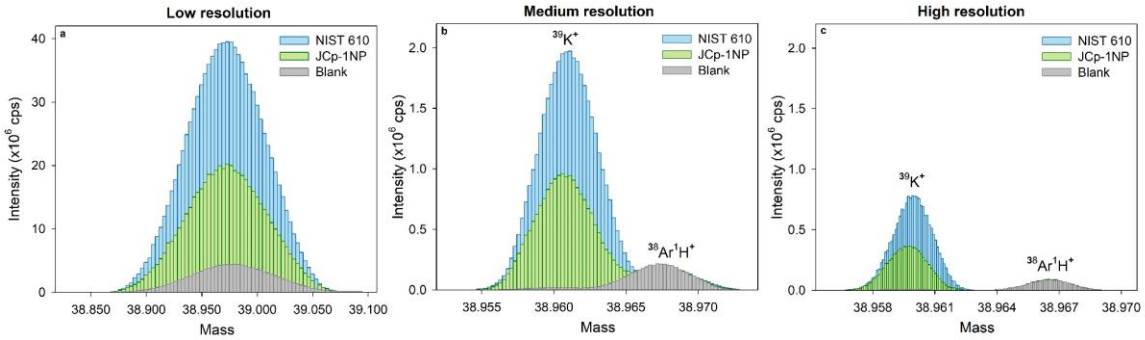

Figure 2. Representative spectral interference of $^{38}Ar^{1}H^{+}$ on $^{39}K^{+}$ in a) low, b) medium, and c) high mass resolution measurement modes. The y-axis scale is the same in panel b and c, showing the degree of sensitivity decrease between these modes. Ablation was carried out by line scan analysis with a beam size of 60 µm and repetition rate of 6 Hz.

The degree of separation of $^{38}Ar^{1}H^{+}$ and $^{39}K^{+}$ during the analysis of NIST SRM610 and JCp-1NP measured using LA-ICP-MS in low mass resolution (LR), medium mass resolution (MR), and high mass resolution (HR) is shown in Figure 2. The measurement in LR is incapable of resolving the spectral interference. In MR, the tail of the $^{38}Ar^{1}H^{+}$ peak interferes with the $^{39}K^{+}$ peak, whereas the $^{38}Ar^{1}H^{+}$ and $^{39}K^{+}$ peaks are fully separated in HR. However, sensitivity is reduced by a factor of 2-3 at HR relative to MR, such that the decrease in sensitivity may become the limiting factor in the trade-off between mass resolution and limit of detection. For instance, the limit of detection for the measurement in MR is 7.3 µg/g (K/Ca: 0.02 mmol/mol), whilst in HR it is 13.0 µg/g (K/Ca: 0.04 mmol/mol). Thus, the signal to background ratio is maximised in MR, which is therefore likely to be the optimum resolution for low-K marine carbonate measurements (e.g., foraminifera, corals, bivalves, etc.

with [K] <200 µg/g), provided the ArH^+ contribution remains sufficiently stable that it can be accurately quantified and corrected for.

We initially investigated whether the degree of ArH^+ and K^+ peak separation offered by MR is sufficient to produce accurate and precise data using geological reference materials with K mass fractions ranging from ~90 to 22000 µg/g. Since MR does not entirely resolve the polyatomic interference from ArH^+, K/Ca was determined in two ways. In our method, 40 channels were selected for the K mass window, with the interference of the ArH^+ peak tail dominantly impacting the right side of the ^{39}K peak (Figure 2). Using these data, we 1) included all 40 channels when calculating K/Ca, and 2) only the first 25 channels (left side of the peak), for which the ArH^+ interference is much lower (background less than 2×10^4 cps compared to 94×10^4 cps (NIST 610) and 49×10^4 cps (JCp-1), when averaging all channels). Although reducing the number of channels resulted in a decrease in precision, we observed that the mean values fall within uncertainty of each other (Figure S2). The difference in the mean value calibrated with the same standard (NIST SRM610/2) was less than 2% for all reference materials except MACS-3NP (3%) (Figure S2).

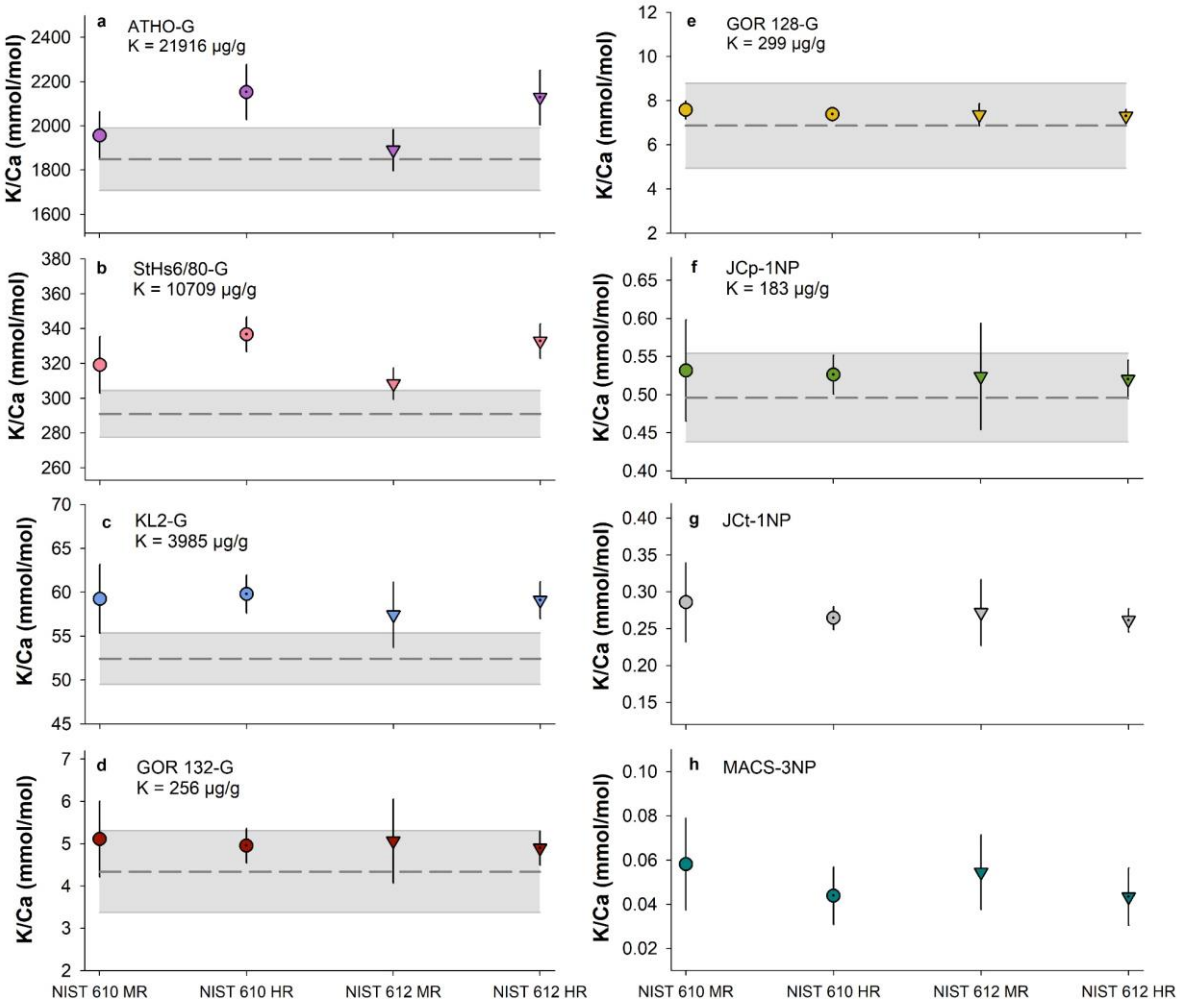

Figure 3. LA-ICP-MS K/Ca measurements in high mass resolution (HR) and medium mass resolution (MR). The dashed lines and grey shaded regions represent the reported K/Ca values and associated 2SD uncertainty (MPI-DING reference materials: Jochum et al., (2006); JCp-1: Okai et al., (2002)). The standard used for calibration is shown on the x axis. The K/Ca data are derived from one session, with the exception of GOR 128-G, GOR 132-G, JCp-1NP, JCt-1NP, and MACS-3NP measured in MR. In these case, the K/Ca data represents the long-term average values of seven different sessions. Error bars are 2SD.

Given that half-peak measurements resulted in no improvement in data quality, we next compared measurements of all of these reference materials in medium mass resolution to high mass resolution mode in which K^+ and ArH^+ peaks are well resolved (Figure 2), using all available channels. We observed overall very similar accuracies between the two resolutions (Figure 3; Table S1). Specifically, the mean K/Ca values of reference materials measured in HR are within 5% of those measured in MR, demonstrating that full separation of the interference is counterbalanced by the loss in sensitivity. Moreover, comparing the measurements of individual sessions demonstrates that the standard deviation of K/Ca measurements of low K marine carbonate is similar in MR and HR modes (Figure S5). An exception was observed for reference materials with a very high [K], i.e., ATHO-G and StHs/80-G, which were characterised by a difference in mean K/Ca of 10% and 5% respectively (Figure 3). While this exercise demonstrates that NIST SRM610/612-standarised data are similar, we use NIST SRM610 as the calibration standard for all sample K/Ca measurements as we found that this results in an improved long-term reproducibility (see supplementary section 3 for rationale/demonstration of this).

3.3. Matrix-dependent fractionation of alkali metals during laser ablation

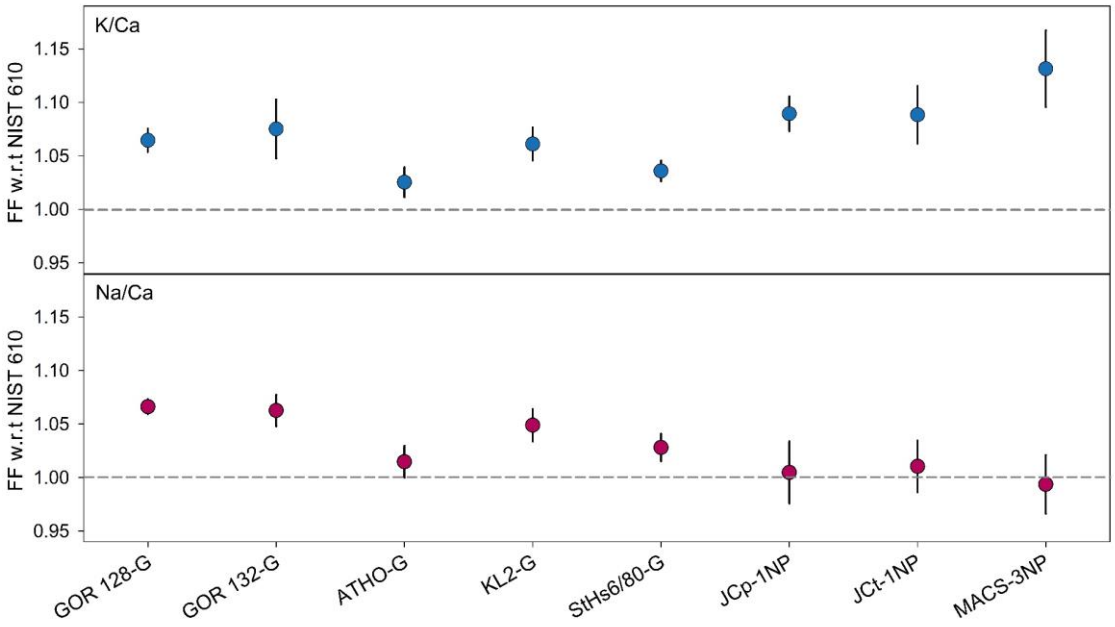

Figure 4. Fractionation factors relative to NIST SRM610 were averaged across seven analytical sessions except for ATHO-G, KL2-G, and STHs6/80-G (one session). Number of replicates (n): n(GOR 128-G): 50, n(GOR 132-G): 49, n(ATHO-G): 5 , n(KL2-G): 7 ,n(StHs6/80-G): 8, n(MACS-3NP): 46, n(JCp-1NP): 47, n(JCt-1NP): 45. Error bars represent the 2SE of all measurements.

Spot analysis in LA-ICP-MS often results in down-hole inter-element/isotope fractionation, which is an additional potential source of inaccuracy when non-matrix-matched standardization is used or if sub-percent level accuracy and precision are required (Paton et al., 2010; Ver Hoeve et al., 2018). Down-hole fractionation depends on the sample matrix, ablation pit aspect ratio, and laser beam power density (Mank and Mason, 1999). We assess whether this is an issue for K/Ca measurements, using the definition of the down-hole 'fractionation factor' (FF) of Fryer et al., (1995) i.e., it is equal to the analyte/internal standard

ratio of the second half of the analysis relative to the first half of a single analysis. In the case of analytes with a similar behaviour to the internal standard (^{43}Ca), such as the alkali earth metals, no significant differences in fractionation factors between the NIST glasses and carbonates were observed when using a 193 nm laser (Evans and Müller, 2018). However, the alkali elements have been observed to be characterised by matrix-dependent down-hole fractionation (Longerich et al., 1996; Míková et al., 2009; Evans and Müller, 2018), which means that this is a possible source of inaccuracy in the measurements performed here. Indeed, Evans and Müller, (2018), reported an accuracy offset in Na, Li, and Rb over a range of ablation and tuning conditions, likely resulting from the differential down-hole fractionation betweem the NIST glasses and $CaCO_3$ reference materials.

The analyses presented here demonstrate that different reference materials are characterised by different down-hole fractionation factors (Figure 4; S4). These results are displayed as the down-hole fractionation of K/Ca and Na/Ca relative to NIST SRM610 in Figure 4 (Table S2). Here, the fractionation factors were estimated for each session and then averaged over all analytical sessions. The K/Ca and Na/Ca fractionation factors (relative to the mean fractionation factor measured in the primary calibration standard NIST SRM610) appear to be strongly matrix dependent. In the case of the MPI-DING glasses, these range between 1.01 and 1.08, with a close correspondence between the Na and K fractionation factors (r^2=0.93), but no clear relationship to the bulk composition of the glass. In contrast, the K/Ca fractionation factor in the carbonate reference material was higher than that of Na/Ca.

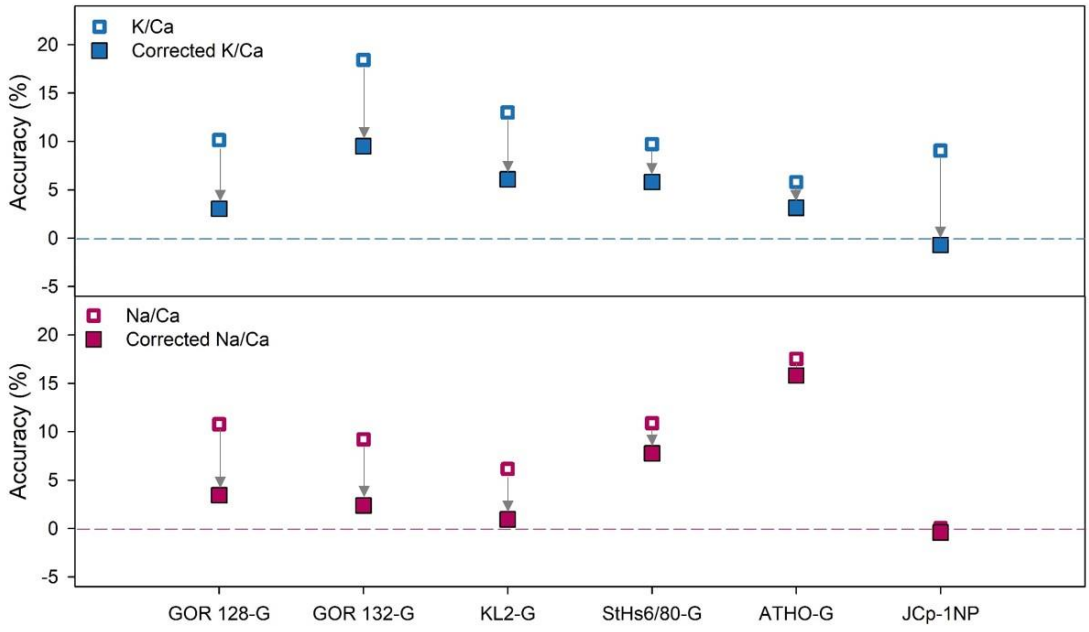

Figure 5. NIST SRM610-standardised Na/Ca and K/Ca accuracy of the MPI-DING glass reference materials and carbonate reference material (JCp-1NP) before and after correction for down-hole fractionation using the fractionation factors from Figure 4.

Given the consistency of the measured fractionation factors between analyses/sessions, we explore whether accuracy can be improved by applying a correction based directly on these measured FF. Correcting for down-hole fractionation in this way, i.e., adjusting the measured element/Ca values by a percentage equal to the fraction factor, we demonstrate an improvement in the accuracy of K and Na in all reference materials considered here of 2-10% (Figure 5). While there are other possible sources of inaccuracy (Lomax-Vogt et al., 2021), we suggest that this is a simple method by which accuracy can be substantially improved in the case of elements characterised by significant matrix-dependent down-hole fractionation in future studies.

3.4. Comparison of K/Ca values of different marine carbonate samples measured by LA and solution ICP-MS

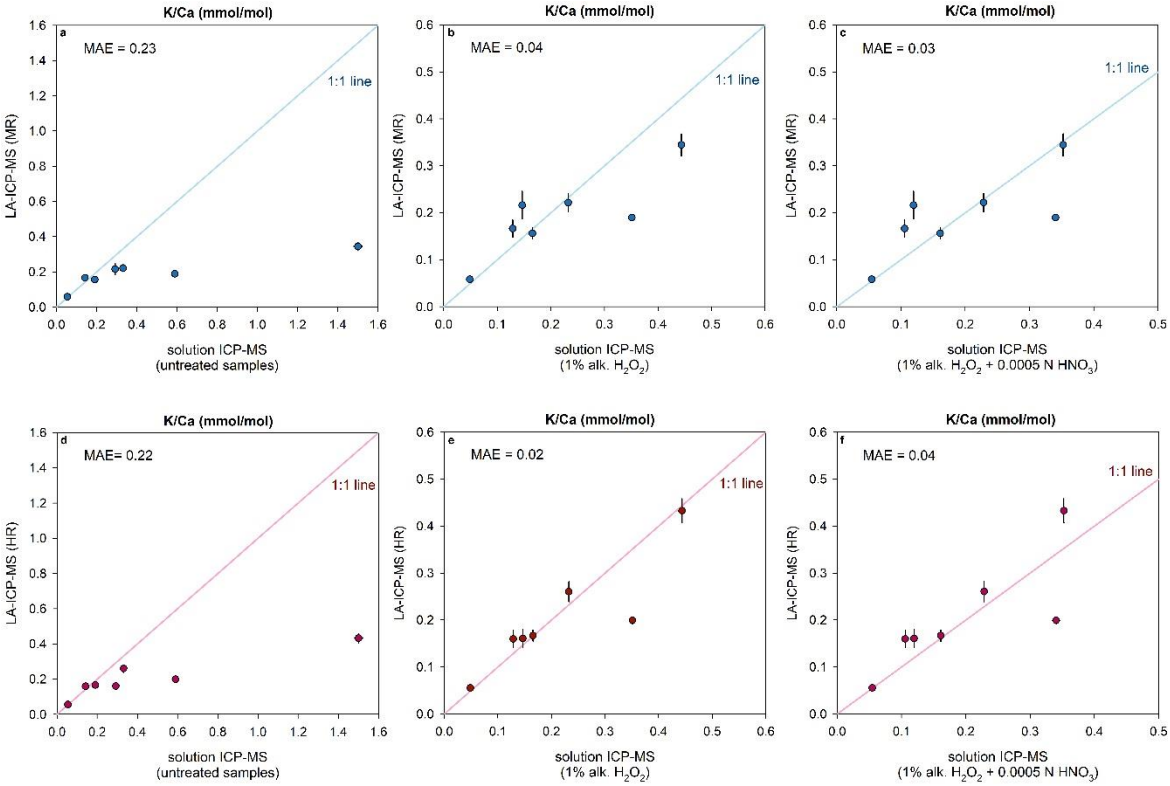

Figure 6. K/Ca values measured in a range of marine carbonate samples by solution-ICP-MS (HR) and LA-ICP-MS (MR, top row, and HR, bottom row). The x axis labels describe the cleaning procedures applied prior to the solution ICP-MS measurments (samples were cleaned in the same way prior to all LA measurements). Error bars are 2SE. The K/Ca data measured using LA-ICP-MS are corrected for down-hole fractionation as described in Sec. 3.3. MR: medium mass resolution mode; HR: high mass resolution mode. MEA: mean absolute error.

To validate the K/Ca values of low-K marine carbonates measured by LA-ICP-MS in both medium and high mass resolution modes following the recommendations outlined above, we measured the K/Ca of a range of marine carbonates including corals, foraminifera,

and molluscs using solution ICP-MS (see Sec. 2.2; Table S3; Figure 6). For the K/Ca measurements by solution SF-ICP-MS in HR, each sample was crushed using an acid-cleaned agate mortar and pestle and subjected to different treatment methods (see section 2.2; Table 2) before dissolution using 0.5 N HNO_3. The solution K/Ca values after each treatment are compared to data from the same samples measured by LA-ICP-MS in Figure 6. All samples showed a decrease in K/Ca when treated with H_2O_2 compared to no treatment when measured by solution ICP-MS, which is likely the result of a substantial portion of the K being present in the organic fraction (as may also be the case for Na, see Gray et al., (2023)). The H_2O_2-treated samples measured by solution ICP-MS are characterised by K/Ca within the uncertainty of both the medium and high mass resolution LA-ICP-MS results (Figure 6). The only exception is modern larger benthic foraminifera (*O. ammonoides*) which is characterised by a lower K/Ca value when measured using LA-ICP-MS. These foraminifera have a complex microstructure and are characterised by substantial inter and intra-individual heterogeneity, such that this is likely to represent real sample variability rather than an analytical issue, given the good agreement obvious in the remainder of the dataset. The same is true when comparing the LA-ICP-MS data to the solution analyses including a further weak acid leach (Figure 6), suggesting that a single oxidative step is sufficient to remove organic-bound and/or surface-adsorbed K in these samples. Furthermore, the results demonstrate that both our medium and high mass resolution LA-ICP-MS data are accurate compared to solution ICP-MS analyses. While we do observe a minor improvement in data quality between medium and high mass resolution, for example, the mean absolute error (MAE) decreases from 0.04 to 0.02 mmol/mol when comparing to the solution results with an H_2O_2 step only

(Figure 6b,e), it may be that an improvement of this magnitude is not sufficient to offset the sensitivity reduction of other simultaneously-collected analytes. Finally, we note that the MAE of our best case comparison (Figure 6e) is around an order of magnitude smaller than the average uncertainty on the LA-ICP-MS measurements. This indicates that the LA uncertainties are dominated by real sample heterogeneity rather than analytical noise, as is also clear when comparing the magnitude of these uncertainty estimates to the reproducibility of the carbonate standards (Figure 3g,h).

3.5. Long-term LA-ICP-MS carbonate reference material K/Ca data compared with solution-ICP-OES and solution-ICP-MS measurements

Given the sparsity of carbonate reference material [K] data, we performed both long-term LA-ICP-MS and solution ICP-MS/OES measurements of three commonly used reference materials, including seven different sessions of JCp-1NP, JCt-1NP, and MACS-3NP, measured in MR using ^{43}Ca as the internal standard and NIST SRM610 as the primary calibration standard.

All Mg/Ca, Sr/Ca, and Na/Ca LA-ICP-MS data fall within uncertainty of the reported values for the three carbonate reference materials. Specifically, Mg/Ca accuracy of JCp-1NP, JCt-1NP, and MACS-3NP measured using LA-ICP-MS in MR was -3%, +11%, and +7%, respectively, relative to the reported values. Sr/Ca accuracy in the same three reference materials was +1%, 3%, and +2%, respectively, while the Na/Ca accuracy was -1%, +6%, and +4%, respectively. Likewise, our ICP-OES data agree within uncertainty with the reported values in all cases except JCp-1 Na/Ca, which showed an offset of -5%.

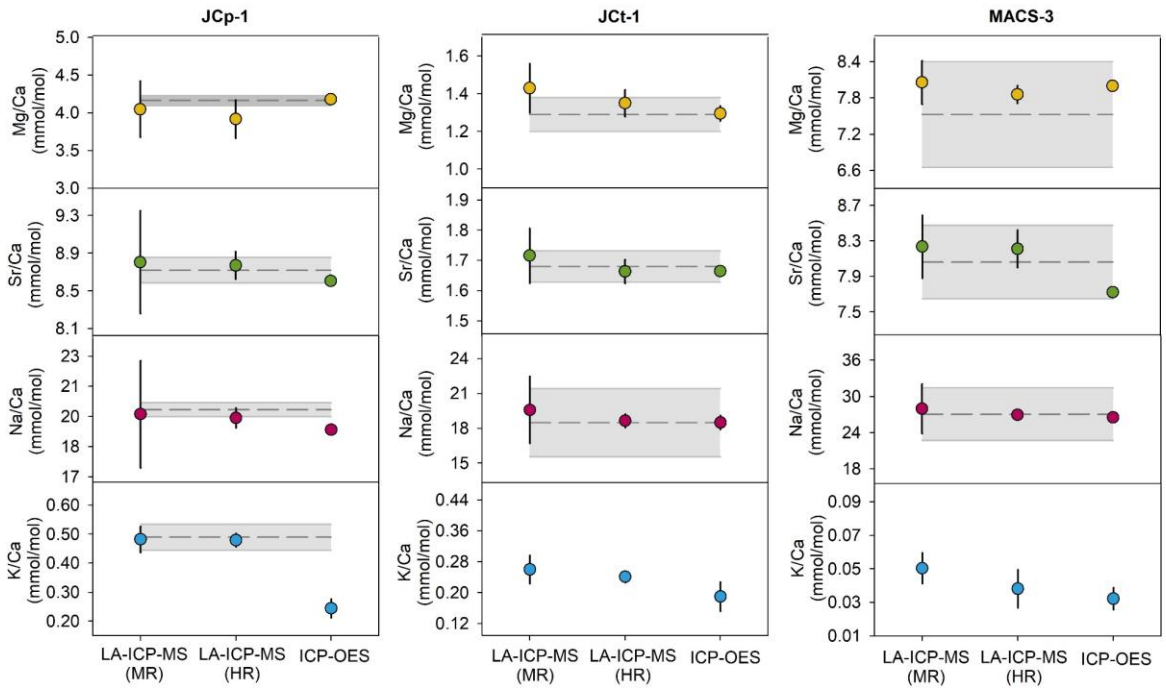

Figure 7. El/Ca ratios in carbonate reference materials measured by LA-SF-ICP-MS (JCp-1NP, JCt-1NP, and MACS-3NP) in high mass resolution (HR) and medium mass resolution (MR) mode and solution ICP-OES (JCp-1, JCt-1, and MACS-3). Error bars are 2SD. The dashed line and grey shaded area represents the mean ± 2SD reported values for JCp-1 (Okai et al., 2002), JCt-1 (Hathorne et al., 2013; Jochum et al., 2019), and MACS-3 (Jochum et al., 2005). The number of replicate measurements for ICP-OES = 5, LA-ICP-MS (MR) = 48, and LA-ICP-MS (HR) = 30. The K/Ca data measured using LA-ICP-MS are corrected for down-hole fractionation (Sec. 3.3).

In contrast, in the case of K/Ca, we find poor agreement between the two techniques. The long-term measured K/Ca in JCp-1NP by LA-ICP-MS in MR (0.48 ± 0.04 mmol/mol) is statistically identical to the K/Ca result from HR (0.48 ± 0.02 mmol/mol). These LA-ICP-MS values are with 2% of the K/Ca value (0.49 mmol/mol) in JCp-1 reported by Okai et al., (2002). However, the K/Ca in JCP-1 measured by ICP-OES is ~50% lower than by LA-ICP-MS. This

cannot simply represent an analytical bias between the two techniques given that we find good agreement between our LA-ICP-MS and solution ICP-OES data for JCt-1 and MACS-3 (Figure 7; Table S4). In addition, we note that we find poor agreement between our MACS-3 data and previously reported values, which range from 0.74 to 1.5 µg/g (excluding one extreme outlier), with a suggested compiled value of 1.1 µg/g (GEOREM database version 34; Jochum et al., (2005)); however, good agreement between our LA and ICP-OES results indicate that this value should be revised.

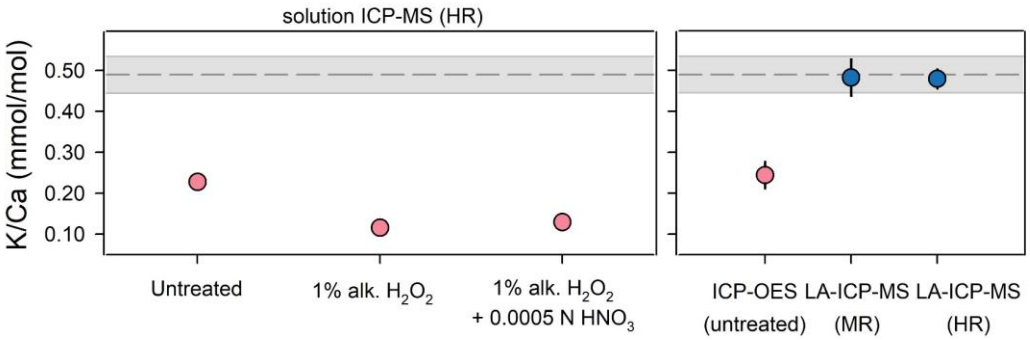

Figure 8. K/Ca measured in JCp-1 by solution SF-ICP-MS in high mass resolution mode (HR), following different treatment procedures before dissolution in 0.5 N HNO_3. The data shown in pink circles are measurements of the JCp-1 reference material powder, whereas blue circles are the nanopellet form of the reference material. Error bars are 2SD. The dashed line represents the reported value and the grey shaded regions represent the 2SD uncertainty as originally reported (Okai et al., 2002). The K/Ca results from LA-ICP-MS measurement in MR represent values averaged from seven analytical sessions whereas the K/Ca in HR respresents one measurement session. The K/Ca data measured using LA-ICP-MS are corrected for down-hole fractionation.

We further investigate the cause of the difference in measured JCp-1 K/Ca between LA-ICP-MS and solution ICP-OES, by comparing the latter data to measurements made by solution-SF-ICP-MS in HR, following the different treatment procedures outlined in Section 2.2 (see Table 2 and Figure. 8).

This exercise demonstrates that while the K/Ca values in JCp-1NP measured by LA-ICP-MS in medium resolution and high mass resolution agree well, the K/Ca value in JCp-1 measured using solution-ICP-MS in HR is ~50% lower (Figure 8; Table S5), similar to the K/Ca results from ICP-OES (Figure 7). Although we observe a decrease in K/Ca values after H_2O_2 treatment, suggesting the presence of K in an easily leachable phase such as remnant organics in JCp-1 (Figure 8), the solution ICP-MS measurement of the untreated powder is nonetheless substantially lower than our LA data, or the reported value of Okai et al., (2002). The further conundrum in these conflicting results is that while our LA-ICP-MS data agree well with the information value of Okai et al., (2002) the K/Ca ratio of 0.49 mmol/mol is far higher than expected for *Porites* coral, from which this reference material is derived (see Mitsuguchi and Kawakami, (2012)) and compare to sample J1 in Table S3). One possible explanation for this is that both our LA data and the original analysis by Okai et al., (2002) target a contaminant phase which is not present in our solution ICP-OES/MS data).

The overall elemental composition of JCp-1 has been previously well characterised (Okai et al., 2002; Inoue et al., 2004; Jochum et al., 2019). However, the K concentration in JCp-1 is only reported in one article (i.e., Okai et al., (2002)). The lower K/Ca in JCp-1 measured using solution ICP-MS (HR) and ICP-OES compared to LA-ICP-MS may be due to

the presence of more than one K-bearing phase as reported in the case of Na in planktonic foraminifera (Gray et al., 2023), which is differentially sampled by different techniques or cleaning procedures, or that the powder of this carbonate standard (and therefore the LA pellets) gained K during the initial preparation of the original JCp-1 powder.

JCp-1 was prepared from a *Porites* sp. coral colony which was crushed and cleaned with pure water in an ultrasonic bath before a final milling process using balls made of "high alumina" for about four days (Okai et al., 2002). Previous work on K incorporation into corals has shown that the expected K/Ca should fall between 0.16 – 0.22 mmol/mol (Mitsuguchi and Kawakami, 2012; Ram and Erez, 2021), as we also measure here using solution ICP-MS/OES. Hence, it is more likely that the higher K/Ca value measured by LA-ICP-MS in this study as well as the AAS measurement following strong acid digestion of JCp-1 with $HF/HNO_3/HClO_4$ reported by Okai et al., (2002) is due to K contamination during the sample preparation, which is not present in our solution analyses. One possible source of contamination could be from the alumina balls, which is also evidenced by the higher than expected Al content of this reference material (Al: ~480 µg/g; Al/Ca: ~1.90 mmol/mol; Okai et al., 2002) compared to pristine coral aragonite (Al/Ca: <0.01 mmol/mol; see sample J1 in Table S3). In contrast to our LA analysis, which potentially samples contaminant phases in the powder, and the AAS analysis by Okai et al., (2002), which used an extremely aggressive dissolution procedure; the solution measurements that we report use a much milder dissolution step (0.5 N HNO_3), which may not dissolve the K fraction contributed during milling or via another method of contamination. As such, we suggest careful consideration of the dissolution process during solution-based analysis for the purposes of reference

material characterisation for microanalysis, and overall our results serve to highlight the potential large offsets that may exist between different analytical techniques that are related more to the characteristics of the material than any potential analytical bias.

4. Conclusion

Determining the K/Ca of marine carbonates provides a potential method of reconstructing the oceanic potassium cycle, as well as offering constraints on the biomineralisation of important $CaCO_3$-producing organisms (Nambiar et al., 2023). However, the relatively low K concentration typical of $CaCO_3$, along with the ArH^+ interference on K^+ when performing these measurements using ICP-MS, means that accurately and precisely determining K/Ca is challenging. To address this, we overcome these and other issues via a number of methodological improvements using laser-ablation as a sampling technique that is demonstrably accurate and usefully precise, summarized as follows:

1) When analysing the lower [K] NIST 61x glasses, we observed that an initial K spike could bias the standardization procedure, suggesting easy surface contamination of K. To overcome this, careful data processing and the elimination of potential contamination by either pre-cleaning procedure or pre-ablation should be undertaken.
2) Previous work has shown that the NIST SRM61x glasses are suitable reference materials for investigating lithophile elements in carbonates using 193 nm laser ablation systems (Jochum et al., 2012; Evans and Müller, 2018). We observe no difference in K/Ca accuracy when standardizing with NIST SRM610/612 but a

much higher standard deviation in the raw K/Ca count ratio of the NIST SRM612 glasses, likely as a result of its lower K mass fraction. As such, we recommend the use of NIST SRM610 as the primary calibration standard.

3) Although ArH^+ and K^+ are not fully resolved in medium mass resolution mode (MR), the mean value of K/Ca measured in a number of silicate and carbonate reference materials was statistically indistinguishable from the K/Ca value in HR mode (which fully resolves the analyte and ArH^+ interference). Hence, K/Ca measurement in MR likely provides the optimal trade-off between peak separation and sensitivity for most applications.
4) We show that down-hole fractionation of K/Ca and Na/Ca with respect to NIST SRM610 varied to a large degree between different reference materials, with Na and K fractionation factors following a similar matrix-dependent trend within the MPI-DING reference materials. Correcting K/Ca data based on simultaneously measured fractionation factors improves the accuracy of the measurement.
5) We provide new HR solution ICPMS measurements of three commonly used carbonate reference materials, and highlight a possible Al and K contamination of JCp-1 reference material. Although well homogenised, the choice of dissolution process during solution-based measurement may lead to the very different values that we measure using different analytical techniques, and note that both our LA results and the original reported [K] are difficult to reconcile with several studies that have characterised the K/Ca of coral aragonite. This highlights the need to carefully consider the effect of different cleaning

procedures on reference material reported values, particularly when more than one phase may be present.

Overall, our measurements, conducted over multiple sessions spanning 6 months, demonstrate that medium mass resolution is sufficiently capable of minimizing the effect of ArH^+ interference on the K^+ peak, yielding accurate results (<1%) with a long-term precision (intermediate reproducibility) of <6% (RSD) in JCp-1NP. Reproducible results of K/Ca in a range of marine carbonate measured by LA-ICP-MS in MR and solution-SF-ICP-MS in HR further confirm that K/Ca measurements made using LA-ICP-MS in MR have the potential to provide accurate and precise datasets, and is an advantageous method in particular for samples with low [K].

Supplementary material to accompany 'Accurate measurement of K/Ca in low [K] carbonate samples using LA-SF-ICP-MS'

Romi Nambiar, Jorit F Kniest, Alexander Schmidt, Jacek Raddatz, Wolfgang Müller, David Evans

1. Comparing element/calcium count rate ratios in different NIST SRM 61x reference materials

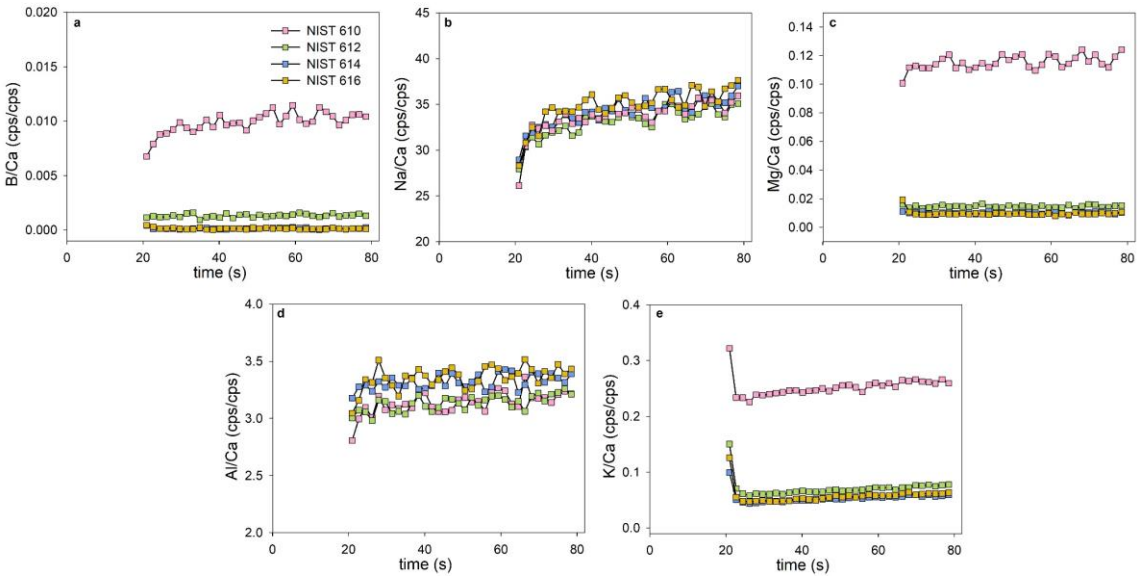

Figure S1. Representative element/Ca count rate ratios during ablation of the NIST SRM61x glasses (an equivalent plot with individual element cps are shown in Figure 1 of the main text). Background values are omitted from the plot.

An initial spike in the K/Ca count ratio was observed in NIST SRM 610/2/4/6, while other elements investigated in this study, i.e., B/Ca, Na/Ca, Mg/Ca and Al/Ca, showed no such initial spike. Investigating individual elemental counts during ablation of the NIST SRM 61x glasses (main text Figure 1), suggests that the initial peak K/Ca in the lower [K] NIST glasses (NIST 612/4/6) which is less visible in NIST SRM610 as a result of the higher [K] and because in this example the surface ablation coincided with an ICPMS sweep that also contained some background measurement. Modifying our cleaning procedure for the NIST glasses (wiping the surface with a few drops of 0.01 M HNO_3, followed by sonication in ultra-pure ethanol and Milli-Q rinsing), removed the initial peaks for K, confirming the initial peak resulting due to surface contamination. Hence, when investigating samples with a low [K], it is necessary to follow an effective surface cleaning procedure, pre-ablation cleaning, or removal of the initial portion of the dataset while processing the data.

2. Comparing K/Ca data calculated from A) all channels and B) the first 25 channels measured using LA-ICP-MS in medium mass resolution mode

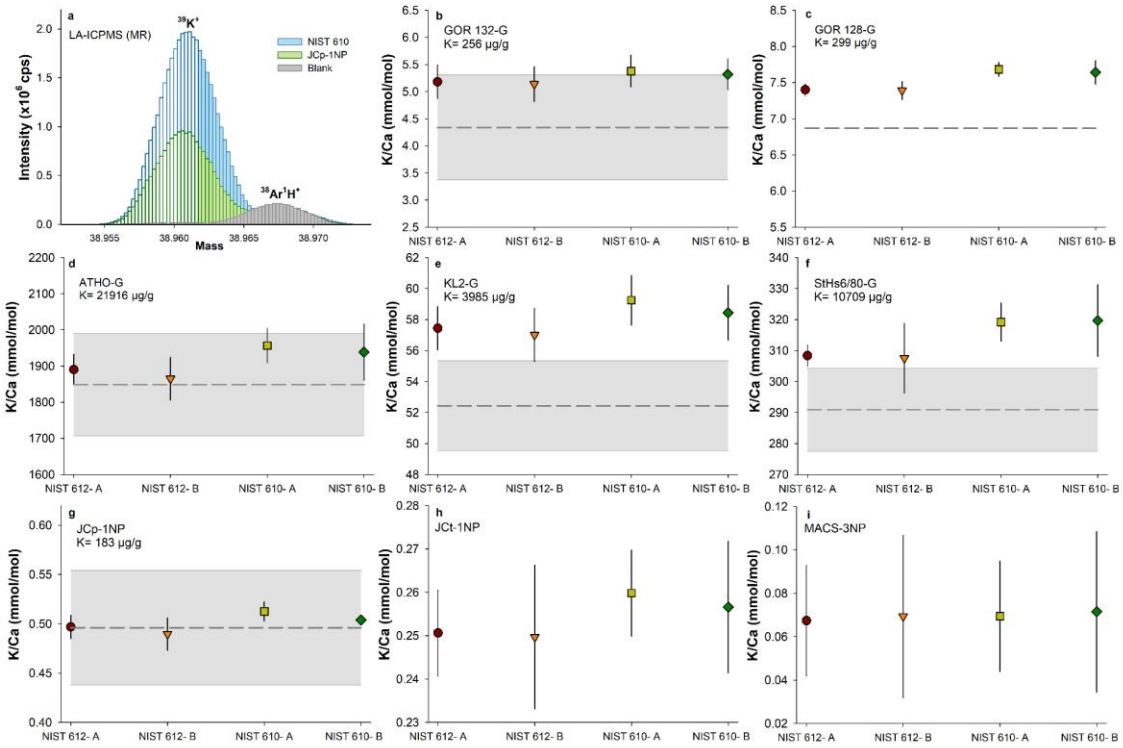

Figure S2. a) Representation of the channels monitored when measuring ^{39}K in MR. The bars filled with white colour depict the first 25 channels, explored here as a way of avoiding the ArH interference on the right side of ^{39}K peak, given that the two are not fully separated in medium resolution mode. b-i) K/Ca calculated considering: (A) all 40 channels and (B) the leftmost 25 channels (represented by white bars). The NIST 61x labelled on the x axis represents the reference material used for primary calibration. Error bars are 2SE. The dashed line represents the reported K/Ca values of the MPI-DING glasses, the grey shaded regions are 2SD (MPI-DING reference materials: Jochum et al., (2006); JCp-1: Okai et al., (2002)).

3. Choice of calibration standard

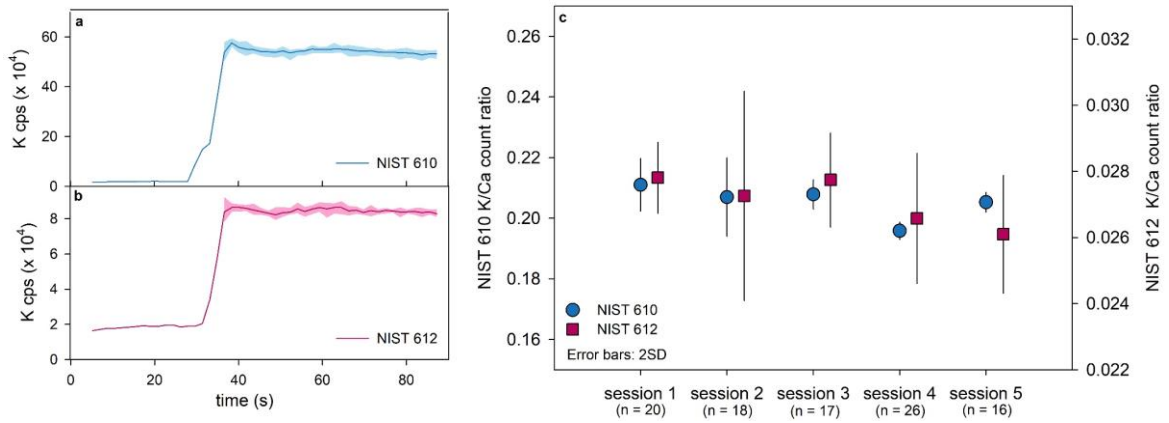

Figure S3. a,b) Laser ablation tracks across NIST glasses (line scans; 75 µm spot size, 15 Hz repetition rate). Shaded region shows the spread (i.e., maximum and minimum) of K cps for four replicates during the same session on four completely different regions of the same NIST pellet, demonstrating excellent repeatability between different parts of the reference material. c) The mean and standard deviation of the K/Ca count ratio on NIST SRM610/612 across five different sessions measured by laser spot analysis (50 µm, 3 Hz repetition rate). Note that the different absolute K/Ca count ratios between sessions is very likely driven by instrument tuning rather than K heterogeneity, i.e. it is the standard deviation of the measurements within a given session that is of interest here. Error bars are 2SD.

One of the challenges associated with quantifying LA-ICPMS measurements is the (often) limited availability of well-characterised, homogeneous matrix-matched standards. The NIST glasses were not produced with laser ablation analysis in mind; thus, it is important to investigate potential (µm-scale) heterogeneity in these materials. Indeed, spatial heterogeneity for elements such as B, As, Pb in NIST SRM61x has been reported (Eggins and

Shelley, 2002). We tested whether this is also the case for K by placing laser tracks (line-scans) across the glasses (Figure S2a,b). In addition, we compared results of K/Ca count ratios measured by spot analysis across five different sessions using the same laser ablation parameters used to analyse the samples and reference materials in the main text (i.e., 50 µm spot size, 3 Hz repetition rate; Figure 2c).

Line scan analyses are characterised by a relative standard deviation of K cps of 1.7% (K/Ca: 0.87%) and 1.4% (K/Ca: 0.83%) for NIST SRM610 and NIST SRM612, respectively, based on four replicate line-scan (track) measurements on different regions of the same NIST pellet. While these lines scans do not show evidence of K heterogeneity in the NIST SRM61x glasses, comparing the inter-spot repeatability of K/Ca count ratios between sessions highlights that NIST SRM612 is routinely characterized by a SD far worse than that of NIST SRM610 during spot analysis (RSD of K/Ca counts for NIST SRM610: 0.73-3.13% and NIST SRM612: 1.6-5.8%; Figure S2c). The mass fraction of K in NIST SRM612 is 62 µg/g whereas NIST SRM610 has a mass fraction around 7 times higher (464 µg/g) (Jochum et al., 2011). Therefore, the difference observed in the inter-spot RSD between the two glasses could result either from inhomogeneity that was not identified in our laser tracks, or simply their differing K mass fractions. Irrespective of the cause, we recommend the use of the NIST SRM610 glass as a calibration standard for K/Ca measurements in order to improve reproducibility via minimising noise in the calibration standard.

4. Down-hole fractionation of Na/Ca and K/Ca observed during LA-ICP-MS measurement

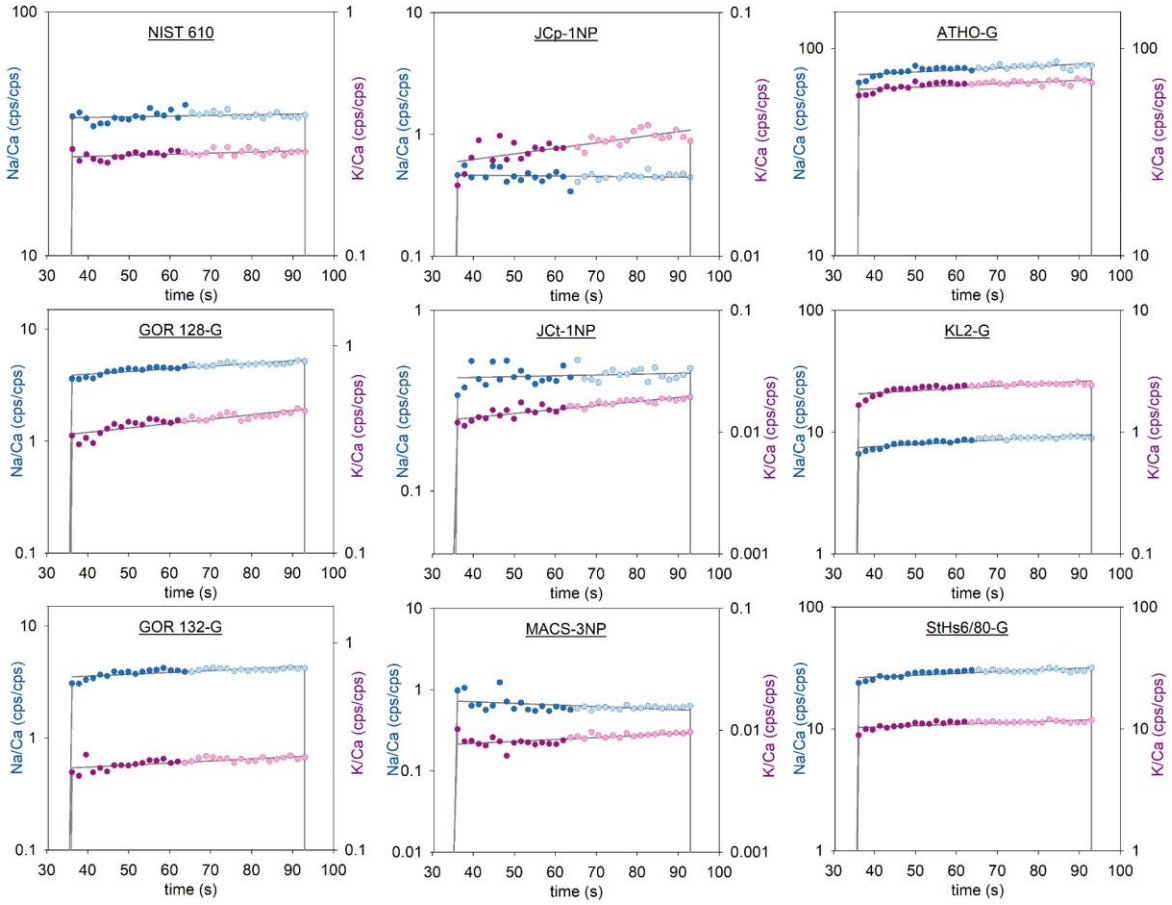

Figure S4. Representation of down-hole fractionation of K/Ca and Na/Ca in different reference materials. The y axis shows the ratio of raw element to calcium intensity (cps). The dark coloured symbol represent first half of the analysis and light coloured symbol represents second half of the analysis (Na/Ca: blue and K/Ca: pink).

5. Comparison of K/Ca data measured using LA-ICP-MS in MR with LA-ICP-MS in HR.

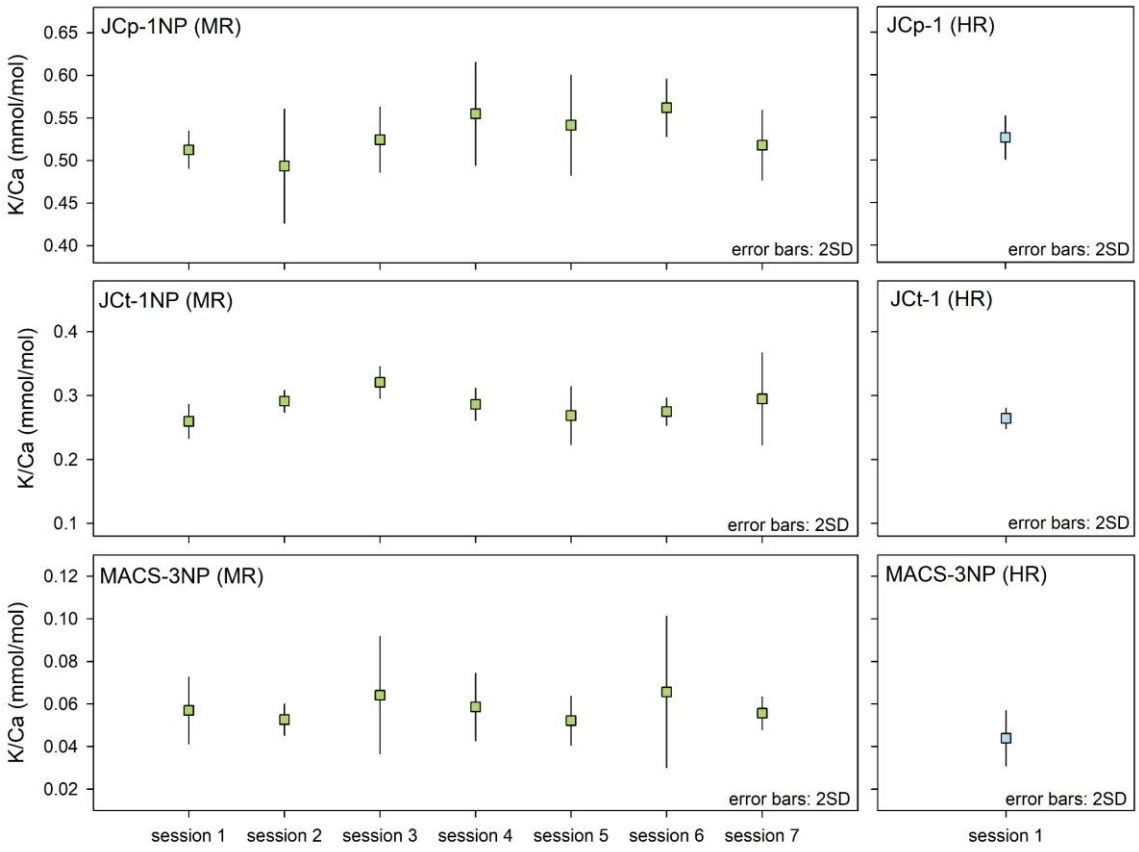

Figure S5. Comparison of K/Ca values in carbonate reference materials measured using LA-ICP-MS in MR during each session to K/Ca measured using LA-ICP-MS in HR.

Table S1. Data for Figure 3

Reference material	Calibration reference material/ resolution mode	K/Ca (mmol/mol)		
		Average	2SD	2SE
GOR 128	NIST 610 MR	7.58	0.41	0.06
	NIST 610 HR	7.39	0.31	0.06
	NIST 612 MR	7.36	0.51	0.07
	NIST 612 HR	7.30	0.30	0.06
GOR 132	NIST 610 MR	5.11	0.89	0.13
	NIST 610 HR	4.95	0.41	0.08
	NIST 612 MR	5.06	0.99	0.14
	NIST 612 HR	4.89	0.40	0.07
ATHO-G	NIST 610 MR	1957	107	48
	NIST 610 HR	2153	126	23
	NIST 612 MR	1891	94	42
	NIST 612 HR	2128	124	23
KL2-G	NIST 610 MR	59.2	3.9	1.6
	NIST 610 HR	59.8	2.2	0.4
	NIST 612 MR	57.4	3.7	1.4
	NIST 612 HR	59.1	2.1	0.4
StHs-80-G	NIST 610 MR	319.2	16.3	6.1
	NIST 610 HR	336.7	10.0	1.8
	NIST 612 MR	308.4	9.1	3.4
	NIST 612 HR	332.8	9.9	1.8
JCp-1	NIST 610 MR	0.532	0.067	0.010
	NIST 610 HR	0.526	0.026	0.005
	NIST 612 MR	0.524	0.070	0.011
	NIST 612 HR	0.520	0.025	0.005
JCt-1	NIST 610 MR	0.286	0.054	0.008
	NIST 610 HR	0.264	0.016	0.003
	NIST 612 MR	0.272	0.045	0.007
	NIST 612 HR	0.261	0.016	0.003
MACS-3	NIST 610 MR	0.058	0.021	0.003
	NIST 610 HR	0.044	0.013	0.002
	NIST 612 MR	0.055	0.017	0.002
	NIST 612 HR	0.043	0.013	0.002

MR: medium mass resolution mode; HR: high mass resolution mode;

Table S2. Data for Figure 4

Na/Ca	Fractionation factor wrt NIST 610	2SE	K/Ca	Fractionation factor wrt NIST 610	2SE	no. of sessions	no. of replicates
ATHO-G	1.01	0.015	ATHO-G	1.03	0.014	1	5
KL2-G	1.05	0.015	KL2-G	1.06	0.016	1	7
StHs6/80-G	1.03	0.013	StHs6/80-G	1.04	0.010	1	8
GOR 128-G	1.07	0.007	GOR 128-G	1.06	0.011	7	50
GOR 132-G	1.06	0.015	GOR 132-G	1.08	0.028	7	49
JCp-1NP	1.00	0.029	JCp-1NP	1.09	0.016	7	47
JCt-1NP	1.01	0.024	JCt-1NP	1.09	0.027	7	45
MACS-3NP	0.99	0.028	MACS-3NP	1.13	0.036	7	46

Table S3. Data for Figure 6

Marine carbonate	ID	K/Ca (mmol/mol)									
		Solution-HR-ICPMS (Untreated)		Solution-HR-ICPMS: 1% alk. H_2O_2 treatment		Solution-HR-ICPMS: 1% alk. H_2O_2 treatment + 0.0005 N HNO_3		LAICPMS MR_FFcorr		LAICPMS HR_FFcorr	
		Avg.	2SE	Avg.	2SE	Avg.	2SE	Avg.	2SE	Avg.	2SE
Coral (*Porites* sp.)	J1	0.33	0.002	0.23	0.001	0.23	0.003	0.22	0.020	0.26	0.021
Coral (*Tubipora musica*)	J4	1.50	0.021	0.44	0.005	0.35	0.003	0.34	0.024	0.43	0.026
Coral (*Pocillopora* sp.)	J6	0.19	0.001	0.17	0.001	0.16	0.000	0.16	0.011	0.17	0.012
Molluscs (*Tridacna crocea*)	J8	0.29	0.002	0.15	0.003	0.12	0.001	0.22	0.030	0.16	0.019
Foraminifera (*Marginopora vertebralis*)	J9	0.14	0.001	0.13	0.001	0.11	0.001	0.17	0.018	0.16	0.018
LBF (*Nummulites* sp.)	WB6	0.05	0.001	0.05	0.000	0.05	0.000	0.06	0.007	0.06	0.005
LBF *Operculina ammonoides*)	Eil	0.59	0.007	0.35	0.006	0.34	0.006	0.19	0.004	0.20	0.007

LBF: Large benthic foraminifera. MR: medium mass resolution mode; HR: high mass resolution mode; FF_corr: values corrected for downhole fractionation, ns: no. of sessions; nr: no. of replicate measurements. 1 % alk. H_2O_2 : 1% H2O2 prepared in 0.1 N NH4OH.

Table S4. Data for Figure 7

		Na/Ca	2SD	K/Ca	2SD	Mg/Ca	2SD	Sr/Ca	2SD	ns	nr
JCp-1NP	LA-ICP-MS_MR FF_corr	19.6	2.67	0.48	0.045	4.0	0.37	8.8	0.54	7	42
JCp-1NP	LA-ICP-MS_HR FF_corr	19.4	0.50	0.48	0.023	3.9	0.25	8.8	0.14	1	30
JCp-1	ICP-OES	18.8	0.26	0.24	0.033	4.2	0.05	8.6	0.03	1	5
JCt-1NP	LA-ICP-MS_MR FF_corr	19.7	3.06	0.26	0.037	1.4	0.12	1.7	0.09	7	46
JCt-1NP	LA-ICP-MS_HR FF_corr	18.6	0.59	0.24	0.015	1.3	0.07	1.7	0.04	1	30
JCt-1	ICP-OES	18.5	0.60	0.19	0.038	1.3	0.04	1.7	0.01	1	5
MACS-3NP	LA-ICP-MS_MR FFcorr	28.3	4.08	0.05	0.009	8.1	0.30	8.3	0.36	7	46
MACS-3NP	LA-ICP-MS_HR FFcorr	26.9	0.73	0.04	0.011	7.9	0.14	8.2	0.21	1	30
MACS-3	ICP-OES	26.5	0.33	0.03	0.007	8.0	0.04	7.7	0.04	1	5

All El/Ca values are in mmol/mol. MR: medium mass resolution mode; HR: high mass resolution mode; FF_corr: values corrected for downhole fractionation, ns: no. of sessions; nr: no. of replicate measurements.

Table S5. Data for Figure 8

		Treatment:	K/Ca (mmol/mol)			ns	nr
			Average	2SD	2SE		
Solution ICP-MS (HR)	JCp-1	untreated	0.23	0.003	0.002	1	3
	JCp-1	1% alk. H_2O_2	0.12	0.003	0.002	1	3
	JCp-1	1% alk. H_2O_2 treatment + 0.0005 N HNO_3	0.13	0.002	0.001	1	3
ICP-OES	JCp-1	untreated	0.24	0.033	0.015	1	5
LA-ICP-MS (MR)_FFcorr	JCp-1NP	untreated	0.48	0.045	0.017	7	42
LA-ICP-MS (HR)_Ffcorr	JCp-1NP	untreated	0.48	0.023	0.009	1	30

MR: medium mass resolution mode; HR: high mass resolution mode; FF_corr: values corrected for downhole fractionation, ns: no. of sessions; nr: no. of replicate measurements. 1 % alk. H_2O_2 : 1% H2O2 prepared in 0.1 N NH4OH

Authors contributions

RN: Conceptualization; methodology; formal analysis; investigation; writing-original draft; writing - review & editing. **JFK and AS**: Investigation; writing - review & editing. **JR:** Resources; writing - review & editing. **WM and DE:** conceptualization; methodology; resources; writing - review & editing.

Acknowledgments

This work is part of the VeWA consortium funded by the Hessen State Ministry for Higher Education, Research, and the Arts through the LOEWE program. We thank Jonathan Erez for providing us with samples for this study. FIERCE is financially supported by the Wilhelm and Else Heraeus Foundation and by the Deutsche Forschungsgemeinschaft (DFG: INST 161/921-1 FUGG, INST 161/923-1 FUGG and INST 161/1073-1 FUGG), which is gratefully acknowledged. We gratefully acknowledge the thoughtful comments of two reviewers, which improved the clarity of this contribution.

References

Allen K. A. and Hönisch B. (2012) The planktic foraminiferal B/Ca proxy for seawater carbonate chemistry: A critical evaluation. *Earth and Planetary Science Letters* 345–348, 203–211.

Audetat A., Gunther D. and Heinrich C. A. (1998) Formation of a magmatic-hydrothermal ore deposit: Insights with LA-ICP-MS analysis of fluid inclusions. *Science* 279, 2091–2094.

Bell T., Iguchi A., Suzuki A., Seki A. and Yokoyama Y. (2018) Testing possible relationships between Acropora digitifera genes, seawater chemistry and skeletal elements. *Geochemical Journal* 52, 263–272.

Cooper J. A. (1963) The flame photometric determination of potassium in geological materials used for potassium argon dating. *Geochimica et Cosmochimica Acta* 27, 525–546.

Delaney M. L., Popp B. N., Lepzelter C. G. and Anderson T. F. (1989) Lithium-to-calcium ratios in Modern, Cenozoic, and Paleozoic articulate brachiopod shells. *Paleoceanography* 4, 681–691.

Diwakar P. K., Harilal S. S., Lahaye N. L., Hassanein A. and Kulkarni P. (2013) The influence of laser pulse duration and energy on ICP-MS signal intensity, elemental fractionation, and particle size distribution in NIR fs-LA-ICP-MS. *Journal of Analytical Atomic Spectrometry* 28, 1420–1429.

Drava G. and Minganti V. (2020) Influence of an internal standard in axial ICP OES analysis of trace elements in plant materials. *Journal of Analytical Atomic Spectrometry* 35, 301–306.

Eggins S., De Deckker P. and Marshall J. (2003) Mg/Ca variation in planktonic foraminifera tests: Implications for reconstructing -palaeo-seawater temperature and habitat migration. *Earth and Planetary Science Letters* 212, 291–306.

Eggins S. M. and Shelley J. M. G. (2002) Compositional Heterogeneity in NIST SRM 610-617 Glasses. *Geostandards and Geoanalytical Research* 26, 269–286.

Eiden G. C., Barinaga C. J. and Koppenaal D. W. (1996) Selective removal of plasma matrix ions in plasma source mass spectrometry. *Journal of Analytical Atomic Spectrometry* 11, 317–322.

Evans D., Erez J., Oron S. and Müller W. (2015) Mg/Ca-temperature and seawater-test chemistry relationships in the shallow-dwelling large benthic foraminifera Operculina ammonoides. *Geochimica et Cosmochimica Acta* 148, 325–342.

Evans D. and Müller W. (2018) Automated Extraction of a Five-Year LA-ICP-MS Trace Element Data Set of Ten Common Glass and Carbonate Reference Materials: Long-Term Data Quality, Optimisation and Laser Cell Homogeneity. *Geostandards and Geoanalytical Research* 42, 159–188.

Evans D. and Müller W. (2013) LA-ICPMS elemental imaging of complex discontinuous carbonates: An example using large benthic foraminifera. *Journal of Analytical Atomic Spectrometry* 28, 1039–1044.

Evans D., Sagoo N., Renema W., Cotton L. J., Müller W., Todd J. A., Saraswati P. K., Stassen P., Ziegler M., Pearson P. N., Valdes P. J. and Affek H. P. (2018) Eocene greenhouse climate revealed by coupled clumped isotope-Mg/Ca thermometry. *Proceedings of the National Academy of Sciences of the United States of America* 115, 1174–1179.

Fryer B. J., Jackson S. E. and Longerich H. P. (1995) The design, operation and role of the laser-ablation microprobe coupled with an inductively coupled plasma-mass spectrometer (LAM- ICP-MS) in the Earth sciences. *Canadian Mineralogist* 33, 303–312.

Gale A., Dalton C. A., Langmuir C. H., Su Y. and Schilling J. G. (2013) The mean composition of ocean ridge basalts. *Geochemistry, Geophysics, Geosystems* 14, 489–518.

Garbe-Schönberg D. and Müller S. (2014) Nano-particulate pressed powder tablets for LA-ICP-MS. *Journal of Analytical Atomic Spectrometry* 29, 990–1000.

Geerken E., de Nooijer L. J., Roepert A., Polerecky L., King H. E. and Reichart G. J. (2019) Element

banding and organic linings within chamber walls of two benthic foraminifera. *Scientific Reports* 9, 1–15.

Gray A. L. (1985) Solid sample introduction by laser ablation for inductively coupled plasma source mass spectrometry. *Analyst* 110, 551–556.

Gray W. R. and Evans D. (2019) Nonthermal Influences on Mg/Ca in Planktonic Foraminifera: A Review of Culture Studies and Application to the Last Glacial Maximum. *Paleoceanography and Paleoclimatology* 34, 306–315.

Gray W. R., Evans D., Henehan M., Weldeab S., Lea D. W., Müller W. and Rosenthal Y. (2023) Sodium incorporation in foraminiferal calcite: An evaluation of the Na/Ca salinity proxy and evidence for multiple Na-bearing phases. *Geochimica et Cosmochimica Acta* 348, 152–164.

Günther D., Hattendorf B. and Audétat A. (2001) Multi-element analysis of melt and fluid inclusions with improved detection capabilities for Ca and Fe using laser ablation with a dynamic reaction cell ICP-MSPresented at the 2001 European Winter Conference on Plasma Spectrochemistry, Lillehammer, Norway. *Journal of Analytical Atomic Spectrometry* 16, 1085–1090.

Günther D. and Heinrich C. A. (1999) Enhanced sensitivity in laser ablation-ICP mass spectrometry using helium-argon mixtures as aerosol carrier. *Journal of Analytical Atomic Spectrometry* 14, 1363–1368.

Halter W. E., Pettke T., Heinrich C. A. and Rothen-Rutishauser B. (2002) Major to trace element analysis of melt inclusions by laser-ablation ICP-MS: Methods of quantification. *Chemical Geology* 183, 63–86.

Hathorne E. C., Alard O., James R. H. and Rogers N. W. (2003) Determination of intratest variability of trace elements in foraminifera by laser ablation inductively coupled plasma-mass spectrometry. *Geochemistry, Geophysics, Geosystems* 4.

Hathorne E. C., Gagnon A., Felis T., Adkins J., Asami R., Boer W., Caillon N., Case D., Cobb K. M., Douville E., Demenocal P., Eisenhauer A., Garbe-Schönberg D., Geibert W., Goldstein S., Hughen K., Inoue M., Kawahata H., Kölling M., Cornec F. L., Linsley B. K., McGregor H. V., Montagna P., Nurhati I. S., Quinn T. M., Raddatz J., Rebaubier H., Robinson L., Sadekov A., Sherrell R., Sinclair D., Tudhope A. W., Wei G., Wong H., Wu H. C. and You C. F. (2013) Interlaboratory study for coral Sr/Ca and other element/Ca ratio measurements. *Geochemistry, Geophysics, Geosystems* 14, 3730–3750.

Hauzer H., Evans D., Müller W., Rosenthal Y. and Erez J. (2018) Calibration of Na partitioning in the calcitic foraminifer Operculina ammonoides under variable Ca concentration: Toward reconstructing past seawater composition. *Earth and Planetary Science Letters* 497, 80–91.

Heinrich C. A., Pettke T., Halter W. E., Aigner-Torres M., Audétat A., Günther D., Hattendorf B., Bleiner D., Guillong M. and Horn I. (2003) Quantitative multi-element analysis of minerals, fluid and melt inclusions by laser-ablation inductively-coupled-plasma mass-spectrometry. *Geochimica et Cosmochimica Acta* 67, 3473–3497.

Ver Hoeve T. J., Scoates J. S., Wall C. J., Weis D. and Amini M. (2018) Evaluating downhole fractionation corrections in LA-ICP-MS U-Pb zircon geochronology. *Chemical Geology* 483, 201–217.

Inoue M., Nohara M., Okai T., Suzuki A. and Kawahata H. (2004) Concentrations of trace elements in carbonate reference materials coral JCp-1 and giant clam JCt-1 by inductively coupled plasma-mass spectrometry. *Geostandards and Geoanalytical Research* 28, 411–416.

Jochum K. P., Garbe-Schönberg D., Veter M., Stoll B., Weis U., Weber M., Lugli F., Jentzen A., Schiebel R., Wassenburg J. A. and others (2019) Nano-powdered calcium carbonate reference materials: Significant progress for microanalysis? *Geostandards and Geoanalytical Research* 43, 595–609.

Jochum K. P., Nohl U., Herwig K., Lammel E., Stoll B. and Hofmann A. W. (2005) GeoReM: a new geochemical database for reference materials and isotopic standards. *Geostandards and Geoanalytical Research* 29, 333–338.

Jochum K. P., Scholz D., Stoll B., Weis U., Wilson S. A., Yang Q., Schwalb A., Börner N., Jacob D. E. and Andreae M. O. (2012) Accurate trace element analysis of speleothems and biogenic calcium carbonates by LA-ICP-MS. *Chemical Geology* 318–319, 31–44.

Jochum K. P., Stoll B., Herwig K., Willbold M., Hofmiann A. W., Amini M., Aarburg S., Abouchami W., Hellebrand E., Mocek B., Raczek I., Stracke A., Alard O., Bouman C., Becker S., Dücking M., Brätz H., Klemd R., De Bruin D., Canil D., Cornell D., De Hoog C. J., Dalpé C., Danyushevshy L., Eisenhauer A., Gao Y., Snow J. E., Groschopf N., Günther D., Latkoczy C., Guillong M., Hauri E. H., Höfer H. E., Lahaye Y., Horz K., Jacob D. E., Kasemann S. A., Kent A. J. R., Ludwig T., Zack T., Mason P. R. D., Meixner A., Rosner M., Misawa K., Nash B. P., Pfänder J., Premo W. R., Sun W. D., Tiepolo M., Vannucci R., Vennemann T., Wayne D. and Woodhead J. D. (2006) MPI-DING reference glasses for in situ microanalysis: New reference values for element concentrations and isotope ratios. *Geochemistry, Geophysics, Geosystems* 7.

Jochum K. P., Weis U., Stoll B., Kuzmin D., Yang Q., Raczek I., Jacob D. E., Stracke A., Birbaum K., Frick D. A., Günther D. and Enzweiler J. (2011) Determination of reference values for NIST SRM 610-617 glasses following ISO guidelines. *Geostandards and Geoanalytical Research* 35, 397–429.

Kent A. J. R. and Ungerer C. A. (2006) Analysis of light lithophile elements (Li, Be, B) by laser ablation ICP-MS: Comparison between magnetic sector and quadrupole ICP-MS. *American Mineralogist* 91, 1401–1411.

Levi A., Müller W. and Erez J. (2019) Intrashell Variability of Trace Elements in Benthic Foraminifera Grown Under High CO2 Levels. *Frontiers in Earth Science* 7.

Li S., Li W., Beard B. L., Raymo M. E., Wang X., Chen Y. and Chen J. (2019) K isotopes as a tracer for continental weathering and geological K cycling. *Proceedings of the National Academy of Sciences of the United States of America* 116, 8740–8745.

Li W., Li S. and Beard B. L. (2019) Geological cycling of potassium and the K isotopic response: insights from loess and shales. *Acta Geochimica* 38, 508–516.

Lomax-Vogt M. C., Liu F. and Olesik J. W. (2021) A searchable/filterable database of elemental, doubly charged, and polyatomic ions that can cause spectral overlaps in inductively coupled plasma-mass spectrometry. *Spectrochimica Acta Part B: Atomic Spectroscopy* 179, 106098.

Longerich H. P., Günther D. and Jackson S. E. (1996) Elemental fractionation in laser ablation inductively coupled plasma mass spectrometry. *Fresenius' Journal of Analytical Chemistry* 355, 538–542.

Mank A. J. G. and Mason P. R. D. (1999) A critical assessment of laser ablation ICP-MS as an analytical tool for depth analysis in silica-based glass samples. *Journal of Analytical Atomic Spectrometry* 14, 1143–1153.

Marschall H. R. and Ludwig T. (2004) The low-boron contest: minimising surface contamination and analysing boron concentrations at the ng/g-level by secondary ion mass spectrometry. *Mineralogy and Petrology* 81, 265–278.

Martin J.-M. and Whitfield M. (1983) The significance of the river input of chemical elements to the ocean. In *Trace metals in sea water* Springer. pp. 265–296.

Míková J., Košler J., Longerich H. P., Wiedenbeck M. and Hanchar J. M. (2009) Fractionation of alkali elements during laser ablation ICP-MS analysis of silicate geological samples. *Journal of Analytical Atomic Spectrometry* 24, 1244–1252.

Mitsuguchi T. and Kawakami T. (2012) Potassium and other minor elements in Porites corals: Implications for skeletal geochemistry and paleoenvironmental reconstruction. *Coral Reefs* 31, 671–681.

Müller W., Shelley M., Miller P. and Broude S. (2009) Initial performance metrics of a new custom-designed ArF excimer LA-ICPMS system coupled to a two-volume laser-ablation cell. *Journal of Analytical Atomic Spectrometry* 24, 209–214.

Murphy K. E., Long S. E., Rearick M. S. and Ertas Ö. S. (2002) The accurate determination of potassium and calcium using isotope dilution inductively coupled "cold" plasma mass spectrometry. *Journal of Analytical Atomic Spectrometry* 17, 469–477.

Nambiar R., Hauzer H., Gray W. R., Henehan M. J., Cotton L., Erez J., Rosenthal Y., Renema W., Müller W. and Evans D. (2023) Controls on potassium incorporation in foraminifera and other marine calcifying organisms. *Geochimica et Cosmochimica Acta* 351, 125–138.

O'Brien S. E., Acon B. W., Boulyga S. F., Becker J. S., Dietze H. J. and Montaser A. (2003) Reduction of molecular ion interferences with hexapole collision cell in direct injection nebulization-inductively coupled plasma mass spectrometry. *Journal of Analytical Atomic Spectrometry* 18, 230–238.

Okai T., Suzuki A., Kawahata H., Terashima S. and Imai N. (2002) Preparation of a new Geological Survey of Japan geochemical reference material: Coral JCp-1. *Geostandards Newsletter* 26, 95–

99.

Palme H., O'Neill H. S. C., Holland H. D. and Turekian K. K. (2014) Treatise on geochemistry. *2nd ed*, 15.

Parendo C. A., Jacobsen S. B. and Wang K. (2017) K isotopes as a tracer of seafloor hydrothermal alteration. *Proceedings of the National Academy of Sciences of the United States of America* 114, 1827–1831.

Paton C., Woodhead J. D., Hellstrom J. C., Hergt J. M., Greig A. and Maas R. (2010) Improved laser ablation U - Pb zircon geochronology through robust downhole fractionation correction. *Geochemistry, Geophysics, Geosystems* 11.

Pearce N. J. G., Perkins W. T., Westgate J. A., Gorton M. P., Jackson S. E., Neal C. R. and Chenery S. P. (1997) A compilation of new and published major and trace element data for NIST SRM 610 and NIST SRM 612 glass reference materials. *Geostandards newsletter* 21, 115–144.

Ram S. and Erez J. (2021) The Distribution Coefficients of Major and Minor Elements in Coral Skeletons Under Variable Calcium Seawater Concentrations. *Frontiers in Earth Science* 9, 1–14.

Rice T. D. (1976) An interlaboratory study of potassium determination in rocks and minerals. *Talanta* 23, 359–367.

Rickaby R. E. M. and Elderfield H. (1999) Planktonic foraminiferal Cd/Ca: paleonutrients or paleotemperature? *Paleoceanography* 14, 293–303.

Rosenthal Y., Boyle E. A. and Slowey N. (1997) Temperature control on the incorporation of magnesium, strontium, fluorine, and cadmium into benthic foraminiferal shells from Little Bahama Bank: Prospects for thermocline paleoceanography. *Geochimica et Cosmochimica Acta* 61, 3633–3643.

Rosenthal Y. and Katz A. (1989) The applicability of trace elements in freshwater shells for paleogeochemical studies. *Chemical Geology* 78, 65–76.

Russell B., Goddard S. L., Mohamud H., Pearson O., Zhang Y., Thompkins H. and Brown R. J. C. (2021) Applications of hydrogen as a collision and reaction cell gas for enhanced measurement capability applied to low level stable and radioactive isotope detection using ICP-MS/MS. *Journal of Analytical Atomic Spectrometry* 36, 2704–2714.

Russo R. E., Mao X. L., Borisov O. V. and Haichen L. (2000) Influence of wavelength on fractionation in laser ablation ICP-MS. *Journal of analytical atomic spectrometry* 15, 1115–1120.

Sader J. A. and Ryan S. (2020) Advances in ICP-MS technology and the application of multi-element geochemistry to exploration. *Geochemistry: Exploration, Environment, Analysis* 20, 167–175.

Santiago Ramos D. P., Morgan L. E., Lloyd N. S. and Higgins J. A. (2018) Reverse weathering in marine sediments and the geochemical cycle of potassium in seawater: Insights from the K isotopic

composition (41K/39K) of deep-sea pore-fluids. *Geochimica et Cosmochimica Acta* 236, 99–120.

Scheffler G. L. and Pozebon D. (2013) Internal standardization in axially viewed inductively coupled plasma optical emission spectrometry (ICP OES) combined with pneumatic nebulization and aerosol desolvation. *Analytical Methods* 5, 4371–4377.

Schönbächler M. (2016) Inductively Coupled Plasma Mass Spectrometry (ICP-MS). *Encyclopedia of Geochemistry: A Comprehensive Reference Source on the Chemistry of the Earth*.

Stoll H. M., Müller W. and Prieto M. (2012) I-STAL, a model for interpretation of Mg/Ca, Sr/Ca and Ba/Ca variations in speleothems and its forward and inverse application on seasonal to millennial scales. *Geochemistry, Geophysics, Geosystems* 13.

Tanner S. D. (1995) Characterization of ionization and matrix suppression in inductively coupled "cold" plasma mass spectrometry. *Journal of Analytical Atomic Spectrometry* 10, 905–921.

Taylor S. R. and McLennan S. M. (1995) The geochemical evolution of the continental crust. *Reviews of Geophysics* 33, 241–265.

Tiepolo M., Zanetti A. and Vannucci R. (2005) Determination of lithium, beryllium and boron at trace levels by laser ablation-inductively coupled plasma-sector field mass spectrometry. *Geostandards and Geoanalytical Research* 29, 211–224.

Treble P. C., Chappell J., Gagan M. K., McKeegan K. D. and Harrison T. M. (2005) In situ measurement of seasonal $δ$18O variations and analysis of isotopic trends in a modern speleothem from southwest Australia. *Earth and Planetary Science Letters* 233, 17–32.

de Villiers S., Greaves M. and Elderfield H. (2002) An intensity ratio calibration method for the accurate determination of Mg/Ca and Sr/Ca of marine carbonates by ICP-AES. *Geochemistry, Geophysics, Geosystems* 3, n/a-n/a.

Vogiatzis C. and Zachariadis G. (2011) An evaluation of the use of yttrium and beryllium as internal standards in inductively coupled plasma emission spectrometry for untreated aqueous solutions in presence of high concentrations of organic solvents and matrices. *Journal of Analytical Atomic Spectrometry* 26, 2030–2038.

Weldeab S., Lea D. W., Schneider R. R. and Andersen N. (2007) 155,000 years of West African monsoon and ocean thermal evolution. *science* 316, 1303–1307.

Chapter 3: Evaluating accuracy improvements of laser ablation ICPMS element analysis in silicate glasses and carbonates via downhole fractionation correction

Citation:
Nambiar R., Müller W. and Evans D. Evaluating accuracy improvements of laser ablation ICPMS element analysis in silicate glasses and carbonates via downhole fractionation correction – an old problem re-assessed (submitted to *Journal of Analytical Atomic Spectrometry*).

Evaluating accuracy improvements of laser ablation ICPMS element analysis in silicate glasses and carbonates via downhole fractionation correction – an old problem re-assessed

Romi Nambiar[1,2,*], Wolfgang Müller[1,2], David Evans[1,2,†]

[1]Institute of Geosciences, Goethe University, Frankfurt, Altenhöferallee 1, 60438 Frankfurt am Main, Germany

[2]FIERCE, Frankfurt Isotope & Element Research Center, Goethe University, 60438 Frankfurt am Main, Germany

[†]Present address: School of Ocean and Earth Science, University of Southampton, Southampton, SO14 3ZH, UK

*Corresponding author: Email address: Nambiar@geo.uni-frankfurt.de (R. Nambiar)

Abstract

Non-matrix-matched calibration of laser ablation ICPMS (trace) elemental data is a common quantification strategy. However, depth-profiling analysis introduces downhole elemental fractionation, potentially causing inaccuracies if the fractionation magnitude between the sample and reference material (RM) differs. Here, we estimate fractionation factors (FF) for different analytes in a range of RMs relative to NIST SRM610/612 ($FF_{El/Ca\text{-}NIST}$) and evaluate element-specific corrections for downhole fractionation using these measured $FF_{El/Ca\text{-}NIST}$. Significantly different mean El/Ca values before and after correction were observed, particularly for the alkali elements (all RMs), and B, Fe, and Zn (some RMs), improving accuracy for the alkali elements in particular. Given that this phenomenon should be accounted for, this may help identify underlying issues in reported/reference values for RMs in cases where this methodology does not result in an accuracy improvement. Overall,

we suggest that cautious application of an FF correction, as outlined here, could be routinely applied.

1. Introduction

When using laser ablation (LA) as an ICPMS sample introduction system for spatially-resolved compositional analysis, elemental and isotopic fractionation occurs, related to matrix-dependent particle-size distribution, laser-sample coupling, preferential ablation of volatile elements or deposition of those with lower condensation temperatures (Russo et al., 2000; Kuhn and Günther, 2003; Horn and von Blanckenburg, 2007), in addition to plasma loading and heterogeneity, and matrix-dependent ionisation efficiency (Guillong and Günther, 2002; Kroslakova and Günther, 2007; Fietzke and Frische, 2016). For example, Jeffries et al., (1998) showed that switching from a 1064 nm laser to shorter wavelengths (213 and 266 nm) improved the ablation behaviour of geological materials that enhanced overall measurement accuracy, as a result of improved laser-sample coupling. Following this work, several studies have demonstrated that the use of shorter wavelength lasers improves data quality for a wide range of geological reference materials, as most minerals show better absorption at shorter wavelengths (Günther et al., 1997; Guillong and Günther, 2002; Guillong et al., 2003; Hathorne et al., 2008; Müller and Fietzke, 2016; Sylvester and Jackson, 2016), with 193 nm LA now being common given that matrix-matched standardisation is often not possible.

When utilising LA as a sampling methodology, spot analysis (depth-profiling) remains the approach with the highest (vertical) spatial resolution, revealing elemental heterogeneity at sub-μm resolution in samples with growth banding perpendicular to the

laser beam. This has provided insights into diverse mineral formation processes from elemental zoning in igneous minerals (Neubeck et al., 2016) to biominerals formed by marine calcifying organisms (Eggins et al., 2003; Hathorne et al., 2003; Evans et al., 2015; Fietzke et al., 2015; Müller and Fietzke, 2016). However, during LA spot analysis, ablation-induced fractionation as a function of time, largely a function of element volatility/condensation temperature (Craig et al., 1989), usually referred to as 'downhole fractionation', can be a significant source of inaccuracy, particularly when the magnitude of this effect differs between the sample and calibration reference material. These phenomena of downhole fractionations were already reported in the early days of the LA pioneer period in the 1990s (Fryer et al., 1995). Downhole fractionation is usually influenced by an analyte's geochemical affinity with the chosen internal standard, with elements from the same grouping in Goldschmidt's geochemical classifications (Goldschmidt, 1937), characterised by similar behaviour (Longerich et al., 1996). However, there are some exceptions; for example, the alkali elements often do not fractionate in the same way as other lithophile elements (Míková et al., 2009; Evans and Müller, 2018).

Efforts to minimise potential sources of inaccuracy due to downhole fractionation have focused on hardware solutions and related analytical approaches, with the broad shift to 193 nm ArF lasers in the Earth and Environmental Sciences resulting in substantially lower downhole element fractionation compared to 213 nm lasers (Günther and Heinrich, 1999). In addition: 1) the ablation pit geometry (depth-diameter ratio) has been shown to exert an influence on downhole fractionation, with higher depth/width aspect ratios largely resulting in more pronounced fractionation (Jackson et al., 1992; Mank and Mason, 1999), and 2) downhole fractionation is less pronounced in a helium atmosphere compared to argon at a

similar depth/diameter ratio (Eggins et al., 1998; Mank and Mason, 1999). To overcome issues related to downhole fractionation, the most ideal approach would be using matrix-matched reference materials. Where these are unavailable, calibration or characterisation of this issue using in-house standards has also been proposed, e.g., by co-precipitation of elements into a $CaCO_3$ matrix (Bellotto and Miekeley, 2000) or adding standard solutions to a powder base (Craig et al., 2000; Traub et al., 2009). However, these approaches, in turn, require the (time-consuming) comprehensive characterization of the composition and homogeneity of any standard materials before they are used for this purpose.

Correction for downhole fractionation is common practise when high precision (permil-level) accuracy and precision are required, for example, for U-Pb geochronology (Paton et al., 2010; Allen and Campbell, 2012; Ver Hoeve et al., 2018). However, to our knowledge, only one study has attempted to correct for downhole fractionation associated with trace element determinations following non-matrix matched standardisation (Paul et al., 2023), using a model derived from the compositionally-matching reference material applied to the sample (i.e., matrix matched standardisation is still ideally required).

Here, we determine fractionation factors for various common analytes including the alkali elements (Li, Na, K), alkaline earth metals (Mg, Sr, Ba), metalloid (B) and transition metals (Fe, Zn) in a range of reference materials including the silicate MPI-DING glasses, GOR128-G, GOR132-G, KL2-G, and ATHO-G as well as nano-pellets of carbonate reference materials JCp-1NP, JCt-1NP and MACS-3NP (Garbe-Schönberg and Müller, 2014). We compare this information to the respective values in NIST SRM610/612, the most commonly used primary standards, and evaluate the contribution of downhole fractionation to

inaccuracy. Finally, we show how measured fractionation factors, inherently available in the data collected in any case, can be used to directly correct for element-specific fractionation.

2. Instrumentation

All measurements were conducted using the LA-ICPMS instrumentation at the Frankfurt Isotope and Element Research Center (FIERCE), Goethe University Frankfurt. The setup consists of a RESOlution 193 nm ArF laser ablation system (Applied Spectra Inc., formerly Resonetics LLC), with a Laurin Technic S-155 two-volume laser ablation cell (Müller et al., 2009), coupled to a magnetic sector-field ICPMS (ThermoFisher Scientific Element XR). The details of the laser ablation system and ICPMS operating parameters are given in Table 1. Standardisation from count ratios to molar El/Ca was performed using an in-house Matlab script (Evans and Müller, 2018), that identifies the sample counts, subtracts the adjacent background values, and calibrates the data using a depth-dependent measured/reported element/^{43}Ca ratio derived from repeat analysis of the NIST SRM61X glasses. In this way, downhole fractionation is already accounted for to a degree as we do not simply use the mean NIST count rates, but different fractionation behaviour between matrices is not. The values for NIST SRM610 and NIST SRM612 were taken from Jochum et al., (2011) with the exception of Mg, for which we follow the suggestion of Evans and Müller, (2018) and use a [Mg] value for NIST SRM610/612 of 465 µg/g (Pearce et al., 1997) and 62.4±0.91 µg/g (n = 2245) (Evans and Müller, 2018), respectively. We assess the accuracy and matrix-dependent fractionation using the MPI-DING glasses (Jochum et al., 2006) and nano-pellets of three commonly used carbonate reference materials (RMs). In the latter case, we assess accuracy using the values reported by Jochum et al., (2019) and the GEOREM database, version 34 (Jochum et al., 2005) (preferred values). In the case of K/Ca, we use an ICP-OES value of the

original JCp-1 reference material (Okai et al., 2002), which agrees with its nano-pellet (JCp-1NP) K/Ca value measured using LA-ICPMS (Nambiar et al., 2024). For the K/Ca value in JCt-1NP and MACS-3NP, we referred to the average of the medium/high-resolution LA-ICPMS measurements as recently reported (Nambiar et al., 2024).

Table 1 LA- ICPMS operating conditions.

Laser Ablation (LA) System	
Wavelength	193 nm
Sampling mode	Spot (depth profiling) analysis
Fluence / repetition rate	~6.3 J cm^{-2} / 3 Hz
Ablation Spot size / ablation time	50 µm / 60 s
He flow	300 - 400 mL min^{-1}
N_2 flow	2.5 - 4.0 mL min^{-1}
Inductively Coupled Plasma Mass Spectrometry (ICPMS)	
mass resolution	medium mass resolution
Torch RF power	1300 - 1380 W
Sample cone / Skimmer cone	Ni Jet cone / Ni H cone
Sample gas flow	0.86 - 1.00 L min^{-1}
Auxiliary gas flow	0.65 - 0.90 L min^{-1}
Monitored elements (m/z)	^{7}Li, ^{11}B, ^{23}Na, ^{25}Mg, ^{39}K, ^{43}Ca, ^{56}Fe, ^{66}Zn, ^{88}Sr, and ^{138}Ba (^{43}Ca used as internal standard)
Sensitivity measured on NIST 612 (60 µm; 6 Hz)	>4.5 million cps on ^{238}U
ThO^+/Th^+ (m/z 248/232)	<1 %
doubly charged production rate (m/z 22/44)	<2 %

3. Result and discussion

3.1. Ablation-induced fractionation

Downhole elemental fractionation can be estimated using the fractionation factor (FF) as suggested by Fryer et al., (1995), which is calculated by dividing the count rate ratio during the second half of an analysis by the first half, normalised to an internal standard, in this case, ^{43}Ca:

$$FF = (X/^{43}Ca_{0.5t\text{-}1t})/(X/^{43}Ca_{0\text{-}0.5t}),$$

Where t= ablation time, in this case 60 seconds. Both NIST SRM610 and NIST SRM612 glass RMs have a similar matrix, consisting principally of Na, Al, Si, and Ca oxides, spiked with an additional 61 elements at target concentrations of ~500 and 50 µg/g, respectively (Kane, 1998; Eggins and Shelley, 2002). We first investigated any potential differences in downhole fractionation of a number of analytes, including B, Li, Na, K, Mg, Fe, Zn, Sr, and Ba in different reference materials relative to NIST SRM610 and NIST SRM612 during measurements from multiple sessions (n = 14) spanning over ~18 months (Figure 1), in order to determine the extent of downhole fractionation using overall matrix matched standardisation.

Averaging over all measurements, a tight correlation close to a 1:1 line was observed between the fractionation factor relative to NIST SRM610 versus NIST SRM612 for all elements and reference materials, as expected, given their very similar matrix. Only the Ba FFs showed a poorer correlation between the seven RMs (R^2 = 0.51, p = 0.07; Figure S1), although all values are within the error of a 1:1 line. Overall, this is in good agreement with the earlier finding that the fractionation of elements in NIST SRM610 relative to NIST SRM612 using a 193 nm ArF laser were non-resolvable with the exception of a few volatile elements such as V, Zn, and Pb (Evans and Müller, 2018). Given that overall FF relative to NIST SRM610 and NIST SRM612 are comparable, in the next section, we use the NIST SRM610 calibrated data to demonstrate the utility of downhole fractionation correction but note that our results imply that a correction based on either standard would function in the same way.

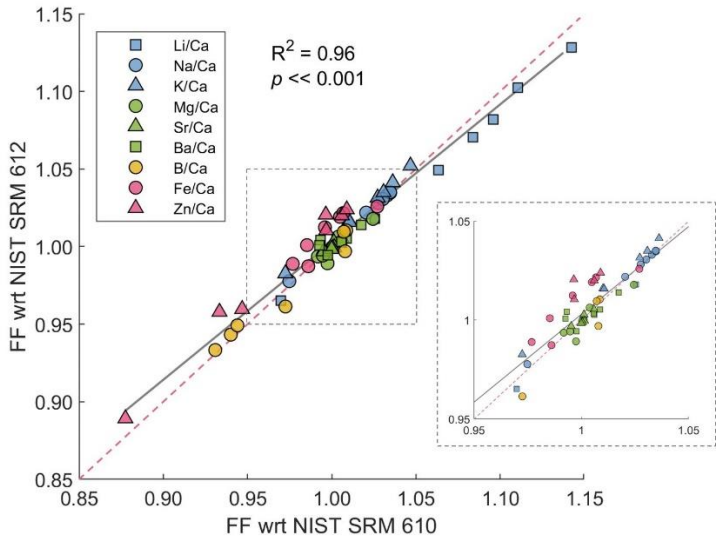

Figure 1. The relationship between the downhole fractionation factors (FF) of several elements in different reference materials relative to NIST SRM612 versus NIST SRM610 shows a tight correlation close to a 1:1 line (red dashed line). Different symbols represent different elements, depicting the alkali elements (blue), alkaline earth metals (green), metalloids (yellow), and transition metals (pink). Each set of symbols consists of seven distinct reference materials. For an equivalent plot that distinguishes between the various reference materials, see Figure S1. The number of session (s) and replicates/spots (r) were: GOR128-G (s=14, r=150); GOR132-G (s=14, r=146); ATHO-G (s=2, r=23); KL2-G (s=2, r=25); JCp-1NP (s=14, r=148); JCt-1NP (s=14, r=148) and MACS-3NP (s=14, r=147).

This exercise also further highlights that the alkali and volatile elements (Li and Zn in particular) are substantially offset from values of 1, i.e., characterised by substantially differing downhole fractionation between RMs. Specifically, the percentage differences between the RMs and NIST SRM610 fractionation factors were -3 % to 18 % for Li/Ca, the element displaying the highest degree of downhole fractionation. The $FF_{El/Ca\_percent}$ of Na/Ca and K/Ca ranged between -3 to 4 % and -3 to 5 %, respectively. In contrast, the alkaline earth metals showed the lowest $FF_{El/Ca\_percent}$ with all values ranging from -1 % to 2 %, which is one

reason that non-matrix matched standardisation produces accurate data in these cases (Evans and Müller, 2018). In the case of B/Ca, the carbonate reference materials were characterised by greater offsets compared to NIST SRM610 (JCp-1NP= -8 %, JCt-1NP= -6 %, MACS-3NP= -8 %) than the MPI-DING reference materials. In addition, Fe/Ca and Zn/Ca fractionation factors were offset by -2 % to 3 % and -15 % to 2 %, respectively. In the case of Zn/Ca, relatively lower degrees of offset (<2 %) were observed for one carbonate and three MPI-DING glasses, in contrast to ATHO-G (-7 %), JCp-1NP (-15 %) and JCt-1NP (-10 %). However, the RSD of the measured fractionation factor was ~50% for JCp-1NP and JCt-1NP, possibly resulting from the low [Zn] of these materials or inhomogeneity.

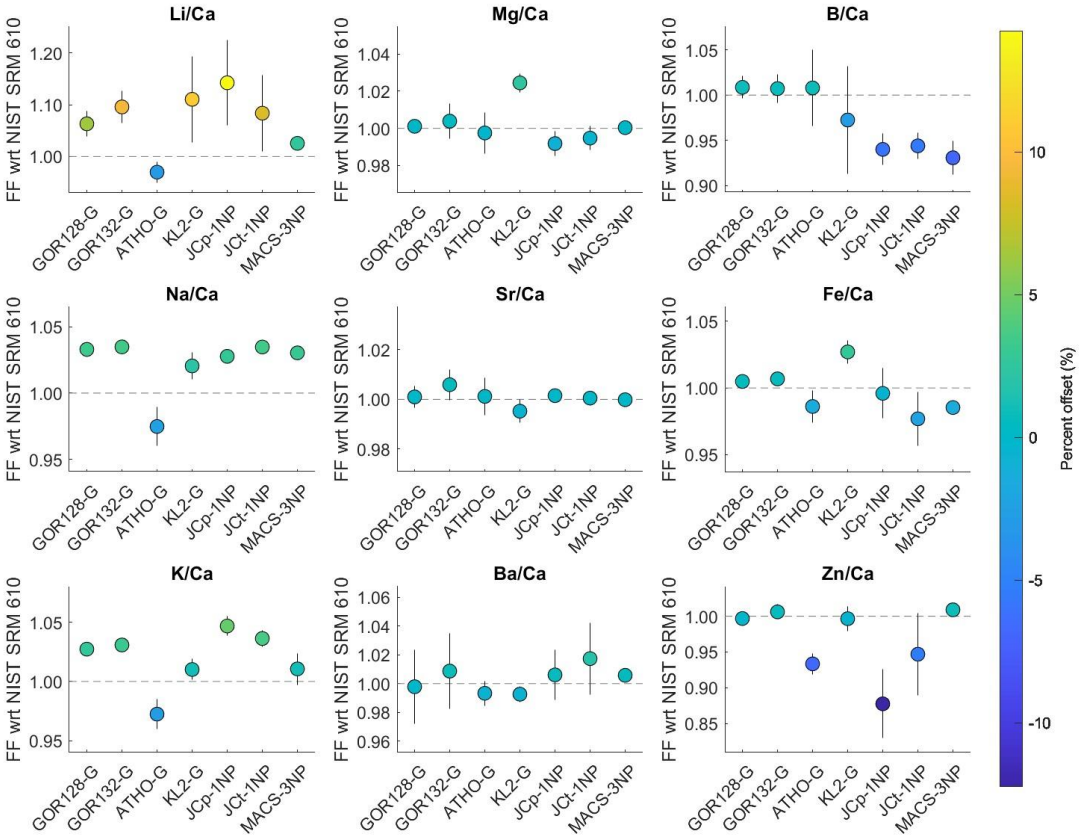

Figure 2. Long-term average of downhole fractionation of El/Ca in different reference materials relative to NIST SRM610. The error bars depict 2SE uncertainties estimated overall analyses from different sessions spanning ~18 months. The dashed line represents the ideal case in which no fractionation occurs relative to the NIST primary reference material. The symbol colour shows the percentage offset of fractionation from the ideal case. The number of session (s) and replicates/spots (r) were: GOR128-G (s=14, r=150); GOR132-G (s=14, r=146); ATHO-G (s=2, r=23); KL2-G (s=2, r=25); JCp-1NP (s=14, r=148); JCt-1NP(s=14, r=148) and MACS-3NP (s=14, r=147).

3.2. Downhole fractionation correction

In this section, we explore whether the use of a systematic correction based on downhole fractionation factors can result in an improvement in data quality for a range of elements (Li, B, Na, Mg, K, Fe, Zn, Sr, and Ba) when different geological reference materials are treated as unknowns. To do so, we used the measured fractionation factors of each individual spot analysis to apply an accuracy correction on an analysis-specific basis via the following steps:

1. The molar El/Ca value was standardised using the in-house Matlab script as described in the method section (here denoted El/Ca_{cal}).
2. The fractionation factor (FF) relative to the NIST primary calibration standard (averaged over the session/single instrument run) was determined for each individual spot analysis of the sample (here denoted $FF_{El/Ca\text{-}NIST}$):

$$\mathrm{FF}_{\mathrm{El/Ca-NIST}} = \left(\frac{\mathrm{El/Ca_{sample}\ 2nd\ half\ counts}}{\mathrm{El/Ca_{sample}\ \ 1st\ half\ counts}}\right) \Big/ \left(\frac{\mathrm{El/Ca_{NIST}\ 2nd\ half\ counts}}{\mathrm{El/Ca_{NIST}\ \ 1st\ half\ counts}}\right) \quad \text{(Eq. 1)}$$

3. A correction was then applied to the (primary) standardised El/Ca_{cal} values using $FF_{El/Ca\text{-}NIST}$ estimated for each individual spot analysis:

$$\mathrm{El/Ca_{corrected}} = \mathrm{El/Ca_{cal}} / \mathrm{FF_{El/Ca-NIST}} \quad \text{(Eq. 2)}$$

In practical terms, this is approximately equivalent to regressing the analyte/internal standard count ratios versus time back to the respective y-axis intercept (as proposed in the case of U-Pb analysis (Košler et al., 2002), which we avoid here simply because this approach may be sensitive to outliers. The resulting change in the accuracy of the measurements for the seven geological RMs, before and after applying the fractionation factor using Eq. 2,

measured over an ~18 month period, is shown in Figure 3. We determined the cases for which the mean measured El/Ca in the RMs before and after downhole fractionation correction are statistically different, using a Student's t-test at the 95% confidence interval. As expected, we find that analytes characterised by a greater degree of downhole fractionation relative to the NIST glass (Figure 2) are associated with statistically significant changes (El/Ca_{cal} versus $El/Ca_{corrected}$). In particular, the alkali elements resulted in significantly different mean values after the correction described above (Eqs. 1-2). Specifically, Li/Ca, Na/Ca, and K/Ca accuracy were broadly improved in almost all RMs utilised here (Figure 3), with a ~10% improvement in the case of Li/Ca in most cases and ~5% in the case of Na/Ca and K/Ca. In contrast, applying a correction to the alkaline earth metals, which are characterised by the lowest degree of downhole fractionation relative to the primary NIST standard (Figure 2), resulted in statistically indistinguishable mean values except for Mg in KL2-G (however, the long-term accuracy of Mg/Ca before and after fractionation correction were within ±4%). In the case of B/Ca, we find a significant shift in accuracy (5–7 %) for the carbonate RMs characterised by higher $FF_{El/Ca\text{-}NIST}$ (Figure 2) but not the MPI-DING glasses (Figure 3). This correction results in a substantial improvement in accuracy in the case of JCt-1NP (2 %) but a worsening of accuracy in the case of JCp-1NP and MACS-3NP. Finally, significant shifts in Zn/Ca and Fe/Ca accuracy resulted from the procedure outlined here, resulting in a worse apparent accuracy in the case of Zn/Ca in ATHO-G but an improvement in Zn/Ca accuracy in JCp-1NP and Fe/Ca accuracy in KL2-G.

The above results demonstrate a substantial improvement in data quality (accuracy) for several analytes in the reference materials studied here (while exerting no appreciable impact on precision). At the very least, this exercise serves to highlight specific cases in which

such a correction is warranted, namely, the non-matrix-matched standardisation of the alkali elements, and we nonetheless still suggest that the approach taken here should be routinely applied and built into data reduction software. The rationale for this is that the reference values for many analytes in many reference materials are not well-characterised, a well-known issue with LA-ICPMS trace element analysis (Jochum et al., 2005), and these have often been determined with a degree of circularity (i.e., the reported/reference values are derived to a large extent from LA measurements). Given that downhole fractionation is demonstrably a complication for some of the analyte/matrix combinations reported here (e.g., B in carbonates), this is an analytical phenomenon that should be accounted for. The worsening of accuracy that we observe in some cases (Figure 3) may, therefore, point towards an issue with the reported values, previously masked to a degree by a coincident (analytical) offset in the same direction. In the case that the reported/reference values were derived (mainly) from LA measurements, an apparent worsening in accuracy following our procedure may also result from the previous lack of a correction along the lines of that suggested here (for example, the available values of [B] in JCp-1NP, JCt-1NP, and MACS-3NP are based on LA-ICPMS/LA-MC-ICPMS; GEOREM database, version 35; Jochum et al., 2005).

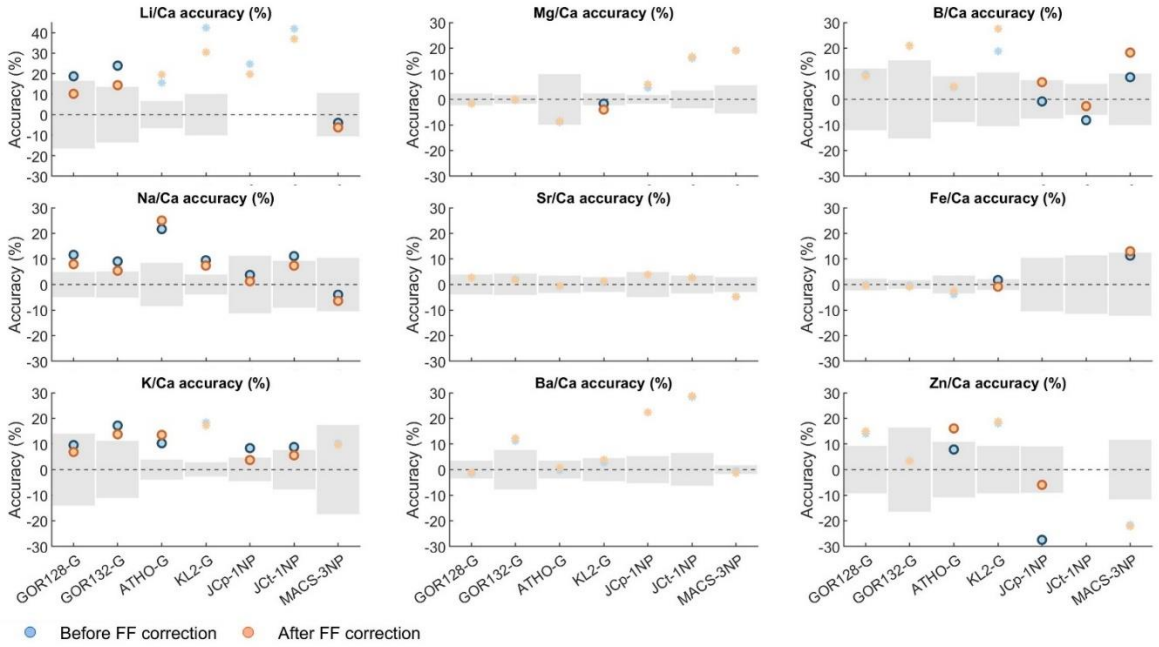

Figure 3. Accuracy of El/Ca in different geological reference materials before (blue) and after (orange) a downhole fractionation correction (Eq. 1-2). Square symbols represent analyte/standard combinations characterised by statistically different population means before and after downhole fractionation correction based on a Student's t-test (95% CI); asterisks depict combinations for which the correction made no significant difference. Where data points are missing, analytes were below the limit of detection, and/or there is no reported value. The grey-shaded region represents the uncertainty in the reported values (MPI-DING reference materials: 95% CL; carbonate reference material: 1SD).

Conclusion

In this study, we evaluated the data quality of trace/major element measurements in seven commonly used reference materials conducted over multiple sessions spanning ~18 months and under similar ablation and tuning conditions. As is well-known, we observed substantial downhole fractionation for several elements, such as the alkali elements, B, and Zn, relative to the primary NIST calibration standard, which is likely to be a significant source

of analytical bias when using this (common) analytical approach. For this reason, we propose the application of element-specific downhole fractionation corrections on an individual analysis basis, using the measured sample/reference material fractionation factor ratio measured simultaneously. Applying this to our long-term dataset, we show that this correction results in an overall substantial improvement in accuracy, especially for the alkali elements, but a worsening of apparent accuracy in some other cases. However, given that downhole fractionation is clearly an issue for some analyte/matrix combinations, we suggest that these latter cases may point towards instances in which potential unidentified issues with the reported values may be a fruitful line of future investigation, rather than an issue with the correction suggested here per se. Overall, the results of this study highlight the importance of identifying element-specific downhole fractionation and the utility of applying a correction based on this information to improve accuracy overall.

Supplementary material

1. Comparison of down-hole fractionation factors estimated with respect to NIST SRM 610 and NIST SRM 612

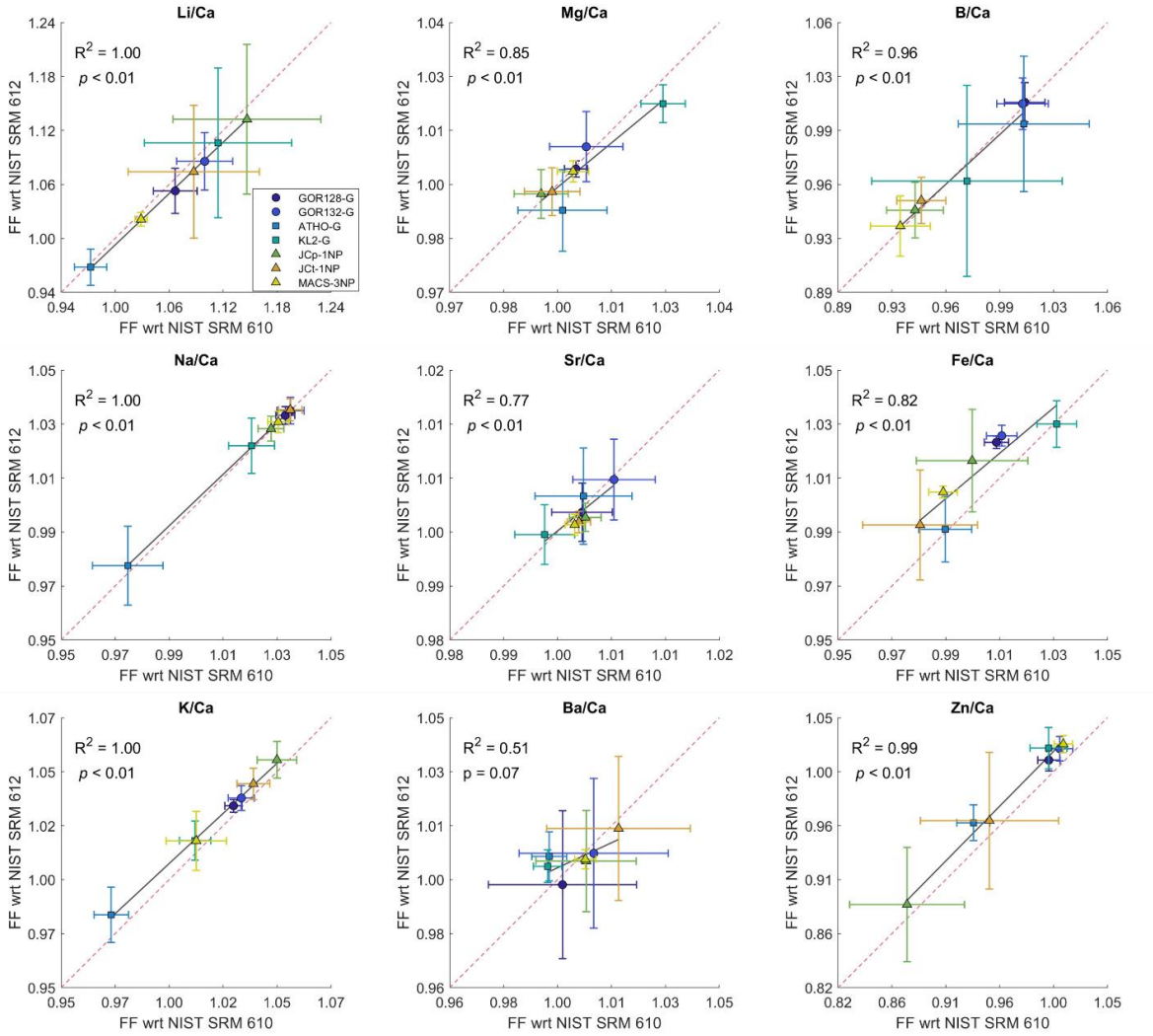

Figure S4. The relationship between down-hole fractionation factors of different elements in a range of geological reference materials relative to NIST SRM 612 and NIST SRM 610. The solid and dashed lines represent the linear least-squares regression and 1:1 line, respectively. The error bars are 2SE.

2. Long-term average of down-hole fractionation with respect to NIST SRM 612

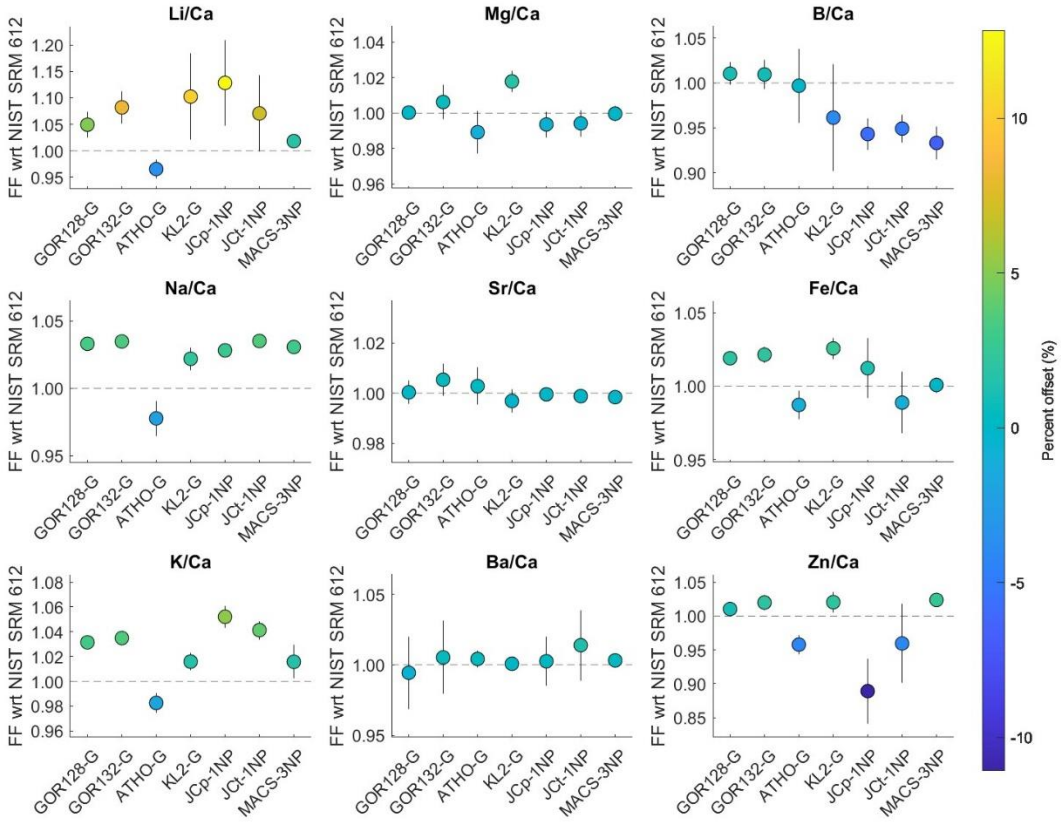

Figure S5. Long-term average of down-hole fractionation of El/Ca in different standards with respect to NIST SRM 612. The error bars show 2SE estimated over all individual data points from different sessions spanning ~18 months. The dashed line represents the ideal case for which no fractionation relative to the NIST glass occurs. Symbol colour shows the percentage offset of fractionation from the ideal case. The number of sessions (s) and replicates/spots (r) were: GOR 128-G (s=14, r=150); GOR 132-G (s=14, r=146); ATHO-G (s=2, r=23); KL2-G (s=2, r=25); JCp-1NP (s=14, r=148); JCt-1NP(s=14, r=148) and MACS-3NP (s=14, r=147).

Authors contribution

RN: Conceptualization; methodology; formal analysis; investigation; writing-original draft; writing - review & editing. **WM and DE:** conceptualization; methodology; resources; writing - review & editing.

Acknowledgements

This work is part of the VeWA consortium funded by the Hessen State Ministry for Higher Education, Research, and the Arts (HMWK) through the LOEWE program. FIERCE is financially supported by the Wilhelm and Else Heraeus Foundation and by the Deutsche Forschungsgemeinschaft (DFG: INST 161/921-1 FUGG, INST 161/923-1 FUGG and INST 161/1073-1 FUGG), which is gratefully acknowledged.

References

Allen C. M. and Campbell I. H. (2012) Identification and elimination of a matrix-induced systematic error in LA--ICP--MS 206Pb/238U dating of zircon. *Chemical Geology* 332, 157–165.

Bellotto V. R. and Miekeley N. (2000) Improvements in calibration procedures for the quantitative determination of trace elements in carbonate material (mussel shells) by laser ablation ICP-MS. *Fresenius' Journal of Analytical Chemistry* 367, 635–640.

Craig C. A., Jarvis K. E. and Clarkej L. J. (2000) An assessment of calibration strategies for the quantitative and semiquantitative analysis of calcium carbonate matrices by laser ablationinductively coupled plasma-mass spectrometry (LA-ICP-MS). *Journal of Analytical Atomic Spectrometry* 15, 1001–1008.

Craig C. A., Jarvis K. E., Clarkej L. J., Koch J., Günther D., Moens L. J., Vanhaecke F. F., Bandura D. R., Baranov V. I., Tanner S. D., Section P., Láska L., Jungwirth K., Králiková B., Krása J., Pfeifer M., Rohlena K., Skála J., Ullschmied J., Badziak J., Parys P., Wolowski J., Woryna E., Gammino S., Torrisi L., Boody F. P., Hora H., Darke S. A., Long S. E., Pickford C. J., Tyson J. F., Fisher A., Hill S. J., Norman M. D., McCulloch M. T., O'Neill H. S. C., Yaxley G. M., Longerich H. P., Günther D., Jackson S. E. and Gäbler H. E. (1989) Elimination of isobaric interferences in ICP-MS, using ion-molecule reaction chemistry: Rb/Sr age determination of magmatic rocks, a case study. *Journal of Analytical Atomic Spectrometry* 75, 526–532.

Eggins S., De Deckker P. and Marshall J. (2003) Mg/Ca variation in planktonic foraminifera tests:

Implications for reconstructing -palaeo-seawater temperature and habitat migration. *Earth and Planetary Science Letters* 212, 291–306.

Eggins S. M., Kinsley L. P. J. and Shelley J. M. G. (1998) Deposition and element fractionation processes during atmospheric pressure laser sampling for analysis by ICP-MS. *Applied Surface Science* 127, 278–286.

Eggins S. M. and Shelley J. M. G. (2002) Compositional Heterogeneity in NIST SRM 610-617 Glasses. *Geostandards and Geoanalytical Research* 26, 269–286.

Evans D., Erez J., Oron S. and Müller W. (2015) Mg/Ca-temperature and seawater-test chemistry relationships in the shallow-dwelling large benthic foraminifera Operculina ammonoides. *Geochimica et Cosmochimica Acta* 148, 325–342.

Evans D. and Müller W. (2018) Automated Extraction of a Five-Year LA-ICP-MS Trace Element Data Set of Ten Common Glass and Carbonate Reference Materials: Long-Term Data Quality, Optimisation and Laser Cell Homogeneity. *Geostandards and Geoanalytical Research* 42, 159–188.

Fietzke J. and Frische M. (2016) Experimental evaluation of elemental behavior during LA-ICP-MS: influences of plasma conditions and limits of plasma robustness. *Journal of Analytical Atomic Spectrometry* 31, 234–244.

Fietzke J., Ragazzola F., Halfar J., Dietze H., Foster L. C., Hansteen T. H., Eisenhauer A. and Steneck R. S. (2015) Century-scale trends and seasonality in pH and temperature for shallow zones of the Bering Sea. *Proceedings of the National Academy of Sciences* 112, 2960–2965.

Fryer B. J., Jackson S. E. and Longerich H. P. (1995) The design, operation and role of the laser-ablation microprobe coupled with an inductively coupled plasma-mass spectrometer (LAM- ICP-MS) in the Earth sciences. *Canadian Mineralogist* 33, 303–312.

Garbe-Schönberg D. and Müller S. (2014) Nano-particulate pressed powder tablets for LA-ICP-MS. *Journal of Analytical Atomic Spectrometry* 29, 990–1000.

Goldschmidt V. M. (1937) The principles of distribution of chemical elements in minerals and rocks. The seventh Hugo Müller Lecture, delivered before the Chemical Society on March 17th, 1937. *Journal of the Chemical Society (Resumed)*, 655–673.

Guillong M. and Günther D. (2002) Effect of particle size distribution on ICP-induced elemental fractionation in laser ablation-inductively coupled plasma-mass spectrometry. *Journal of Analytical Atomic Spectrometry* 17, 831–837.

Guillong M., Horn I. and Günther D. (2003) A comparison of 266 nm, 213 nm and 193 nm produced from a single solid state Nd:YAG laser for laser ablation ICP-MS. *Journal of Analytical Atomic Spectrometry* 18, 1224–1230.

Günther D., Frischknecht R., Heinrich C. A. and Kahlert H. J. (1997) Capabilities of an Argon Fluoride 193 nm excimer laser for laser ablation inductively coupled plasma mass spectometry microanalysis of geological materials. *Journal of Analytical Atomic Spectrometry* 12, 939–944.

Günther D. and Heinrich C. A. (1999) Comparison of the ablation behaviour of 266 nm Nd : YAG and 193 nm ArF excimer lasers for LA-ICP-MS analysis. *Journal of Analytical Atomic Spectrometry* 14, 1369–1374.

Hathorne E. C., Alard O., James R. H. and Rogers N. W. (2003) Determination of intratest variability of trace elements in foraminifera by laser ablation inductively coupled plasma-mass spectrometry. *Geochemistry, Geophysics, Geosystems* 4.

Hathorne E. C., James R. H., Savage P. and Alard O. (2008) Physical and chemical characteristics of particles produced by laser ablation of biogenic calcium carbonate. *Journal of Analytical Atomic Spectrometry* 23, 240–243.

Ver Hoeve T. J., Scoates J. S., Wall C. J., Weis D. and Amini M. (2018) Evaluating downhole fractionation corrections in LA-ICP-MS U-Pb zircon geochronology. *Chemical Geology* 483, 201–217.

Horn I. and von Blanckenburg F. (2007) Investigation on elemental and isotopic fractionation during 196 nm femtosecond laser ablation multiple collector inductively coupled plasma mass spectrometry. *Spectrochimica Acta - Part B Atomic Spectroscopy* 62, 410–422.

Jackson S. E., Longerich H. P., Dunning G. R. and Fryer B. J. (1992) The application of laser-ablation microprobe - inductively coupled plasma-mass spectrometry (LAM-ICP-MS) to in situ trace-element determinations in minerals. *Canadian Mineralogist* 30, 1049–1064.

Jeffries T. E., Jackson S. E. and Longerich H. P. (1998) Application of a frequency quintupled Nd:YAG source (λ = 213 nm) for laser ablation inductively coupled plasma mass spectrometric analysis of minerals. *Journal of analytical atomic spectrometry* 13, 935–940.

Jochum K. P., Garbe-Schönberg D., Veter M., Stoll B., Weis U., Weber M., Lugli F., Jentzen A., Schiebel R., Wassenburg J. A. and others (2019) Nano-powdered calcium carbonate reference materials: Significant progress for microanalysis? *Geostandards and Geoanalytical Research* 43, 595–609.

Jochum K. P., Nohl U., Herwig K., Lammel E., Stoll B. and Hofmann A. W. (2005) GeoReM: a new geochemical database for reference materials and isotopic standards. *Geostandards and Geoanalytical Research* 29, 333–338.

Jochum K. P., Stoll B., Herwig K., Willbold M., Hofmiann A. W., Amini M., Aarburg S., Abouchami W., Hellebrand E., Mocek B., Raczek I., Stracke A., Alard O., Bouman C., Becker S., Dücking M., Brätz H., Klemd R., De Bruin D., Canil D., Cornell D., De Hoog C. J., Dalpé C., Danyushevshy L., Eisenhauer A., Gao Y., Snow J. E., Groschopf N., Günther D., Latkoczy C., Guillong M., Hauri E. H., Höfer H. E., Lahaye Y., Horz K., Jacob D. E., Kasemann S. A., Kent A. J. R., Ludwig T., Zack T., Mason P. R. D., Meixner A., Rosner M., Misawa K., Nash B. P., Pfänder J., Premo W. R., Sun W. D., Tiepolo M., Vannucci R., Vennemann T., Wayne D. and Woodhead J. D. (2006) MPI-DING reference glasses for in situ microanalysis: New reference values for element concentrations and isotope ratios. *Geochemistry, Geophysics, Geosystems* 7.

Jochum K. P., Weis U., Stoll B., Kuzmin D., Yang Q., Raczek I., Jacob D. E., Stracke A., Birbaum K., Frick D. A., Günther D. and Enzweiler J. (2011) Determination of reference values for NIST SRM 610-617 glasses following ISO guidelines. *Geostandards and Geoanalytical Research* 35, 397–429.

Kane J. S. (1998) A history of the development and certification of NIST glass SRMs 610-617. *Geostandards Newsletter* 22, 7–13.

Košler J., Fonneland H., Sylvester P., Tubrett M. and Pedersen R. B. (2002) U-Pb dating of detrital zircons for sediment provenance studies - A comparison of laser ablation ICPMS and SIMS techniques. *Chemical Geology* 182, 605–618.

Kroslakova I. and Günther D. (2007) Elemental fractionation in laser ablation-inductively coupled plasma-mass spectrometry: Evidence for mass load induced matrix effects in the ICP during ablation of a silicate glass. *Journal of Analytical Atomic Spectrometry* 22, 51–62.

Kuhn H. R. and Günther D. (2003) Elemental fractionation studies in laser ablation inductively coupled plasma mass spectrometry on laser-induced brass aerosols. *Analytical Chemistry* 75, 747–753.

Longerich H. P., Günther D. and Jackson S. E. (1996) Elemental fractionation in laser ablation inductively coupled plasma mass spectrometry. *Fresenius' Journal of Analytical Chemistry* 355, 538–542.

Mank A. J. G. and Mason P. R. D. (1999) A critical assessment of laser ablation ICP-MS as an analytical tool for depth analysis in silica-based glass samples. *Journal of Analytical Atomic Spectrometry* 14, 1143–1153.

Míková J., Košler J., Longerich H. P., Wiedenbeck M. and Hanchar J. M. (2009) Fractionation of alkali elements during laser ablation ICP-MS analysis of silicate geological samples. *Journal of Analytical Atomic Spectrometry* 24, 1244–1252.

Müller W. and Fietzke J. (2016) The role of LA-ICP-MS in palaeoclimate research. *Elements* 12, 329–334.

Müller W., Shelley M., Miller P. and Broude S. (2009) Initial performance metrics of a new custom-designed ArF excimer LA-ICPMS system coupled to a two-volume laser-ablation cell. *Journal of Analytical Atomic Spectrometry* 24, 209–214.

Nambiar R., Kniest J. F., Schmidt A., Raddatz J., Müller W. and Evans D. (2024) Accurate measurement of K/Ca in low [K] carbonate samples using laser-ablation sector-field inductively coupled plasma mass spectrometry. *Rapid Communications in Mass Spectrometry* 38. *doi: 10.1002/rcm.9692*.

Neubeck A., Tulej M., Ivarsson M., Broman C., Riedo A., McMahon S., Wurz P. and Bengtson S. (2016) Mineralogical determination in situ of a highly heterogeneous material using a miniaturized laser ablation mass spectrometer with high spatial resolution. *International Journal of Astrobiology* 15, 133–146.

Okai T., Suzuki A., Kawahata H., Terashima S. and Imai N. (2002) Preparation of a new Geological Survey of Japan geochemical reference material: Coral JCp-1. *Geostandards Newsletter* 26, 95–99.

Paton C., Woodhead J. D., Hellstrom J. C., Hergt J. M., Greig A. and Maas R. (2010) Improved laser ablation U-Pb zircon geochronology through robust downhole fractionation correction.

Geochemistry, Geophysics, Geosystems 11.

Paul B., Petrus J., Savard D., Woodhead J., Hergt J., Greig A., Paton C. and Rayner P. (2023) Time resolved trace element calibration strategies for LA-ICP-MS. *Journal of Analytical Atomic Spectrometry* 38, 1995–2006.

Pearce N. J. G., Perkins W. T., Westgate J. A., Gorton M. P., Jackson S. E., Neal C. R. and Chenery S. P. (1997) A compilation of new and published major and trace element data for NIST SRM 610 and NIST SRM 612 glass reference materials. *Geostandards newsletter* 21, 115–144.

Russo R. E., Mao X. L., Borisov O. V. and Haichen L. (2000) Influence of wavelength on fractionation in laser ablation ICP-MS. *Journal of analytical atomic spectrometry* 15, 1115–1120.

Sylvester P. J. and Jackson S. E. (2016) A brief history of laser ablation inductively coupled plasma mass spectrometry (LA-ICP-MS). *Elements* 12, 307–310.

Traub H., Wälle M., Koch J., Panne U., Matschat R., Kipphardt H. and Günther D. (2009) Evaluation of different calibration strategies for the analysis of pure copper and zinc samples using femtosecond laser ablation ICP-MS. *Analytical and Bioanalytical Chemistry* 395, 1471–1480.

Chapter 4: Controls on potassium incorporation in foraminifera and other marine calcifying organisms

Citation:
Nambiar R., Hauzer H., Gray W. R., Henehan M. J., Cotton L., Erez J., Rosenthal Y., Renema W., Müller W. and Evans D. (2023) Controls on potassium incorporation in foraminifera and other marine calcifying organisms. *Geochimica et Cosmochimica Acta* 351, 125–138.

Controls on potassium incorporation in foraminifera and other marine calcifying organisms

Romi Nambiar[a,b,*], Hagar Hauzer[c,d], William R. Gray[e], Michael J. Henehan[f], Laura Cotton[g], Jonathan Erez[c], Yair Rosenthal[h], Willem Renema[i,j], Wolfgang Müller[a,b], David Evans[a,b]

[a]Institute of Geosciences, Goethe University, Frankfurt, Altenhöferallee 1, 60438 Frankfurt am Main, Germany

[b]FIERCE, Frankfurt Isotope & Element Research Center, Goethe University, Altenhöferallee 1, 60438 Frankfurt am Main, Germany

[c]The Fredy & Nadine Herrmann Institute of Earth Sciences, the Hebrew University of Jerusalem, Israel

[d]Israel Oceanographic and Limnological Research, National Institute of Oceanography, Haifa, Israel

[e]Laboratoire des Sciences du Climat et de l'Environnement (LSCE/IPSL), Université Paris-Saclay, Gif-sur-Yvette, France

[f]Section 3.3 Earth Surface Geochemistry, Deutsches GeoForschungsZentrum GFZ, 14473, Potsdam, Germany

[g]Natural History Museum of Denmark, University of Copenhagen, Denmark

[h]Department of Marine and Coastal Sciences, Rutgers, State University of New Jersey, New Brunswick, NJ, USA

[i]Naturalis Biodiversity Center, Leiden, Netherlands

[j]University of Amsterdam, Institute for Biodiversity and Ecosystem Dynamics, Amsterdam, NL

*Corresponding author: Nambiar@geo.uni-frankfurt.de (R. Nambiar)

Abstract

Seawater chemistry exerts an important control on the incorporation of trace elements into the shells of marine calcifying organisms. Variability in the major ion chemistry of seawater is also an indicator of past geological processes, and so the influence of seawater chemistry on carbonate trace element incorporation can be harnessed to determine changes

in the composition of seawater through time. Here, we investigate whether key oceanographic parameters (temperature, salinity, and the carbonate system) affect the incorporation of potassium (K) into foraminiferal calcite, and explore the utility of K/Ca ratios in foraminifera as an indicator of past variability in the seawater Ca^{2+} concentration. We measured both low-Mg and high-Mg modern foraminifera, including planktonic (*Globigerinoides ruber*) and shallow-dwelling larger benthic (*Operculina ammonoides*) species, using laser-ablation sector-field inductively-coupled plasma mass spectrometry (LA-SF-ICPMS). Both species show no resolvable influence of temperature, salinity, pH, or $[CO_3^{2-}]$ on K incorporation. In order to determine the effect of the seawater Ca concentration ($[Ca^{2+}]_{sw}$) on K incorporation, we analysed laboratory-cultured *O. ammonoides*, the close living relative of the abundant Eocene *Nummulites*, grown at four different $[Ca^{2+}]_{sw}$. We find a significant relationship between seawater and shell K/Ca, albeit with a shallower slope compared to most other trace elements which we suggest is driven by a crystal growth rate effect on K incorporation, constrained using culture experiments of *O. ammonoides* grown at different pH. If the K^+ concentration has remained relatively constant throughout the Phanerozoic Eon, our data may pave the way forward for the use of K/Ca as a direct proxy for past $[Ca^{2+}]_{sw}$ variability. Alternatively, coupling K/Ca with the Na/Ca proxy would allow more accurate reconstruction of $[Ca^{2+}]_{sw}$ or verification of whether $[K^+]_{sw}$ or $[Na^+]_{sw}$ has indeed remained within narrow bounds.

1. Introduction

Trace elements in marine carbonates are widely used for palaeoclimatic reconstruction. Foraminifera are an important archive for this purpose because of their widespread abundance and good preservation potential. However, shell precipitation from the surrounding seawater is a complex, biologically controlled process (Bentov et al., 2009; De Nooijer et al., 2009). The biogeochemical imprints of this process, termed 'vital effects', are not necessarily predictable from a simple chemical thermodynamic perspective (e.g. Erez, 2003), which means that the relationship between shell chemistry and ambient physical or chemical conditions must currently be empirically calibrated (Lea et al., 1999; Keul et al., 2013; Hauzer et al., 2018; Zhou et al., 2021). Using this approach, a wide range of chemical signatures in marine carbonates have been established as palaeo-proxies. For example, trace element ratios have been extensively applied to reconstruct parameters such as ocean temperature (Mg/Ca and Li/Mg; Rosenthal et al., 1997; Lea et al., 1999; Anand et al., 2003; Marchitto et al., 2018; Gray and Evans, 2019), the carbonate system (B/Ca, Zn/Ca; Marchitto et al., 2000; Yu et al., 2010; Brown et al., 2011; Allen and Hönisch, 2012; Van Dijk et al., 2017), salinity (Ba/Ca; Weldeab et al., 2007), nutrient concentration (Cd/Ca; Boyle, 1981; Rickaby and Elderfield, 1999). On longer (multi-million year) timescales, the application of foraminiferal trace element proxies is complicated by the fact that variability in seawater chemistry also affects the incorporation of trace elements into foraminifer's shells. For instance, variability in seawater Mg/Ca affects the Mg/Ca of foraminifera and thus complicates its use as palaeotemperature proxy (Segev and Erez, 2006; Hasiuk and Lohmann, 2010; Evans and Müller, 2012). Because ocean chemistry has undergone substantial secular

changes throughout the Phanerozoic (Wilkinson and Algeo, 1989; Lowenstein et al., 2001; Turchyn and DePaolo, 2019), this issue constitutes a major source of uncertainty in the application of element/Ca proxies in deep time. To enable the accurate application of trace element-based palaeoclimatic proxies beyond the residence time of calcium (~1 Myr; Broecker and Pend, 1982), precise and accurate reconstructions of seawater major ion chemistry are required.

Long-term changes in seawater chemistry are driven by variations in geological factors such as hydrothermal discharge from the global mid-ocean ridge system, the rate and type of material being terrestrially weathered, dolomitisation, and reverse weathering (e.g. Lowenstein et al., 2014; Coogan and Dosso, 2015; Higgins and Schrag, 2015). Moreover, the major ion chemistry of seawater is in itself a potential tracer of these geochemical processes. Several studies have reconstructed seawater El/Ca with a temporal resolution similar to that of the residence time of Ca^{2+} in seawater using different marine carbonates (Delaney et al., 1989; Dickson, 2002; Coggon et al., 2010; Gothmann et al., 2015; Wit et al., 2017; Evans et al., 2018a). Recently, the Na/Ca ratio of foraminifera calcite has shown to be much more sensitive to changes in $[Ca^{2+}]_{sw}$ than seawater salinity, and given the long residence time of Na^{+} in seawater (~100 Myr; Broecker and Pend, 1982), Na/Ca may be interpreted purely in terms of $[Ca^{2+}]_{sw}$ changes (Hauzer et al., 2018; Le Houedec et al., 2021; Zhou et al., 2021). The approach of directly reconstructing $[Ca^{2+}]_{sw}$ using a trace element ratio containing an element with an extremely long residence time suggests the possibility that other elements with a long-term near-constant concentration may offer similar information.

Potassium is a major element in seawater (K_{sw}), with a present-day concentration of 10.2 mmol kg^{-1} and a residence time of ~12 million years (Broecker and Peng, 1982). The major source of potassium in the ocean is from riverine input and high-temperature hydrothermal processes, whereas removal of K^+ from seawater takes places by formation of authigenic clay formation by reverse weathering and low temperature hydrothermal processes (Bloch and Bischoff, 1979; Kronberg, 1985; Michalopoulos and Aller, 1995). The seawater Sr, Li and Os isotope records have been used to argue for a substantial increase in continental weathering through the Cenozoic (particularly the Neogene) (Raymo and Ruddiman, 1992; McCauley and DePaolo, 1997; Misra and Froelich, 2012), although several other processes may impact these systems (e.g. Coogan and Dosso, 2015). Indeed, other processes, such as a decrease in reverse weathering (Misra and Froelich, 2012; Higgins and Schrag, 2015; Dunlea et al., 2017; Isson and Planavsky, 2018), high-temperature hydrothermal processes (Hardie, 1996; Horita et al., 2002), and low-temperature hydrothermal processes (Coogan and Dosso, 2015) have also been proposed to have driven seawater chemistry changes over the same interval.

Despite evidence for past variability in several processes that are important components of the K cycle, the concentration of K_{sw} has been suggested to have remained relatively constant throughout the Phanerozoic (9-11 mmol kg^{-1}) on the basis of modelling data from fluid inclusions trapped in evaporitic sequences (Lowenstein et al., 2001; Horita et al., 2002). If K_{sw} has indeed remained within narrow bounds, the K/Ca ratio of marine carbonates may be an additional direct tool for the reconstruction of past changes in $[Ca^{2+}]_{sw}$. Moreover, coupling this system with Na/Ca, within a multi-proxy approach, would allow (e.g.)

the constancy of Phanerozoic K_{sw} to be verified. To evaluate the potential of K/Ca measurements of marine carbonates for this purpose, we investigated 1) two symbiont-bearing species collected from the modern ocean: the low-Mg calcite planktonic foraminifera *Globigerinoides ruber* (white) and the high-Mg calcite, larger benthic foraminifera *Operculina* sp. from globally distributed sites characterised by a wide range in seawater parameters to determine the impact of environmental parameters on K incorporation, 2) cultured *Operculina ammonoides* grown at different seawater [Ca^{2+}] and temperature (Hauzer et al., 2018) to determine whether the proxy functions as hypothesised, and 3) cultured *O. ammonoides* grown at different pH values beyond the modern range, to understand whether the changing seawater carbonate system might influence foraminifera K/Ca. Finally, we compiled literature data of the K/Ca and Na/Ca of a diverse range of biogenic $CaCO_3$ to understand the broader controls on K and Na incorporation.

2. Materials and methods

2.1. Modern foraminifera

Larger benthic foraminifera (LBF) of the genus *Operculina* were hand-sampled from SW Sulawesi, NE Kalimantan, Jakarta Bay, the Gulf of Eilat (*Operculina ammonoides*) and the Great Barrier Reef (*Operculina* sp.) (Tab. 1). These samples have been previously investigated for the purposes of producing a Mg/Ca–temperature field calibration (Evans et al., 2013), with further details of sample collection given in Renema (2006; 2008).

In order to relate shell geochemistry to environmental parameters, mean annual sea surface temperature (SST) and salinity data were taken from the 1° resolution version of the World Ocean Atlas 2018 (Locarnini et al., 2018; Zweng et al., 2019) for all *Operculina* samples

except those from the Gulf of Eilat (Eil 19), for which data from the monitoring station of the Interuniversity Institute for Marine Sciences in Eilat (https://www.iui-eilat.ac.il) was used. These samples were earlier measured for Mg/Ca variability along the whorl which coincide with seawater temperature dataset (Evans and Müller, 2013). In contrast to the other sample sites, the Gulf of Eilat is characterised by a large seasonal variability in temperature. Given that the samples analysed here represents the last ~6 months, the November–April mean was used, i.e. the six-month period before the sample collection date. (for detailed information, see Evans et al., 2013). In order to determine the possible influence of the seawater carbonate system on shell geochemistry, the nearest available pH values were taken from Gregor and Gruber (2021). Seawater [CO_3^{2-}] was calculated using CO2sys_v3.0 (Pierrot et al., 2021) using the *in situ* temperature and salinity from the WOA and total alkalinity (TAlk) as the second carbonate system parameter, taken from Gregor and Gruber (2021). The dissociation constants for $KHSO_4$ from Dickson et al., (1990) and the total boron–salinity relationship by Lee et al., (2010) were used. The values of the carbonate system dissociation constants K_1 and K_2 were those from Lueker et al., (2000). The larger benthic foraminifera investigated in this study span a range in seawater temperature, salinity, pH, and [CO_3^{2-}] ranging from 21.9 to 28.5°C, 32.4 to 40.7 on the practical salinity scale, 8.05 to 8.19 pH units and 207.2 to 284.1 µmol kg^{-1}, respectively (Tab. 1).

Globigerinoides ruber (white) were sampled from sediment traps in the Arabian Sea (AS02-M5) and Bay of Bengal (NBT-09, CBBT-06, and SBBT-09). These samples have been previously investigated for the purposes of refining the Mg/Ca-temperature calibration by Gray et al. (2018). Foraminifera were picked from the 200 to 400 µm size fraction.

Temperature and salinity used in this study are the same as those reported in Gray et al. (2018) (Tab. 1). In addition, we analysed *G. ruber* (white) from a globally-spaced set of core-top samples which have been previously investigated to better understand B/Ca as a potential carbonate system proxy (Henehan et al., 2015). These foraminifera were picked from the 300-350 µm size fraction except for sample MC420, which was picked from the 355-400 µm fraction. Temperature and salinity used to relate shell geochemistry are those reported in Henehan et al. (2015) (Tab. 1). *In situ* carbonate chemistry data have been previously reported from both the sediment trap and core to sample sets utilized here, but were calculated in different ways. To ensure consistency in data treatment, the carbonate system parameters were therefore recalculated here. The [CO_3^{2-}] values was calculated using CO2sys_v3.0 (Pierrot et al., 2021) taking the nearest available pH and TAlk values from Gregor and Gruber (2021). The constants of Lueker et al., (2000), Lee et al., (2010), and Dickson et al., (1990) were used. The sample location details of all *G. ruber* measured in this study are given in Tab. 1. Together, the planktonic foraminifera investigated in this study from both sediment traps and core tops span a range in seawater temperature, salinity, pH, and [CO_3^{2-}] ranging from 22.0 to 28.7°C, 32.7 to 36.4 on the practical salinity scale, 8.05 to 8.12 pH units (total scale) and 204.1 to 238.8 µmol kg^{-1}, respectively (Tab. 1).

Tab. 1. Sample site details of the modern foraminifera analysed here.

i) Larger Benthic foraminifera; all species are *Operculina ammonoides* except SS 07G14 (*Operculina* sp.)

Sample ID	latitude	longitude	Water depth (m)	T (°C)	SD	S	SD	pH (total scale)	SD	$[CO_3^{2-}]$* (µM)	SD	n
Pd 2805[a]	-5.03	119.33	20	28.0	1.1	33.4	0.9	8.06	0.02	209.0	11.2	4
KKE30[b]	-5.11	119.29	30	27.7	1.1	33.5	0.9	8.06	0.02	208.2	11.3	5
SER 33[c]	-5.86	106.7	14-24	28.5	0.8	32.4	0.8	8.07	0.02	212.1	10.3	4
SS 07G14[b]	-19.73	150.22	74	24.9	1.0	35.3	0.2	8.09	0.03	219.9	14.4	7
Eil 19[b]	29.54	34.97	10-15	21.9	0.8	40.7	0.1	8.19	0.02	284.1	14.2	7
BBx 49A[b]	1.39	118.82	48	27.8	0.9	34.2	0.2	8.05	0.02	207.2	10.0	8
Pd 2801[a]	-5.03	119.33	20	28.0	1.1	33.4	0.9	8.06	0.02	209.0	11.2	4

ii) Planktonic foraminifera (*Globigerinoides ruber*)

Sample ID	latitude	longitude	Water depth (m)	T (°C)	SD	S	SD	pH (total scale)	SD	$[CO_3^{2-}]$* (µM)	SD	n
NBBT-09 No.5[d]	17.38	89.70	1450	27.1	1.0	32.7	0.7	8.07	0.02	204.1	11.3	5
CBBT-06 No.9[d]	11.03	84.43	899	28.6	0.5	33.8	0.3	8.07	0.02	217.2	9.5	9
SBBT-09 No.4[d]	5.40	86.77	886	28.2	0.4	34.3	0.3	8.06	0.01	219.4	8.9	10
SBBT-09 No.2[d]	5.40	86.77	886	28.2	0.3	34.3	0.2	8.06	0.01	219.1	8.8	10
AS02-M5 No.4[d]	10.00	65.01	2363	27.2	0.6	36.1	0.4	8.06	0.01	229.6	10.1	9
AS02-M5 No12[d]	10.00	65.01	2363	28.7	0.4	36.0	0.2	8.06	0.01	238.8	10.1	10
MC423[e]	17.75	-65.59	1813	27.5	1.0	35.6	0.4	8.07	0.02	231.2	12.5	10
MC420[e]	17.04	-66.00	4705	27.6	0.5	35.5	0.2	8.07	0.02	229.4	11.4	10
MC497[e]	23.53	63.31	1000	26.9	1.8	36.4	0.1	8.05	0.02	227.4	14.8	10
G4[e]	-28.42	167.25	831	22.0	2.0	35.8	0.1	8.12	0.02	218.3	15.4	10

a:Renema, 2002; b: Evans et al., 2013; c: Renema, 2008; d: Gray et al., 2018; e :Henehan et al., 2015; *derived using CO2Sys_v3.0 (see text for detail); n= no. of sample analysed; T= temperature; S=salinity

2.2. Cultured foraminifera

We investigated two sets of laboratory culture experiments in which *Operculina ammonoides* were grown at: 1) varying seawater Ca^{2+} concentration, repeated for three sets of temperature, and 2) varying seawater pH at constant DIC. Details of the culture procedure are given in Evans et al., (2015), Hauzer et al., (2018) and Hauzer, (2022). Briefly, live *O. ammonoides* from the 475-690 µm size fraction were collected from the North Beach, Eilat, Israel, at a depth of ~20-25 m. Prior to the experiment, foraminifera were placed in seawater labelled with the fluorescent marker calcein (50 µM) for 4-5 days and those that showed at least one fluorescent chamber were then transferred to seawater with the desired experimental conditions. The culture seawater medium was additionally spiked with 0.15 µM $BaCl_2$ solution (74 nM ^{135}Ba) in order to unambiguously identify newly precipitated calcite (Evans et al., 2016). Foraminifera grown under the culture conditions typically had between 3-13 non-fluorescent chambers grown after the calcein mark (Hauzer et al., 2018). These specimens were selected for further analysis; only data from chambers characterised by $^{135}Ba/^{138}Ba$ higher than the natural abundance were considered in our data analysis.

The culture experiment with varying $[Ca^{2+}]_{sw}$ used in this study is the same as that described in Hauzer *et al*. (2018) and Hauzer (2022), and was originally performed to determine the sensitivity of Na, Mg, Sr and Li incorporation into *O. ammonoides* to changing $[Ca^{2+}]_{sw}$, with the principal aim of establishing Na/Ca as a proxy for past changes in $[Ca^{2+}]_{sw}$. Comprehensive details of the experiment are given in Hauzer et al., (2018). The seawater calcium concentration was modified by adding $CaCl_2$, resulting in $[Ca^{2+}]_{sw}$ of 10.7, 12.7, 15.3, and 18.0 mmol kg^{-1}. Given that calcification in the culture jars results in lower TAlk and DIC,

the seawater carbonate chemistry was monitored and replaced regularly in order to maintain quasi-constant conditions. This experiment was conducted at three different temperatures: 22°C, 25°C, and 28°C.

The culture experiment at varying pH with constant DIC was conducted by modifying the TAlk of natural Gulf of Eilat seawater to the desired values by addition of HCl and NaOH (Hauzer, 2022, also see Evans *et al*., 2018 for further experimental details). As in the case of the $[Ca^{2+}]_{sw}$ experiment, the seawater was changed at regular intervals in order to, as far as possible, maintain constant conditions. pH and TAlk were monitored throughout the experimental period in both the culture jars as well as the seawater reservoirs, enabling us to report our trace element data against average measured values throughout the course of the experiments. Seawater pH, adjusted via changing the seawater TAlk at constant DIC, was experimentally varied between 7.5 to 8.3 (NBS scale). The saturation state (Ω_c), calculated using CO2sys using TAlk and pH measured during experimental period showed variability between 1.3 to 8.5 (Tab. S6).

At the end of both experiments, the foraminifera were cleaned with deionised water, treated with 1.5% NaOCl overnight to remove any organic material present, and then washed thoroughly several times with deionised water.

2.3. LA-SF-ICPMS analysis

Prior to analysis, all foraminifera were treated once again with 10% sodium hypochlorite (NaOCl) to oxidise any possible remnant organic material. The samples were then rinsed 3–4 times by ultrasonication in 18.2 MΩcm deionised water, followed by a final ultra-sonication cleaning step in methanol. The sample mounting procedure of the

foraminifera in the laser ablation cell differed depending on the species being analysed. Each larger benthic foraminifera was mounted by placing it into pressure-sensitive adhesive. Cultured specimens were placed vertically to target the marginal cord and the newly formed chambers were ablated starting from the final chamber and working backwards (3-5 chambers total). Most (modern) field-collected LBF specimens were placed horizontally in order to measure the knobs (pustules) (see Fig. 2), while some were analysed on both the knob regions and the marginal cord, in order to compare the data derived from the two areas. In general, the knobs were targeted where possible (i.e. in modern samples) because the calcite in this region is non-porous, unlike the marginal chord, thus minimizing the risk of contamination from sedimentary particles (see Sec. 3.2 for further details). Planktonic foraminifera were placed directly onto double-sided carbon tape with the umbilical side down, allowing the final three chambers to be ablated.

Trace element measurements were performed using a sector-field ICP-MS (Thermo Element XR) combined with a RESOlution 193 nm ArF laser ablation system equipped with a Laurin Technic S-155 two-volume laser-ablation cell (see Müller et al., 2009) at the Frankfurt Isotope and Element Research Center (FIERCE), Goethe University Frankfurt. Ablation was carried in an atmosphere of He and Ar with an additional diatomic gas, N_2, added downstream of the ablation cell. The instrument was tuned for maximum sensitivity while maintaining Th/U between 0.9-1.0 and ThO^+/Th^+ <1 %. The detailed operating parameters of the LA and ICPMS setup as applied specifically to this study are described in Tab. S1. Monitored masses (m/z) were ^{23}Na, ^{24}Mg, ^{25}Mg, ^{27}Al, ^{39}K, ^{43}Ca, and ^{55}Mn, with Al/Ca and Mn/Ca used to check that sample cleaning removed all remnant sedimentary particles and

that there were no diagenetic overgrowths. Standardisation of the data followed established protocols (Heinrich et al., 2003), using ^{43}Ca as the internal standard and the NIST SRM610 glasses as the external standard, analysed in an identical manner to the samples. Data reduction was performed using an in-house Matlab script (Evans and Müller, 2018) which automatically identifies sample and gas blank data, subtracts the latter from the former, and calibrates trace element ratios using a depth-dependent measured/reported element/^{43}Ca ratio derived from repeat analysis of the NIST SRM61x glasses.

Planktonic foraminifera were analysed in high mass resolution mode (Δm/m = 10,000) whereas the larger benthic foraminifera were analysed in medium mass resolution (Δm/m = 4000). Although high-resolution is required for complete resolution of ArH^+ on K^+ and was initially used to assess whether sufficient data quality could only be achieved when these are fully separated, we observed that medium-resolution is sufficiently capable of minimizing the effect of the ArH^+ interference (Fig. S1), such that we chose medium-resolution for most of the measurements that we report here as the best trade-off between separation of $^{38}ArH^+$ and $^{39}K^+$ and sensitivity. All samples were calibrated using sample-standard bracketing by analysing NIST SRM610 under identical conditions to the samples every ~20-30 minutes (i.e., blocks of ~10 analyses). The reported NIST SRM610 values of Jochum et al., (2011) were used with the exception of Mg, for which we use that of Pearce et al., (1997) following the recommendation of Evans and Müller, (2018). The MPI-DING komatiite glass GOR-128G (Jochum et al., 2006) and the nanopellet form (Garbe-Schönberg and Müller, 2014; Jochum et al., 2019) of the carbonate standard JCp-1 (Okai et al., 2002)

were measured at random intervals within the sequence using the same analytical conditions in order to assess the accuracy and precision of our sample data.

The accuracy of Mg/Ca, Sr/Ca, Al/Ca, and Mn/Ca in GOR-128G were within ±5%, whereas accuracy for Na/Ca and K/Ca was around 10.9% and 10.3% respectively. The higher offset from the true value in GOR-128G in the case of the alkali elements has previously been shown to be a result of a difference in the down-hole fractionation factor for the alkali metals in the GOR glass standards with respect to NIST SRM610 (Evans and Müller, 2018). This is demonstrated by the fact that our long-term Na/Ca accuracy is <5% in JCp-1, which was also the case for Al/Ca, Sr/Ca and Mg/Ca, whereas our Na/Ca and K/Ca data in GOR-128G are inaccurate to a similar degree. Assessing the accuracy of K/Ca measurements by LA-ICPMS is challenging because few $CaCO_3$ secondary standard materials exist. We measure a long-term average value of JCp-1 that is offset by 8.6% from that given by Okai et al., (2002), determined by Atomic Absorption Spectroscopy, but we do not apply an accuracy correction to our data because this reported value is based on a measurement from one laboratory. Nonetheless, it is possible that an accuracy correction on our data of the order of ~9% may be warranted in future if the value of Okai et al., (2002) is reproduced in other laboratories and/or in other test portions of the JCp-1 powder. Precision estimated from repeat measurement of these two secondary standards across the full analytical period represented here (~2 years) was <6% for all element/Ca ratios in GOR-128G (2σ). The precision for K/Ca, Mg/Ca and Sr/Ca in our JCp-1 nanopellet was less than 7% (2σ), whereas Na/Ca and Al/Ca precision was ~10% (2σ), which we attribute to the lower concentration and possible

presence of minor inhomogeneities in this standard material. Precise details of data quality are given in Tab. S2.

3. Results

3.1. Influence of seawater parameters on K incorporation in *Globigerinoides ruber* (white)

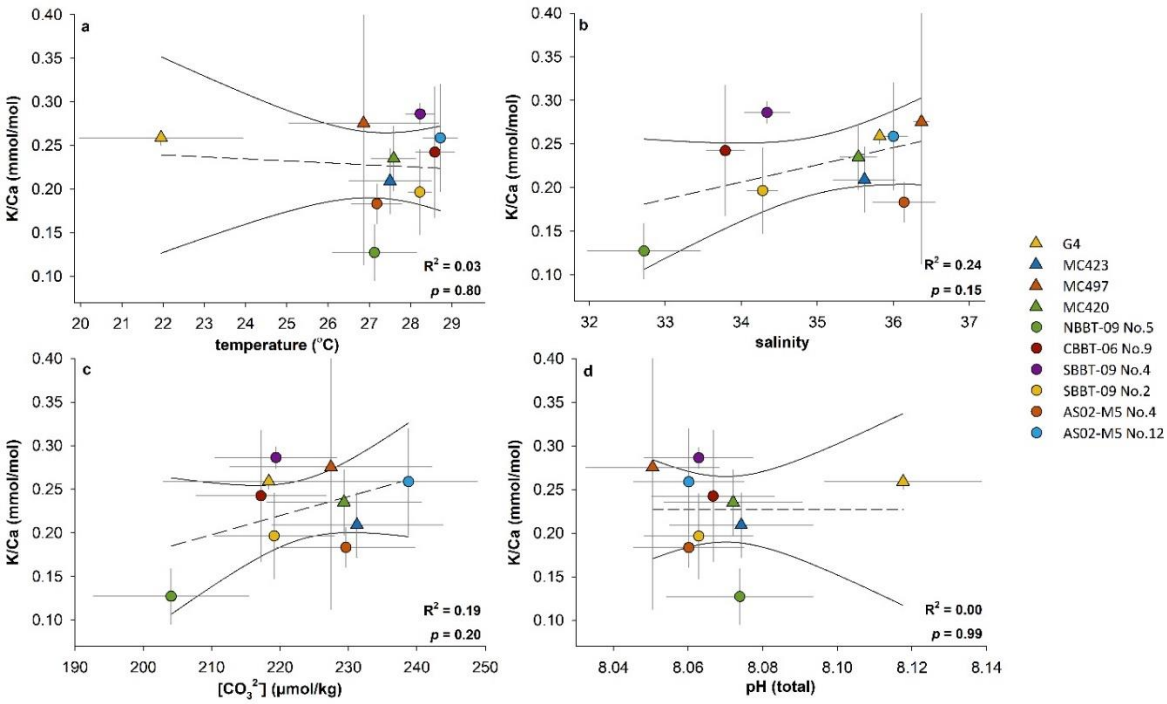

Fig. 1. K/Ca values of modern *G. ruber* plotted against a) temperature, b) salinity, c) [CO_3^{2-}] and d) pH. Sediment trap-collected foraminifera are depicted with circles and core top foraminifera with triangles. All error bars are 1SD. The solid line represents the 95% confidence interval on the linear regressions. Sample site details are given in Tab. 1.

The Al/Ca and Mn/Ca of all the planktonic foraminifera were lower than 0.15 mmol mol^{-1} (Tab. S3), demonstrating that contamination from remnant detrital material, if present, was effectively removed by our cleaning procedure. The mean value of K/Ca in *G. ruber* from sediment-trap samples (0.22±0.05 mmol mol^{-1}) and core-top (0.24±0.03 mmol mol^{-1})

samples are statistically indistinguishable based on a Student's t-test at the 95% confidence interval, such that we combine both datasets together. The similarity in the mean value of *G. ruber* K/Ca measured in core-top samples and sediment trap samples suggests minimal to no effect of early-stage diagenesis. The K/Ca in modern *G. ruber* ranges from 0.13 to 0.29 mmol mol^{-1} (Fig. 1; Tab. S3). We find no significant relationship between K/Ca and temperature (R^2 = 0.03; p = 0.80), salinity (R^2 = 0.24; p = 0.15), [CO_3^{2-}] (R^2 = 0.19; p = 0.20), or pH (R^2 = 0.00; p = 0.99). Multiple linear regression analysis of K/Ca against all possible combinations of pH, temperature, [CO_3^{2-}], and salinity also yielded no statistically significant relationship, demonstrating no resolvable influence of seawater composition on K incorporation into the shells of this species. However, considering only sediment trap samples, a significant relationship of K/Ca with temperature is observed (m = 0.068, R^2 = 0.66; p = 0.049).

3.2. Influence of seawater parameters on K incorporation in *Operculina ammonoides* collected from the modern ocean

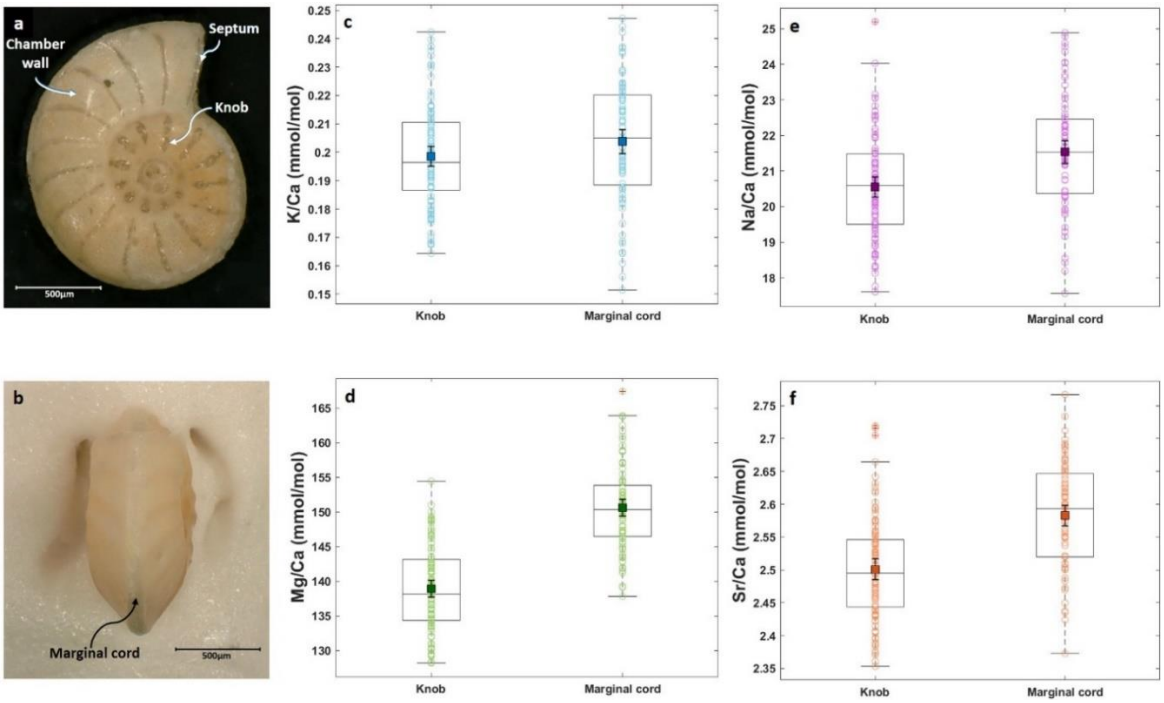

Fig. 2. Possible intra-shell element heterogeneity of *Operculina ammonoides* investigated using samples from the Gulf of Eilat (Eil 19). a,b) Representative specimens of *Operculina ammonoides* showing the regions of the shell investigated here (knob areas and marginal cord). c-f) Box plots of the measurements performed on knobs (n=18) and marginal cord (n=13). Each open circles represents an individual ablated spot. Filled squares shows the average value. Error bars on the average values are 2SE.

The larger benthic foraminifera *O. ammonoides* forms a complex shell structure with several distinct structural components (Carpenter, 1862; Hohenegger, 2011), consisting of septa, chamber walls, knob structures, and the marginal cord (see Fig. 2). To first understand whether measured trace element ratios in *O. ammonoides* are sensitive to the choice of which part of the shell is being analysed, i.e. to investigate possible heterogeneity in shell geochemistry, and given that elemental banding in the chamber wall of benthic foraminifera

(including K/Ca) has been reported (Geerken et al., 2019), we analysed both the marginal cord (porous) and knob (non-porous) regions of *O. ammonoides* from the Gulf of Eilat (sample Eil 19; Fig. 2). In addition, we investigated Mg/Ca, Na/Ca and Sr/Ca to compare the variability in their elemental ratios in these two regions of the shell, to understand whether trace element data from this species is sensitive to the region analysed. While we do observe ±20% K/Ca variability between individual laser spots (Fig. 2), the K/Ca ratio of the knobs (0.199±0.004 mmol mol^{-1}) and marginal cord (0.205±0.005 mmol mol^{-1}) are statistically indistinguishable based on a Student's t-test at the 95% confidence interval. The difference in the average value of Sr/Ca in both regions was 3.2%, whereas the average Na/Ca and Mg/Ca values were about 4.6% and 7.8% higher along the marginal cord, respectively (Fig. 2). Marginally higher values of Mg/Ca along the marginal cord have been previously reported (Evans et al., 2015). While this demonstrates that a consistent choice regarding the part of the shell to be analysed should be made in the case of Na, Mg, and Sr, the same is not true in the case of K/Ca. Hence, we performed all measurements on the non-porous knob region in all modern LBF to minimise possible contamination.

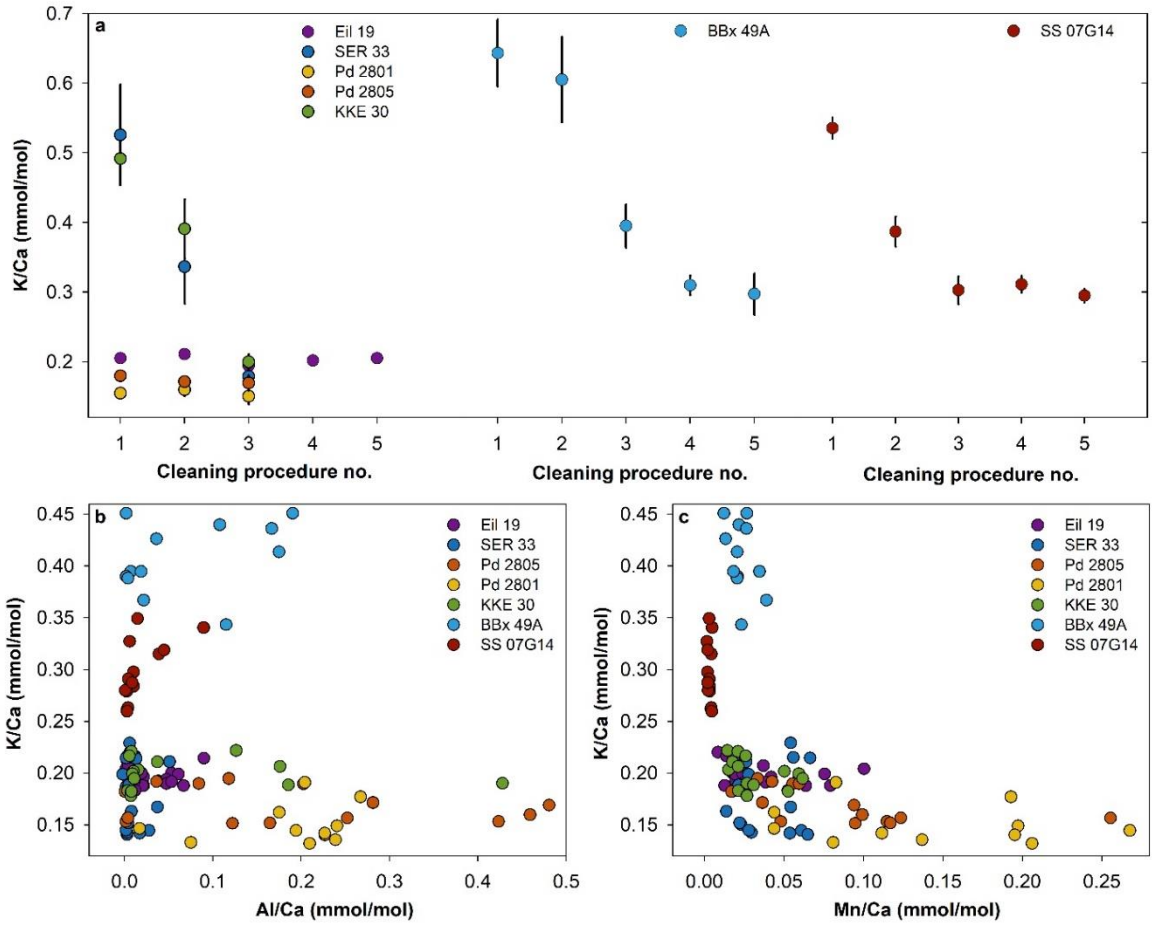

Fig. 3. a) Variation in K/Ca values during repeated cleaning steps (step 1: 10% NaOCl + methanol + deionised water; step 2-5: methanol + deionised water). The relationship of K/Ca in modern *Operculina* sp. with b) Al/Ca and c) Mn/Ca following the final cleaning process (see Methods).

The K/Ca measurements performed on *Operculina* sp. were repeated 3-5 times after repeated cleaning procedures (in addition to those described in the Methods section) to assess whether the initial cleaning steps were sufficient to remove all contaminant phases from the shell. This additional cleaning step consisted solely of a further ~10-15 minute ultrasonication in methanol followed by several deioinised water (18.2 MΩcm) rinses. Further oxidative cleaning steps were not conducted because we suspect that possible remnant contaminant phases are sedimentary particles that require physical removal, rather than the

result of (e.g.) incomplete oxidation of organic material. Al/Ca and Mn/Ca were monitored to determine contamination-free measurements after each cleaning step, and the overall change in K/Ca after each sequential step was used to determine whether incomplete removal of possible contaminant phases during this process biased the mean sample values. We observe a decrease in measured K/Ca in the first three cleaning steps in four out of the seven samples investigated here, indicating that a single oxidative cleaning step followed by several deioinised water rinses is unlikely to be sufficient to remove K contamination in the majority of cases, even when analysing non-porous regions of the shell. Specifically, samples Pd 2801, Pd 2805, and Eil 19 were characterised by no significant change in K/Ca with further cleaning, whereas SS 07G14, KKE 30 and SER 33 needed three additional cleaning steps (Fig. 3a). The K/Ca of *Operculina* from NE Kalimantan (BBx 49A) continued to decrease even after the third cleaning step (Fig. 3a). The decrease in the K/Ca after cleaning step-2 represents possible clay contamination. . Even after five cleaning steps the K/Ca of BBx 49A and SS 07G14 remained substantially elevated compared to the other larger benthic foraminifera samples, but we retain both in our data analysis because there is no reason to treat these data points as outliers. After the final cleaning step, all samples that were considered in this study were characterised by Al/Ca and Mn/Ca lower than 0.5 mmol mol^{-1} and 0.3 mmol mol^{-1}, respectively (Fig. 3b,c). Due to higher Al/Ca, we had to remove one foraminifera each from Pd 2805, Pd 2801, and BBx 49A.

Within the subset of samples that were unambiguously not affected by remnant contamination, K/Ca in modern *Operculina* sp. varied between 0.15±0.01 mmol mol^{-1} to 0.31±0.01 mmol mol^{-1} (Tab. S4). The relationship between K/Ca in modern *Operculina* sp.

and key oceanographic parameters is shown in Fig. 4. These data demonstrate that there is no clear relationship between K/Ca in modern *Operculina* and temperature, salinity, [CO_3^{2-}] or pH (R^2 of K/Ca versus temperature, salinity, [CO_3^{2-}] and pH were 0.07, 0.02, 0.00, and 0.00, respectively), implying no resolvable influence of these seawater parameters on K incorporation in *Operculina* species, although we note that the addition of further modern data is a priority, given the relatively small sample number.

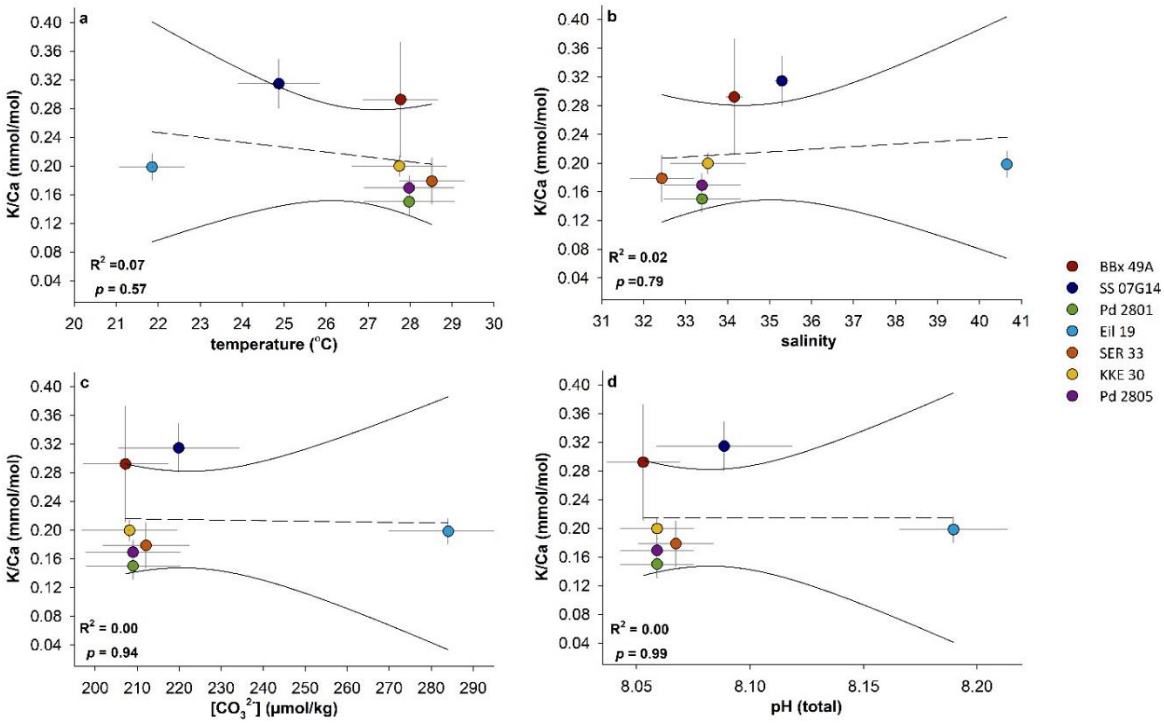

Fig. 4. K/Ca in modern *Operculina* sp. as a function of temperature, salinity, pH, and [CO_3^{2-}]. All error bars are 1SD. The solid line represents the 95% confidence interval on the linear regressions. Sample site details are given in Tab. 1.

3.3. Incorporation of K in cultured *Operculina ammonoides* grown in seawater with variable $[Ca^{2+}]_{sw}$ and variable pH

O. ammonoides were cultured at three different temperatures and four different $[Ca^{2+}]_{sw}$ (12 experiments in total, (see Hauzer et al., (2018)). The K/Ca of *O. ammonoides*

grown at elevated $[Ca^{2+}]_{sw}$ were broadly reproducible irrespective of the culture temperature. For example, at the highest $[Ca^{2+}]_{sw}$ value investigated here (18 mmol kg^{-1}), K/Ca = 0.180±0.016, 0.193±0.017, and 0.195±0.013 mmol mol^{-1} at 28, 25, and 22°C respectively (Fig. 5a). The exception to this was the lowest $[Ca^{2+}]_{sw}$ experiment (10.7 mmol kg^{-1}, equivalent to modern seawater at salinity = 37), in which K/Ca was 0.189±0.018, 0.210±0.010, and 0.261±0.009 mmol mol^{-1} at 28, 25, and 22°C respectively (Fig. 5a). However, the K/Ca of cultured foraminifera overall falls within the range of the modern field samples described above, in which we find no clear relationship between K incorporation and seawater temperature, salinity, or carbonate chemistry. As such, we pool the data together from the three temperature experiments conducted for each $[Ca^{2+}]_{sw}$ (Tab. S5), treating the three experiments as replicate cultures at a given $[Ca^{2+}]_{sw}$ to examine the overall relationship between seawater and shell K/Ca. The average K/Ca_{LBF} values are tightly correlated with $[Ca^{2+}]_{sw}$, albeit with a very shallow slope (the least squares linear regression has m = 0.072±0.013). Because the shell K/Ca ratio must equal 0 at K/Ca_{sw} = 0, we fit a distribution function through the data (see Hauzer et al., (2018) for terminology). This yields a power relationship ($y=ax^b$) with K/Ca_{sw} (b = 0.29, R^2 = 0.93, p = 0.04), again, with a shallow slope compared to other major/trace elements (Na/Ca: b = 0.54; Mg/Ca: b = 0.72; Evans et al., (2015); Hauzer et al., (2018)).

The Na/Ca data of this study are a test of analytical external reproducibility, given that Na/Ca of the same samples was previously reported by Hauzer et al. (2018), measured in a different laboratory and using a different type of mass spectrometer. Our LA-SF-ICPMS results agree well with the previously reported LA-Q-ICPMS Na/Ca data (Fig. 5b),

demonstrating that a power function between Na/Ca_{sw}-Na/Ca_{shell} best describes the culture experiment. This adds confidence to the inter-laboratory comparability of laser ablation trace element data using different mass spectrometers (note that the data reported here use NIST SRM610 as a primary calibration standard, whereas Hauzer et al. (2018) used NIST SRM612 for Na/Ca quantification).

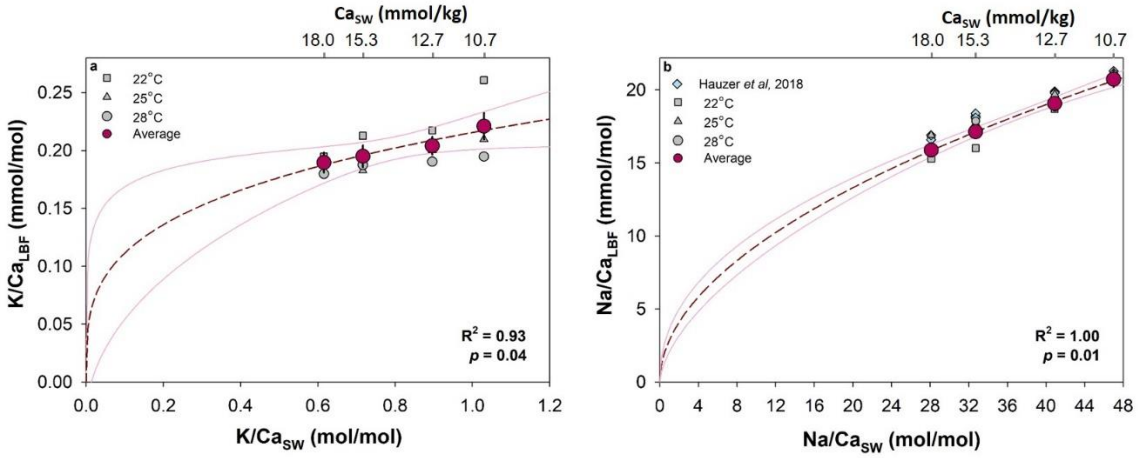

Fig. 5. a) The relationship between *Operculina ammonoides* and seawater K/Ca. b) The relationship between *Operculina ammonoides* and seawater Na/Ca. Error bars represent 2SE. The solid line represents the 95% confidence interval on the power regressions. The seawater Ca_{sw} values are taken from Hauzer et al., (2018)

Measured K/Ca values in foraminifera grown at different pH (constant DIC) are shown in Fig. 6, with the data reported in Tab. S6. Although we find no resolvable relationship between K/Ca and pH in the modern *O. ammonoides* samples (Fig. 4), K/Ca and pH shows significant relationship in this culture experiment (R^2 = 0.96; p = 0.01), conducted over a much larger pH range (~7.5 to 8.3) (Fig. 6a). The saturation state (Ω_c) of the experimental seawaters was estimated using the Matlab program CO2SYS.m (Van Heuven et al., 2011) using the total alkalinity (TAlk) and pH measurements made during experimental period. This exercise demonstrates that a significant relationship exists between *O. ammonoides* K/Ca

and seawater saturation state (Ω_c) (R^2 = 0.96; p = 0.01; Fig. 6b), with a slope of 0.0067 mmol mol^{-1} per unit change in Ω_c.

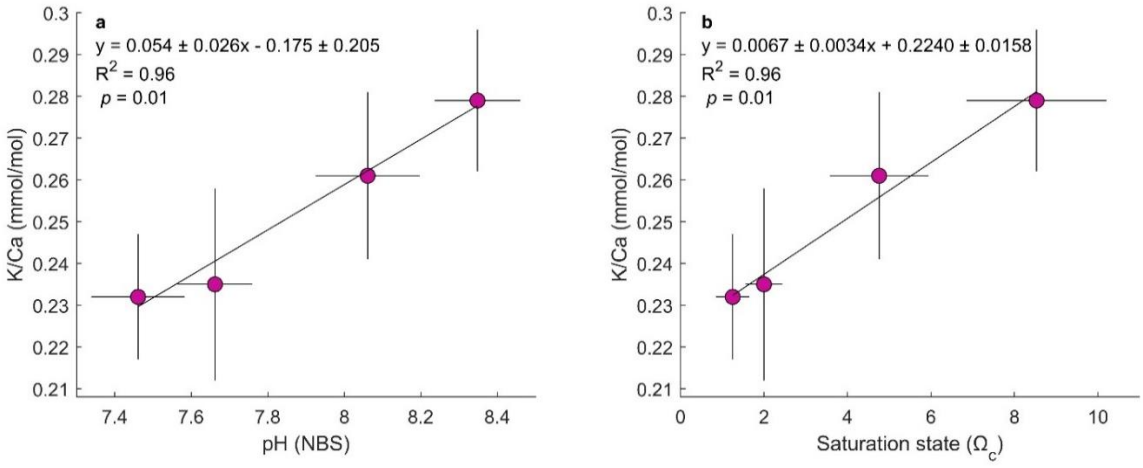

Fig. 6. The relationship between K/Ca in cultured *O. ammonoides* and a) pH and b) saturation state (Ω_c). The equation represents the York-fit linear regression line (solid line), accounting for the uncertainties in both axes (York et al., 2004). R^2 and p values represents least square fit line. Error bars are 2SE.

4. Discussion

4.1. Controls on modern high-Mg benthic and low-Mg planktonic foraminifera K/Ca

We investigated the effect of a wide range of seawater carbonate chemistry and physical parameters on K/Ca in both the shallow dwelling, warm water high-Mg calcite larger benthic foraminifera (*Operculina sp.*) and the low-Mg calcite planktonic foraminifera (*G. ruber*). The contrasting mineralogy of these species, as well as the wide range of ambient conditions investigated here in both laboratory culture and the natural environment, means that the sample set is well-placed to identify whether any of these factors drive changes in K incorporation.

With regards to the effect of mineralogy, we observe Na/Ca 2-3 times higher in the high-Mg foraminifera than the low-Mg foraminifera, as previously reported (e.g. Delaney et al., 1985; Evans et al., 2015; van Dijk et al., 2017; Bertlich et al., 2018). This has been previously ascribed to Mg-induced lattice distortion (Evans et al., 2015; Hauzer et al., 2018), while the presence of Na at relatively high concentration in organic-rich layers within the shell has also been described (Branson et al., 2016; Bonnin et al., 2019). In contrast to Na (and Sr; Mucci and Morse, (1983); Evans et al., (2015)), we observe that the average value of K/Ca in modern high-Mg foraminifera *Operculina* sp. (0.21±0.02 mmol mol^{-1}) falls in the same range as the average of all modern low-Mg planktonic species *G. ruber* (0.23±0.03 mmol mol^{-1}). This possibly suggests a similar incorporation mechanism of K in these foraminifera and/or no effect of mineralogy on the K distribution coefficient.

Previous work has shown that salinity exerts a control on the incorporation of alkali ions (i.e., Na and Li) in both biogenic marine carbonates and inorganic calcite (Marriott et al., 2004; Wit et al., 2013; Allen et al., 2016; Hauzer et al., 2021). For example, the effect of salinity on alkali element incorporation in *O. ammonoides* was observed to be 1.38% per salinity unit in the case of Na/Ca and 2.05% for Li/Ca (Hauzer et al., 2021). The effect of salinity on *G. ruber* Na/Ca appears to differ between plankton-tow and core-top samples, and/or depending on how the samples are analysed (laser ablation versus solution ICPMS). For example, Allen et al., (2016) report a 1.09% change in Na/Ca per salinity unit in laboratory culture measured by solution ICPMS, whereas Mezger et al., (2016) report a slope of 0.57 (plankton-tow samples measured by LA). In this study, we observed no relationship between K/Ca and salinity in *O. ammonoides* and *G. ruber*. While we cannot rule out that a salinity

control exists, e.g., if a wider range of salinities were to be investigated, this – at least – indicates that other factors readily mask any salinity control on K incorporation in foraminifera.

We find no significant relationship between pH or [CO_3^{2-}] and K/Ca in modern (sediment trap/core-top) *G. ruber* or *O. ammonoides*. Laboratory culture experiments have previously demonstrated no carbonate system control on Li/Ca and Na/Ca in *G. ruber* (Allen et al., 2016), suggesting that seawater carbonate chemistry is not a first-order control on alkali element incorporation in any of these foraminifera in their natural environment. In contrast, we do find a positive relationship between K/Ca and pH in laboratory cultures of *O. ammonoides* conducted over a much wider pH range than that of the modern ocean (Fig. 6a), and some previous studies have demonstrated a Li/Ca sensitivity to the carbonate system in other species (Vigier et al., 2015; Roberts et al., 2018). There is also a significant relationship between K/Ca and the seawater saturation state, discussed in more detail below (Sec. 4.3).

Overall, we show that the K/Ca ratio of modern *Operculina* sp. and *G. ruber* is similar, and in both cases not resolvably driven by any key oceanographic parameters or the carbonate chemistry of seawater, to the extent that these vary in the modern (sub) tropics.

Finally, we note that the absolute K/Ca ratios that we report for *G. ruber* are ~0.1 mmol mol^{-1} higher than the four planktonic foraminifera samples reported by Li et al., (2021); further data will be required to understand whether this represents real variability in natural samples greater than that reported here, or if it is an artefact of the different analytical or sample preparation procedures.

4.2. Sensitivity of foraminiferal K/Ca to seawater K/Ca

The laboratory culture experiments were conducted at $[Ca^{2+}]_{sw}$ of 10.7, 12.7, 15.3, and 18.0 mmol kg^{-1}, with repetitions of each experiment at three temperatures (22°C, 25°C, and 28°C). We observed similar K/Ca for all temperature experiments in the three experiments with elevated $[Ca^{2+}]_{sw}$, whereas in the control experiment with normal $[Ca^{2+}]_{sw,}$ K/Ca of *O. ammonoides* grown at 22°C was higher than that at 25°C and 28°C. It is not clear why the lower temperature and low $[Ca^{2+}]_{sw}$ favoured the higher incorporation of K/Ca in this foraminifera. Although foraminifera in this experiment were characterised by the lowest growth rates of the set overall (Hauzer *et al*., 2018) such that this may relate to physiological stress. The modern *ammonoides* sp. datasets presented here suggest that temperature is unlikely to play a substantial role in K incorporation given that, if temperature were the controlling factor, we would also expect to see this effect at cultures conducted under elevated $[Ca^{2+}]_{sw}$.

Averaging the results of the three temperature experiments together (Fig. 5), results in a significant but extremely shallow relationship between K/Ca_{shell}-K/Ca_{sw}; to our knowledge, shallower than other trace element reported so far for the surface-dwelling foraminifera (e.g. Li, Mg, Sr, Ba; Delaney et al., 1985; Hönisch et al., 2013; Allen et al., 2015; Evans et al., 2015; Hauzer et al., 2018). The insensitivity of shell K/Ca to seawater K/Ca most likely results either from a biological vital effect, acting to increase the $[K^+]$ of the calcification site as $[Ca^{2+}]_{sw}$ increases to drive a much shallower relationship between shell-seawater K/Ca than would otherwise be expected, or from a kinetic effect on K incorporation into calcite

driven by the differential $[Ca^{2+}]_{sw}$. We first briefly explore the former possibility here, and the latter in more detail in Sec. 4.3.

Transmembrane alkali element pumps are ubiquitous (e.g. Nakao and Gadsby, 1986; Skou and Esmann, 1992; Gouaux and MacKinnon, 2005). In foraminifera, proton pumping is known to accompany calcification (Bentov et al., 2009; Toyofuku et al., 2017). Li-proton pumps have been implicated in controlling the carbonate chemistry of the calcification site (Vigier et al., 2015), with Na-proton pumps another likely candidate given the abundance of Na^+ in seawater (see e.g. Erez, 2003; McNicholl et al., (2019)). Given that K^+ is present at a concentration of 10.2 mmol kg^{-1} in seawater and at much higher concentrations in the cytosol of marine cells (>100 mM; Eppley, 1958; Dodd et al., 1966; Thompson and MacLeod, 1974), the use of a K-proton pump as a means of regulating vacuole or calcification site pH may be a likely possibility. At face value, the shallow slope resulting in elevated K/Ca_{LBF} at higher $[Ca^{2+}]_{sw}$ would imply a greater degree of proton elevation and therefore a higher $[K^+]$ at the calcification site in experiments with a higher-than-natural $[Ca^{2+}]_{sw}$. This may seem unintuitive, given that at higher $[Ca^{2+}]_{sw}$, the saturation state of seawater (Ω_c) is higher, thus requiring a lower degree of pH elevation to achieve a similar degree of calcite precipitation. However, an alternative possibility is that a greater $[Ca^{2+}]_{sw}$ means that the organism can continue to precipitate calcite from the same package of seawater for longer, because more Ca^{2+} is available for calcification. If so, this continued precipitation would require a greater degree of proton pumping given that calcification releases protons, in order to maintain an elevated pH through this process to promote precipitation and CO_2 diffusion from the cytosol to the calcification site (as calcification is carbon limited in unmodified seawater).

However, while calcification from seawater with an elevated [Ca^{2+}] may well be associated with a greater degree of Li/Na/K pumping, as the organism makes use of the extra Ca^{2+} available, the high concentration of K^+ in seawater (K^+/H^+ = ~10^6) means that the calcification site [K^+] is likely to be negligibly modified by this process (in contrast to Li; Vigier et al., 2015, we note that the same logic also applies to the calcification site [Na^+]). Thus, we argue that the highly nonlinear seawater-shell K/Ca relationship that we observe is perhaps more likely to represent a kinetic effect, driven by the control that $[Ca^{2+}]_{sw}$ has on the rate of mineral precipitation.

4.3. Evidence for a kinetic effect on K incorporation

The seawater [Ca^{2+}] in the culture experiments utilised here was varied independently of all other parameters. As a result, the saturation state of these seawaters with respect to calcite (Ω_c) covaried with $[Ca^{2+}]_{sw}$, as [CO_3^{2-}] remained constant. Because the carbonate chemistry of seawater is known to be an important control on both inorganic calcite precipitation and the calcification of foraminifera (e.g. Erez, 2003; Wolthers et al., 2012; Oron et al., 2020), it is possible that the experimental design could have affected not only the growth rate of the foraminifera (Hauzer et al., 2018), but also the crystal growth rates at the calcification site. Here, we explore whether this phenomenon could explain the observed shallow slope of the relationship between seawater-shell K/Ca, i.e., if the elevated $[Ca^{2+}]_{sw}$ drove higher surface-area normalised crystal growth rates and therefore higher shell K/Ca for a given $[Ca^{2+}]_{sw}$ than would otherwise be expected if Ω_c had remained constant in these experiments.

In the culture experiment, population-scale calcification rate was calculated based on measurements of alkalinity depletion (Hauzer et al., 2018).. However, population-scale calcification rates may not necessarily represent crystal-precipitation rates for two reasons: i) not all foraminifera in our experiments calcified at the same rate. Because it is not practically feasible to weigh individual foraminifera to estimate the growth rate that is characteristic of the calcifying specimens (e.g. approximately 20% of foraminifera did not add any new chambers in culture), the overall calcification rate is biased downwards by specimens that did not grow in culture, and/or ii) irrespective of this complication, bulk calcification rate could be decoupled from surface area normalised precipitation rate at the calcification site because calcification is almost certainly a discontinuous process; chamber formation usually takes place at discrete intervals every few days. This is important because it is surface area-normalised precipitation rates that ultimately exert a large control on trace element incorporation into the growing mineral (Watson, 2004). To avoid these issues, and given that Ω_c and $[Ca^{2+}]_{sw}$ covaried in the culture experiment with varying Ca_{SW} (Fig. 5), we alternatively explore the extent to which Ω_c-driven crystal growth rate effect could impact our results by deriving an empirical relationship between Ω_c and K/Ca in *O. ammonoides* from the culture experiment in which *O. ammonoides* was grown at variable pH/Ω_c but constant DIC. In the supplementary materials we additionally formulate a theoretical relationship to account for the effect of variable $[Ca^{2+}]_{sw}$ on crystal growth rate and thus El/Ca_{LBF} (based on empirical growth rate equations and information from inorganic precipitation experiments regarding the rate control on alkali element incorporation), demonstrating that the direction of this effect is the same in both inorganic and foraminiferal

calcite. We stress that a precipitation rate-driven kinetic effect on K incorporation is not the only potential explanation for the strong deviation of the data from a constant apparent distribution coefficient. For example, differences in the degree of Ca utilization within the pool at the calcification site may also be important (Elderfield et al., 1996), as may be large degrees of K^+ transport or leakage. However, we focus on a kinetic effect here because our data demonstrate an impact of seawater carbonate chemistry on foraminiferal K/Ca.

The results of this exercise are shown in Fig. 7. Here, a correction was applied to the seawater-shell Na-K/Ca data using a relationship between shell El/Ca and Ω_c based on culture experiment at varying pH (details in supplementary material). The results of this correction suggest that a substantial portion of the apparent insensitivity of shell K/Ca to K/Ca_{sw} (Fig. 5) is mechanistically explicable via a growth-rate driven kinetic control on K incorporation into calcite. Given that rate has been shown to impact the incorporation of the alkali elements to a much greater degree than the alkali earth elements in calcite (e.g. Lorens, 1981; Nehrke et al., 2007; Füger et al., 2019), Ω_c-driven rate effect on K/Ca in our $[Ca^{2+}]_{sw}$ laboratory culture data should be accounted for before using these results to understand the relationship between seawater and shell K/Ca. We note that even following this correction, to our knowledge, the power relationship between seawater-shell K/Ca has a lower power coefficient than any trace element studied so far, which could relate to a biological vital effect (e.g. a higher $[K^+]$ of the calcification site driven by processes other than alkali-proton pumps), or further kinetic effects (e.g. if the calcification site Ω_c is not characterised by a 1:1 relationship to seawater Ω_c, when saturation state changes are driven by $[Ca^{2+}]_{sw}$.

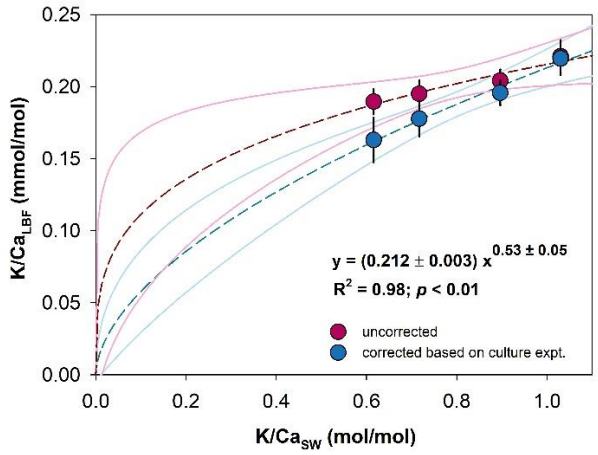

Fig. 7. The relationship between K/Ca_{LBF} and $K/Ca_{sw.}$ A growth rate correction, explored here because $[Ca^{2+}]_{sw}$ in these culture experiments covaried with Ω_c is shown using the relationship between K/Ca and Ω_c from the experiment in which pH was varied at constant (modern) Ω_c. Error bars are 2SE. Solid lines depict the 95% confidence intervals of the least-squares power regressions. The equations given in the panels are those through the corrected K/Ca data.

In terms of using the laboratory culture calibration as a potential tool to reconstruct changes in $[Ca^{2+}]_{sw}$, we advocate for the use of the Ω_c-corrected equation (Fig 7). This is because Ω_c varied by 3.74 units in the seawater $[Ca^{2+}]_{sw}$ experiment, but is not thought to have undergone substantial variation in the (sub)tropical surface ocean through the Cenozoic (e.g. (Tyrrell and Zeebe, 2004; Anagnostou et al., 2016)). Therefore, if the notion that $[K^+]_{sw}$ was constant throughout the Cenozoic, as suggested by Horita et al., (2002) is correct, then the K/Ca calibration established in this study may be used for direct reconstruction of $[Ca^{2+}]_{sw.}$

4.4. Incorporation of K in $CaCO_3$

A better understanding of the processes by which marine carbonates incorporate trace elements from seawater is important in improving the accuracy of reconstructions

based of shell geochemistry. Given that there is a limited amount of previous work on K incorporation in marine carbonates, we summarise most of the data published so far and place it in the context of inorganic precipitation work in an attempt to identify the broad controls on K incorporation into biogenic $CaCO_3$.

Inorganic $CaCO_3$: Several studies have investigated the influence of various solution chemistry and physical parameters on alkali metal incorporation into calcite and aragonite. Ishikawa and Ichikuni (1984) examined the uptake of Na and K in inorganically precipitated calcite primarily as a function of solution $[Na^+]$ and $[K^+]$ and observed a clear control of solution El/Ca on their incorporation, demonstrating that both trace elements have a distribution coefficient in both $CaCO_3$ polymorphs. White (1977) investigated the mechanism of K incorporation in inorganically precipitated aragonite and observed that Na and K incorporation decreases with decreasing pH and increasing temperature, in addition to demonstrating an inhibition of K incorporation in the presence of high concentrations of Na, implying competition between these elements for certain sites or spaces within the lattice (although the range of solution alkali metal/Ca ratios investigated were far higher than those of our study). While we also observe a clear Na and K distribution coefficient (function) into biogenic high-Mg calcite, the overall much larger parameter space investigated in the inorganic experimental work conducted to-date likely explains why we do not observe many of these factors in marine biogenic $CaCO_3$.

Calcitic organisms: The nummulitid larger benthic foraminifer *Operculina* sp. analysed in the present study are formed of high-Mg calcite (Blackmon and Todd, 1959; Cotton et al., 2020). To the best of our knowledge, our data represent the first report of K/Ca

in high-Mg calcite. These foraminifera have K/Ca = 0.21±0.100 (2SD) and D_K =2.2×10^{-4} (averaged across all of our field and culture data) which is similar to the range of *G. ruber* reported here (0.23±0.097 (2SD); D_K =2.3×10^{-4}) and other low-Mg calcitic marine organisms (deep sea corals, brachiopods; (Li et al., (2021) Fig. 8) with only the bivalves offset to significantly lower values. As such, there is no evidence for a mineralogical control on K incorporation, in contrast to Na and Sr, and possibly other trace elements (Evans et al., 2015; van Dijk et al., 2017). The *O. ammonoides* culture experiment presented here is the first time that the relationship between K/Ca_{shell} and K/Ca_{sw} has been assessed for a foraminifer species, demonstrating that K/Ca_{shell} is governed by K/Ca_{sw}, albeit with a shallow slope. Interestingly, this relationship is substantially shallower that those that have been described between Na/Ca_{shell} and Na/Ca_{sw} (Hauzer et al., 2018; Le Houedec et al., 2021; Zhou et al., 2021; Fig. 9). If the shallow slope of the seawater-shell K/Ca ratio in this experiment is indeed driven in part by kinetic processes (Sec. 4.3), this may imply a greater sensitivity of K incorporation to factors such as growth rate. Curiously, this is intuitively difficult to reconcile with the relative constancy between K/Ca across multiple groups of marine calcitic organisms, while the incorporation of other trace elements differs widely between these groups (Raja et al., 2007; Van Dijk et al., 2017; Ulrich et al., 2021); further work will be required to understand why this is the case. While it is beyond the scope of this study to investigate this in more detail, we note that the commonality of the power relationship between Na/Ca with Na/Ca_{sw} in all foraminifera studied so far, and a similar observation for K/Ca in biogenic calcite (Fig. 9a,b), suggests – at least – that the mechanism of Na and K incorporation may be similar in low-Mg planktic foraminifera and high-Mg large benthic foraminifera.

Aragonitic organisms: As is the case for the calcitic organisms, the K/Ca of a number of biogenic aragonites (corals, bivalves, gastropods) is characterised by a relatively narrow range (K/Ca: 0.20 to 0.25 mmol mol^{-1}), and absolute values that are indistinguishable from most biogenic calcites. This is in contrast to Na/Ca, which is a factor of ~2 higher in biogenic aragonite compared to biogenic low-Mg calcite (Schleinkofer et al., 2019). Thus, there is no evidence for a first-order mineralogical control on K incorporation into $CaCO_3$, potentially implying that the calcification site K/Ca and K distribution coefficient may be similar across a large range of marine calcifying organisms, if shell K/Ca is alternatively primarily determined by K/Ca_{sw}. A review of the limited amount of existing research indicates that this assumption of a primary K/Ca_{sw} control is the case for some aragonitic organisms but not others. K/Ca measured in the aragonitic shells of gastropods showed no relationship with fluid K/Ca (Rosenthal and Katz, 1989), although this study reported data for a freshwater species. In contrast, K/Ca and Na/Ca of aragonitic scleractinian corals follow a near linear relationship with El/Ca_{sw} (Ram and Erez, 2021), which has similarly been shown to be the case for inorganically precipitated K/Ca and Na/Ca (at least up to seawater-like K-Na/Ca ratios; Okumura and Kitano, 1986).

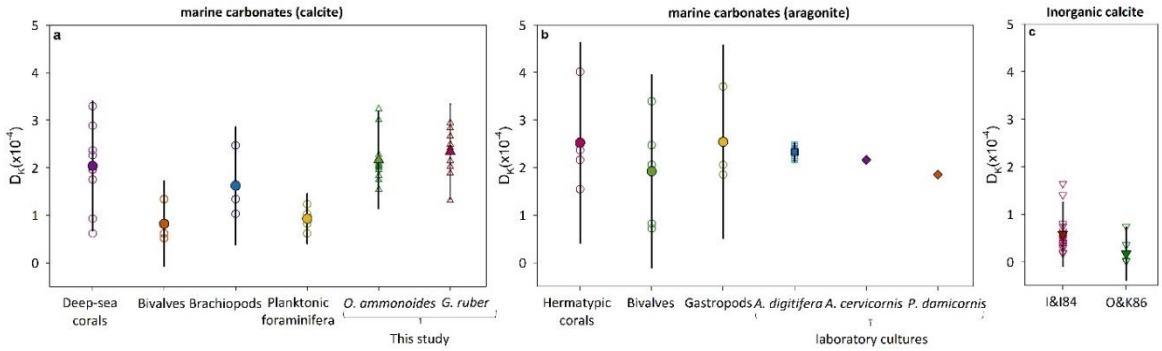

Fig. 8. The D_K in a) calcitic biogenic marine carbonates, b) aragonitic marine carbonates and c) inorganic calcite. The D_K estimations are based on solution K and Ca concentrations, except in the case of the inorganic calcite study of I&I84, in which the D_K values are based on K activity. The symbols denote: this study (triangles; open triangles indicate specimens from different locations and culture study), Li et al., 2021 (circle; open circles indicate different species); Bell et al., 2018 (square; open squares indicate different specimens); Ram and Erez, 2021 (diamond) and inverted triangles (I&I84: Ishikawa and Ichikuni, 1984; O&K,86: Okumura and Kitano, 1986). Solid symbols are average values. In all cases error bars denote the 2SD of each dataset, but note that each dataset represents a wide range of sample collection types (multiple/single species, culture/natural populations etc., see brackets in the earlier part of the figure caption for brief descriptions).

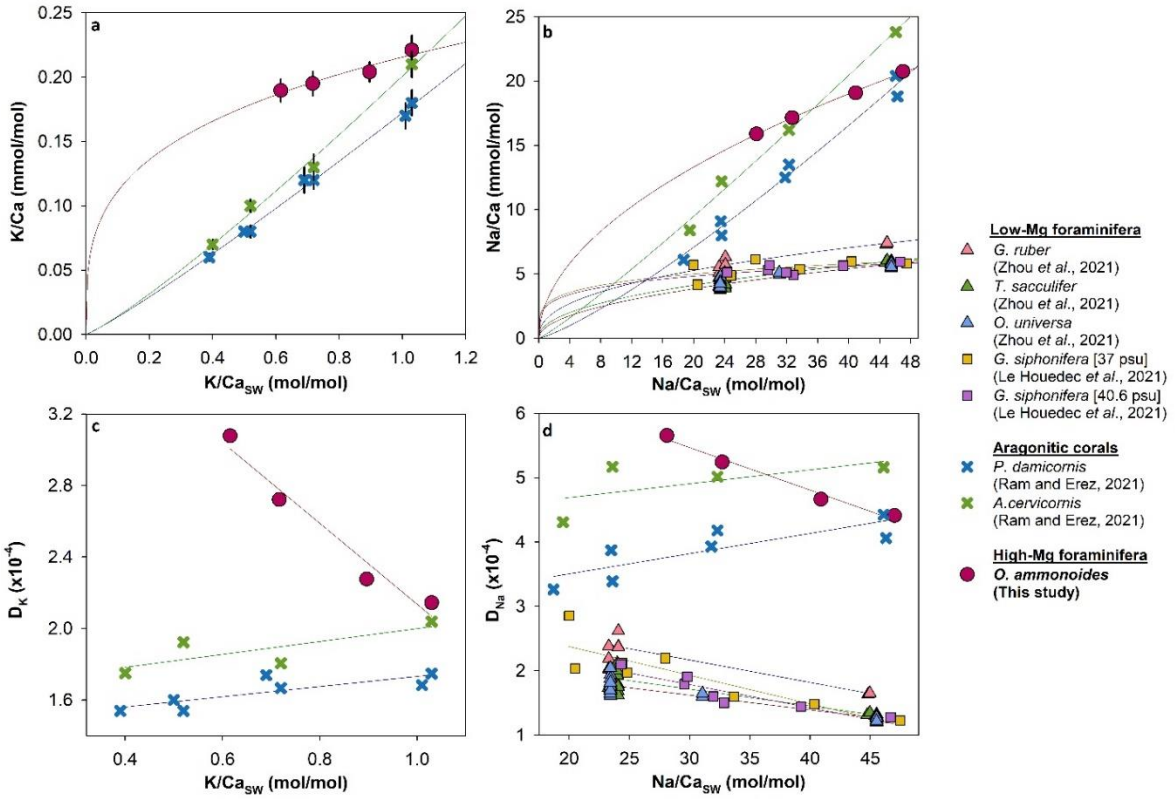

Fig. 9. a,b) The relationship between K/Ca and Na/Ca of different marine carbonates and El/Ca$_{sw}$. c,d) The relationship between the apparent distribution coefficient of K (D_K) and Na (D_{Na}) with their El/Ca$_{sw}$. All error bars are 2SE.

Both our work and a previous study (Ram and Erez, 2021) demonstrate that the partition of K in marine carbonates is governed to large degree by the K/Ca$_{sw}$ ratio. The apparent distribution coefficient of K in *O. ammonoides*, calculated as D_{El} = (El/Ca)$_{shell}$/(El/Ca)$_{sw}$, decreases with increasing K/Ca$_{sw}$, a behaviour which is similar to that of Na (Fig. 9c,d) and Mg in a wide range of biogenic calcites (Hasiuk and Lohmann, 2010) and inorganic calcite (Mucci and Morse, 1983). To facilitate the comparison of K and Na distribution coefficients presented here to other marine carbonates, we compile apparent distribution coefficient data as a function of the respective seawater ratio (Fig. 9c,d). The D_{Na} of both planktonic foraminifera and larger benthic foraminifera showed a decreasing trend

with increasing seawater Na/Ca, whereas the D_K and D_{Na} of two aragonitic scleractinian corals is characterised by a shallow positive slope with El/Ca_{sw} (Ram and Erez, 2021). As we discuss above, this is perhaps most parsimoniously explained by a kinetic (growth rate) effect on the incorporation of K and Na in the foraminifera which results in higher D_{El} with increasing Ca_{sw}, although we again note that understanding the degree of Rayleigh fractionation at the calcification site of calcifying organisms is also key in terms of understanding bulk calcite trace element geochemistry (Elderfield et al., 1996; Evans et al., 2018b). Culture experiments that vary $[K^+]_{sw}$ rather than $[Ca^{2+}]_{sw}$ would be one way in which this hypothesis could be tested. In addition, inorganic precipitation experiments focusing on both calcite and aragonite are required to understand why this affect does not seem to have biased the coral data, given that the foraminifera $[Ca^{2+}]_{sw}$ experiment discussed here was experimentally similar to that of Ram and Erez, (2021).

5. Summary

In this study, we investigated the influence of a wide range of seawater parameters on the incorporation of K into the planktonic foraminifer, *Globigerinoides ruber* (white) and larger benthic foraminifer, *Operculina* sp.. In both cases, no significant correlation of K/Ca with temperature, salinity, pH, or $[CO_3^{2-}]$ was observed, which suggests that the incorporation of K is independent of these seawater parameters, or that other factors act to easily mask these effects. The similar K/Ca of low-Mg planktonic foraminifera and high-Mg benthic foraminifera suggest no major effect of mineralogy on K incorporation, which also appears to be more broadly the case (i.e. between calcite and aragonite) based on a compilation of published data.

In addition, we investigated K/Ca in marine carbonate as a potential proxy for the seawater K/Ca ratio, based on laboratory cultures of *Operculina ammonoides*. Given that previous work has suggested that large changes in $[K^+]_{sw}$ have not occurred (Horita et al., 2002), this may be an additional tool for understanding past changes in $[Ca^{2+}]_{sw}$. We show that a power relationship best describes seawater-shell K/Ca, implying a variable apparent distribution coefficient. Indeed, the slope of the K/Ca - K/Ca_{sw} relationship is very shallow, indicating another major control on K incorporation into foraminifera. We suggest that this shallow relationship is, at least in part, the result of a kinetic growth rate effect on K incorporation in *O. ammonoides* cultured at elevated $[Ca^{2+}]_{sw}$, although further work will be required to conclusively rule out other possibilities such as K transport into the calcifying fluid. The mechanistic basis of this could be that in the laboratory culture experiment reported here, $[Ca^{2+}]_{sw}$ was varied in isolation, which means that $[Ca^{2+}]_{sw}$ and the saturation state of seawater (Ω_c) covaried. Because Ω_c is one of the dominant controls on surface area-normalised precipitation rate, we propose that a crystal growth rate effect may explain the shallow seawater-shell K/Ca relationship, driving K/Ca to higher ratios at elevated $[Ca^{2+}]_{sw}$. We corrected for this using a relationship between Ω_c and K/Ca derived from a second culture experiment in which *O. ammonoides* was grown at different seawater pH values, which has the effect of increasing the slope of the seawater-shell K/Ca relationship. Given that surface ocean Ω_c has likely not varied to a large degree over the Cenozoic (e.g. Tyrrell and Zeebe, 2004; Ridgwell and Zeebe, 2005), we argue that this corrected relationship should be applied in the geologic past, and that the slope of this curve is sufficiently steep to make K/Ca a potentially useful tool for unravelling past changes in seawater major ion chemistry.

Given that other seawater parameters show no resolvable influence on K incorporation into foraminifera, and if the notion that the seawater [K^+] has remained constant through the Phanerozoic Eon is correct (Horita et al., 2002), this calibration could therefore be used as a tool to reconstruct $[Ca^{2+}]_{sw.}$ Ultimately, combining Na/Ca (Hauzer et al., 2018; Zhou et al., 2021) and K/Ca data from the same specimens may be a potential means of further improving the accuracy of reconstructions of the history of seawater [Ca^{2+}] variability, or could be used to determine whether seawater [Na^+] and [K^+] have indeed remained within narrow bounds. Because *O. ammonoides* are a close relative of the nummulitid foraminifera which were abundant during the Paleogene (Hallock, 1985; Holzmann et al., 2003), this group, and the calibration presented here, may represent a good target for the reconstruction of Cenozoic seawater chemistry, opening up new possibilities in terms of understanding the processes that govern the seawater Ca cycle.

Supplementary materials to accompany 'Controls on potassium incorporation in foraminifera and other marine calcifying organisms'

Romi Nambiar, Hagar Hauzer, William R. Gray, Michael Henehan, Laura Cotton, Jonathan Erez, Yair Rosenthal, Willem Renema, Wolfgang Müller, David Evans

1. LA-SF-ICPMS measurement of K/Ca within the context of the ArH^+ interference

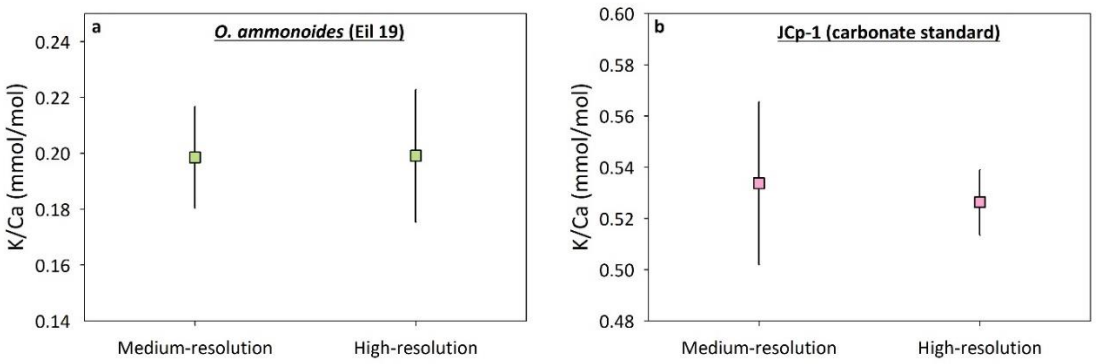

Fig. S10. Comparing the K/Ca values of a) *O. ammonoides* and b) JCp-1 measured in medium resolution (MR) and high resolution (HR) using LA-SF-ICPMS. The error bars are 1SD.

The K^+ measurement by ICPMS is complicated by a larger ArH^+ interference, as discussed in the Methods section of the main text. The ArH^+ interference is not entirely separated from K^+ in medium resolution using the Element XR ($m/\Delta m$ = ~4000), which is achievable in high resolution. However, given the sensitivity sacrifice that comes with high-resolution measurements, we assessed whether the complete separation of this interference is beneficial. We observed that medium-resolution is capable of sufficiently minimising the effect of $^{38}Ar^1H^+$ interference on the $^{39}K^+$ peak, with no resolvable difference in accuracy or precision between the different resolutions. The K/Ca values in *O. ammonoides* measured

using LA-SF-ICPMS in medium and high-resolution were 0.199±0.018 (1SD) and 0.199±0.024 (1SD), respectively. Similarly, the average values of the JCp-1 carbonate standard measured in MR and HR resolution were within the uncertainty of each other (Fig S1).

2. Co-incorporation of Na and K in *O. ammonoides*

In the experiment with varying $[Ca^{2+}]_{sw}$, both Na/Ca and K/Ca in *O. ammonoides* demonstrated a significant power relationship with the seawater El/Ca, possibly suggesting a common controlling factor. We explored the K/Ca and Na/Ca data of individual spot analysis carried out in the *O. ammonoides* collected from the modern seawater and culture experiment to assess the relationship between the intra-test variability of the Na/Ca and K/Ca (Fig. S2). Comparing the individual spot data of K/Ca and Na/Ca in *O. ammonoides*, we found a weak positive relationship measured at the non-porous knob region as well as newly formed chambers in laboratory culture experiments at different $[Ca^{2+}]_{sw}$ (measured at the marginal cord). However, Na/Ca and K/Ca measurements of the porous marginal cord of modern field samples showed a significant positive relationship (R^2 = 0.55; p < 0.01). While the positive relationship between Na/Ca and K/Ca in *O. ammonoides* measured at the marginal cord and the knob implies a common driving process (e.g., growth rate, seawater $[Ca^{2+}]_{sw}$), we cannot rule out the possibility of additional control on their individual incorporation.

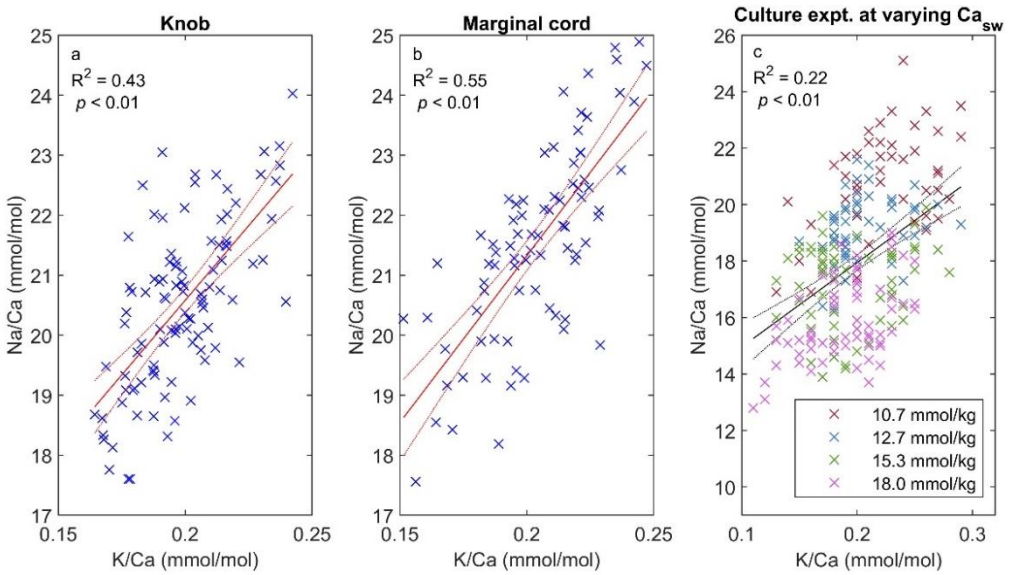

Fig. S11 The relationship between Na/Ca and K/Ca in modern *O. ammonoides* measured at a) the knob, b) the marginal cord, and c) newly grown chambers from a laboratory culture experiment at different $[Ca^{2+}]_{sw}$.

3. Carbonate chemistry culture experiment data treatment.

The experiment of varying pH at constant DIC was investigated to estimate the effect of saturation state (Ω_c) on the K incorporation into *O. ammonoides* (see main text Sec. 3.3). In this experiment, the carbonate chemistry of both the culture jars as well as the seawater reservoirs used to replace the water in the cultures was monitored throughout the course of the experiment (Hauzer, 2022) (summarized in Tab. S6). This yields three sets of carbonate system values to which the shell geochemistry results can be compared: the reservoir values, the average of the culture jars immediately before the water was exchanged, or the average of the cultures and reservoirs. The best choice of parameters is not immediately clear, for example, because the evolution of the carbonate chemistry in the culture jars as a function of time is unlikely to be linear. Here, we used the average of the culture jars and reservoir as this may represent the closest to the average conditions that the foraminifera experienced.

While we note that other decisions may be justifiable, our choice of carbonate chemistry measurements has little impact on the slope of the relationship between K/Ca and the carbonate system that we determine (Fig. S3).

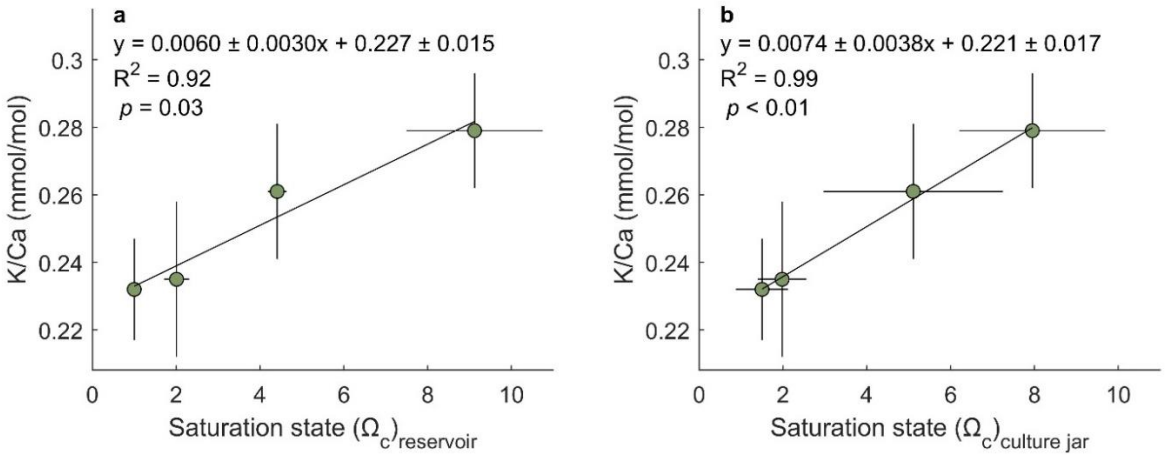

Fig. S3 The relationship between K/Ca in cultured *O. ammonoides* and saturation state (Ω_c) of a) reservoir seawater and b) average value before the seawater in the culture jar was exchanged.

In order to identify the newly grown chamber during the culture experiment, the culture seawater medium was spiked with 74nM ^{135}Ba. Chambers grown under culture conditions were subsequently identified as being those with a non-natural ^{135}Ba/^{138}Ba. In general, and in the seawater [Ca^{2+}] experiment, we only considered laser ablation analyses with ^{135}Ba/^{138}Ba within an uncertainty of the culture seawater ratio. However, in the case of the variable pH experiment, we alternatively used all analyses that were characterized by ^{135}Ba/^{138}Ba higher than natural because only a small number of chambers in the lowest pH experiment had fully elevated ^{135}Ba/^{138}Ba, which likely results from the difficulty in the growth of foraminifera at the lower saturation state of this experimental seawater (Fig. S4). Interrogation of the individual laser ablation profiles demonstrated that calcite with intermediate ^{135}Ba/^{138}Ba is best explicable via chambers with an intermediate ratio rather than analytical mixing between pre-culture material with that grown in culture. These

intermediate ratios are thus best explained by the presence of an internal Ca^{2+} pool, such that all chambers with non-natural $^{135}Ba/^{138}Ba$ must have been formed in culture. However, we caveat our results with the possibility that the characteristics of the internal pool, and thus, to a possible extent, the characteristics of the calcification site were influenced by pre-culture conditions, although excluding chambers with intermediate $^{135}Ba/^{138}Ba$ does not substantially change the slope of the relationship between shell K/Ca and Ω_c (Fig. S3). Further work will be required to determine the precise relationship between K/Ca and the carbonate chemistry of seawater in *O. ammonoides*. Not least because despite including all chambers with 135Ba/138Ba above natural in order to determine the mean K/Ca of each experiment with greater certainty, the confidence intervals on these measured shell K/Ca values remain relatively large.

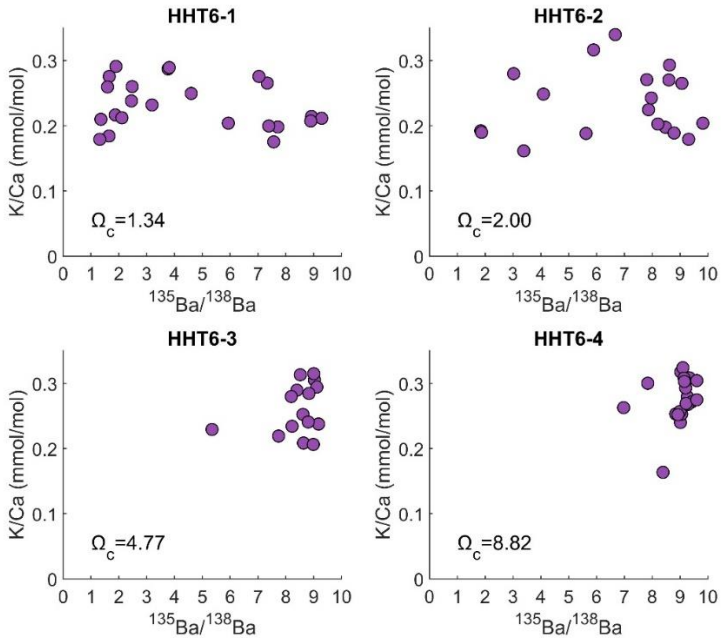

Fig. S4 K/Ca and $^{135}Ba/^{138}Ba$ values measured in *O. ammonoides* grown by varying the pH. Each circle represents individual spot measurements.

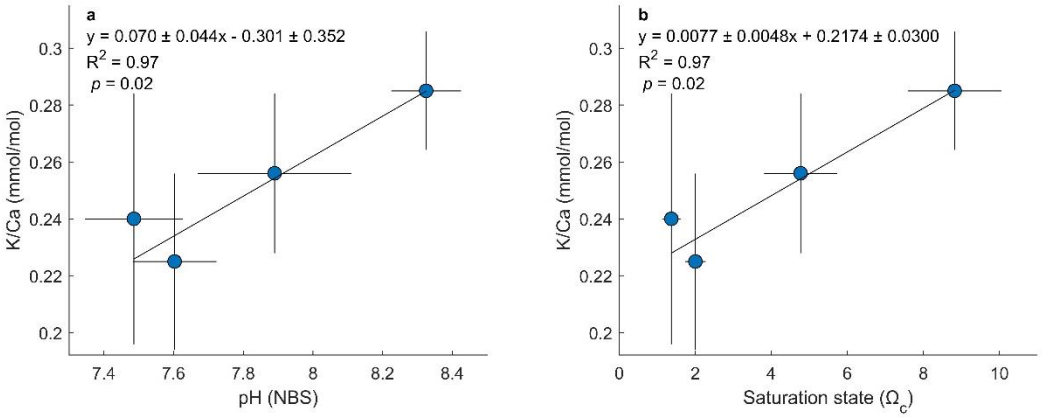

Fig. S5. The relationship between K/Ca in cultured *O. ammonoides* and a) pH and b) saturation state (Ω_c). The K/Ca values corresponding to $^{135}Ba/^{138}Ba$ ratio within an uncertainty of the culture seawater ratio are shown. Considering only fully elevated $^{135}Ba/^{138}Ba$ results in higher error in the K/Ca values but does not substantially change the slope. Error bars are 2SE.

4. K/Ca correction based on El/Ca-Ω_c relationship

We observed the K/Ca_{LBF} values are tightly correlated with K/Ca_{sw}, albeit with a very shallow slope (Fig. 5). In this experiment, since Ω_c and $[Ca^{2+}]_{sw}$ covaried, we used the relationship between the K/Ca- Ω_c (Fig. 6) to correct for the effect of growth rate on the K/Ca_{LBF}-K/Ca_{sw} relationship (Fig. 7). Specifically, we first use the slope of the El/Ca-Ω_c relationship (Fig. 6) to subtract out the Ω_c-driven component of the seawater-shell El/Ca relationship. In order to do so, Ω_c of the experimental seawater at each $[Ca^{2+}]_{sw,}$ i.e., 10.7, 12.7, 15.3, and 18.0 mmol $kg^{-1,}$ was calculated relative to that of the control experiment (10.7 mmol kg^{-1}) to give $\Delta\Omega_c$. The K/Ca was then corrected by quantifying the change in K/Ca attributable to $\Delta\Omega_c$ using the culture K/Ca-Ω_c relationship (Fig. 6). The corrected shell K/Ca data are related to K/Ca_{sw} by the following power relationship (Fig. 7):

$$K/Ca_{LBF} = 0.212 \pm 0.003 \times (K/Ca)_{sw}^{0.53 \pm 0.05} \quad \text{(Eq. S1)}$$

Coefficient uncertainties represent 2 x standard error (2SE). We stress that the uncertainty in the relationship between K/Ca and Ω_c is relatively large due to the difficulty in making the measurements combined with the limited growth of the foraminifera at low Ω_c (Fig. S4) such that further work is required to improve the correction applied here to generate Eq. S1.

5. Formulating a theoretical relationship to account for the effect of variable $[Ca^{2+}]_{sw}$ on crystal growth rate and thus El/Ca_{LBF} based on inorganic precipitation experiments.

In order to explore the relationship between growth rate and trace element incorporation into calcite, we used the process-based growth rate model of Wolthers et al., (2012) to provide the necessary information regarding how calcite growth rates are likely to change in response to a change in the Ca^{2+} concentration of seawater, and couple these constraints with published empirical relationships between alkali metal incorporation into calcite as a function of surface area normalized growth rate. Specifically, we use the empirical growth rate equation for growth in artificial seawater solutions, which also takes ionic strength into account (Eq. 35 of Wolthers et al., 2012):

$$R_{p\,sw} = I^{0.36}\, pH^{-10.99}\, r_{aq}^{0.71}\, (S-2)^2 \qquad \text{(Eq. S2)}$$

where R = growth rate (ms^{-1}); I = Ionic strength (M); r = the calcium/carbonate activity ratio $\{Ca^{2+}\}/\{CO_3^{2-}\}$ and S =saturation ratio (the square root of Ω). From this, we estimated the degree to which the growth rate varies as $[Ca^{2+}]_{sw}$ is changed in isolation. Since we don't know the degree to which an organism changes the carbonate chemistry in response to different $[Ca^{2+}]_{sw}$, we calculated r and S values of the experimental seawaters to determine the relative change in S values for each $[Ca^{2+}]_{sw}$ with respect to experimental seawater to

calculate the change in growth rate. We stress that the results of this exercise are unlikely to be accurate, for example, because calcification site and ambient seawater Ω are probably not linearly related. The aim is rather to explore which direction and to broadly what extent we might expect the growth rate to be an important control on the incorporation of alkali metals in foraminiferal calcite.

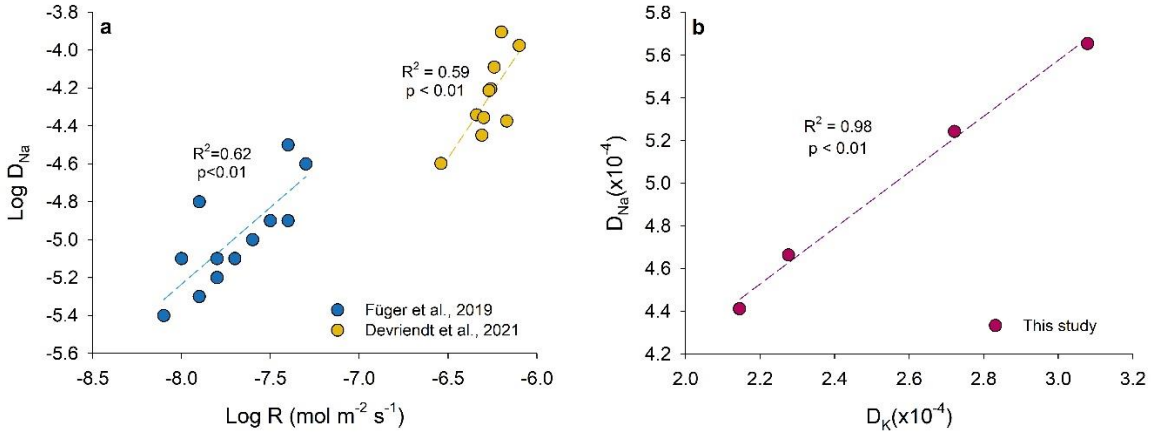

Fig. S6. a) Apparent partition coefficient of Na plotted as a function of calcite surface area-normalised growth rate. b) Relationship between D_{Na} and D_K in *O. ammonoides*.

To explore the possible relationship between growth rate and $D_{K/Na}$ in foraminifera, the growth rate estimates from Wolthers *et al.* (2012) must be coupled with empirical data on the relationship between surface area normalized growth rates and the distribution coefficients of the alkali metals. We used the relationship between D_{Na} and growth rate from inorganic precipitation experiments by Füger et al., (2019) and Devriendt et al., (2021). The experiment conducted by Füger et al., (2019) was carried out over a range of pH values (6.29-9.59). To avoid any potential additional influence of pH, we considered the results of experiments only within the pH range of 8.20-8.35. The experiment by Devriendt et al., 2021 conducted at pH 8.3 was used for comparison (Fig. S6a). The slopes of the relationship

between D_{Na} and R from these two studies are 0.81 (Füger et al., 2019) and 1.40 (Devriendt et al., 2021) (Fig. S6a). Coupling this relationship between rate and D_{Na} from these inorganic experiments with the calculated change in growth rate in the seawater [Ca^{2+}] culture experiment described above enables to provide a broad estimation of how much of the change in D_K is driven by rate, and how much is driven by K/Ca_{sw}. In order to do so, we extrapolate the results of the inorganic experimental work on D_{Na} incorporation (Fig. S6a) to D_K, because there are to our knowledge no high-quality experimental studies on K incorporation into inorganic calcite with which to calculate this directly. The close correspondence between D_{Na} and D_K in the foraminifera studied here means that this may be reasonable (Fig S6b), although this extrapolation is of course another reason that the details of these exploratory results should be treated with caution. The results of this exercise are shown in Fig. S7.

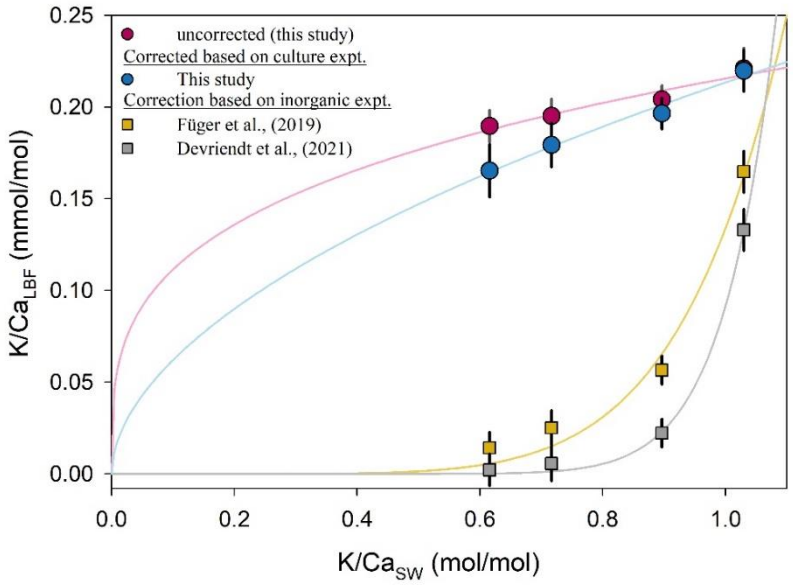

Fig. S7. Corrected K/Ca-K/Ca_{sw} relationship based on culture and inorganic precipitation experiments.

Correcting the foraminifera K/Ca data for rate based on the inorganic experiments as decsribed above results in a correction that is in the same direction as that which we ultimately apply based on the relationship between K/Ca-Ω outlined in the main text. However, the correction dervied from the inorganic calcite data is almost certainly too large to be realistic, implying that almost all K incorporation into foraminifera can be explained by an increase in growth rate at below normal Ω. As such, while the inorganic datasets highlight that growth rate is likely to be an important control on the incorporation of the alkali metals, which we also argue for on the basis of our foraminiferal results in the main text, the relationship between rate and D_{Na} in the inorganic experimental data appears to be much too steep to be applicable to the foraminifera. Possible reasons for this discrepancy include i) a calcification site environment that is buffered against external carbonate chemistry changes, biasing our estimates of foraminiferal calcite growth rates to an artificially wide range, or ii) that some other process acts to offset the strong control that growth rate has on alkali metal incorporation into calcite.

Table S1 Laser ablation and ICPMS parameters for the analyses conducted here.

Laser Ablation System (RESOlution M-50 + S155 cell):	
Sampling mode	Spot (depth profiling) analysis
Wavelength	193 nm
Fluence	~6.3 J cm^{-2}
Repetition rate (Hz)	3 Hz
He flow	300 - 400 mL min^{-1}
N_2 flow	3.5 - 4.0 mL min^{-1}
Beam diameter	50 µm
ICP-MS (ThermoFisher Scientific Element XR)	
Torch RF power (W)	1330 - 1380 W
Sample cone	Ni Jet cone
Skimmer cone	Ni H cone
Sample gas flow	0.86 - 1.00 L min^{-1}
Auxiliary gas flow	0.65 - 0.90 L min^{-1}
Sensitivity	4-7 Million counts of ^{238}U (NIST SRM 612, 60 um, 6 Hz)
ThO^+/Th^+	0.65 - 0.90 %
U/Th	0.94 - 0.97

Table S2 Laser-ablation accuracy and precision based on analyses of the MPI-DING komatiite glasses GOR128 and carbonate standard JCp-1 calibrated with NIST 610. All values are in mmol/mol.

GOR128-G (n=49)	**Na/Ca**	**Mg/Ca**	**Al/Ca**	**K/Ca**	**Mn/Ca**	**Sr/Ca**
Average	184.7	5690.2	1818.4	7.58	22.8	0.31
2SE	1.2	22.1	6.7	0.06	0.09	0.002
Accuracy (%)	10.9	-1.9	4.1	10.3	2.2	2.3
RSD (2σ) (%)	4.4	2.7	2.6	5.4	2.9	4.3
JCP-1 (n=41)	**Na/Ca**	**Mg/Ca**	**Al/Ca**	**K/Ca**	**Mn/Ca**	**Sr/Ca**
Average	20	4.1	1.9	0.53	n.d	8.74
2SE	0.6	0.06	0.06	0.01	-	0.08
Accuracy (%)	1.3	-3	4.3	8.6	-	0.4
RSD (2σ) (%)	9.7	4.7	9.5	6.3	-	3

Table S3 High-resolution LA-SF-ICPMS El/Ca results for modern planktic foraminifera (Low Mg calcite). All values are in mmol/mol.

	Planktic foraminifera (*G. ruber*)							
Sample type	**Sample ID**	**K/Ca**	**1SD**	**2 SE**	**Al/Ca**	**2 SE**	**Mn/Ca**	**2 SE**
sediment trap samples	NBBT-09 No.5	0.13	0.03	0.03	0.04	0.0250	0.11	0.0320
	CBBT-06 No.9	0.24	0.08	0.05	0.01	0.0100	0.042	0.0100
	SBBT-09 No.4	0.29	0.01	0.01	0.01	0.0030	0.005	0.0020
	SBBT-09 No.2	0.20	0.05	0.03	0.00	0.0010	0.004	0.0010
	AS02-M5 No.4	0.18	0.02	0.02	0.01	0.0043	0.002	0.0005
	AS02-M5 No.12	0.26	0.06	0.04	0.00	0.0019	0.003	0.0009
core-top samples	MC423	0.21	0.04	0.03	0.03	-	0.011	-
	MC420	0.24	0.04	0.03	0.13	-	0.063	-
	MC497	0.28	0.16	0.10	0.02	-	0.022	-
	G4	0.26	0.01	0.01	0.04	-	0.079	-

Table S4 LA-SF-ICPMS El/Ca results for modern larger benthic foraminifera (High Mg calcite). All values are in mmol/mol.

Sample ID	**Larger benthic foraminifera [all samples are *O. ammonoides* except BBx 49A (Operculina sp.)]**												
	Na/Ca	**2SE**	**Mg/Ca**	**2SE**	**Al/Ca**	**2SE**	**K/Ca**	**1SD**	**2SE**	**Mn/Ca**	**2SE**	**Sr/Ca**	**2SE**
Pd 2805	18.9	0.3	148.7	2.7	0.19	0.09	0.17	0.02	0.01	0.09	0.03	2.48	0.03
KKE 30	20.0	0.4	156.9	2.6	0.07	0.04	0.20	0.01	0.01	0.03	0.01	2.50	0.04
SER 33	17.6	0.6	153.9	2.4	0.01	0.01	0.18	0.03	0.02	0.04	0.01	2.45	0.03
SS 07G14	22.1	0.8	141.4	1.4	0.03	0.01	0.31	0.03	0.01	0.00	0.00	2.54	0.04
Eil 19	20.5	0.3	139.0	1.3	0.04	0.01	0.20	0.02	0.00	0.04	0.40	2.50	0.02
BBx 49A	19.6	0.5	151.3	1.4	0.03	0.01	0.29	0.08	0.03	0.02	0.00	2.38	0.03
Pd 2801	17.4	0.9	151.7	3.2	0.19	0.05	0.15	0.02	0.01	0.14	0.05	2.41	0.08

Table S5 Average El/Ca values in O. ammonoides grown at varying $[Ca^{2+}]_{sw}$.

Seawater (Hauzer et. al., 2018)			*O. ammonoides* shell (mmol/mol)*						Growth-rate corrected values (mmol/mol); this study	
Ca_{sw}	K/Ca_{sw}	Na/Ca_{sw}	Hauzer et. al., 2018		This study					
mmol/kg	mol/mol	mol/mol	Na/Ca	2 SE	K/Ca	2 SE	Na/Ca	2 SE	K/Ca	2 SE
10.7	1.03	47	22.4	1.2	0.220	0.011	20.7	0.5	0.218	0.011
12.7	0.9	40.9	19.6	0.6	0.204	0.008	19.1	0.3	0.196	0.009
15.3	0.72	32.7	18.2	0.2	0.196	0.010	17.1	0.4	0.180	0.012
18	0.62	28.1	16.5	0.5	0.190	0.009	15.9	0.4	0.165	0.015

*The El/Ca were calibrated against NIST SRM612 in Hauzer et. al., 2018, whereas in this study the El/Ca values were calibrated against NIST SRM610.

Table S6 K/Ca values of foraminifera grown at varying pH (constant DIC).

average of reservoir seawater value (Hauger, 2022)				average of culture seawater (Hauger, 2022)				average of reservoir and culture seawater (Hauger, 2022)				K/Ca (mmol/mol) This study	2SE
Ω_{Ca}	2SE	pH (NBS)	2SE	Ω_{Ca}	2SE	pH (NBS)	2SE	Ω_{Ca}	2SE	pH (NBS)	2SE		
1.00	0.16	7.359	0.072	1.50	0.62	7.563	0.172	1.3	0.40	7.461	0.122	0.232	0.015
2.01	0.30	7.654	0.070	1.98	0.58	7.670	0.124	2.0	0.44	7.662	0.098	0.235	0.023
4.41	0.22	8.021	0.028	5.11	2.14	8.101	0.242	4.8	1.18	8.061	0.136	0.261	0.020
9.12	1.62	8.341	0.118	7.95	1.74	8.354	0.106	8.5	1.68	8.348	0.112	0.279	0.017

Authors contribution

RN: Conceptualization; methodology; formal analysis; investigation; writing-original draft; writing - review & editing. **HH and JE:** Conceptualization; methodology; investigation; resources; writing - review & editing. **WRG, MJH, LC and WR:** resources; writing - review & editing. **YR:** conceptualization; writing - review & editing. **WM and DE:** conceptualization; methodology; resources; writing - review & editing.

Acknowledgments

This work is part of the VeWA consortium funded by the Hessen State Ministry for Higher Education, Research, and the Arts through the LOEWE program. MJH gratefully acknowledges the provision of sample materials by Michal Kucera and Helen Bostock. The foraminifera culture work of HH and DE was carried out in the laboratory of J.Erez and funded by ISF grant # 1886/20. FIERCE is financially supported by the Wilhelm and Else Heraeus Foundation and by the Deutsche Forschungsgemeinschaft (DFG: INST 161/921-1 FUGG, INST 161/923-1 FUGG and INST 161/1073-1 FUGG), which is gratefully acknowledged. This is FIERCE contribution No. 126. We gratefully thank the associate editor Tom Marchitto, as well as Sambuddha Misra and an anonymous reviewer for their thoughtful consideration of this work.

References

Allen K. A. and Hönisch B. (2012) The planktic foraminiferal B/Ca proxy for seawater carbonate chemistry: A critical evaluation. *Earth and Planetary Science Letters* 345–348, 203–211.

Allen K. A., Hönisch B., Eggins S. M., Haynes L. L., Rosenthal Y. and Yu J. (2016) Trace element proxies for surface ocean conditions: A synthesis of culture calibrations with planktic foraminifera. *Geochimica et Cosmochimica Acta* 193, 197–221.

Anagnostou E., John E. H., Edgar K. M., Foster G. L., Ridgwell A., Inglis G. N., Pancost R. D., Lunt D. J. and Pearson P. N. (2016) Changing atmospheric CO2 concentration was the primary driver of early Cenozoic climate. *Nature* 533, 380–384.

Anand P., Elderfield H. and Conte M. H. (2003) Calibration of Mg/Ca thermometry in planktonic foraminifera from a sediment trap time series. *Paleoceanography* 18.

Bell T., Iguchi A., Suzuki A., Seki A. and Yokoyama Y. (2018) Testing possible relationships between Acropora digitifera genes, seawater chemistry and skeletal elements. *Geochemical Journal* 52, 263–272.

Bentov S., Brownlee C. and Erez J. (2009) The role of seawater endocytosis in the biomineralization process in calcareous foraminifera. *Proceedings of the National Academy of Sciences of the United States of America* 106, 21500–21504.

Bertlich J., Nürnberg D., Hathorne E. C., De Nooijer L. J., Mezger E. M., Kienast M., Nordhausen S., Reichart G. J., Schönfeld J. and Bijma J. (2018) Salinity control on Na incorporation into calcite tests of the planktonic foraminifera Trilobatus sacculifer - Evidence from culture experiments and surface sediments. *Biogeosciences* 15, 5991–6018.

Blackmon P. D. and Todd R. (1959) Mineralogy of some foraminifera as related to their classification and ecology. *Journal of Paleontology*, 1–15.

Bloch S. and Bischoff J. L. (1979) The effect of low-temperature alteration of basalt on the oceanic budget of potassium. *Geology* 7, 193–196.

Bonnin E. A., Zhu Z., Fehrenbacher J. S., Russell A. D., Hönisch B., Spero H. J. and Gagnon A. C. (2019) Submicron sodium banding in cultured planktic foraminifera shells. *Geochimica et Cosmochimica Acta* 253, 127–141.

Boyle E. A. (1981) Cadmium, zinc, copper, and barium in foraminifera tests. *Earth and Planetary Science Letters* 53, 11–35.

Branson O., Bonnin E. A., Perea D. E., Spero H. J., Zhu Z., Winters M., Hönisch B., Russell A. D., Fehrenbacher J. S. and Gagnon A. C. (2016) Nanometer-scale chemistry of a calcitebiomineralization template: Implications Forskeletal composition and nucleation. *Proceedings of the National Academy of Sciences of the United States of America* 113, 12934–12939.

Broecker W. S. and Peng T. H. (1982) Tracers in the Sea, Lamont-Doherty geological observatory. *Palisades, New York*.

Brown R. E., Anderson L. D., Thomas E. and Zachos J. C. (2011) A core-top calibration of B/Ca in the benthic foraminifers Nuttallides umbonifera and Oridorsalis umbonatus: A proxy for Cenozoic bottom water carbonate saturation. *Earth and Planetary Science Letters* 310, 360–368.

Carpenter W. B. (1862) *Introduction to the Study of the Foraminifera: By William B. Carpenter, Assisted by William K. Parker and T. Rupert Jones. Publ. for the Ray Society*., Hardwicke.

Coggon R. M., Teagle D. A. H., Smith-Duque C. E., Alt J. C. and Cooper M. J. (2010) Reconstructing Past Seawater Mg/Ca. *Science* 327, 1114–1117.

Coogan L. A. and Dosso S. E. (2015) Alteration of ocean crust provides a strong temperature dependent feedback on the geological carbon cycle and is a primary driver of the Sr-isotopic composition of seawater. *Earth and Planetary Science Letters* 415, 38–46.

Cotton L. J., Evans D. and Beavington-penney S. J. (2020) The High-Magnesium Calcite Origin of

Nummulitid Foraminifera and Implications for the Identification of Calcite Diagenesis. *Palaios* 35, 421–431.

Delaney M. L., Bé A. W. H. and Boyle E. A. (1985) Li, Sr, Mg, and Na in foraminiferal calcite shells from laboratory culture, sediment traps, and sediment cores. *Geochimica et Cosmochimica Acta* 49, 1327–1341.

Delaney M. L., Popp B. N., Lepzelter C. G. and Anderson T. F. (1989) Lithium-to-calcium ratios in Modern, Cenozoic, and Paleozoic articulate brachiopod shells. *Paleoceanography* 4, 681–691.

Devriendt L. S., Mezger E. M., Olsen E. K., Watkins J. M., Kaczmarek K., Nehrke G., de Nooijer L. J. and Reichart G.-J. (2021) Sodium incorporation into inorganic CaCO3 and implications for biogenic carbonates. *Geochimica et Cosmochimica Acta* 314, 294–312.

Dickson A. G., Wesolowski D. J., Palmer D. A. and Mesmer R. E. (1990) Dissociation constant of bisulfate ion in aqueous sodium chloride solutions to 250. degree. C. *Journal of Physical Chemistry* 94, 7978–7985.

Dickson J. A. D. (2002) Fossil echinoderms as monitor of the Mg/Ca ratio of Phanerozoic oceans. *Science* 298, 1222–1224.

Van Dijk I., Nooijer De L. J. and Reichart G. J. (2017) Trends in element incorporation in hyaline and porcelaneous foraminifera as a function of pCO2. *Biogeosciences* 14, 497–510.

van Dijk I., de Nooijer L. J., Wolthers M. and Reichart G.-J. (2017) Impacts of pH and [CO32-] on the incorporation of Zn in foraminiferal calcite. *Geochimica et Cosmochimica Acta* 197, 263–277.

Dodd W., Pitman M. and West K. (1966) Sodium and Potassium Transport in the Marine Alga Chaetomorpha Darwinii. *Australian Journal of Biological Sciences* 19, 341.

Dunlea A. G., Murray R. W., Santiago Ramos D. P. and Higgins J. A. (2017) Cenozoic global cooling and increased seawater Mg/Ca via reduced reverse weathering. *Nature Communications* 8, 1–7.

Elderfield H., Bertram C. J. and Erez J. (1996) A biomineralization model for the incorporation of trace elements into foraminiferal calcium carbonate. *Earth and Planetary Science Letters* 142, 409–423.

Eppley R. W. (1958) Sodium exclusion and potassium retention by the red marine alga, Porphyra perforata. *The Journal of General Physiology* 41, 901.

Erez J. (2003) The source of ions for biomineralization in foraminifera and their implications for paleoceanographic proxies. *Reviews in mineralogy and geochemistry* 54, 115–149.

Evans D., Badger M. P. S., Foster G. L., Henehan M. J., Lear C. H. and Zachos J. C. (2018a) No substantial long-term bias in the Cenozoic benthic foraminifera oxygen-isotope record. *Nature Communications* 9, 17–19.

Evans D., Erez J., Oron S. and Müller W. (2015) Mg/Ca-temperature and seawater-test chemistry relationships in the shallow-dwelling large benthic foraminifera Operculina ammonoides. *Geochimica et Cosmochimica Acta* 148, 325–342.

Evans D. and Müller W. (2018) Automated Extraction of a Five-Year LA-ICP-MS Trace Element Data Set of Ten Common Glass and Carbonate Reference Materials: Long-Term Data Quality, Optimisation and Laser Cell Homogeneity. *Geostandards and Geoanalytical Research* 42, 159–188.

Evans D. and Müller W. (2012) Deep time foraminifera Mg/Ca paleothermometry: Nonlinear correction for secular change in seawater Mg/Ca. *Paleoceanography* 27.

Evans D. and Müller W. (2013) LA-ICPMS elemental imaging of complex discontinuous carbonates: An example using large benthic foraminifera. *Journal of Analytical Atomic Spectrometry* 28, 1039–1044.

Evans D., Müller W. and Erez J. (2018b) Assessing foraminifera biomineralisation models through trace element data of cultures under variable seawater chemistry. *Geochimica et Cosmochimica Acta* 236, 198–217.

Evans D., Müller W., Oron S. and Renema W. (2013) Eocene seasonality and seawater alkaline earth reconstruction using shallow-dwelling large benthic foraminifera. *Earth and Planetary Science Letters* 381, 104–115.

Evans D., Wade B. S., Henehan M., Erez J. and Müller W. (2016) Revisiting carbonate chemistry controls on planktic foraminifera Mg / Ca: Implications for sea surface temperature and hydrology shifts over the Paleocene-Eocene Thermal Maximum and Eocene-Oligocene transition. *Climate of the Past* 12, 819–835.

Füger A., Konrad F., Leis A., Dietzel M. and Mavromatis V. (2019) Effect of growth rate and pH on lithium incorporation in calcite. *Geochimica et Cosmochimica Acta* 248, 14–24.

Garbe-Schönberg D. and Müller S. (2014) Nano-particulate pressed powder tablets for LA-ICP-MS. *Journal of Analytical Atomic Spectrometry* 29, 990–1000.

Geerken E., de Nooijer L. J., Roepert A., Polerecky L., King H. E. and Reichart G. J. (2019) Element banding and organic linings within chamber walls of two benthic foraminifera. *Scientific Reports* 9, 1–15.

Gothmann A. M., Stolarski J., Adkins J. F., Schoene B., Dennis K. J., Schrag D. P., Mazur M. and Bender M. L. (2015) Fossil corals as an archive of secular variations in seawater chemistry since the Mesozoic. *Geochimica et Cosmochimica Acta* 160, 188–208.

Gouaux E. and MacKinnon R. (2005) Principles of selective ion transport in channels and pumps. *Science* 310, 1461–1465.

Gray W. R. and Evans D. (2019) Nonthermal Influences on Mg/Ca in Planktonic Foraminifera: A Review of Culture Studies and Application to the Last Glacial Maximum. *Paleoceanography and Paleoclimatology* 34, 306–315.

Gray W. R., Weldeab S., Lea D. W., Rosenthal Y., Gruber N., Donner B. and Fischer G. (2018) The effects of temperature, salinity, and the carbonate system on Mg/Ca in Globigerinoides ruber (white): A global sediment trap calibration. *Earth and Planetary Science Letters* 482, 607–620.

Gregor L. and Gruber N. (2021) OceanSODA-ETHZ: A global gridded data set of the surface ocean carbonate system for seasonal to decadal studies of ocean acidification. *Earth System Science Data* 13, 777–808.

Hallock P. (1985) Why are larger foraminifera large? *Paleobiology* 11, 195–208.

Hardie L. A. (1996) Secular variation in seawater chemistry: An explanation for the coupled secular variation in the mineralogies of marine limestones and potash evaporites over the past 600 m.y. *Geology* 24, 279–283.

Hasiuk F. J. and Lohmann K. C. (2010) Application of calcite Mg partitioning functions to the reconstruction of paleocean Mg/Ca. *Geochimica et Cosmochimica Acta* 74, 6751–6763.

Hauzer H. (2022) Development of new foraminiferal proxies for paleochemistry of the oceans. PhD thesis. *the Hebrew University of Jerusalem*.

Hauzer H., Evans D., Müller W., Rosenthal Y. and Erez J. (2018) Calibration of Na partitioning in the calcitic foraminifer Operculina ammonoides under variable Ca concentration: Toward reconstructing past seawater composition. *Earth and Planetary Science Letters* 497, 80–91.

Hauzer H., Evans D., Müller W., Rosenthal Y. and Erez J. (2021) Salinity Effect on Trace Element Incorporation in Cultured Shells of the Large Benthic Foraminifer Operculina ammonoides. *Paleoceanography and Paleoclimatology* 36, 1–19.

Heinrich C. A., Pettke T., Halter W. E., Aigner-Torres M., Audétat A., Günther D., Hattendorf B., Bleiner D., Guillong M. and Horn I. (2003) Quantitative multi-element analysis of minerals, fluid and melt inclusions by laser-ablation inductively-coupled-plasma mass-spectrometry. *Geochimica et Cosmochimica Acta* 67, 3473–3497.

Henehan M. J., Foster G. L., Rae J. W. B., Prentice K. C., Erez J., Bostock H. C., Marshall B. J. and Wilson P. A. (2015) Evaluating the utility of B/Ca ratios in planktic foraminifera as a proxy for the carbonate system: A case study of Globigerinoides ruber. *Geochemistry, Geophysics, Geosystems* 16, 1052–1069.

Van Heuven S., Pierrot D., Rae J. W. B., Lewis E. and Wallace D. W. R. (2011) MATLAB program developed for CO2 system calculations. *ORNL/CDIAC-105b* 530.

Higgins J. A. and Schrag D. P. (2015) The Mg isotopic composition of Cenozoic seawater - evidence for a link between Mg-clays, seawater Mg/Ca, and climate. *Earth and Planetary Science Letters* 416, 73–81.

Hohenegger J. (2011) *Large foraminifera: greenhouse constructions and gardeners in the oceanic microcosm*., Kagoshima University Museum.

Holzmann M., Hohenegger J. and Pawlowski jan (2003) Molecular data reveal parallel evolution in nummulitid foraminifera. *The Journal of Foraminiferal Research* 33, 277–284.

Horita J., Zimmermann H. and Holland H. D. (2002) Chemical evolution of seawater during the Phanerozoic: Implications from the record of marine evaporites. *Geochimica et Cosmochimica Acta* 66, 3733–3756.

Le Houedec S., Erez J. and Rosenthal Y. (2021) Testing the Influence of Changing Seawater Ca Concentration on Elements/Ca Ratios in Planktic Foraminifera: A Culture Experiment. *Geochemistry, Geophysics, Geosystems* 22.

Ishikawa M. and Ichikuni M. (1984) Uptake of sodium and potassium by calcite. *Chemical geology* 42, 137–146.

Isson T. T. and Planavsky N. J. (2018) Reverse weathering as a long-term stabilizer of marine pH and planetary climate. *Nature* 560, 471–475.

Jochum K. P., Garbe-Schönberg D., Veter M., Stoll B., Weis U., Weber M., Lugli F., Jentzen A., Schiebel R., Wassenburg J. A. and others (2019) Nano-powdered calcium carbonate reference materials: Significant progress for microanalysis? *Geostandards and Geoanalytical Research* 43, 595–609.

Jochum K. P., Stoll B., Herwig K., Willbold M., Hofmiann A. W., Amini M., Aarburg S., Abouchami W., Hellebrand E., Mocek B., Raczek I., Stracke A., Alard O., Bouman C., Becker S., Dücking M., Brätz H., Klemd R., De Bruin D., Canil D., Cornell D., De Hoog C. J., Dalpé C., Danyushevshy L., Eisenhauer A., Gao Y., Snow J. E., Groschopf N., Günther D., Latkoczy C., Guillong M., Hauri E. H., Höfer H. E., Lahaye Y., Horz K., Jacob D. E., Kasemann S. A., Kent A. J. R., Ludwig T., Zack T., Mason P. R. D., Meixner A., Rosner M., Misawa K., Nash B. P., Pfänder J., Premo W. R., Sun W. D., Tiepolo M., Vannucci R., Vennemann T., Wayne D. and Woodhead J. D. (2006) MPI-DING reference glasses for in situ microanalysis: New reference values for element concentrations and isotope ratios. *Geochemistry, Geophysics, Geosystems* 7.

Jochum K. P., Weis U., Stoll B., Kuzmin D., Yang Q., Raczek I., Jacob D. E., Stracke A., Birbaum K., Frick D. A., Günther D. and Enzweiler J. (2011) Determination of reference values for NIST SRM 610-617 glasses following ISO guidelines. *Geostandards and Geoanalytical Research* 35, 397–429.

Keul N., Langer G., De Nooijer L. J. and Bijma J. (2013) Effect of ocean acidification on the benthic foraminifera Ammonia sp. is caused by a decrease in carbonate ion concentration. *Biogeosciences* 10, 6185–6198.

Kronberg B. I. (1985) Weathering dynamics and geosphere mixing with reference to the potassium cycle. *Physics of the Earth and Planetary Interiors* 41, 125–132.

Lea D. W., Mashiotta T. A. and Spero H. J. (1999) Controls on magnesium and strontium uptake in planktonic foraminifera determined by live culturing. *Geochimica et Cosmochimica Acta* 63, 2369–2379.

Lee K., Kim T.-W., Byrne R. H., Millero F. J., Feely R. A. and Liu Y.-M. (2010) The universal ratio of boron to chlorinity for the North Pacific and North Atlantic oceans. *Geochimica et Cosmochimica Acta* 74, 1801–1811.

Li W., Liu X. M., Wang K., Fodrie F. J., Yoshimura T. and Hu Y. F. (2021) Potassium phases and isotopic composition in modern marine biogenic carbonates. *Geochimica et Cosmochimica Acta* 304, 364–380.

Locarnini M., Mishonov A. V, Baranova O. K., Boyer T. P., Zweng M. M., Garcia H. E., Seidov D., Weathers K., Paver C., Smolyar I. and others (2018) World ocean atlas 2018, volume 1: Temperature.

Lorens R. B. (1981) Sr, Cd, Mn and Co distribution coefficients in calcite as a function of calcite precipitation rate. *Geochimica et Cosmochimica Acta* 45, 553–561.

Lowenstein T. K., Kendall B. and Anbar A. D. (2013) *The Geologic History of Seawater*. 2nd ed., Elsevier Ltd.

Lowenstein T. K., Timofeeff M. N., Brennan S. T., Hardie L. A. and Demicco R. V. (2001) Oscillations in Phanerozoic seawater chemistry: Evidence from fluid Inclusions. *Science* 294, 1086–1088.

Lueker T. J., Dickson A. G. and Keeling C. D. (2000) Ocean pCO2 calculated from dissolved inorganic carbon, alkalinity, and equations for K1 and K2: validation based on laboratory measurements of CO2 in gas and seawater at equilibrium. *Marine chemistry* 70, 105–119.

Marchitto Jr T. M., Curry W. B. and Oppo D. W. (2000) Zinc concentrations in benthic foraminifera reflect seawater chemistry. *Paleoceanography* 15, 299–306.

Marchitto T. M., Bryan S. P., Doss W., McCulloch M. T. and Montagna P. (2018) A simple biomineralization model to explain Li, Mg, and Sr incorporation into aragonitic foraminifera and corals. *Earth and Planetary Science Letters* 481, 20–29.

Marriott C. S., Henderson G. M., Belshaw N. S. and Tudhope A. W. (2004) Temperature dependence of δ7Li, δ44Ca and Li/Ca during growth of calcium carbonate. *Earth and Planetary Science Letters* 222, 615–624.

McCauley S. E. and DePaolo D. J. (1997) The marine 87 Sr/86 Sr and $δ$ 18 O records, Himalayan alkalinity fluxes, and Cenozoic climate models. *Tectonic uplift and climate change*, 427–467.

McNicholl C., Koch M. S. and Hofmann L. C. (2019) Photosynthesis and light-dependent proton pumps increase boundary layer pH in tropical macroalgae: A proposed mechanism to sustain calcification under ocean acidification. *Journal of Experimental Marine Biology and Ecology* 521, 151208.

Mezger E. M., de Nooijer L. J., Boer W., Brummer G. J. A. and Reichart G. J. (2016) Salinity controls on Na incorporation in Red Sea planktonic foraminifera. *Paleoceanography* 31, 1562–1582.

Michalopoulos P. and Aller R. C. (1995) Rapid clay mineral formation in Amazon delta sediments: Reverse weathering and oceanic elemental cycles. *Science* 270, 614–617.

Misra S. and Froelich P. N. (2012) Lithium isotope history of cenozoic seawater: Changes in silicate weathering and reverse weathering. *Science* 335, 818–823.

Mucci A. and Morse J. W. (1983) The incorporation of Mg2+ and Sr2+ into calcite overgrowths: influences of growth rate and solution composition. *Geochimica et Cosmochimica Acta* 47, 217–233.

Mucci A. and Morse J. W. (1984) The solubility of calcite in seawater solutions of various magnesium concentration, It = 0.697 m at 25 °C and one atmosphere total pressure. *Geochimica et Cosmochimica Acta* 48, 815–822.

Müller W., Shelley M., Miller P. and Broude S. (2009) Initial performance metrics of a new custom-

designed ArF excimer LA-ICPMS system coupled to a two-volume laser-ablation cell. *Journal of Analytical Atomic Spectrometry* 24, 209–214.

Nakao M. and Gadsby D. C. (1986) Voltage dependence of Na translocation by the Na/K pump. *Nature* 323, 628–630.

Nehrke G., Reichart G. J., Van Cappellen P., Meile C. and Bijma J. (2007) Dependence of calcite growth rate and Sr partitioning on solution stoichiometry: Non-Kossel crystal growth. *Geochimica et Cosmochimica Acta* 71, 2240–2249.

De Nooijer L. J., Toyofuku T. and Kitazato H. (2009) Foraminifera promote calcification by elevating their intracellular pH. *Proceedings of the National Academy of Sciences of the United States of America* 106, 15374–15378.

Okai T., Suzuki A., Kawahata H., Terashima S. and Imai N. (2002) Preparation of a new Geological Survey of Japan geochemical reference material: Coral JCp-1. *Geostandards Newsletter* 26, 95–99.

Okumura M. and Kitano Y. (1986) Coprecipitation of alkali metal ions with calcium carbonate. *Geochimica et Cosmochimica Acta* 50, 49–58.

Oron S., Evans D., Abramovich S., Almogi-Labin A. and Erez J. (2020) Differential Sensitivity of a Symbiont-Bearing Foraminifer to Seawater Carbonate Chemistry in a Decoupled DIC-pH Experiment. *Journal of Geophysical Research: Biogeosciences* 125, 1–16.

Pearce N. J. G., Perkins W. T., Westgate J. A., Gorton M. P., Jackson S. E., Neal C. R. and Chenery S. P. (1997) A compilation of new and published major and trace element data for NIST SRM 610 and NIST SRM 612 glass reference materials. *Geostandards newsletter* 21, 115–144.

Pierrot D., Epitalon J.-M., Orr J. C., Lewis E. and Wallace D. W. R. (2021) MS Excel program developed for CO2 system calculations–version 3.0.

Raja R., Saraswati P. K. and Iwao K. (2007) A field-based study on variation in Mg/Ca and Sr/Ca in larger benthic foraminifera. *Geochemistry, Geophysics, Geosystems* 8.

Ram S. and Erez J. (2021) The Distribution Coefficients of Major and Minor Elements in Coral Skeletons Under Variable Calcium Seawater Concentrations. *Frontiers in Earth Science* 9, 1–14.

Raymo M. E. and Ruddiman W. F. (1992) Tectonic forcing of late Cenozoic climate. *Nature* 359, 117–122.

Renema W. (2008) Habitat selective factors influencing the distribution of larger benthic foraminiferal assemblages over the Kepulauan Seribu. *Marine Micropaleontology* 68, 286–298.

Renema W. (2006) Habitat variables determining the occurrence of large benthic foraminifera in the Berau area (East Kalimantan, Indonesia). *Coral Reefs* 25, 351–359.

Rickaby R. E. M. and Elderfield H. (1999) Planktonic foraminiferal Cd/Ca: paleonutrients or paleotemperature? *Paleoceanography* 14, 293–303.

Ridgwell A. and Zeebe R. E. (2005) The role of the global carbonate cycle in the regulation and evolution of the Earth system. *Earth and Planetary Science Letters* 234, 299–315.

Roberts J., Kaczmarek K., Langer G., Skinner L. C., Bijma J., Bradbury H., Turchyn A. V, Lamy F. and Misra S. (2018) Lithium isotopic composition of benthic foraminifera: A new proxy for paleo-pH reconstruction. *Geochimica et Cosmochimica Acta* 236, 336–350.

Rosenthal Y., Boyle E. A. and Slowey N. (1997) Temperature control on the incorporation of magnesium, strontium, fluorine, and cadmium into benthic foraminiferal shells from Little Bahama Bank: Prospects for thermocline paleoceanography. *Geochimica et Cosmochimica Acta* 61, 3633–3643.

Rosenthal Y. and Katz A. (1989) The applicability of trace elements in freshwater shells for paleogeochemical studies. *Chemical Geology* 78, 65–76.

Schleinkofer N., Raddatz J., Freiwald A., Evans D., Beuck L., Rüggeberg A. and Liebetrau V. (2019) Environmental and biological controls on Naĝ•Ca ratios in scleractinian cold-water corals. *Biogeosciences* 16, 3565–3582.

Segev E. and Erez J. (2006) Effect of Mg/Ca ratio in seawater on shell composition in shallow benthic foraminifera. *Geochemistry, Geophysics, Geosystems* 7, 1–8.

Skou J. C. and Esmann M. (1992) The Na,K-ATPase. *Journal of Bioenergetics and Biomembranes* 24, 249–261.

Thompson J. and MacLeod R. A. (1974) Potassium transport and the relationship between intracellular potassium concentration and amino acid uptake by cells of a marine pseudomonad. *Journal of Bacteriology* 120, 598–603.

Toyofuku T., Matsuo M. Y., De Nooijer L. J., Nagai Y., Kawada S., Fujita K., Reichart G. J., Nomaki H., Tsuchiya M., Sakaguchi H. and Kitazato H. (2017) Proton pumping accompanies calcification in foraminifera. *Nature Communications* 8, 6–11.

Turchyn A. V and DePaolo D. J. (2019) Seawater chemistry through Phanerozoic time. *Annual Review of Earth and Planetary Sciences* 47, 197–224.

Tyrrell T. and Zeebe R. E. (2004) History of carbonate ion concentration over the last 100 million years. *Geochimica et Cosmochimica Acta* 68, 3521–3530.

Ulrich R. N., Guillermic M., Campbell J., Hakim A., Han R., Singh S., Stewart J. D., Román-Palacios C., Carroll H. M., De Corte I., Gilmore R. E., Doss W., Tripati A., Ries J. B. and Eagle R. A. (2021) Patterns of Element Incorporation in Calcium Carbonate Biominerals Recapitulate Phylogeny for a Diverse Range of Marine Calcifiers. *Frontiers in Earth Science* 9, 1–26.

Vigier N., Rollion-Bard C., Levenson Y. and Erez J. (2015) Lithium isotopes in foraminifera shells as a novel proxy for the ocean dissolved inorganic carbon (DIC). *Comptes Rendus Geoscience* 347, 43–51.

Watson E. B. (2004) A conceptual model for near-surface kinetic controls on the trace- element and stable isotope composition of abiogenic calcite crystals. *Geochimica et Cosmochimica Acta* 68,

1473–1488.

Weldeab S., Lea D. W., Schneider R. R. and Andersen N. (2007) 155,000 years of West African monsoon and ocean thermal evolution. *science* 316, 1303–1307.

White A. F. (1977) Sodium and potassium coprecipitation in aragonite. *Geochimica et Cosmochimica Acta* 41, 613–625.

Wilkinson and Algeo T. J. (1989) Sedimentary carbonate record of calcium-magnesium cycling. *American Journal of Science* 289, 1158–1194.

Wit J. C., de Nooijer L. J., Haig J., Jorissen F. J., Thomas E. and Reichart G. J. (2017) Towards reconstructing ancient seawater Mg/Ca by combining porcelaneous and hyaline foraminiferal Mg/Ca-temperature calibrations. *Geochimica et Cosmochimica Acta* 211, 341–354.

Wit J. C., De Nooijer L. J., Wolthers M. and Reichart G. J. (2013) A novel salinity proxy based on na incorporation into foraminiferal calcite. *Biogeosciences* 10, 6375–6387.

Wolthers M., Nehrke G., Gustafsson J. P. and Van Cappellen P. (2012) Calcite growth kinetics: Modeling the effect of solution stoichiometry. *Geochimica et Cosmochimica Acta* 77, 121–134.

York D., Evensen N. M., Mart\ínez M. L. and De Basabe Delgado J. (2004) Unified equations for the slope, intercept, and standard errors of the best straight line. *American journal of physics* 72, 367–375.

Yu J., Foster G. L., Elderfield H., Broecker W. S. and Clark E. (2010) An evaluation of benthic foraminiferal B/Ca and δ11B for deep ocean carbonate ion and pH reconstructions. *Earth and Planetary Science Letters* 293, 114–120.

Zhou X., Rosenthal Y., Haynes L., Si W., Evans D., Huang K. F., Hönisch B. and Erez J. (2021) Planktic foraminiferal Na/Ca: A potential proxy for seawater calcium concentration. *Geochimica et Cosmochimica Acta* 305, 306–322.

Zweng M. M., Seidov D., Boyer T., Locarnini M., Garcia H., Mishonov A., Baranova O. K., Weathers K., Paver C. R., Smolyar I. and others (2019) World ocean atlas 2018, volume 2: Salinity.

Chapter 5: Reconstructing Eocene seawater major ion concentrations and magnesium isotopic composition using large benthic foraminifera

Citation:
Nambiar R., Coenen D., Henehan M. J., Khanolkar S., Stassen P., Renema W., Leroy A., Moreau F., Bartolini A., Merle D., Cotton L., Müller W. and Evans D. Reconstructing Eocene seawater major ion concentrations and magnesium isotopic composition using large benthic foraminifera. (in preparation).

Reconstructing Eocene seawater major ion concentrations and magnesium isotopic composition using large benthic foraminifera

Romi Nambiar[1,2,*], Douglas Coenen[1,2], Michael J. Henehan[3], Sonal Khanolkar[4], Peter Stassen[5,6], Willem Renema[7,8], Arnaud Leroy[9], Fabrice Moreau[10], Annachiara Bartolini[11], Didier Merle[11], Laura Cotton[12], Wolfgang Müller[1,2], David Evans[1,2,13]

[1]Institute of Geosciences, Goethe University, Frankfurt am Main, Germany
[2]FIERCE, Frankfurt Isotope & Element Research Center, Goethe University, Frankfurt am Main, Germany
[3]GFZ German Research Centre for Geosciences, Potsdam, Germany
[4]GEOMAR, Helmholtz Centre for Ocean Research, Germany
[5]Department of Earth and Environmental Sciences, KU Leuven, Leuven, Belgium
[6]Royal Belgian Institute of Natural Sciences, Brussels, Belgium
[7]Naturalis Biodiversity Center, Leiden, Netherlands
[8]University of Amsterdam, Institute for Biodiversity and Ecosystem Dynamics, Amsterdam, NL
[9]9 rue des Allées, Septmonts, France
[10]112 Quai de Bezons, Argenteuil, France
[11]Natural History Museum of Paris, Paris, France
[12]The Natural History Museum, Research and Collections, University of Copenhagen, Denmark
[13]Now at: School of Ocean and Earth Science, University of Southampton, Southampton, UK

*Corresponding author: Email address: Nambiar@geo.uni-frankfurt.de (R. Nambiar)

Abstract

The Cenozoic era has experienced substantial changes in the atmospheric CO_2. However, the geological processes driving the variability in atmospheric CO_2 are still under debate. Changes in seawater chemistry are closely associated with the global carbon cycle and can be used to identify the geological processes that control the long-term changes in seawater chemistry and the global carbon cycle. In this study, we utilise larger benthic foraminifera (*Nummulites sp.*) that were abundant during Paleogene and applied a multi-proxy approach, established based on calibration experiments, in order to reconstruct the long-term changes in seawater $[K^+]$, $[Ca^{2+}]$, $[Mg^{2+}]$ and Mg isotope

($\delta^{26}Mg_{sw}$). Our results showed that Eocene $[Ca^{2+}]_{sw}$ were 1.6-2 times higher compared to present-day seawater, and the $[K^{+}]_{sw}$ were ~2 times lower. Additionally, the $[Mg^{2+}]_{sw}$ decreased from early Eocene to late Eocene, followed by an increase towards present-day seawater values, whereas variability in $\delta^{26}Mg_{sw}$ values remained within ~0.3 ‰ of modern seawater signature. Combining our results with existing records suggests that the evolution of seawater chemistry depends on multiple processes, among which the decrease in seafloor-spreading rate and decrease in reverse weathering may have played an important role during the Cenozoic.

Introduction

The Cenozoic era has experienced substantial changes in atmospheric CO_2 (Royer, 2014; Anagnostou et al., 2016; O'Brien et al., 2017; Rae et al., 2021). Long-term variation of the global carbon cycle has been proposed to be controlled by terrestrial weathering, marine organic carbon production and burial, reverse weathering, and volcanic degassing (Berner et al., 1983; Li et al., 2009). These same processes also affect the element and isotopic composition of seawater. Thus, seawater chemistry plays an important link to carbon cycling, and reconstruction of seawater chemistry is one way to constrain the processes that have driven the carbon cycle. During the past decades, several processes have been identified as a driver of changes in Cenozoic atmospheric CO_2 and, thus, seawater chemistry. Earlier studies have suggested that the drawdown of Cenozoic atmospheric CO_2 is driven by negative feedback from temperature-controlled silicate weathering (Walker et al., 1981; Caldeira and Berner, 1998); however, the increase in the silicate weathering during the Cenozoic can be attributed to tectonic activity (Raymo and Ruddiman, 1992; Misra and Froelich, 2012) or an increase in land surface reactivity (Caves Rugenstein et al., 2019; Deng et al., 2022). Moreover, a few studies have also suggested that a decrease in reverse weathering has contributed to the decline of atmosphere CO_2 over the Cenozoic (Dunlea et al., 2017; Isson and Planavsky, 2018). Additionally, the role of a decrease in the seafloor spreading rate and associated hydrothermal processes has also been proposed to play a significant role in driving Cenozoic carbon cycling (Coggon et al., 2010; Coogan and Dosso, 2015). More recently, it has been noted that seawater $[Ca^{2+}]$, in itself, can drive long-term atmospheric CO_2, given that the $[Ca^{2+}]_{sw}$ influences seawater Ω_c and plays a significant role in $CaCO_3$ production and burial rates (Evans et al., in preparation). Thus, reconstruction of seawater

chemistry is essential to gain insights into the drivers of long-term changes in the carbon cycle.

Reconstruction of seawater elemental concentrations and El/Ca ratio has previously been achieved by means of fluid inclusion records in marine halite (Horita et al., 2002; Lowenstein et al., 2003; Brennan et al., 2013), $CaCO_3$ veins (CCVs) (Coggon et al., 2010), marine carbonate (Evans et al., 2016, 2018; Gothmann et al., 2017). While the majority of investigation has studied the element/Ca ratio in seawater (Dickson 2004; Coggon et al., 2010; Gothmann et al., 2015; Evans et al., 2016, 2018), the record of long-term changes in individual elemental concentration in the seawater during Cenozoic is limited (Horita et al., 2002; Brennan et al., 2013). To the best of our knowledge, only one study has reported $[Ca^{2+}]_{sw}$ reconstruction with high temporal resolution (sub-million years), offering a record spanning the past 16 million years (Zhou et al., 2021). In addition to seawater elemental composition, changes in the isotopic signature of seawater elements have also been widely investigated to understand the evolution of seawater chemistry and thus identify their driving processes, e.g., Li, Sr, and Os isotopes (DePaolo and Ingram, 1985; Hess et al., 1986; Pegram and Turekian, 1999; Peucker-Ehrenbrink and Ravizza, 2000; Misra and Froelich, 2012; Coogan et al., 2017; McArthur et al., 2020; Kalderon-Asael et al., 2021). Magnesium is one such element closely associated with long-term carbon cycling, and its isotopic signature can be a potential indicator for processes driving the global carbon cycle. Attempts have been made to reconstruct seawater Mg isotope ($\delta^{26}Mg_{sw}$) using different archives, including planktic foraminifera (Pogge Von Strandmann et al., 2014), pelagic carbonates (Higgins and Schrag, 2015), and corals (Gothmann et al., 2017). However, the existing records of reconstructed seawater $\delta^{26}Mg$ are not in agreement and thus suggests a different mechanism for driving the Cenozoic seawater Mg cycle (Pogge Von Strandmann et al., 2014; Higgins and Schrag,

2015; Gothmann et al., 2017). While Pogge Von Strandmann et al. (2014) proposed that dolomite formation and the riverine Mg flux are the primary controls of seawater $\delta^{26}Mg$, Gothmann et al. (2017) and Higgins and Schrag (2015) suggest a different mechanism. They suggested silicate weathering and authigenic clay formation as important factors driving the Mg cycle and argue that carbonate weathering or dolomitisation processes do not play a significant role.

Shallow-dwelling larger benthic foraminifera (LBF) have been increasingly investigated for testing their potential for paleoclimatic reconstruction (Wefer and Berger, 1980; Purton and Brasier, 1999; Raja et al., 2007; Evans et al., 2015; Maeda et al., 2017; Hauzer et al., 2018; Yoshimura et al., 2019; Nambiar et al., 2023). Moreover, larger benthic foraminifera has been successfully utilised for both seasonality reconstruction and long-term paleo-reconstructions (Evans et al., 2013, 2018). The Nummulitidae family comprises various genera including Nummulites, Cycloclypeus, Heterostegina, Operculina, and other LBFs (Holzmann and Pawlowski, 2017). *Operculina ammonoides* is the closest living relative of the abundant Paleogene *Nummulites* sp., which forms a high-Mg calcite shell (Blackmon and Todd, 1959; Cotton et al., 2020). A strong relationship between El/Ca (Na, K, Sr, and Mg) in LBF and El/Ca in seawater is reported from culture experiment of *O. ammonoides* grown at varying seawater major ion composition (Evans et al., 2015; Hauzer et al., 2018; Nambiar et al., 2023), which acts as potential proxies for seawater chemistry reconstructions. Moreover, fossils of *Operculina* and *Nummulites* sp. collected from the same bed have been shown to have an identical chemical composition (Evans et al., 2013), allowing the calibration established based on *O. ammonoides* to be applied to *Nummulites* fossils. In this study, we aim to reconstruct the concentration of individual elements (Ca, Mg, and K) and $\delta^{26}Mg$ signature of Eocene seawater using multi-proxy records in high-Mg larger benthic foraminifera (LBF), *Nummulites* sp. fossil. With

this, we aim to combine our results of seawater chemistry with existing records during the Cenozoic to better understand their driving process.

Methodology

Eocene *Nummulites sp.* collected from the Paris basin, Hampshire basin, and several locations with the global tropics were investigated for their El/Ca and Mg isotopic signature. Since the Mg isotopic composition of high-Mg larger benthic foraminifera (LBFs) and its correlations with seawater parameters have not been previously reported, we also investigated modern *Operculina ammonoides* collected from different locations with varying seawater parameters. These samples have previously been investigated for Mg/Ca-temperature calibration (Evans et al., 2013) and to investigate the effect of seawater parameters on K/Ca (Nambiar et al., 2023). The mean annual temperature and salinity values were taken from the nearest located values in World Ocean Atlas 2018 (Locarnini et al., 2018; Zweng et al., 2019). Sample from the Gulf of Eilat was an exception for which the daily SST monitoring from the Interuniversity Institute for Marine Sciences in Eilat (http://www.iui-eilat.ac.il) was used (for detailed information, refer Evans et al., 2013).

All samples were cleaned with 1 % sodium hypochlorite (NaOCl) followed by 3-4 times rinsing by ultrasonication in 18.2 MΩ cm deionised water (Milli-Q water). The samples were then rinsed 1-2 times with methanol and 2-3 times with deionised water in ultrasonication bath. Finally, samples were air-dried in a clean flow bench. The fossil samples were screened for SEM images to check their preservation (Figure S1). Well-preserved samples were further investigated for their trace elements and $\delta^{26}Mg$ signatures.

For trace element composition, samples were analysed using sector-field ICP-MS connected to a RESOlution 193 nm ArF laser ablation system with a Laurin Technic S-155 two-volume laser-ablation cell (see Müller et al., 2009) at the Frankfurt Isotope and Element Research Center (FIERCE), Goethe University Frankfurt. The operating parameter of LA-ICP-MS was followed as described in Nambiar et al., (2024). Briefly, all ablations (spot size: 50 µm; repetition rate: 3 Hz) were carried out in He atmosphere with Ar mixed into the top of the inner volume and N_2 gas added downstream of the cell. The instrument was tuned using NIST SRM 612 to achieve maximum sensitivity (^{238}U > 4.5 million cps) while maintaining Th^+/U^+ ratio between 0.9 and 1 and ThO^+/Th^+<1%. Monitored masses (m/z) were ^{23}Na, ^{24}Mg, ^{25} Mg, ^{27}Al, ^{39}K, ^{43}Ca, ^{55}Mn and ^{88}Sr, where ^{43}Ca was used as the internal standard. The Al/Ca, Mg/Ca, and Sr/Ca ratios were monitored to verify the sample cleaning procedure as well as the preservation of the fossil samples (Figure S1). The operating parameters are mentioned in Table S1. Data reduction following established protocols (Heinrich et al., 2003) and in-house Matlab script (Evans and Müller, 2018) was performed using ^{43}Ca as the internal standard and the NIST SRM610 glasses as the external standard analysed identically to the samples. In brief, the script identifies the data, subtracts the blank data from the sample data, and calibrates trace element ratios using a depth-dependent measured/reported element/^{43}Ca ratio. Repeat measurements of reference materials, including GOR-128G and nano-pellet carbonate standards (JCP-1NP) were analysed in the same session and under the same conditions as the samples. The reported NIST SRM610 values of Jochum et al. (2011) were used with the exception of Mg, for which we use that of Pearce et al. (1997) following the recommendation of Evans and Müller, (2018). The recommended values of GOR-128G and JCP-1 reported by Jochum et al., (2006) and Okai et al., (2002), respectively were used to assess the accuracy. The accuracy of Mg/Ca, Al/Ca, and Mn/Ca

in GOR-128G, and Na/Ca, Mg/Ca, Al/Ca, and K/Ca in JCp-1NP were within ±5 %, whereas accuracy for Na/Ca and K/Ca in GOR-128G were within ±10 %.

For the Mg isotopes measurement, clean samples were crushed using agate mortar and pestle. Foraminifera, with a diameter of less than 1500 µm, were crushed using two clean glass slides following the method suggested by (Barker et al., 2003). Samples containing pyrite were subjected to additional treatment by oxidative cleaned 3-4 times with 200 µL of 1 % H_2O_2 + 0.1 N NH_4OH at 80°C for 5 min and were repeatedly rinsed with deionised water. All crushed samples were ultrasonicated and rinsed with methanol, followed by repeated rinsing with deionised water. Mg isotope measurement was performed at the Helmholtz Laboratory for the Geochemistry of the Earth Surface (HELGES) lab, GFZ, Potsdam. Briefly, column chemistry was performed to separate Mg from the sample matrix, where samples containing ~30 µg Mg were dissolved in 1N HNO_3 and passed through cation exchange resin Bio-Rad AG-50W-X12 (200-400 mesh). Samples were then evaporated and cooked with H_2O_2 at 150°C for ~2 hours, following evaporation at 110°C and re-dilution with 0.3 M HNO_3. Each column batch included column blank, seawater standard (IAPSO), and carbonate standards (JCp-1, MACS-3, or KSCp-1), processed in the same manner. The sample purity and recovery were verified using quadrupole ICP-MS (Thermo iCAP-Qc). For Mg isotope measurements, purified samples were diluted with 0.3 N HNO_3 to achieve 500 ppb Mg. Mg isotope measurements were performed on a ThermoFisher Scientific Neptune Plus MC-ICP-MS. The operating condition is mentioned in Table S2. The measurement was done using a sample bracketing technique using a DSM-3 solution. Reference material including Cambridge-1, IAPSO seawater sample and JCp-1 were analysed to verify the analytical performance. A summary of reference standard measurements is given in Table S3.

Reconstruction of seawater [Mg^{2+}] and [Ca^{2+}]

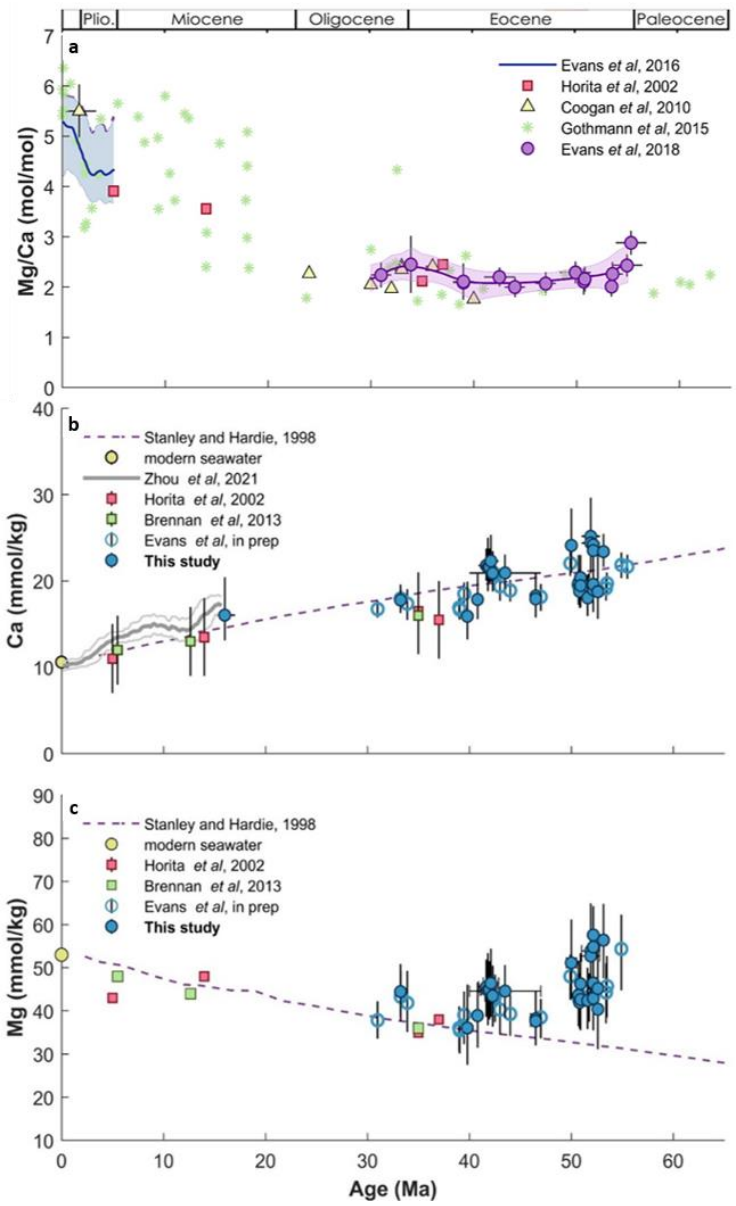

Figure 1. Temporal variation of seawater a) Mg/Ca, b) [Ca^{2+}], and c) [Mg^{2+}] since 65 Ma. Data from Age > 65 Ma are omitted from the plot. The error bars represent 1SD.

To reconstruct the Cenozoic seawater [Ca^{2+}], we referred to the Na/Ca proxy established using *O. ammonoides* grown at varying $[Ca^{2+}]_{sw}$ in laboratory culture experiments (Hauzer et al., 2018). In this study, we used SEM images and elemental

composition to verify the preservation of our fossil samples. We rejected samples showing evidence of poor preservation in SEM images and/or significantly low Mg/Ca and Sr/Ca values (Figure S1). Our results showed that the Eocene $[Ca^{2+}]_{sw}$ varied from $21.7^{+1.37}_{-1.44}$ mmol kg^{-1} at ~55 Ma to $16.7^{+0.94}_{-0.97}$ mmol kg^{-1} at ~31 Ma, which is ~1.6-2 times higher than the present-day value (Figure 1). Our results agree well with previously reported $[Ca^{2+}]_{sw}$ derived from fluid inclusion in marine halite (Horita et al., 2002; Brennan et al., 2013) and modelled $[Ca^{2+}]_{sw}$ (Stanley and Hardie, 1998). Evans et al., 2018 reconstructed Eocene seawater Mg/Ca with high temporal resolution (~1 Ma) by coupled clumped isotope (Δ_{47}) - Mg/Ca measurements of LBFs and observed 2-3 times lower Mg/Ca values than present-day seawater. We combined our reconstructed $[Ca^{2+}]_{sw}$ values with interpolation using the nearest data point from seawater Mg/Ca reported by Evans et al., (2018) to estimate $[Mg^{2+}]_{sw}$. The results demonstrated a decrease in $[Mg^{2+}]_{sw}$ from $54.3^{+7.9}_{-9.6}$ mmol kg^{-1} at ~55 Ma to $37.8^{+4.4}_{-4.3}$ mmol kg^{-1} at ~31 Ma which increased towards present day value of 53 mmol kg^{-1}, suggesting the long term changes in Cenozoic Mg/Ca_{SW} was majorly driven by seawater Ca.

Reconstruction of seawater $[K^+]$

To the best of our knowledge, there are very limited studies that have investigated the incorporation of K in marine carbonate as a function of change in seawater $[Ca^{2+}]$ (Aragonitic corals: Ram and Erez, 2021, high-Mg LBF: Nambiar et al., 2023). The significant relationship between K/Ca_{shell}-K/Ca_{SW} (Ram and Erez, 2021; Nambiar et al., 2023) makes K/Ca proxy a potential tool for unravelling past changes in seawater chemistry. A significant correlation is observed between K/Ca_{LBF}-K/Ca_{SW} based on the laboratory culture experiment of *O. ammonoides*, best described as a power relation (Nambiar et al., 2023). Investigation on additional controlling factors on the

incorporation of K in LBF using modern *O. ammonoides* collected from globally distributed sites characterised by a wide range of seawater parameters demonstrated no resolvable influence of temperature, salinity, $[CO_3^{2-}]$ or pH on K/Ca_{LBF} (Nambiar et al., 2023). However, the culture experiment of *O. ammonoides* grown at varying pH and constant DIC showed a significant effect of pH on K/Ca_{LBF} (R^2 = 0.96; p = 0.01), conducted over a much larger pH range (~7.5 to 8.3).

We proposed to estimate Eocene seawater $[K^+]$ in two ways: 1) directly using K/Ca proxy established using *O. ammonoides* and incorporating the $[Ca^{2+}]_{sw}$ value derived from Na/Ca proxy, 2) Indirect approach, in which we eliminate the effect of seawater Ca by combining the variation of Na/Ca_{LBF} and K/Ca_{LBF} in *O. ammonoides* grown at different $[Ca^{2+}]_{sw}$ and compare value of K/Na_{LBF} value from the culture experiment and fossil K/Na_{LBF} in order to reconstruct $[K^+]_{sw}$ (calibration details in supplementary material). The results of both are shown in Figure 2. We observed the values reconstructed $[K^+]_{sw}$ using K/Ca proxy were lower than those obtained using K/Na approach. One possibility could be the effect of Mg/Ca on the D_K of foraminifera. Earlier studies have shown that the Mg/Ca of foraminifera shell and inorganic calcite influences the incorporation of elements such as Na and Sr (Mucci and Morse, 1983; Evans et al., 2015). Given that a significant correlation was observed between D_{Na} and D_K of *O. ammonoides* grown at different $[Ca^{2+}]_{sw}$ (Nambiar et al., 2023), it is possible that K incorporation also experiences the influence of Mg/Ca_{LBF}, which results in lower K/Ca_{LBF} value in fossil and lower $[K^+]_{sw}$. While we emphasise that further investigation regarding the incorporation of K in marine carbonate can improve the accuracy of seawater $[K^+]$, using the K/Ca proxy, our results based on both approaches highlight that seawater $[K^+]_{sw}$ has varied in the past and was ~~2 times lower during the Eocene compared to present-day $[K^+]_{sw}$ (~11 mmol kg^{-1}).

This finding contradicts from the earlier suggestion of consistency of $[K^+]_{sw}$ throughout the last ~541 Myr (Horita et al., 2002).

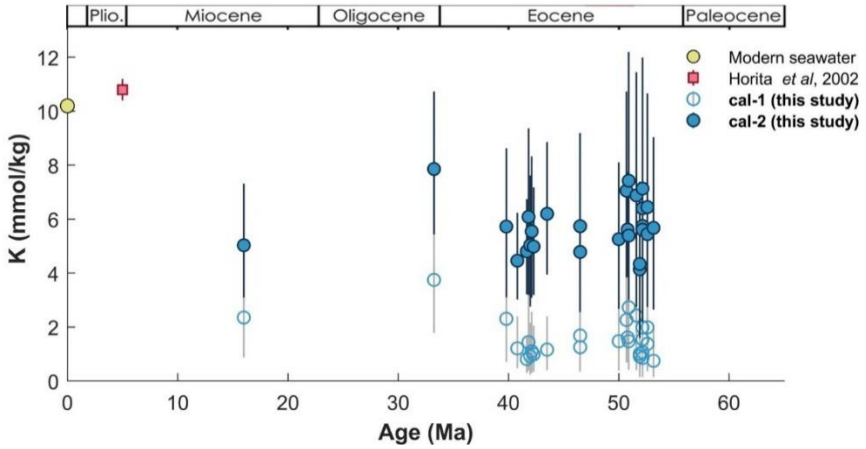

Figure 2. Temporal variation of seawater $[K^+]$ since 65 Ma. The error bars represent 1SD. The red dashed line is a fit-line for data from Horita et al. (2002). Data from Age > 65 Ma are omitted from the plot.

Record of Cenozoic $\delta^{26}Mg_{sw}$

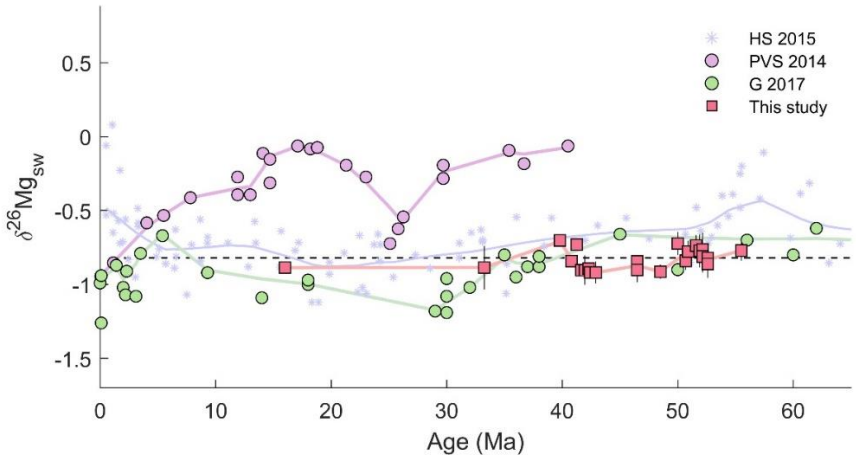

Figure 3. Temporal variation of $\delta^{26}Mg_{sw}$ (‰) since 65 Ma derived from different marine carbonates, including pelagic carbonate (Higgins and Schrag, 2015), low-Mg planktonic foraminifera (Pogge Von Strandmann et al., 2014), aragonitic corals (Gothmann et al., 2017) and high-Mg LBF (this study). Error bars are 1SD. The solid lines are Lowess smoothing curves with a

smoothing span of 0.2. The black dashed line represents the present-day $\delta^{26}Mg_{sw}$ value (-0.82 ‰; Foster et al. (2010)).

With the emerging use of $\delta^{26}Mg$ in marine carbonates for reconstructing long-term change in seawater $\delta^{26}Mg$ composition (Pogge Von Strandmann et al., 2014; Higgins and Schrag, 2015; Gothmann et al., 2017), several studies have pointed out the possibility of post-depositional alteration of trace element and their isotope signature in marine carbonate (Chanda and Fantle, 2017; Fantle et al., 2020). Such diagenesis of carbonate is accompanied by the loss of elements such as Mg, Sr, Ba, and Mn (Stehli and Hower, 1961; Dickson, 1995). In this study, we used only well-preserved sample verified using SEM images and elemental composition (Figure S1). Then, the $\delta^{26}Mg$ value of all samples were corrected for their isotopic fractionation (-2.30 ‰ based on the mean of several modern samples) in order to estimate $\delta^{26}Mg_{sw}$ (details in supplementary material). Our results demonstrated that the Eocene $\delta^{26}Mg_{sw}$ varied between -0.92 ± 0.02 ‰ to -0.70 ± 0.02 ‰, showing variability of ~0.3 ‰. Our Eocene records aligns well with previous reported values derived using aragonitic corals (Gothmann et al., 2017). Additionally, our investigation of sample from 16 Ma that indicated a $\delta^{26}Mg_{sw}$ value of -0.89 ± 0.02 ‰, aligning with values reported in previous studies (Higgins and Schrag, 2015; Gothmann et al., 2017), however, this finding disagree with record reported by Pogge Von Strandmann et al., (2014).

Driving Processes of Cenozoic seawater chemistry

Most Eocene seawater absolute elemental concentration records are derived from fluid inclusion in marine halite; however, these records have low temporal resolution due to limited availability of evaporites (Horita et al., 2002; Brennan et al., 2013). The records based on Eocene *Nummulites* fossils are capable of seawater chemistry

reconstruction at relatively higher temporal resolution, as these species were abundant throughout the Paleogene (Hallock, 1985). Our results showed that average values for Eocene seawater $[Ca^{2+}]$, $[Mg^{2+}]$, $[K^{+}]$ were 19.9, 43.7, and 5.7 mmol kg^{-1}. While our average reconstructed Eocene $[Ca^{2+}]_{sw}$ values were ~1.6-2 times higher, $[K^{+}]_{sw}$ were ~2 times lower than the present day, and $[Mg^{2+}]_{sw}$ decreased from the early to late Eocene, followed by an increase toward the present. Our Eocene $[Ca^{2+}]_{sw}$ and $[Mg^{2+}]_{sw}$ results agree well with records derived from the fluid inclusion studies. However, our Eocene $[K^{+}]_{sw}$ values are in disagreement with the study based on fluid inclusions in marine halite, which suggested no significant changes in $[K^{+}]_{sw}$ throughout the Phanerozoic eon (~541 Ma) (Horita et al., 2002) despite having a residence time of ~12 Ma (Broecker and Peng, 1982). This result is based on the consistency in K/Br value in fluid inclusion, and given that Br has a long residence time in seawater, the $[K^{+}]_{sw}$ has been suggested to be invariant through the Phanerozoic (Horita et al., 2002).

The Cenozoic $\delta^{26}Mg$ reconstructions previously reported are not in agreement (Pogge Von Strandmann et al., 2014; Higgins and Schrag, 2015; Gothmann et al., 2017), requiring further investigation to understand the driver of the Mg cycle. Our seawater $\delta^{26}Mg$ reconstructions using LBF suggested that the variability remained in narrow bound (~0.3 ‰), which agrees well with the previously reported results based on aragonitic corals (Gothmann et al., 2017). In contrast, Pogge Von Strandmann et al., 2014, showed relatively larger variability with ~0.8 ‰ heavier $\delta^{26}Mg_{sw}$ values than present-day seawater using low-Mg planktonic foraminifera. We argue that such larger variability could be a result of using low-Mg planktonic foraminifera as an archive for $\delta^{26}Mg$ reconstructions. It has been noted that low-Mg planktonic foraminifera have relatively larger fractionation ($\Delta^{26}Mg_{carb\text{-}sol}$ = -4.49 to -3.85; see supplementary material), likely to be influenced, by vital effects and thus, $\delta^{26}Mg$ signature of low-Mg foraminifera can be influenced by any

potential evolution in the degree of vital effects. Whereas, the $\Delta^{26}Mg_{carb\text{-}sol}$ in high-Mg LBF (-2.33 to -2.28) is close to inorganic calcite (-2.70 ‰ at 4°C to -2.22 ‰ at 45°C; Li et al., 2012) showing minimal vital effects (Figure S3). Similarly, $\Delta^{26}Mg_{carb\text{-}sol}$ in marine aragonite (-1.07 to -0.85; see Figure S3) is close to that of inorganic aragonite (-1.09 to -0.81; Wang et al., 2013). The agreement between the LBF and coral records, as well as that derived from bulk $CaCO_3$ suggests that marine aragonite and high-Mg marine calcite may be more reliable archives for $\delta^{26}Mg$ reconstruction.

The Cenozoic experienced a change in ~1000 ppm of atmospheric CO_2 with a long-term decreasing trend toward the present (Rae et al., 2021). The long-term cooling and decline in CO_2 are thought to result from an increase in silicate weathering driven by temperature feedback (Walker et al., 1981; Caldeira and Berner, 1998), an increase in weathering rate by tectonic activity (Raymo and Ruddiman, 1992; Misra and Froelich, 2012) or land surface reactivity (Caves Rugenstein et al., 2019; Deng et al., 2022) and organic carbon burial (Raymo and Ruddiman, 1992). Silicate weathering is the major source of cations such as Na^+, Mg^{2+}, $Ca^{2+,}$ and K^+, which are delivered to the ocean via riverine systems (Emerson and Hedges, 2008). Our results show an increase in seawater [Mg^{2+}] and [K^+] towards the present; however, seawater [Ca^{2+}] decreases, suggesting other (additional) processes have influenced the seawater chemistry. Moreover, Mg is supplied during both silicate and carbonate weathering, while K is primarily supplied by silicate weathering (>90%) (Meybeck, 1987; Berner and Berner, 1996). In addition, the proportion of cation (expressed as % of total cations) released by continental weathering of silicate minerals shows a higher Mg (31 %) proportion compared to K (7 %) (Meybeck, 1987). Hence, our result with a marginal increase in [Mg^{2+}] compared to a ~2 times increase in $[K^+]_{sw}$ further suggests the possibility of additional or alternative processes influencing the Cenozoic seawater chemistry.

Several studies have suggested that there has been a decrease in the seafloor-spreading rate during the Cenozoic (Gaffin, 1987; Dalton et al., 2022), leading to a reduction in the hydrothermal processes which can explain the changes in the Cenozoic seawater chemistry (Stanley and Hardie, 1998; Demicco et al., 2005; Coogan and Dosso, 2015). High-temperature hydrothermal processes are a source of Ca and K and a sink for Mg (Elderfield and Schultz, 1996; Coogan and Dosso, 2012). Our results with existing proxy records agree well with the decrease in $[Ca^{2+}]_{sw}$ modelled by Stanley and Hardie, 1998 (Figure 1), which suggested seawater chemistry is driven by hydrothermal fluxes associated with seafloor spreading rates. While a decrease in the seafloor spreading rate supports the magnitude of our observed decrease in $[Ca^{2+}]_{sw}$, it cannot explain the seawater $[K^{+}]$ increase, as it should have also shown a decreasing trend if primarily controlled by high-temperature hydrothermal processes. Reverse weathering, i.e., authigenic clay formation, has been considered an important process to balance the silica and alkalinity brought to the ocean (Fred T Mackenzie and Garrels, 1966). Formation of authigenic clay minerals consumes elements such as Na, Fe, Mg, and K (F. T. Mackenzie and Garrels, 1966; Isson and Planavsky, 2018), with ~10% of global riverine K consumed during clay formation at shelf region (Michalopoulos and Aller, 1995). Dunlea et al., (2017) emphasised the importance of volcanic ash and biogenic Si as key reactants in the formation of authigenic clay. They further proposed that a decrease in reverse weathering, following the evolution of biogenic silicates (sponges, radiolarians and, later, diatoms), which limits the availability of free silica, significantly influences Cenozoic seawater chemistry. This hypothesis was further supported by a modelling study (Isson and Planavsky, 2018). The formation of authigenic clay mineral has also been suggested to play a major role in driving the long-term changes in seawater chemistry, as indicated by reconstructed seawater lithium isotope ($\delta^{7}Li_{sw}$) (Misra and Froelich, 2012; Kalderon-

Asael et al., 2021). The δ^7Li_{sw} record by Kalderon-Asael et al. (2021) supports the proposed link between the evolution of biogenic silica and the authigenic clay formation, influencing the seawater chemistry as suggested by Dunlea et al., (2017). Authigenic clay is also formed during low-temperature hydrothermal processes occurring at the mid-ocean ridge flanks, which are a sink for K and Mg and source of Ca (Bloch and Bischoff, 1979; Elderfield and Schultz, 1996; Wheat and Mottl, 2000). Wheat and Mottl, 2000 estimated that the flux of K sink on the ridge flank is 25% of riverine flux. While Dunlea et al., 2017 favour a decrease in the uptake of Mg in authigenic clay as a result of an increase in biogenic silica as a significant driver, whereas model based on Mg/Ca and Mg isotopic reconstruction by Higgins and Schrag, 2015, suggested a decrease in Mg sink in low-temperature clay formation could account for Cenozoic Mg changes in seawater. Decrease in the deep ocean temperature since Eocene, can be responsible for the decrease in low-temperature clay formation as these process is temperature dependent (Higgins and Schrag, 2015). Several other studies have highlighted the importance of role of low-temperature clay formation on seawater chemistry changes (Demicco et al., 2005; Coogan and Dosso, 2012, 2015; Coogan and Gillis, 2018); however, further investigations are required to accurately estimate elemental concentration and fluxes in the low-temperature hydrothermal system.

Our LBF-based $\delta^{26}Mg_{sw}$ reconstruction aligns well with existing records reconstructed using aragonitic corals (Gothmann et al., 2017) and pelagic carbonate (Higgins and Schrag, 2015). Both studies, employing a box model, implicated silicate weathering and authigenic clay formation as key drivers in the Mg cycle. They suggested that carbonate weathering or dolomitisation processes do not play a significant role. However, Pogge Von Strandmann et al., 2014 observed ~0.8 ‰ variation with a decline in $\delta^{26}Mg_{sw}$ values during the Oligocene and present, suggested to be the result of a

decrease in dolomite formation, aligning with major cooling. The role of dolomitization on seawater chemistry changes has been suggested to be a more important process by some studies (Holland and Zimmermann, 2000; Zimmermann, 2000; Holland, 2005). On the contrary, other studies, including both model and proxy investigation, suggest that change in dolomitisation has a less pronounced on Cenozoic seawater chemistry (Higgins and Schrag, 2015; Gothmann et al., 2017) and global carbon cycle (Berner et al., 1983).

While, our reconstructed $[Ca^{2+}]_{sw}$ values aligns well with previous model study indicating that the alterations can be accounted for by a reduction in hydrothermal fluxes linked to a decrease in seafloor spreading rates throughout the Cenozoic (Stanley and Hardie, 1998). Combining our results of relatively constant Cenozoic $\delta^{26}Mg_{sw}$ values and marginal increase in Mg during Cenozoic along with existing records, highlights the role of decreasing authigenic clay mineral as significant processes affecting the seawater chemistry. This _explanation is supported by the increase in the seawater _$[K^{+}]_{sw}$. Our finding highlights the role of seafloor spreading rates and the formation of authigenic clay may have significant implications for seawater chemistry, warranting further investigations.

Conclusion

The reconstruction of seawater chemistry changes offers a key to a better understanding of the geological processes that have driven the long-term carbon cycle. We investigated large benthic foraminifera, *Nummulites* sp., in order to reconstruct the past variability in seawater chemistry by utilising a multi-proxy approach (Na/Ca and K/Ca) along with $\delta^{26}Mg$ measurements. Our results demonstrate that the Eocene $[Ca^{2+}]_{sw}$ values were ~1.6-2 times higher, and $[K^{+}]_{sw}$ were ~2 times lower than present-day seawater values. The $[Mg^{2+}]_{sw}$ decreased from early Eocene to late Eocene, following

which it increased towards the present, while the variability in $\delta^{26}Mg_{sw}$ over the Cenozoic period remained within ~0.3 ‰. Combining our results with existing records suggests that decrease in seafloor spreading rate and reverse weathering could potentially drive Cenozoic seawater chemistry changes.

Suplementary material to accompany "Reconstructing Eocene seawater major ion concentrations and magnesium isotopic composition using large benthic foraminifera"

Romi Nambiar, Douglas Coenen, Michael J. Henehan, Sonal Khanolkar, Peter Stassen, Willem Renema, Arnaud Leroy, Fabrice Moreau, Annachiara Bartolini, Didier Merle, Laura Cotton, Wolfgang Müller, David Evans

1. Sample preservation check

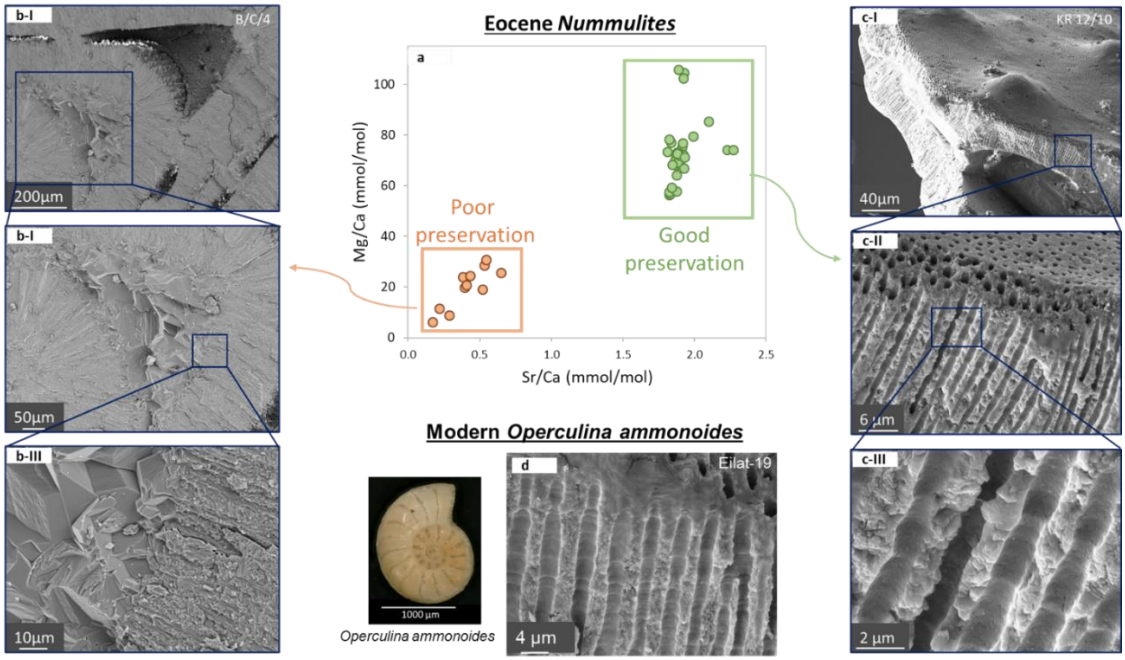

Figure S4. a) Mg/Ca vs Sr/Ca plot for all the fossil samples. SEM images of larger benthic foraminifera b-c) Nummulites sp. and d) modern Operculina ammonoides.

High Mg-calcite may undergo diagenetic alteration by transformation to a more stable form of low-Mg calcite by the loss of Mg and other elements (Turner et al., 1986; Bischoff et al., 1993). While SEM images have been widely used to investigate the diagenetic alteration in fossil samples, some studies have demonstrated that the Mg loss

from high Mg foraminifera can occur without visible alteration in crystal (Towe and Hemleben, 1976; Budd and Hiatt, 1993). One advantage of using high-Mg larger benthic foraminifera as an archive is that the signature of post depositional transformation due to diagenesis can be identified by its elemental composition, with diagenetically altered samples resulting in significantly lower Mg value. Moreover, the distribution coefficient of Mg in these larger benthic foraminifera of Nummulitidae family is much less than unity (Evans et al., 2015), and thus, diagenetic alteration will result in preference loss of Mg from calcite. Hence, we chose to combine information from SEM images and trace element composition to verify the preservation of fossil samples. All the fossils with higher Al/Ca (>0.5 mmol/mol) values were rejected. Further, to investigate the preservation using elemental composition, we also looked into the Mg/Ca and Sr/Ca values of fossil samples. We observed that the poorly preserved samples showing clear recrystallised structure had Mg/Ca and Sr/Ca values an order of magnitude lower than the fossil samples with better preservation and with no infilling or calcite overgrowth (Figure S1). We also checked the SEM images of modern Operculina ammonoides that were collected live from the Gulf of Eilat (Figure S1d). The SEM images of well-preserved (high Mg/Ca and Sr/Ca) *Nummulites* fossil samples (Figure S1c) demonstrated a structure similar to the modern *Operculina ammonoides*.

2. Na/Ca and K/Ca proxy

Laboratory culture experiments of modern larger benthic foraminifera (LBF), *O. ammonoides* grown in different seawater [Ca^{2+}] demonstrated significant relationship for Na/Ca_{LBF}-Na/Ca_{SW} (Hauzer et al., 2018) and K/Ca_{LBF}-K/Ca_{SW} (Nambiar et al., 2023), best described with power relationship, opening up the possibility of using these proxies in LBF of Nummulitidae family for seawater chemistry reconstructions. However, given that

these samples were grown in different seawater [Ca^{2+}], the experiment seawater would experience a change in saturation state (Ω_c), thus affecting the growth rate of foraminifera. The extent to which Ω_c-driven crystal growth rate effect could influence these proxies was investigated based on the second set of culture experiments, where *O. ammonoides* was grown at variable pH/Ω_c but constant DIC, which demonstrated that a one unit change in Ω_c results in 0.0067 mmol mol^{-1} change in K/Ca ratio (Nambiar et al., 2023). The results also demonstrated that a unit change in Ω_c resulted in a 0.766 mmol mol^{-1} change in Na/Ca ratio. In addition, the culture experiment of *O. ammonoides* grown at different $[Mg^{2+}]_{sw}$ showed that the D_{Na} in *O. ammonoides* is influenced by Mg/Ca_{LBF} (Evans et al., 2015). We adjusted the fossil Na/Ca following the recommendation by (Evans et al., in prep.), where the linear relationship between Na/Ca_{LBF} and Mg/Ca_{LBF} is used to estimate the Mg/Ca_{LBF} induced value of Na/Ca_{LBF}, using Mg/Ca_{fossil} and mean culture Mg/Ca_{LBF} of 120 mmol/mol:

$$\mathrm{Na/Ca_{LBF-corrected}} = (120 - \mathrm{Mg/Ca_{LBF}}) \times 0.0679 + \mathrm{Na/Ca_{LBF}} \quad \text{(eq. 1)}$$

this results in the following growth-rate corrected Na/Ca and K/Ca shell-seawater relationships:

$$\mathrm{K/Ca_{LBF}} = 0.212 \pm 0.003 \times \mathrm{K/Ca_{sw}^{0.53 \pm 0.05}} \quad (R^2 = 0.98;\ p = 0.01) \quad \text{(eq. 2)}$$

$$\mathrm{Na/Ca_{LBF-corrected}} = 0.475 \pm 0.009 \times \mathrm{Na/Ca_{sw}} \quad (R^2 = 0.98;\ p = 0.01) \quad \text{(eq. 3)}$$

Where the unit of El/Ca_{LBF} is mmol/mol and K/Ca_{SW} is mol/mol. Given that the residence time of Na in seawater is ~100 million years (Broecker and Peng, 1982), the Na/Ca proxy can be a direct tool to reconstruct seawater [Ca^{2+}]. Moreover, by combining the Na/Ca and K/Ca proxy, we can estimate the variability in the seawater [K^+]. While the correction results in a linear relationship for the Na/Ca proxy, the K/Ca proxy is best described with

power relation. It has to be noted that, here the Na/Ca proxy is corrected for the effect of Mg/Ca on D_{Na}. Considering earlier studies that have demonstrated Mg/Ca of foraminifera shell and inorganic calcite influences the incorporation of elements such as Na and Sr, and noting that a significant correlation observed between D_{Na} and D_K of *O. ammonoides* grown at different $[Ca^{2+}]_{sw}$ (Nambiar et al., 2023), it is plausible that K incorporation may also be subject to the impact of Mg/Ca_{LBF}. However, further investigation is essential to assess the potential effect.

We also chose an alternative approach to estimate changes in seawater $[K^+]$ based on the experiment where *O. ammonoides* was grown at varying $[Ca^{2+}]_{sw}$. In this experiment, the distribution of Na and K showed a strong correlation, primarily governed by the seawater El/Ca ratio (Nambiar et al., 2023 and reference therein). Thus, to delineate the effect of $[Ca^{2+}]_{sw}$ on Na and K incorporation, we took the ratio of K/Ca_{LBF} and Na/Ca_{LBF}. We observed that the variation in the K/Na_{LBF} was within the narrow bound (10.68 - 12.89; average value: 11.56 ± 1.02 (1 SD) mmol/mol), which reflects the values at constant $[K^+]_{sw}$ and $[Na^+]_{sw}$ (K/Na_{sw} = 0.021 mol/mol). Given that $[Na^+]_{sw}$ has remained relatively constant for ~100 Ma, we estimate the past $[K^+]_{sw}$ using the following equation:

$$K_{sw} = \left[\frac{0.021 \times K/Na_{LBF}}{(11.56 \pm 1.02)}\right] \times Na_{sw} \qquad \text{(eq. 4)}$$

Where the unit of Na_{sw} and K_{sw} is mol/Kg, and K/Na_{LBF} is in mmol/mol

3. Mg isotope in modern *Operculina ammonoides*:

Several studies have investigated the $\delta^{26}Mg$ in different marine carbonates (Von Strandmann, 2008; Hippler et al., 2009; Yoshimura et al., 2011; Saenger et al., 2013; Dämmer et al., 2021). Overall, the $\delta^{26}Mg$ values in different marine carbonate are characterized by mineralogy-related variability , with low-Mg calcite showing the most

depleted values, followed by high-Mg calcite, and aragonite displaying the highest $\delta^{26}Mg$ values. The average offset of $\delta^{26}Mg$ with respect to modern seawater for low-Mg calcite, high-Mg calcite, and aragonite were -3.66 ‰, -2.11 ‰ and -1.22 ‰, respectively. The average $\delta^{26}Mg$ offset observed for the modern high-Mg *Operculina ammonoides* investigated in this study (-2.30 ‰) is comparable to previously reported high-Mg marine carbonates (Figure S2). While the data from different marine carbonate suggests a possible mineralogical control (Figure S2) is the dominant driver of the different isotopic compositions of the various archives, the effect of temperature, growth rate, and vital effect cannot be ruled out. Indeed, an effect of temperature on $\delta^{26}Mg$ in some marine carbonates has been reported, including high-Mg calcitic biogenic carbonate (benthic foraminifera, *Amphistegina lessonii* (Dämmer et al., 2021); deep-water corals, *Corallium* sp. (Yoshimura et al., 2011) and aragonitic biogenic carbonate (shallow water corals, *Porites* sp. (Saenger et al., 2013) (Figure S3). We observed no significant effect of seawater temperature and salinity on the $\delta^{26}Mg$ in high-Mg modern larger benthic foraminifera, *Operculina ammonoides* (Figure S3). To compare different marine carbonates, we plot a compilation of Mg isotope fractionation between carbonate and solution ($\Delta^{26}Mg_{carb\text{-}sol}$) against the temperature of this study with previously reported studies (Figure S3). We observe that $\Delta^{26}Mg_{carb\text{-}sol}$ for high-Mg biogenic calcite lies close to that of inorganic calcite, whereas low-Mg biogenic calcite has more negative values. One possible reason could be the significant vital effect in the case of low-Mg biogenic calcite, possibly driven by the modification of the calcification site Mg/Ca fractionating the Mg isotopic composition. Whereas, high-Mg biogenic calcite (e.g., larger benthic foraminifera, *O. ammonoides*) showed a more similar distribution coefficient of Mg (D_{Mg}) to inorganic calcite (Evans et al., 2018), i.e., the Mg/Ca ratio of calcifying fluid is not modified as in case of low-Mg biogenic carbonate. Moreover, the $\Delta^{26}Mg_{carb\text{-}sol}$ in modern

O. ammonoides showed variability between -2.28 to -2.33 ‰, which is close to the inorganic calcite that varied from 2.70 ‰ at 4°C to 2.22 ‰ at 45°C (2SD: 0.1-0.3 ‰) (Li et al., 2012). Given that *O. ammonoides* is a close relative of the nummulitid foraminifera, we use the Mg fractionation of *O. ammonoides* to adjust our *Nummulites* fossil $\delta^{26}Mg$ records in order to estimate past seawater $\delta^{26}Mg$.

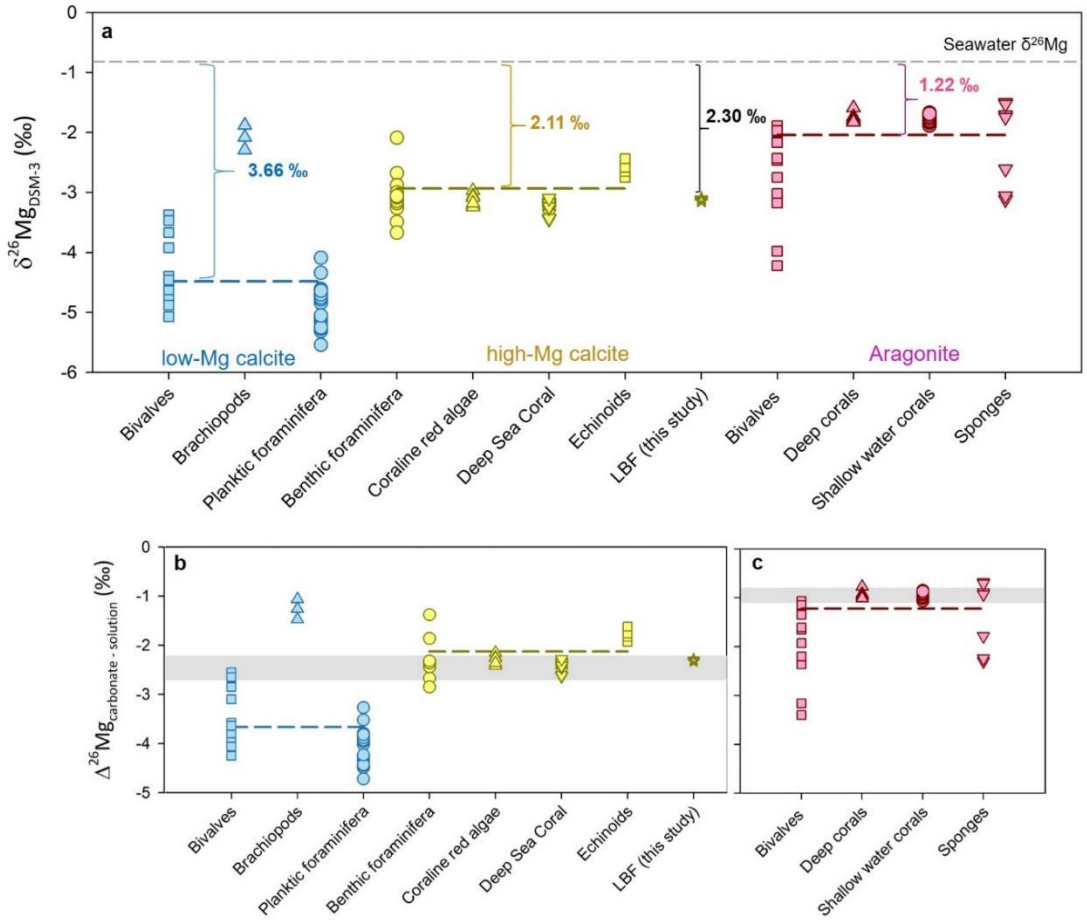

Figure S5. a) Compilation of $\delta^{26}Mg_{DSM-3}$ in modern larger benthic foraminifera, *O. ammonoides* (this study) with existing records of different marine carbonate (Von Strandmann, 2008; Hippler et al., 2009; Yoshimura et al., 2011; Saenger et al., 2013; Dämmer et al., 2021). The dashed line represents present-day seawater $\delta^{26}Mg$ value. The values mention the average offset in the $\delta^{26}Mg$ value of marine carbonate with respect to $\delta^{26}Mg_{sw}$. b,c) $\Delta^{26}Mg_{carb\text{-}solution}$. Shaded region represents

inorganic calcite (ranging from -2.70 ‰ at 4°C to -2.22 ‰ at 45°C; Li et al., 2012) and inorganic aragonite (ranging from -1.09 ‰ at 25°C to -0.81 ‰ at 55°C; Wang et al., 2013).

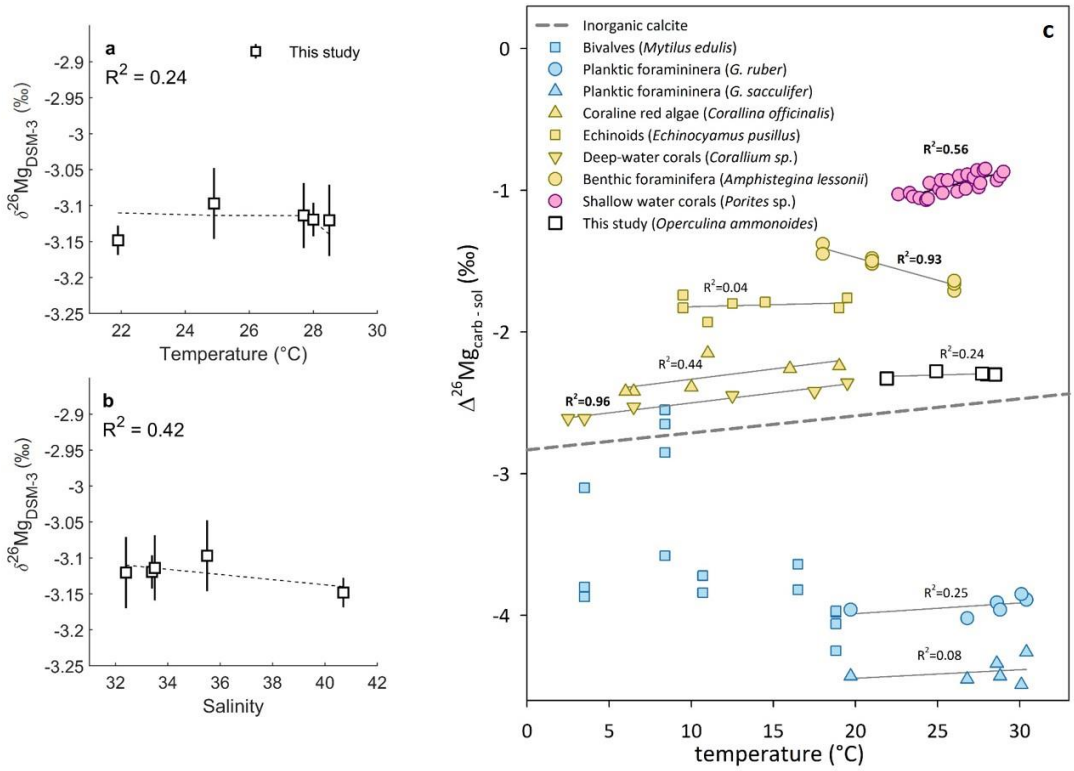

Figure S6. The $\delta^{26}Mg_{DSM-3}$ values in modern *O. ammonoides* plotted against a) temperature and b) salinity. The dashed line represents linear fit, and the error bar represents 1SD. c) Compilation of $\Delta^{26}Mg_{carb-sol}$ against the temperature for *O. ammonoides* (this study) with existing records for different carbonates (Von Strandmann, 2008; Hippler et al., 2009; Yoshimura et al., 2011; Li et al., 2012; Saenger et al., 2013; Dämmer et al., 2021). The symbols represent low-Mg calcitic biogenic marine (blue), high-Mg calcitic biogenic marine (yellow), and aragonitic marine carbonate (pink), and the dashed line represents the best-fit linear line for inorganic calcite.

Table S1. Details of the laser ablation system and ICP-MS operating parameters

Laser Ablation (RESOlution M-50)	
Sampling mode	Spot
Wavelength	193 nm
Fluence	~6.3 J cm^{-2}
Repetition rate	3 Hz
Spot size	50 µm
He	300 - 400 mL min^{-1}
N_2	3.5 - 4.0 mL min^{-1}
SF-ICP-MS (ThermoFisher Scientific Element XR)	
Resolution mode	medium mas resolution (R= ~4000)
Torch RF power	1330 - 1380 W
Sample cone	Ni Jet cone
Skimmer cone	Ni H cone
Sample gas flow	0.80 - 1.00 l min^{-1}
Auxiliary gas flow	0.60 - 0.90 l min^{-1}

Table S2. Details of the MC-ICP-MS operating parameters

MC-ICP-MS (ThermoFisher Scientific Neptune Plus)	
Resolution mode	medium mas resolution
Torch RF power	1200 W
Sample gas flow	1.00 l min^{-1}
Auxiliary gas flow	0.78 l min^{-1}
spray chamber	SIS quartz
Nebulise uptake	~131 µL min^{-1}
Sample cone	standard Ni cone
Skimmer cone	Ni X cone
Sensitivity	~16 V at 500 ppb ^{24}Mg

Table S3. Details of the laser ablation system and ICP-MS operating parameters

	This study (‰)					**Compiled values from Literature (‰)**			
Standard	$\delta^{26}Mg_{DSM-3}$	2SD	$\delta^{25}Mg_{DSM-3}$	2SD	n	$\delta^{26}Mg_{DSM-3}$	2SD	$\delta^{25}Mg_{DSM-3}$	2SD
Cambridge-1[a]	-2.66	0.12	-1.37	0.06	3	-2.62	0.03	-1.34	0.04
IAPSO[a]	-0.80	0.03	-0.42	0.03	3	-0.83	0.05	-0.43	0.04
JCp-1[b]	-2.12	0.13	-1.09	0.06	1	-1.97	0.06	-1.04	0.03
MACS-3	-2.19	0.32	-1.19	0.25	3	-	-	-	-
KCSp-1	-3.65	0.11	-1.89	0.06	5	-	-	-	-

n: no. of replicates. a: Shalev et al., (2018); b: average of published values taken from GEOREM database, version 35 (Jochum et al., 2005).

Acknowledgments

This work is part of the VeWA consortium funded by the Hessen State Ministry for Higher Education, Research, and the Arts through the LOEWE program. We would like to extend our thanks to Pratul Saraswati for providing the samples used in our study. RN would like to thank Jutta Schlegel and Josefine Holtz, for their help during Mg isotope measurements at GFZ, Potsdam. FIERCE is financially supported by the Wilhelm and Else Heraeus Foundation and by the Deutsche Forschungsgemeinschaft (DFG: INST 161/921-1 FUGG, INST 161/923-1 FUGG and INST 161/1073-1 FUGG), which is gratefully acknowledged.

References

Anagnostou E., John E. H., Edgar K. M., Foster G. L., Ridgwell A., Inglis G. N., Pancost R. D., Lunt D. J. and Pearson P. N. (2016) Changing atmospheric CO2 concentration was the primary driver of early Cenozoic climate. *Nature* **533**, 380–384.

Barker S., Greaves M. and Elderfield H. (2003) A study of cleaning procedures used for foraminiferal Mg/Ca paleothermometry. *Geochemistry, Geophysics, Geosystems* **4**, 1–20.

Berner E. K. and Berner R. A. (1996) Global environment water, air, and geochemical cycles Prentice-Hall. *Englewood Cliffs, NewJersey*.

Berner R. A., Lasaga A. C. and Garrels R. M. (1983) Carbonate-silicate geochemical cycle and its effect on atmospheric carbon dioxide over the past 100 million years. *Am. J. Sci.;(United States)* **283**.

Bischoff W. D., Bertram M. A., Mackenzie F. T. and Bishop F. C. (1993) Department ofGeology, Wichita State University, Wichita, KS 67260-0027. , 82–89.

Blackmon P. D. and Todd R. (1959) Mineralogy of some foraminifera as related to their classification and ecology. *Journal of Paleontology*, 1–15.

Bloch S. and Bischoff J. L. (1979) The effect of low-temperature alteration of basalt on the oceanic budget of potassium. *Geology* **7**, 193–196.

Brennan S. T., Lowenstein T. K. and Cendon D. I. (2013) The major-ion composition of cenozoic seawater: the past 36 million years from fluid inclusions inmarine halite. *American Journal of Science* **313**, 713–775.

Broecker W. S. and Peng T. H. (1982) Tracers in the Sea, Lamont-Doherty geological observatory. *Palisades, New York*.

Budd D. A. and Hiatt E. E. (1993) Mineralogical stabilization of high-magnesium calcite; geochemical evidence for intracrystal recrystallization within Holocene porcellaneous foraminifera. *Journal of Sedimentary Research* **63**, 261–274.

Caldeira K. and Berner R. A. (1998) The need for mass balance and feedback in the geochemical carbon cycle: Comment and Reply. *Geology* **26**, 478.

Caves Rugenstein J. K., Ibarra D. E. and von Blanckenburg F. (2019) Neogene cooling driven by land surface reactivity rather than increased weathering fluxes. *Nature* **571**, 99–102.

Chanda P. and Fantle M. S. (2017) Quantifying the effect of diagenetic recrystallization on the Mg isotopic composition of marine carbonates. *Geochimica et Cosmochimica Acta* **204**, 219–239.

Coggon R. M., Teagle D. A. H., Smith-Duque C. E., Alt J. C. and Cooper M. J. (2010) Reconstructing Past Seawater Mg/Ca. *Science* **327**, 1114–1117.

Coogan L. A. and Dosso S. (2012) An internally consistent, probabilistic, determination of ridge-axis hydrothermal fluxes from basalt-hosted systems. *Earth and Planetary Science Letters* **323**–**324**, 92–101.

Coogan L. A. and Dosso S. E. (2015) Alteration of ocean crust provides a strong temperature dependent feedback on the geological carbon cycle and is a primary driver of the Sr-isotopic composition of seawater. *Earth and Planetary Science Letters* **415**, 38–46.

Coogan L. A. and Gillis K. M. (2018) Low-Temperature Alteration of the Seafloor: Impacts on Ocean Chemistry. *Annual Review of Earth and Planetary Sciences* **46**, 21–45.

Coogan L. A., Gillis K. M., Pope M. and Spence J. (2017) The role of low-temperature (off-axis) alteration of the oceanic crust in the global Li-cycle: Insights from the Troodos ophiolite. *Geochimica et Cosmochimica Acta* **203**, 201–215.

Cotton L. J., Evans D. and Beavington-penney S. J. (2020) The High-Magnesium Calcite Origin of Nummulitid Foraminifera and Implications for the Identification of Calcite Diagenesis. *Palaios* **35**, 421–431.

Dalton C. A., Wilson D. S. and Herbert T. D. (2022) Evidence for a Global Slowdown in Seafloor Spreading Since 15 Ma. *Geophysical Research Letters* **49**, 1–9.

Dämmer L. K., van Dijk I., de Nooijer L., van der Wagt B., Wilckens F. K., Zoetemelk B. and Reichart G. J. (2021) Temperature Impact on Magnesium Isotope Fractionation in Cultured Foraminifera. *Frontiers in Earth Science* **9**, 1–13.

Demicco R. V., Lowenstein T. K., Hardie L. A. and Spencer R. J. (2005) Model of seawater composition for the Phanerozoic. *Geology* **33**, 877–880.

Deng K., Yang S. and Guo Y. (2022) A global temperature control of silicate weathering intensity. *Nature Communications* **13**, 1–10.

DePaolo D. J. and Ingram B. L. (1985) High-resolution stratigraphy with strontium isotopes. *Science* **227**, 938–941.

Dickson J. A. D. (1995) Paleozoic Mg calcite preserved: implications for the Carboniferous ocean. *Geology* **23**, 535–538.

Dunlea A. G., Murray R. W., Santiago Ramos D. P. and Higgins J. A. (2017) Cenozoic global cooling and increased seawater Mg/Ca via reduced reverse weathering. *Nature Communications* **8**, 1–7.

Elderfield H. and Schultz A. (1996) Mid-ocean ridge hydrothermal fluxes and the chemical composition of the ocean. *Annual Review of Earth & Planetary Sciences* **24**, 191–224.

Emerson S. and Hedges J. (2008) *Chemical oceanography and the marine carbon cycle*., Cambridge University Press.

Evans D., Brierley C., Raymo M. E., Erez J. and Müller W. (2016) Planktic foraminifera shell chemistry response to seawater chemistry: Pliocene-Pleistocene seawater Mg/Ca, temperature and sea level change. *Earth and Planetary Science Letters* **438**, 139–148.

Evans D., Erez J., Oron S. and Müller W. (2015) Mg/Ca-temperature and seawater-test chemistry relationships in the shallow-dwelling large benthic foraminifera Operculina ammonoides. *Geochimica et Cosmochimica Acta* **148**, 325–342.

Evans D. and Müller W. (2018) Automated Extraction of a Five-Year LA-ICP-MS Trace Element Data Set of Ten Common Glass and Carbonate Reference Materials: Long-Term Data Quality, Optimisation and Laser Cell Homogeneity. *Geostandards and Geoanalytical Research* **42**, 159–188.

Evans D., Müller W., Oron S. and Renema W. (2013) Eocene seasonality and seawater alkaline earth reconstruction using shallow-dwelling large benthic foraminifera. *Earth and Planetary Science Letters* **381**, 104–115.

Evans D., Rosenthal Y., Erez J., Hauzer H., Cotton L., Zhou X., Nambiar R., Stassen P., Pearson P., Renema W., Saraswati P. K., Todd J., Müller W. and Affek H. The seawater calcium concentration is a driver of long-term changes in CO2. *(in preparation)*.

Evans D., Sagoo N., Renema W., Cotton L. J., Müller W., Todd J. A., Saraswati P. K., Stassen P., Ziegler M., Pearson P. N., Valdes P. J. and Affek H. P. (2018) Eocene greenhouse climate revealed by coupled clumped isotope-Mg/Ca thermometry. *Proceedings of the National Academy of Sciences of the United States of America* **115**, 1174–1179.

Fantle M. S., Barnes B. D. and Lau K. V. (2020) The Role of Diagenesis in Shaping the Geochemistry of the Marine Carbonate Record. *Annual Review of Earth and Planetary Sciences* **48**, 549–583.

Foster G. L., Pogge Von Strandmann P. A. E. and Rae J. W. B. (2010) Boron and magnesium isotopic composition of seawater. *Geochemistry, Geophysics, Geosystems* **11**, 1–10.

Gaffin S. (1987) Ridge volume dependence on seafloor generation rate and inversion using long term sealevel change. *American Journal of Science* **287**, 596–611.

Gothmann A. M., Stolarski J., Adkins J. F. and Higgins J. A. (2017) A Cenozoic record of seawater Mg isotopes in well-preserved fossil corals. *Geology* **45**, 1039–1042.

Gothmann A. M., Stolarski J., Adkins J. F., Schoene B., Dennis K. J., Schrag D. P., Mazur M. and Bender M. L. (2015) Fossil corals as an archive of secular variations in seawater chemistry since the Mesozoic. *Geochimica et Cosmochimica Acta* **160**, 188–208.

Hallock P. (1985) Why are larger foraminifera large? *Paleobiology* **11**, 195–208.

Hauzer H., Evans D., Müller W., Rosenthal Y. and Erez J. (2018) Calibration of Na partitioning in the calcitic foraminifer Operculina ammonoides under variable Ca concentration: Toward reconstructing past seawater composition. *Earth and Planetary Science Letters* **497**, 80–91.

Heinrich C. A., Pettke T., Halter W. E., Aigner-Torres M., Audétat A., Günther D., Hattendorf B., Bleiner D., Guillong M. and Horn I. (2003) Quantitative multi-element analysis of minerals, fluid and melt inclusions by laser-ablation inductively-coupled-plasma mass-spectrometry. *Geochimica et Cosmochimica Acta* **67**, 3473–3497.

Hess J., Bender M. L. and Schilling J. G. (1986) Evolution of the ratio of strontium-87 to strontium-86 in seawater from cretaceous to present. *Science* **231**, 979–984.

Higgins J. A. and Schrag D. P. (2015) The Mg isotopic composition of Cenozoic seawater - evidence for a link between Mg-clays, seawater Mg/Ca, and climate. *Earth and Planetary Science Letters* **416**, 73–81.

Hippler D., Buhl D., Witbaard R., Richter D. K. and Immenhauser A. (2009) Towards a better understanding of magnesium-isotope ratios from marine skeletal carbonates. *Geochimica et Cosmochimica Acta* **73**, 6134–6146.

Holland H. D. (2005) Sea level, sediments and the composition of seawater. *American Journal of Science* **305**, 220–239.

Holland H. D. and Zimmermann H. (2000) The dolomite problem revisited1. *International Geology Review* **42**, 481–490.

Holzmann M. and Pawlowski J. (2017) An updated classification of rotaliid foraminifera based on ribosomal DNA phylogeny. *Marine Micropaleontology* **132**, 18–34.

Horita J., Zimmermann H. and Holland H. D. (2002) Chemical evolution of seawater during the Phanerozoic: Implications from the record of marine evaporites. *Geochimica et Cosmochimica Acta* **66**, 3733–3756.

Isson T. T. and Planavsky N. J. (2018) Reverse weathering as a long-term stabilizer of marine pH and planetary climate. *Nature* **560**, 471–475.

Jochum K. P., Nohl U., Herwig K., Lammel E., Stoll B. and Hofmann A. W. (2005) GeoReM: a new geochemical database for reference materials and isotopic standards. *Geostandards and Geoanalytical Research* **29**, 333–338.

Jochum K. P., Stoll B., Herwig K., Willbold M., Hofmiann A. W., Amini M., Aarburg S., Abouchami W., Hellebrand E., Mocek B., Raczek I., Stracke A., Alard O., Bouman C., Becker S., Dücking M., Brätz H., Klemd R., De Bruin D., Canil D., Cornell D., De Hoog C. J., Dalpé C., Danyushevshy L., Eisenhauer A., Gao Y., Snow J. E., Groschopf N., Günther D., Latkoczy C., Guillong M., Hauri E. H., Höfer H. E., Lahaye Y., Horz K., Jacob D. E., Kasemann S. A., Kent A. J. R., Ludwig T., Zack T., Mason P. R. D., Meixner A., Rosner M., Misawa K., Nash B. P., Pfänder J., Premo W. R., Sun W. D., Tiepolo M., Vannucci R., Vennemann T., Wayne D. and Woodhead J. D. (2006) MPI-DING reference glasses for in situ microanalysis: New reference values for element concentrations and isotope ratios. *Geochemistry, Geophysics, Geosystems* **7**.

Jochum K. P., Weis U., Stoll B., Kuzmin D., Yang Q., Raczek I., Jacob D. E., Stracke A., Birbaum K., Frick D. A., Günther D. and Enzweiler J. (2011) Determination of reference values for NIST SRM 610-617 glasses following ISO guidelines. *Geostandards and Geoanalytical Research* **35**, 397–429.

Kalderon-Asael B., Katchinoff J. A. R., Planavsky N. J., Hood A. v. S., Dellinger M., Bellefroid E. J., Jones D. S., Hofmann A., Ossa F. O., Macdonald F. A., Wang C., Isson T. T., Murphy J. G., Higgins J. A., West A. J., Wallace M. W., Asael D. and Pogge von Strandmann P. A. E. (2021) A lithium-isotope perspective on the evolution of carbon and silicon cycles. *Nature* **595**, 394–398.

Li G., Ji J., Chen J. and Kemp D. B. (2009) Evolution of the Cenozoic carbon cycle : The roles of tectonics and CO 2 fertilization. **23**, 1–11.

Li W., Chakraborty S., Beard B. L., Romanek C. S. and Johnson C. M. (2012) Magnesium isotope fractionation during precipitation of inorganic calcite under laboratory conditions. *Earth and Planetary Science Letters* **333**–**334**, 304–316.

Locarnini M., Mishonov A. V, Baranova O. K., Boyer T. P., Zweng M. M., Garcia H. E., Seidov D., Weathers K., Paver C., Smolyar I. and others (2018) World ocean atlas 2018, volume 1: Temperature.

Lowenstein T. K., Hardie L. A., Timofeeff M. N. and Demicco R. V (2003) Secular variation in seawater chemistry and the origin of calcium chloride basinal brines. *Geology* **31**, 857–860.

Mackenzie F. T. and Garrels R. M. (1966) Chemical mass balance between rivers and oceans. *American Journal of Science* **264**, 507–525.

Mackenzie Fred T and Garrels R. M. (1966) Silica-Bicarbonate Balance In The Ocean And Early Diagenesis. **36**, 1075–1084.

Maeda A., Fujita K., Horikawa K., Suzuki A., Yoshimura T., Tamenori Y. and Kawahata H. (2017) Evaluation of oxygen isotope and Mg/Ca ratios in high-magnesium calcite from benthic foraminifera as a proxy for water temperature. *Journal of Geophysical Research: Biogeosciences* **122**, 185–199.

McArthur J. M., Howarth R. J., Shields G. A. and Zhou Y. (2020) *Strontium Isotope Stratigraphy*., BV.

Meybeck M. (1987) Global chemical weathering of surficial rocks estimated from river dissolved loads. *American journal of science* **287**, 401–428.

Michalopoulos P. and Aller R. C. (1995) Rapid clay mineral formation in Amazon delta sediments: Reverse weathering and oceanic elemental cycles. *Science* **270**, 614–617.

Misra S. and Froelich P. N. (2012) Lithium isotope history of cenozoic seawater: Changes in silicate weathering and reverse weathering. *Science* **335**, 818–823.

Mucci A. and Morse J. W. (1983) The incorporation of Mg2+ and Sr2+ into calcite overgrowths: influences of growth rate and solution composition. *Geochimica et Cosmochimica Acta* **47**, 217–233.

Müller W., Shelley M., Miller P. and Broude S. (2009) Initial performance metrics of a new custom-designed ArF excimer LA-ICPMS system coupled to a two-volume laser-ablation cell. *Journal of Analytical Atomic Spectrometry* **24**, 209–214.

Nambiar R., Hauzer H., Gray W. R., Henehan M. J., Cotton L., Erez J., Rosenthal Y., Renema W., Müller W. and Evans D. (2023) Controls on potassium incorporation in foraminifera and other marine calcifying organisms. *Geochimica et Cosmochimica Acta* **351**, 125–138.

Nambiar R., Kniest J. F., Schmidt A., Raddatz J., Müller W. and Evans D. (2024) Accurate measurement of K/Ca in low-[K] carbonate samples using laser-ablation sector-field inductively coupled plasmamass spectrometry. *Rapid Communications in Mass Spectrometry*. **38**.

O'Brien C. L., Robinson S. A., Pancost R. D., Sinninghe Damsté J. S., Schouten S., Lunt D. J., Alsenz H., Bornemann A., Bottini C., Brassell S. C., Farnsworth A., Forster A., Huber B. T., Inglis G. N., Jenkyns H. C., Linnert C., Littler K., Markwick P., McAnena A., Mutterlose J., Naafs B. D. A., Püttmann W., Sluijs A., van Helmond N. A. G. M., Vellekoop J., Wagner T. and Wrobel N. E. (2017) Cretaceous sea-surface temperature evolution: Constraints from TEX86 and planktonic foraminiferal oxygen isotopes. *Earth-Science Reviews* **172**, 224–247.

Okai T., Suzuki A., Kawahata H., Terashima S. and Imai N. (2002) Preparation of a new Geological Survey of Japan geochemical reference material: Coral JCp-1. *Geostandards Newsletter* **26**, 95–99.

Pearce N. J. G., Perkins W. T., Westgate J. A., Gorton M. P., Jackson S. E., Neal C. R. and Chenery S. P. (1997) A compilation of new and published major and trace element data for NIST SRM 610 and NIST SRM 612 glass reference materials. *Geostandards newsletter* **21**, 115–144.

Pegram W. J. and Turekian K. K. (1999) The osmium isotopic composition change of Cenozoic sea water as inferred from a deep-sea core corrected for meteoritic contributions. *Geochimica et Cosmochimica Acta* **63**, 4053–4058.

Peucker-Ehrenbrink B. and Ravizza G. (2000) The marine osmium isotope record. *Terra Nova* **12**, 205–219.

Pogge Von Strandmann P. A. E., Forshaw J. and Schmidt D. N. (2014) Modern and Cenozoic records of seawater magnesium from foraminiferal Mg isotopes. *Biogeosciences* **11**, 5155–5168.

Purton L. M. A. and Brasier M. D. (1999) Giant protist Nummulites and its Eocene environment: Life span and habitat insights from $δ$18O and $δ$13C data from Nummulites and Venericardia, Hampshire basin, UK. *Geology* **27**, 711–714.

Rae J. W. B., Zhang Y. G., Liu X., Foster G. L., Stoll H. M. and Whiteford R. D. M. (2021) Atmospheric CO2 over the past 66 million years from marine archives. *Annual Review of Earth and Planetary Sciences* **49**, 609–641.

Raja R., Saraswati P. K. and Iwao K. (2007) A field-based study on variation in Mg/Ca and Sr/Ca in larger benthic foraminifera. *Geochemistry, Geophysics, Geosystems* **8**.

Ram S. and Erez J. (2021) The Distribution Coefficients of Major and Minor Elements in Coral Skeletons Under Variable Calcium Seawater Concentrations. *Frontiers in Earth Science* **9**, 1–14.

Raymo M. E. and Ruddiman W. F. (1992) Tectonic forcing of late Cenozoic climate. *Nature* **359**, 117–122.

Royer D. L. (2014) *Atmospheric CO2 and O2 During the Phanerozoic : Tools , Patterns , and Impacts*. 2nd ed., Elsevier Ltd.

Saenger C., Wang Z., Gaetani G., Cohen A. and Lough J. M. (2013) The influence of temperature and vital effects on magnesium isotope variability in Porites and Astrangia corals. *Chemical Geology* **360**–**361**, 105–117.

Shalev N., Farkaš J., Fietzke J., Novák M., Schuessler J. A., Pogge von Strandmann P. A. E. and Törber P. B. (2018) Mg Isotope Interlaboratory Comparison of Reference Materials from Earth-Surface Low-Temperature Environments. *Geostandards and Geoanalytical Research* **42**, 205–221.

Stanley S. M. and Hardie L. A. (1998) Secular oscillations in the carbonate mineralogy of reef-building and sediment-producing organisms driven by tectonically forced shifts in seawater chemistry. *Palaeogeography, Palaeoclimatology, Palaeoecology* **144**, 3–19.

Stehli F. G. and Hower J. (1961) Mineralogy and early diagenesis of carbonate sediments. *Journal of Sedimentary Research* **31**, 358–371.

Von Strandmann P. A. E. P. (2008) Precise magnesium isotope measurements in core top planktic and benthic foraminifera. *Geochemistry, Geophysics, Geosystems* **9**.

Towe K. M. and Hemleben C. (1976) Diagenesis of magnesian calcite: Evidence from miliolacean foraminifera. *Geology* **4**, 337–339.

Turner J. V., Anderson T. F., Sandberg P. A. and Goldstein S. J. (1986) Isotopic, chemical and textural relations during the experimental alteration of biogenic high-magnesian calcite. *Geochimica et Cosmochimica Acta* **50**, 495–506.

Walker J. C. G., Hays P. B. and Kasting J. F. (1981) Weathering rates in 106 gm km -2 yr -1 of dissolved Si02 . Parentheses signify. *Journal of Geophysical Research* **86**, 9776–9782.

Wang Z., Hu P., Gaetani G., Liu C., Saenger C., Cohen A. and Hart S. (2013) Experimental calibration of Mg isotope fractionation between aragonite and seawater. *Geochimica et Cosmochimica Acta* **102**, 113–123.

Wefer G. and Berger W. H. (1980) Stable isotopes in benthic foraminifera: seasonal variation in large tropical species. *Science* **209**, 803–805.

Wheat C. G. and Mottl M. J. (2000) Composition of pore and spring waters from Baby Bare: Global implications of geochemical fluxes from a ridge flank hydrothermal system. *Geochimica et Cosmochimica Acta* **64**, 629–642.

Yoshimura T., Maeda A., Tamenori Y., Suzuki A., Fujita K. and Kawahata H. (2019) Partitioning and chemical environments of minor elements in individual large benthic foraminifera cultured in temperature-controlled tanks. *Frontiers in Earth Science* **7**, 124.

Yoshimura T., Tanimizu M., Inoue M., Suzuki A., Iwasaki N. and Kawahata H. (2011) Mg isotope fractionation in biogenic carbonates of deep-sea coral, benthic foraminifera, and hermatypic coral. *Analytical and Bioanalytical Chemistry* **401**, 2755–2769.

Zhou X., Rosenthal Y., Haynes L., Si W., Evans D., Huang K. F., Hönisch B. and Erez J. (2021) Planktic foraminiferal Na/Ca: A potential proxy for seawater calcium concentration. *Geochimica et Cosmochimica Acta* **305**, 306–322.

Zimmermann H. (2000) Tertiary seawater chemistry; implications from primary fluid inclusions in marine halite. *American Journal of Science* **300**, 723–767.

Zweng M. M., Seidov D., Boyer T., Locarnini M., Garcia H., Mishonov A., Baranova O. K., Weathers K., Paver C. R., Smolyar I. and others (2019) World ocean atlas 2018, volume 2: Salinity.

Thesis summary

Determining past changes in seawater chemistry is an important link in understanding the large-scale geologic processes that drive long-term changes in the carbon cycle. In this thesis, changes in Eocene $[Ca^{2+}]_{sw}$, $[Mg^{2+}]_{sw}$, $[K^{+}]_{sw}$ and $\delta^{26}Mg_{sw}$ were reconstructed using foraminiferal trace element/calcium proxies (K/Ca, Na/Ca, Mg/Ca) combined with previously reported Mg/Ca_{sw} (Evans et al., 2018) as well as the magnesium isotopes proxy ($\delta^{26}Mg$) in large benthic foraminifera (*Nummulites* sp.).

In Chapter 2, the measurement protocol for measuring K/Ca in low K-containing carbonate samples using LA-ICPMS was developed (Nambiar et al., 2024). A range of reference materials were investigated, including various MPI-DING glasses (GOR 128-G, GOR 132-G, ATHO-G, KL2-G, and StHs 6/80-G), as well as carbonate reference materials (JCp-1NP, JCt-1NP, and MACS-3NP) using LA-ICPMS in medium and high mass resolution modes. The results demonstrate that medium mass resolution (MR) is sufficiently capable of minimizing the effect of ArH^{+} interference on the K^{+} peak, yielding accurate results (<1%) with a long-term precision (intermediate reproducibility) of <6% (RSD) for carbonate reference material, JCp-1NP. In addition, this study demonstrated that potassium is prone to surface contamination and suggests careful surface cleaning, pre-ablation, or data processing by eliminating the initial (surface-influenced) data. Analysing the original powder version of the carbonate reference material JCp-1 revealed potential Al and K contamination. Despite being homogenised, K/Ca values in the original JCp-1 varied depending on the analytical technique and/or choice of dissolution methodology prior to measurement. The results also highlighted different downhole fractionation of K/Ca and Na/Ca in a range of reference materials relative to the calibration reference material (NIST SRM 610). The effect of this downhole fractionation

could be corrected using element-specific fractionation factor value, leading to more accurate measurements.

Following the findings of different downhole fractionation for alkali elements (Chapter 2), further investigation into downhole fractionation for a range of elements in different geological reference materials and correction for its impact was conducted in Chapter 3. In this study, the focus was to 1) evaluate downhole fractionation for elements including Li, B, Na, K, Mg, Fe, Zn, Sr, and Ba in different geological reference materials (RMs) relative to the NIST SRM 610/612 calibration reference material, and 2) evaluate the impact of correction using element-specific downhole fractionation on data quality (Nambiar et al., *submitted*). The results demonstrated that the mean values before and after the proposed element-specific downhole fractionation correction significantly differ, particularly in the case of alkali elements and volatile elements of all reference materials under investigation and boron in the case of the carbonate reference materials. In contrast, alkaline earth metals showed the least fractionation, with the El/Ca values before and after applying the downhole fractionation correction being statistically indistinguishable. The proposed correction for downhole fractionation significantly improved accuracy for elements such as alkali elements, while in a few cases (e.g., B in JCp-1NP), the accuracy worsened, highlighting the potential underlying challenges in the reported values for the reference material. Irrespective, routine application of the correction for the downhole fractionation can improve the data quality of measurements during non-matrix matched calibration using LA-ICPMS.

The methodological developments described above were utilised to investigate K/Ca along with other El/Ca in modern field-collected and laboratory-cultured specimens of the large benthic foraminifera (LBF), *Operculina ammonoides* (Chapter 4). Laboratory-cultured *Operculina ammonoides* were grown at four different $[Ca^{2+}]_{sw}$, repeated for three

sets of temperatures. A significant relationship between K/Ca_{sw} and K/Ca_{LBF} was observed; however, this relationship has a shallower slope compared to most other trace elements reported earlier (e.g., Mg/Ca-Mg/Ca_{sw} and Na/Ca-Na/Ca_{sw}; Evans et al., 2015; Hauzer et al., 2021). This shallow relationship between seawater and shell K/Ca can be driven by a crystal growth rate effect on K incorporation. This was addressed by applying a growth-rate correction using the relationship between K/Ca and saturation state (Ω_C), constrained using another set of culture experiments of *O. ammonoides* grown at different pH. To further test the effect of seawater parameters on the K/Ca proxy, modern *O. ammonoides* collected from different regions were investigated. No resolvable effect of temperature, salinity, pH, or $[CO_3]^{2-}$ on K incorporation in *O. ammonoides* was found, allowing K/Ca_{LBF} as a potential proxy to reconstruct past seawater chemistry. If the concept of constant seawater $[K^+]$ throughout the Phanerozoic is true (Horita et al., 2002), the K/Ca proxy could serve as a direct tool to investigate past changes in seawater $[Ca^{2+}]$, following a similar concept to the Na/Ca proxy (Hauzer et al., 2018). Alternatively, a multi-proxy approach could be used, combining Na/Ca and K/Ca to verify whether seawater $[K^+]$ was constant. This is the first time a K/Ca proxy in foraminifera has been developed for seawater chemistry reconstructions. Since *O. ammonoides* is a close living relative of the nummulitid foraminifera, which were abundant during the Paleogene, this group, along with the calibration presented in this work, may represent a valuable source for the reconstruction of Cenozoic seawater chemistry.

Utilising the K/Ca proxy established in Chapter 4 and other proxies (Na/Ca, Mg/Ca, and Mg isotopes), Eocene *Nummulites* fossils collected from the Paris Basin, Hampshire Basin, and tropical regions (Tanzania, Indonesia, and India) were investigated (Chapter 5). Using the Na/Ca proxy, Eocene $[Ca^{2+}]_{sw}$ were reconstructed, and by combining these reconstructed values of $[Ca^{2+}]_{sw}$ with previously published Mg/Ca_{sw}

values (Evans et al., 2018), $[Mg^{2+}]_{sw}$ were determined. This is the first time the concentrations of seawater Ca and Mg during the Eocene were reconstructed using foraminifera. The reconstructed Eocene $[Ca^{2+}]_{sw}$ values were 1.6-2 times higher than the present, whereas $[Mg^{2+}]_{sw}$ decreased from early Eocene ($54.3^{+7.9}_{-9.6}$ mmol kg^{-1} at ~55 Ma) to late Eocene($37.8^{+4.4}_{-4.3}$ mmol kg^{-1} at ~31 Ma), followed by an increase towards the modern seawater composition. This study is the first to demonstrate that seawater $[K^{+}]$ has varied in the past and was ~2 times lower during the Eocene compared to the modern seawater value. In addition, the reconstructed Eocene $\delta^{26}Mg_{sw}$ value using LBF (*Nummulites* sp.) suggests that $\delta^{26}Mg_{sw}$ during the Cenozoic era remained relatively constant (within ~0.3 ‰ of modern seawater signature). The $\delta^{26}Mg_{sw}$ results align well with values derived from different marine archives in previous studies (pelagic bulk carbonates: Higgins and Schrag, 2015; aragonitic coral: Gothmann et al., 2017). Combining the obtained results with existing records alternatively suggests that the complete suite of elemental and isotopic data considered here can be explained by a decrease in seafloor spreading rates and a reduction in authigenic clay formation, highlighting the importance of these processes in driving long-term changes in the carbon cycle.

Future directions

The main results of this thesis are: i) a method to measure K/Ca in low [K] marine carbonate using LA-ICPMS was established, ii) the K/Ca ratio of LBF as a potential proxy for the reconstruction of the seawater K cycle was developed, allowing iii) changes in Eocene $[Ca^{2+}]_{sw}$, $[Mg^{2+}]_{sw}$, $[K^{+}]_{sw}$ and $\delta^{26}Mg_{sw}$ to be reconstructed using the K/Ca, Na/Ca, Mg/Ca and $\delta^{26}Mg$ proxies. Building on these advances, the following future research directions are suggested:

1. Exploring the incorporation of potassium (K) in inorganic calcite and other commonly used marine carbonates will offer valuable insights into the process of K incorporation in carbonates. Nambiar et al. (2023) showed a significant relationship between K/Ca in *O. ammonoides* and $K/Ca_{sw,}$ albeit with a shallow slope compared to most other trace elements reported earlier (e.g., Mg/Ca and Na/Ca; Evans et al., 2015; Hauzer et al., 2021). This shallow slope was proposed to be driven by a crystal growth rate effect on K incorporation. Correcting for the growth rate effect (as described above), a significant power relation between K/Ca_{LBF} and K/Ca_{sw} was observed, allowing its application to Eocene LBF (*Nummulites* sp.) for the reconstruction of seawater chemistry (Nambiar et al., 2023). In addition, unlike other alkali element proxies (e.g., Na/Ca), similar K/Ca values in a range of marine carbonates were observed, irrespective of their shell mineralogy. While it is difficult to reconcile the relative constancy of K/Ca values in a range of marine carbonates independent of shell mineralogy, further investigation on K incorporation and its host site is essential to unravel the underlying mechanisms. This further investigation would enhance the current understanding of biomineralisation processes and improve the accuracy of seawater chemistry reconstructions using K/Ca proxy.

2. The work presented in this thesis is the first reconstruction of individual elemental concentrations of Eocene seawater, namely, $[Ca^{2+}]_{sw}$, $[Mg^{2+}]_{sw}$, and $[K^{+}]_{sw}$ using larger benthic foraminifera (LBFs). However, there is still a significant period of the Cenozoic era that lacks information (e.g., late Oligocene to early Miocene), reconstruction of which would be critical for understanding the overall changes in Cenozoic seawater chemistry and their driving processes. In addition, while seawater chemistry variability combined with existing records can provide information regarding the possible driving process of seawater chemistry variability, building these new data into box models will help verify the major drivers of seawater chemistry.

3. The potassium isotope system has recently been proposed as a new tracer for global potassium cycling (Santiago Ramos et al., 2018; Li et al., 2019; Zheng et al., 2022). Given that ~90% of riverine K is derived from the silicate weathering process, the reconstruction of $\delta^{41}K_{sw}$ values has been proposed as a potential proxy to determine the intensity of continental weathering (Li et al., 2019). With emerging information on the K isotope in different systems, including global river waters (Wang et al., 2021), reverse weathering (Santiago Ramos et al., 2018) and hydrothermal process (Zheng et al., 2022), the reconstruction of seawater $\delta^{41}K$ values may be a potential tracer for improving current understanding of the K-cycle and better constraining which are the significant geological driving process of the seawater chemistry during the Cenozoic era.

References

Adams C. G., Lee D. E. and Rosen B. R. (1990) Conflicting isotopic and biotic evidence for tropical sea-surface temperatures during the Tertiary. *Palaeogeography, Palaeoclimatology, Palaeoecology* 77, 289–313.

Agterhuis T., Ziegler M., de Winter N. J. and Lourens L. J. (2022) Warm deep-sea temperatures across Eocene Thermal Maximum 2 from clumped isotope thermometry. *Communications Earth and Environment* 3, 1–9.

Allen K. A. and Hönisch B. (2012) The planktic foraminiferal B/Ca proxy for seawater carbonate chemistry: A critical evaluation. *Earth and Planetary Science Letters* 345–348, 203–211.

Anagnostou E., John E. H., Edgar K. M., Foster G. L., Ridgwell A., Inglis G. N., Pancost R. D., Lunt D. J. and Pearson P. N. (2016) Changing atmospheric CO_2 concentration was the primary driver of early Cenozoic climate. *Nature* 533, 380–384.

Beavington-Penney S. J. and Racey A. (2004) Ecology of extant nummulitids and other larger benthic foraminifera: Applications in palaeoenvironmental analysis. *Earth-Science Reviews* 67, 219–265.

Beerling D. J. and Royer D. L. (2011) Convergent Cenozoic CO 2 history. *Nature Geoscience* 4, 418–420.

Bellotto V. R. and Miekeley N. (2000) Improvements in calibration procedures for the quantitative determination of trace elements in carbonate material (mussel shells) by laser ablation ICP-MS. *Fresenius' Journal of Analytical Chemistry* 367, 635–640.

Bentov S., Brownlee C. and Erez J. (2009) The role of seawater endocytosis in the biomineralization process in calcareous foraminifera. *Proceedings of the National Academy of Sciences of the United States of America* 106, 21500–21504.

Berner R. A., Lasaga A. C. and Garrels R. M. (1983) Carbonate-silicate geochemical cycle and its effect on atmospheric carbon dioxide over the past 100 million years. *Am. J. Sci.;(United States)* 283.

Binczewskaa A., Astemanb I. P. and Farmerc E. J. (2015) Foraminifers (Benthic). In *Encyclopedia of Marine Geosciences* pp. 1–8.

Bloch S. and Bischoff J. L. (1979) The effect of low-temperature alteration of basalt on the oceanic budget of potassium. *Geology* 7, 193–196.

Boersma A. (1998) Foraminifera. In *Introduction to marine micropaleontology* Elsevier. pp. 19–77.

BouDagher-Fadel M. K. (2008) Biology and evolutionary history of larger benthic foraminifera. *Developments in palaeontology and stratigraphy* 21, 1–37.

Boyle E. A. (1981) Cadmium, zinc, copper, and barium in foraminifera tests. *Earth and Planetary Science Letters* 53, 11–35.

Brennan S. T., Lowenstein T. K. and Cendon D. I. (2013) The major-ion composition of cenozoic seawater: the past 36 million years from fluid inclusions inmarine halite. *American Journal of Science* 313, 713–775.

Broecker W. S. and Peng T. H. (1982) Tracers in the Sea, Lamont-Doherty geological observatory. *Palisades, New York*.

Brown R. E., Anderson L. D., Thomas E. and Zachos J. C. (2011) A core-top calibration of B/Ca in the benthic foraminifers Nuttallides umbonifera and Oridorsalis umbonatus: A proxy for Cenozoic bottom water carbonate saturation. *Earth and Planetary Science Letters* 310, 360–368.

Caldeira K. and Berner R. A. (1998) The need for mass balance and feedback in the geochemical carbon cycle: Comment and Reply. *Geology* 26, 478.

Caves Rugenstein J. K., Ibarra D. E. and von Blanckenburg F. (2019) Neogene cooling driven by land surface reactivity rather than increased weathering fluxes. *Nature* 571, 99–102.

Coggon R. M., Teagle D. A. H., Smith-Duque C. E., Alt J. C. and Cooper M. J. (2010) Reconstructing Past Seawater Mg/Ca. *Science* 327, 1114–1117.

Coogan L. A. and Dosso S. E. (2015) Alteration of ocean crust provides a strong temperature dependent feedback on the geological carbon cycle and is a primary driver of the Sr-isotopic composition of seawater. *Earth and Planetary Science Letters* 415, 38–46.

Coogan L. A. and Dosso S. E. (2022) Controls on the evolution of Cenozoic seawater chemistry. *Geochimica et Cosmochimica Acta* 329, 22–37.

Coogan L. A. and Gillis K. M. (2013) Evidence that low-temperature oceanic hydrothermal systems play an important role in the silicate-carbonate weathering cycle and long-term climate regulation. *Geochemistry, Geophysics, Geosystems* 14, 1771–1786.

Cotton L. J., Evans D. and Beavington-penney S. J. (2020) The High-Magnesium Calcite Origin of Nummulitid Foraminifera and Implications for the Identification of Calcite Diagenesis. *Palaios* 35, 421–431.

Cowen R. (1983) Algal symbiosis and its recognition in the fossil record. In *Biotic interactions in recent and fossil benthic communities* Springer. pp. 431–478.

Cramer B. S., Toggweiler J. R., Wright J. D., Katz M. E. and Miller K. G. (2009) Ocean overturning since the Late Cretaceous: Inferences from a new benthic foraminiferal isotope compilation. *Paleoceanography* 24.

Demicco R. V., Lowenstein T. K., Hardie L. A. and Spencer R. J. (2005) Model of seawater composition for the Phanerozoic. *Geology* 33, 877–880.

Deng K., Yang S. and Guo Y. (2022) A global temperature control of silicate weathering intensity. *Nature Communications* 13, 1–10.

Dettmering C., Röttger R., Hohenegger J. and Schmaljohann R. (1998) The trimorphic life cycle in

foraminifera: observations from cultures allow new evaluation. *European Journal of Protistology* 34, 363–368.

van Dijk I., de Nooijer L. J., Wolthers M. and Reichart G.-J. (2017) Impacts of pH and [CO_3^{2-}] on the incorporation of Zn in foraminiferal calcite. *Geochimica et Cosmochimica Acta* 197, 263–277.

Diwakar P. K., Harilal S. S., Lahaye N. L., Hassanein A. and Kulkarni P. (2013) The influence of laser pulse duration and energy on ICP-MS signal intensity, elemental fractionation, and particle size distribution in NIR fs-LA-ICP-MS. *Journal of Analytical Atomic Spectrometry* 28, 1420–1429.

Douglas D. N., Managh A. J., Reid H. J. and Sharp B. L. (2015) High-Speed, Integrated Ablation Cell and Dual Concentric Injector Plasma Torch for Laser Ablation-Inductively Coupled Plasma Mass Spectrometry. *Analytical Chemistry* 87, 11285–11294.

Dunlea A. G., Murray R. W., Santiago Ramos D. P. and Higgins J. A. (2017) Cenozoic global cooling and increased seawater Mg/Ca via reduced reverse weathering. *Nature Communications* 8, 1–7.

Durrant S. F. (1994) Feasibility of improvement in analytical performance in laser ablation inductively coupled plasma-mass spectrometry (LA-ICP-MS) by addition of nitrogen to the argon plasma. *Fresenius' journal of analytical chemistry* 349, 768–771.

Eggins S., De Deckker P. and Marshall J. (2003) Mg/Ca variation in planktonic foraminifera tests: Implications for reconstructing -palaeo-seawater temperature and habitat migration. *Earth and Planetary Science Letters* 212, 291–306.

Elderfield H., Bertram C. J. and Erez J. (1996) A biomineralization model for the incorporation of trace elements into foraminiferal calcium carbonate. *Earth and Planetary Science Letters* 142, 409–423.

Emiliani C. (1955) Pleistocene temperatures. *The Journal of geology* 63, 538–578.

Erez J. (2003a) The source of ions for biomineralization in foraminifera and their implications for paleoceanographic proxies. *Reviews in mineralogy and geochemistry* 54, 115–149.

Erez J. (2003b) The Source of Ions for Biomineralization in Foraminifera and Their Implications for Paleoceanographic Proxies. *Reviews in Mineralogy and Geochemistry* 54, 115–149.

Evans D., Brierley C., Raymo M. E., Erez J. and Müller W. (2016) Planktic foraminifera shell chemistry response to seawater chemistry: Pliocene-Pleistocene seawater Mg/Ca, temperature and sea level change. *Earth and Planetary Science Letters* 438, 139–148.

Evans D., Erez J., Oron S. and Müller W. (2015) Mg/Ca-temperature and seawater-test chemistry relationships in the shallow-dwelling large benthic foraminifera Operculina ammonoides. *Geochimica et Cosmochimica Acta* 148, 325–342.

Evans D. and Müller W. (2018) Automated Extraction of a Five-Year LA-ICP-MS Trace Element Data Set of Ten Common Glass and Carbonate Reference Materials: Long-Term Data Quality, Optimisation and Laser Cell Homogeneity. *Geostandards and Geoanalytical Research* 42, 159–188.

Evans D. and Müller W. (2013) LA-ICPMS elemental imaging of complex discontinuous carbonates: An example using large benthic foraminifera. *Journal of Analytical Atomic Spectrometry* 28, 1039–1044.

Evans D., Müller W., Oron S. and Renema W. (2013) Eocene seasonality and seawater alkaline earth reconstruction using shallow-dwelling large benthic foraminifera. *Earth and Planetary Science Letters* 381, 104–115.

Evans D., Sagoo N., Renema W., Cotton L. J., Müller W., Todd J. A., Saraswati P. K., Stassen P., Ziegler M., Pearson P. N., Valdes P. J. and Affek H. P. (2018) Eocene greenhouse climate revealed by coupled clumped isotope-Mg/Ca thermometry. *Proceedings of the National Academy of Sciences of the United States of America* 115, 1174–1179.

Fernández-Suárez J., Sánchez Martínez S. and Fuenlabrada J. M. (2021) Geochemistry in earth sciences: a brief overview. *Journal of Iberian Geology* 47, 3–13.

Fitzsimons I. C. W., Harte B. and Clark R. M. (2000) SIMS stable isotope measurement: counting statistics and analytical precision. *Mineralogical Magazine* 64, 59–83.

Foster G. L., Pogge Von Strandmann P. A. E. and Rae J. W. B. (2010) Boron and magnesium isotopic composition of seawater. *Geochemistry, Geophysics, Geosystems* 11, 1–10.

Galy A., Yoffe O., Janney P. E., Williams R. W., Cloquet C., Alard O., Halicz L., Wadhwa M., Hutcheon I. D., Ramon E. and Carignan J. (2003) Magnesium isotope heterogeneity of the isotopic standard SRM980 and new reference materials for magnesium-isotope-ratio measurements. *Journal of Analytical Atomic Spectrometry* 18, 1352–1356.

Ghosh P., Adkins J., Affek H., Balta B., Guo W., Schauble E. A., Schrag D. and Eiler J. M. (2006) ^{13}C--^{18}O bonds in carbonate minerals: A new kind of paleothermometer. *Geochimica et Cosmochimica Acta* 70, 1439–1456.

Gothmann A. M., Stolarski J., Adkins J. F. and Higgins J. A. (2017) A Cenozoic record of seawater Mg isotopes in well-preserved fossil corals. *Geology* 45, 1039–1042.

Gothmann A. M., Stolarski J., Adkins J. F., Schoene B., Dennis K. J., Schrag D. P., Mazur M. and Bender M. L. (2015) Fossil corals as an archive of secular variations in seawater chemistry since the Mesozoic. *Geochimica et Cosmochimica Acta* 160, 188–208.

Gray A. L. (1985) Solid sample introduction by laser ablation for inductively coupled plasma source mass spectrometry. *Analyst* 110, 551–556.

Gray W. R. and Evans D. (2019) Nonthermal Influences on Mg/Ca in Planktonic Foraminifera: A Review of Culture Studies and Application to the Last Glacial Maximum. *Paleoceanography and Paleoclimatology* 34, 306–315.

Guillong M. and Günther D. (2002) Effect of particle size distribution on ICP-induced elemental fractionation in laser ablation-inductively coupled plasma-mass spectrometry. *Journal of Analytical Atomic Spectrometry* 17, 831–837.

Guillong M., Horn I. and Günther D. (2003) A comparison of 266 nm, 213 nm and 193 nm produced from a single solid state Nd:YAG laser for laser ablation ICP-MS. *Journal of Analytical Atomic Spectrometry* 18, 1224–1230.

Günther D. and Heinrich C. A. (1999) Enhanced sensitivity in laser ablation-ICP mass spectrometry using helium-argon mixtures as aerosol carrier. *Journal of Analytical Atomic Spectrometry* 14, 1363–1368.

Hain M. P., Sigman D. M., Higgins J. A. and Haug G. H. (2015) The effects of secular calcium and magnesium concentration changes on the thermodynamics of seawater acid/base chemistry: Implications for Eocene and Cretaceous ocean carbon chemistry and buffering. *Global Biogeochemical Cycles* 29, 517–533.

Hallock P. (1981) Algal symbiosis: a mathematical analysis. *Marine Biology* 62, 249–255.

Hallock P. (1985) Why are larger foraminifera large? *Paleobiology* 11, 195–208.

Hardie L. A. (1996) Secular variation in seawater chemistry: An explanation for the coupled secular variation in the mineralogies of marine limestones and potash evaporites over the past 600 m.y. *Geology* 24, 279–283.

Hathorne E. C., Alard O., James R. H. and Rogers N. W. (2003) Determination of intratest variability of trace elements in foraminifera by laser ablation inductively coupled plasma-mass spectrometry. *Geochemistry, Geophysics, Geosystems* 4.

Hathorne E. C., James R. H., Savage P. and Alard O. (2008) Physical and chemical characteristics of particles produced by laser ablation of biogenic calcium carbonate. *Journal of Analytical Atomic Spectrometry* 23, 240–243.

Hauzer H., Evans D., Müller W., Rosenthal Y. and Erez J. (2018) Calibration of Na partitioning in the calcitic foraminifer Operculina ammonoides under variable Ca concentration: Toward reconstructing past seawater composition. *Earth and Planetary Science Letters* 497, 80–91.

Hauzer H., Evans D., Müller W., Rosenthal Y. and Erez J. (2021) Salinity Effect on Trace Element Incorporation in Cultured Shells of the Large Benthic Foraminifer Operculina ammonoides. *Paleoceanography and Paleoclimatology* 36, 1–19.

Higgins J. A. and Schrag D. P. (2015) The Mg isotopic composition of Cenozoic seawater - evidence for a link between Mg-clays, seawater Mg/Ca, and climate. *Earth and Planetary Science Letters* 416, 73–81.

Hill P. S., Tripati A. K. and Schauble E. A. (2014) Theoretical constraints on the effects of pH, salinity, and temperature on clumped isotope signatures of dissolved inorganic carbon species and precipitating carbonate minerals. *Geochimica et cosmochimica acta* 125, 610–652.

Hohenegger J., Yordanova E. and Hatta A. (2000) Remarks on West Pacific Nummulitidae (Foraminifera). *Journal of Foraminiferal Research* 30, 3–28.

Holland H. D. (2005) Sea level, sediments and the composition of seawater. *American Journal of Science* 305, 220–239.

Holland H. D. and Zimmermann H. (2000) The dolomite problem revisited1. *International Geology Review* 42, 481–490.

Holzmann M., Hohenegger J. and Pawlowski jan (2003) Molecular data reveal parallel evolution in nummulitid foraminifera. *The Journal of Foraminiferal Research* 33, 277–284.

Horita J., Zimmermann H. and Holland H. D. (2002) Chemical evolution of seawater during the Phanerozoic: Implications from the record of marine evaporites. *Geochimica et Cosmochimica Acta* 66, 3733–3756.

Hyland E. G., Sheldon N. D. and Cotton J. M. (2017) Constraining the early Eocene climatic optimum: A terrestrial interhemispheric comparison. *Bulletin of the Geological Society of America* 129, 244–252.

Isson T. T. and Planavsky N. J. (2018) Reverse weathering as a long-term stabilizer of marine pH and planetary climate. *Nature* 560, 471–475.

Jeffries T. E., Jackson S. E. and Longerich H. P. (1998) Application of a frequency quintupled Nd:YAG source (λ = 213 nm) for laser ablation inductively coupled plasma mass spectrometric analysis of minerals. *Journal of analytical atomic spectrometry* 13, 935–940.

Jochum K. P., Scholz D., Stoll B., Weis U., Wilson S. A., Yang Q., Schwalb A., Börner N., Jacob D. E. and Andreae M. O. (2012) Accurate trace element analysis of speleothems and biogenic calcium carbonates by LA-ICP-MS. *Chemical Geology* 318–319, 31–44.

Jochum K. P., Weis U., Stoll B., Kuzmin D., Yang Q., Raczek I., Jacob D. E., Stracke A., Birbaum K., Frick D. A., Günther D. and Enzweiler J. (2011) Determination of reference values for NIST SRM 610-617 glasses following ISO guidelines. *Geostandards and Geoanalytical Research* 35, 397–429.

Jones P. D. and Bradley R. S. (1992) 13 Climatic variations in the longest instrumental records. *Climate since AD 1500*, 246.

Keul N., Langer G., De Nooijer L. J. and Bijma J. (2013) Effect of ocean acidification on the benthic foraminifera Ammonia sp. is caused by a decrease in carbonate ion concentration. *Biogeosciences* 10, 6185–6198.

King C. (2016) A revised correlation of Tertiary rocks in the British Isles and adjacent areas of NW Europe. In *Geological Society of London*.

Kronberg B. I. (1985) Weathering dynamics and geosphere mixing with reference to the potassium cycle. *Physics of the Earth and Planetary Interiors* 41, 125–132.

Lea D. W., Mashiotta T. A. and Spero H. J. (1999) Controls on magnesium and strontium uptake in planktonic foraminifera determined by live culturing. *Geochimica et Cosmochimica Acta* 63, 2369–2379.

Li G., Ji J., Chen J. and Kemp D. B. (2009) Evolution of the Cenozoic carbon cycle : The roles of tectonics and CO_2 fertilization. 23, 1–11.

Li S., Li W., Beard B. L., Raymo M. E., Wang X., Chen Y. and Chen J. (2019) K isotopes as a tracer for continental weathering and geological K cycling. *Proceedings of the National Academy of Sciences of the United States of America* 116, 8740–8745.

Lowenstein T. K., Kendall B. and Anbar A. D. (2013) *The Geologic History of Seawater*. 2nd ed., Elsevier Ltd.

Lunt D. J., Jones T. D., Heinemann M., Huber M., LeGrande A., Winguth A., Loptson C., Marotzke J., Roberts C. D., Tindall J., Valdes P. and Winguth C. (2012) A model-data comparison for a multi-model ensemble of early Eocene atmosphere-ocean simulations: EoMIP. *Climate of the Past* 8, 1717–1736.

Marchitto Jr T. M., Curry W. B. and Oppo D. W. (2000) Zinc concentrations in benthic foraminifera reflect seawater chemistry. *Paleoceanography* 15, 299–306.

Marchitto T. M., Bryan S. P., Doss W., McCulloch M. T. and Montagna P. (2018) A simple biomineralization model to explain Li, Mg, and Sr incorporation into aragonitic foraminifera and corals. *Earth and Planetary Science Letters* 481, 20–29.

Mayfield K. K., Eisenhauer A., Santiago Ramos D. P., Higgins J. A., Horner T. J., Auro M., Magna T., Moosdorf N., Charette M. A., Gonneea M. E., Brady C. E., Komar N., Peucker-Ehrenbrink B. and Paytan A. (2021) Groundwater discharge impacts marine isotope budgets of Li, Mg, Ca, Sr, and Ba. *Nature Communications* 12, 1–9.

Meckler A. N., Sexton P. F., Piasecki A. M., Leutert T. J., Marquardt J., Ziegler M., Agterhuis T., Lourens L. J., Rae J. W. B., Barnet J., Tripati A. and Bernasconi S. M. (2022) Cenozoic evolution of deep ocean temperature from clumped isotope thermometry. *Science* 377, 86–90.

Michalopoulos P. and Aller R. C. (1995) Rapid clay mineral formation in Amazon delta sediments: Reverse weathering and oceanic elemental cycles. *Science* 270, 614–617.

Miller K. G., Fairbanks R. G. and Mountain G. S. (1987) Tertiary oxygen isotope synthesis, sea level history, and continental margin erosion. *Paleoceanography* 2, 1–19.

Misra S. and Froelich P. N. (2012) Lithium isotope history of cenozoic seawater: Changes in silicate weathering and reverse weathering. *Science* 335, 818–823.

Modestou S. E., Leutert T. J., Fernandez A., Lear C. H. and Meckler A. N. (2020) Warm Middle Miocene Indian Ocean Bottom Water Temperatures: Comparison of Clumped Isotope and Mg/Ca-Based Estimates. *Paleoceanography and Paleoclimatology* 35.

Müller W. and Fietzke J. (2016) The role of LA-ICP-MS in palaeoclimate research. *Elements* 12, 329–334.

Müller W., Shelley M., Miller P. and Broude S. (2009) Initial performance metrics of a new custom-

designed ArF excimer LA-ICPMS system coupled to a two-volume laser-ablation cell. *Journal of Analytical Atomic Spectrometry* 24, 209–214.

Nambiar R., Hauzer H., Gray W. R., Henehan M. J., Cotton L., Erez J., Rosenthal Y., Renema W., Müller W. and Evans D. (2023) Controls on potassium incorporation in foraminifera and other marine calcifying organisms. *Geochimica et Cosmochimica Acta* 351, 125–138.

Nambiar R., Kniest J. F., Schmidt A., Raddatz J., Müller W. and Evans D. (2024) Accurate measurement of K/Ca in low [K] carbonate samples using laser-ablation sector-field inductively coupled plasma mass spectrometry. *Rapid Communications in Mass Spectrometry* 38. *doi: 10.1002/rcm.9692*.

Nambiar R., Müller W. and Evans D. Evaluating accuracy improvement of laser ablation ICPMS element quantification in silicate glasses and carbonates via correction for downhole fractionation – an old problem reassessed. *(submitted)*.

De Nooijer L. J., Toyofuku T. and Kitazato H. (2009) Foraminifera promote calcification by elevating their intracellular pH. *Proceedings of the National Academy of Sciences of the United States of America* 106, 15374–15378.

O'Brien C. L., Robinson S. A., Pancost R. D., Sinninghe Damsté J. S., Schouten S., Lunt D. J., Alsenz H., Bornemann A., Bottini C., Brassell S. C., Farnsworth A., Forster A., Huber B. T., Inglis G. N., Jenkyns H. C., Linnert C., Littler K., Markwick P., McAnena A., Mutterlose J., Naafs B. D. A., Püttmann W., Sluijs A., van Helmond N. A. G. M., Vellekoop J., Wagner T. and Wrobel N. E. (2017) Cretaceous sea-surface temperature evolution: Constraints from TEX86 and planktonic foraminiferal oxygen isotopes. *Earth-Science Reviews* 172, 224–247.

Pagani M., Freeman K. H. and Arthur M. A. (1999) Late Miocene atmospheric CO_2 concentrations and the expansion of C4 grasses. *Science* 285, 876–879.

Pearson P. N. and Palmer M. R. (2000) Atmospheric carbon dioxide concentrations over the past 60 million years. *Nature* 406, 695–699.

Pearson P. N. and Palmer M. R. (1999) Middle Eocene seawater pH and atmospheric carbon dioxide concentrations. *Science* 284, 1824–1826.

Peral M., Daëron M., Blamart D., Bassinot F., Dewilde F., Smialkowski N., Isguder G., Bonnin J., Jorissen F., Kissel C. and others (2018) Updated calibration of the clumped isotope thermometer in planktonic and benthic foraminifera. *Geochimica et Cosmochimica Acta* 239, 1–16.

Pogge Von Strandmann P. A. E., Forshaw J. and Schmidt D. N. (2014) Modern and Cenozoic records of seawater magnesium from foraminiferal Mg isotopes. *Biogeosciences* 11, 5155–5168.

Prazeres M. and Renema W. (2019) Evolutionary significance of the microbial assemblages of large benthic Foraminifera. *Biological Reviews* 94, 828–848.

Rae J. W. B., Zhang Y. G., Liu X., Foster G. L., Stoll H. M. and Whiteford R. D. M. (2021) Atmospheric CO_2 over the past 66 million years from marine archives. *Annual Review of Earth and Planetary*

Sciences 49, 609–641.

Raymo M. E. and Ruddiman W. F. (1992) Tectonic forcing of late Cenozoic climate. *Nature* 359, 117–122.

Renema W. (2007) *Biogeography, time and place: distributions, barriers and islands*., Springer Science \& Business Media.

Renema W. (2002) Larger foraminfera as marine environmental indicators. *Scripta Geologica* 124, 1–260.

Renema W., Bellwood D. R., Braga J. C., Bromfield K., Hall R., Johnson K. G., Lunt P., Meyer C. P., McMonagle L. B., Morley R. J., O'Dea A., Todd J. A., Wesselingh F. P., Wilson M. E. J. and Pandolfi J. M. (2008) Hopping hotspots: Global shifts in marine biodiversity. *Science* 321, 654–657.

Rickaby R. E. M. and Elderfield H. (1999) Planktonic foraminiferal Cd/Ca: paleonutrients or paleotemperature? *Paleoceanography* 14, 293–303.

Rosenthal Y., Boyle E. A. and Slowey N. (1997) Temperature control on the incorporation of magnesium, strontium, fluorine, and cadmium into benthic foraminiferal shells from Little Bahama Bank: Prospects for thermocline paleoceanography. *Geochimica et Cosmochimica Acta* 61, 3633–3643.

Ross C. A. (1974) Evolutionary and ecological significance of large calcareous Foraminiferida (Protozoa), Great Barrier Reef. In *Proceedings of the Second International Coral Reef Symposium* pp. 327–333.

Royer D. L. (2014) *Atmospheric CO_2 and O_2 During the Phanerozoic : Tools , Patterns , and Impacts*. 2nd ed., Elsevier Ltd.

Rundgren M. and Björck S. (2003) Late-glacial and early Holocene variations in atmospheric CO_2 concentration indicated by high-resolution stomatal index data. *Earth and Planetary Science Letters* 213, 191–204.

Russo R. E., Mao X. L., Borisov O. V. and Haichen L. (2000) Influence of wavelength on fractionation in laser ablation ICP-MS. *Journal of analytical atomic spectrometry* 15, 1115–1120.

Santiago Ramos D. P., Morgan L. E., Lloyd N. S. and Higgins J. A. (2018) Reverse weathering in marine sediments and the geochemical cycle of potassium in seawater: Insights from the K isotopic composition ($^{41}K/^{39}K$) of deep-sea pore-fluids. *Geochimica et Cosmochimica Acta* 236, 99–120.

Savin S. M., Douglas R. G. and Stehli F. G. (1975) Tertiary marine paleotemperatures. *Geological Society of America Bulletin* 86, 1499–1510.

Shackleton N. J. (1975) Paleotemperature history of the Cenozoic and the initiation of Antarctic glaciation: oxygen and carbon isotope analyses in DSDP Sites 277, 279, and 281. *Initial Reports Deep Sea Drilling Project* 29, 743–755.

Shalev N., Bontognali T. R. R., Wheat C. G. and Vance D. (2019) New isotope constraints on the Mg

oceanic budget point to cryptic modern dolomite formation. *Nature communications* 10, 5646.

Spencer R. J. and Hardie L. A. (1990) Control of seawater composition by mixing of river waters and mid ocean ridge hydrothermal brines. In *Fluid-mineral interactions: A tribute to H. P. Eugster* pp. 409– 419.

Stanley S. M. and Hardie L. A. (1998) Secular oscillations in the carbonate mineralogy of reef-building and sediment-producing organisms driven by tectonically forced shifts in seawater chemistry. *Palaeogeography, Palaeoclimatology, Palaeoecology* 144, 3–19.

Tipper E. T., Galy A., Gaillardet J., Bickle M. J., Elderfield H. and Carder E. A. (2006) The magnesium isotope budget of the modern ocean: constraints from riverine magnesium isotope ratios. *Earth and Planetary Science Letters* 250, 241–253.

Turchyn A. V and DePaolo D. J. (2019) Seawater chemistry through Phanerozoic time. *Annual Review of Earth and Planetary Sciences* 47, 197–224.

Urey H. C., Lowenstam H. A., Epstein S. and McKinney C. R. (1951) Measurement of paleotemperatures and temperatures of the Upper Cretaceous of England, Denmark, and the southeastern United States. *Geological Society of America Bulletin* 62, 399–416.

Walker J. C. G., Hays P. B. and Kasting J. F. (1981) Weathering rates in 106 gm km -2 yr -1 of dissolved Si02 . Parentheses signify. *Journal of Geophysical Research* 86, 9776–9782.

Wang H. A. O., Grolimund D., Giesen C., Borca C. N., Shaw-Stewart J. R. H., Bodenmiller B. and Günther D. (2013) Fast chemical imaging at high spatial resolution by laser ablation inductively coupled plasma mass spectrometry. *Analytical Chemistry* 85, 10107–10116.

Wang K., Peucker-Ehrenbrink B., Chen H., Lee H. and Hasenmueller E. A. (2021) Dissolved potassium isotopic composition of major world rivers. *Geochimica et Cosmochimica Acta* 294, 145–159.

Wang Z., Hattendorf B. and Günther D. (2006) Analyte Response in Laser Ablation Inductively Coupled Plasma Mass Spectrometry. *Journal of the American Society for Mass Spectrometry* 17, 641–651.

Weldeab S., Lea D. W., Schneider R. R. and Andersen N. (2007) 155,000 years of West African monsoon and ocean thermal evolution. *science* 316, 1303–1307.

Westerhold T., Marwan N., Drury A. J., Liebrand D., Agnini C., Anagnostou E., Barnet J. S. K., Bohaty S. M., De Vleeschouwer D., Florindo F., Frederichs T., Hodell D. A., Holbourn A. E., Kroon D., Lauretano V., Littler K., Lourens L. J., Lyle M., Pälike H., Röhl U., Tian J., Wilkens R. H., Wilson P. A. and Zachos J. C. (2020) An astronomically dated record of Earth's climate and its predictability over the last 66 million years. *Science* 369, 1383–1388.

Westerhold T., Rhl U., Donner B., McCarren H. K. and Zachos J. C. (2011) A complete high-resolution Paleocene benthic stable isotope record for the central Pacific (ODP Site 1209). *Paleoceanography* 26, 1–13.

Westerhold T., Röhl U., Donner B. and Zachos J. C. (2018) Global Extent of Early Eocene Hyperthermal

Events: A New Pacific Benthic Foraminiferal Isotope Record From Shatsky Rise (ODP Site 1209). *Paleoceanography and Paleoclimatology* 33, 626–642.

Wilkinson B. H. and Algeo T. J. (1989) Sedimentary carbonate record of calcium-magnesium cycling. *American Journal of Science* 289, 1158–1194.

Zachos J. C., Dickens G. R. and Zeebe R. E. (2008) An early Cenozoic perspective on greenhouse warming and carbon-cycle dynamics. *Nature* 451, 279–283.

Zachos J., Pagani M., Sloan L., Thomas E. and Billups K. (2001) Trends, rhythms, and aberrations in global climate 65 Ma to present. *science* 292, 686–693.

Zeebe R. E. and Wolf-Gladrow D. (2001) *CO_2 in seawater: equilibrium, kinetics, isotopes*. ed. Elsevier Science, Gulf Professional Publishing.

Zheng X. Y., Beard B. L., Neuman M., Fahnestock M. F., Bryce J. G. and Johnson C. M. (2022) Stable potassium (K) isotope characteristics at mid-ocean ridge hydrothermal vents and its implications for the global K cycle. *Earth and Planetary Science Letters* 593, 117653.

Zhou X., Rosenthal Y., Haynes L., Si W., Evans D., Huang K. F., Hönisch B. and Erez J. (2021) Planktic foraminiferal Na/Ca: A potential proxy for seawater calcium concentration. *Geochimica et Cosmochimica Acta* 305, 306–322.